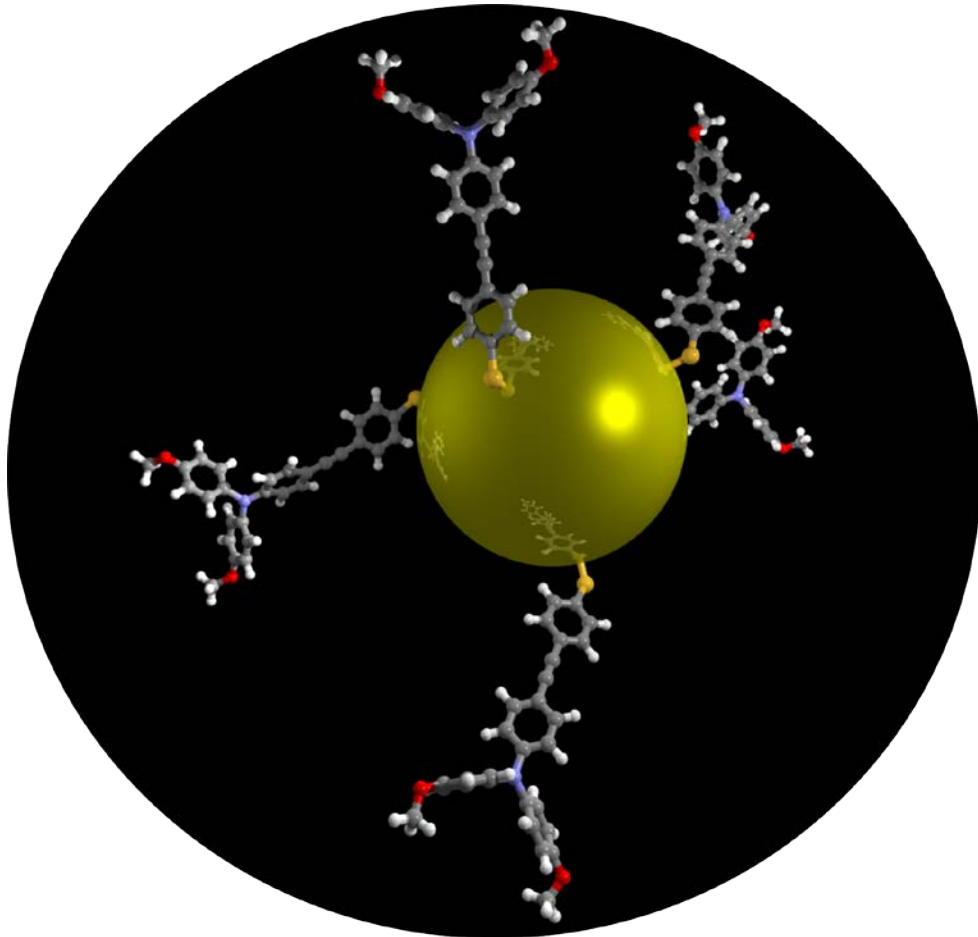


Physical Properties of Chromophore Functionalized Gold Nanoparticles



Dissertation zur Erlangung des
naturwissenschaftlichen Doktorgrades
der Bayerischen Julius-Maximilians-Universität Würzburg

vorgelegt von

Christian Müller

aus Kreuztal-Kredenbach

Würzburg 2011

Eingereicht bei der Fakultät für Chemie und Pharmazie am

Gutachter der schriftlichen Arbeit

1. Gutachter: _____

2. Gutachter: _____

Prüfer des öffentlichen Promotionskolloquiums

1. Prüfer: _____

2. Prüfer: _____

3. Prüfer: _____

Datum des öffentlichen Promotionskolloquiums

Doktorurkunde ausgehändigt am

Die vorliegende Arbeit wurde in der Zeit von November 2005 bis März 2011 am Institut für Organische Chemie der Universität Würzburg angefertigt.

Mein besonderer Dank gilt
Herrn Prof. Dr. Christoph Lambert
für die Vergabe des vielseitigen Themas, die intensive Betreuung und Förderung und das mit
vielen Anregungen und Diskussionen verbundene Interesse an dieser Arbeit.

Contents

Inhalt

1	Introduction	1
1.1	Structure of Spherically Shaped Gold Nanoparticles	4
1.2	Gold Core Structure	5
1.3	Structure of Thiol-Functionalized Gold Nanoparticles.....	6
1.3.1	Au ₁₀₂ (SR) ₄₄	6
1.3.2	[NR' ₄][Au ₂₅ (SR) ₁₈]	7
1.3.3	Au ₃₈ (SR) ₂₄	8
1.3.4	The Superatom Concept.....	9
1.4	Absorption Properties of Metal Nanoparticles.....	10
1.5	Electrochemical Properties of Redox-Center-Functionalized Metal Nanoparticles ..	12
1.6	General Aspects for the Synthesis of Thiol Protected Spherically Shaped Nanoparticles	15
1.7	Analytical Methods	17
2	Optical and Electrochemical Properties of Triarylamine and Perchlorinated Triarylmethyl Functionalized Gold Nanoparticles	18
2.1	Optical and Electrochemical Properties of Triarylamin-Gold-Nanoparticle Conjugates: Short π -Conjugated Bridging Unit.....	20
2.1.1	Synthesis	20
2.1.2	Analysis.....	23
2.1.3	Electrochemical Measurements	27
2.1.4	UV/vis/NIR Absorption Spectroscopy and Fluorescence-Anisotropy Measurements ..	28
2.1.5	Spectroelectrochemistry	30
2.1.6	Conclusion	33
2.2	Optical and Electrochemical Properties of Triarylamin-Gold-Nanoparticle Conjugates: Varying the Bridging Unit	34
2.2.1	Synthesis	35
2.2.2	Analysis.....	39
2.2.3	Electrochemistry	44
2.2.4	UV/vis/NIR Absorption Spectroscopy.....	51

2.2.5	Spectroelectrochemistry	55
2.2.6	Conclusions	58
2.3	Optical and Electrochemical Properties of Perchlorinated Triarylmethyl Radical-Functionalized Gold Nanoparticle Systems	60
2.3.1	Introduction	60
2.3.2	Synthesis	61
2.3.3	Analysis.....	62
2.3.4	Electrochemistry	64
2.3.5	UV/vis/NIR Absorption Spectroscopy.....	65
2.3.6	Spectroelectrochemistry	66
2.3.7	Conclusion	67
2.4	Synthesis of Au-Tara Systems with Short Bridging Units.....	68
2.4.1	Synthesis of Au-Tara5.....	68
2.4.2	Synthesis of Au-Tara6.....	69
2.4.3	Concluding Remarks	70
3	Raman-Reporter Molecules for SERS Application	71
3.1	Introduction	71
3.1.1	Drug Delivery Systems	71
3.1.2	Tuning the Absorption Properties	72
3.1.3	Light Emitting and Scattering Probes	72
3.1.4	Fluorescent Probes	74
3.1.5	Surface Enhanced Raman Spectroscopy (SERS) Probes.....	75
3.2	Synthesis	78
3.3	SERS-Measurements	83
3.4	Immuno-SERS Microscopy	84
3.5	Conclusion	86
4	Summary	87
5	Experimental Section	90
5.1	Analytical Methods	90
5.1.1	General Analytical Methods	90
5.1.2	NMR Spectroscopy	90

5.1.3	Mass Spectroscopy.....	91
5.1.4	Osteryoung Square Wave Voltammetry and Cyclic Voltammetry.....	91
5.1.5	UV/vis/NIR Spectroscopy.....	92
5.1.6	Spectroelectrochemistry.....	92
5.1.7	Polarised Steady-State Fluorescence Spectroscopy.....	92
5.1.8	Scanning Transmission Electron Microscopy (STEM).....	93
5.1.9	X-ray Photoelectron Spectroscopy (XPS).....	93
5.1.10	Thermogravimetric Analysis (TGA).....	94
5.1.11	Recycling-GPC.....	94
5.1.12	IR-Spectroscopy.....	94
5.2	Synthesis.....	95
6	Literature	128
7	Table of Formulas	137
8	Zusammenfassung	140

Abbreviations

APTMS	3-amino- <i>n</i> -propyltrimethoxysilane
CV	cyclic voltammetry
DMTCC	dimethylthiocarbamoyl chloride
DOSY	diffusion ordered NMR Spectroscopy
EDC	ethyl-dimethyl-aminopropylcarbodiimide
GPC	gel permeation chromatography
IVCT	intervalence charge transfer
LSPR	localized surface plasmon resonance
AuNP	thiol protected gold nanoparticle
NHS	<i>N</i> -hydroxy-succinimide
OSWV	Osteryoung square wave voltammetry
PCTM	perchlorinated triarylmethyl
PDT	photodynamic therapy
QDL	quantized double layer
SAH	succinic anhydride
SAM	self-assembled monolayer
SEC	spectroelectrochemistry
SEMA	SERS-marker
SERS	surface enhanced Raman spectroscopy
SPB	surface plasmon band
STEM	scanning transmission electron microscopy
Tara	triarylamine
TBAF	tetrabutylammonium fluoride
TBAH	tetrabutylammonium hexafluorophosphate
TEM	transmission electron microscopy
TEOS	tetraethoxyorthosilicate
TGA	thermogravimetric analysis
XPS	X-ray photoelectron spectroscopy

1 Introduction

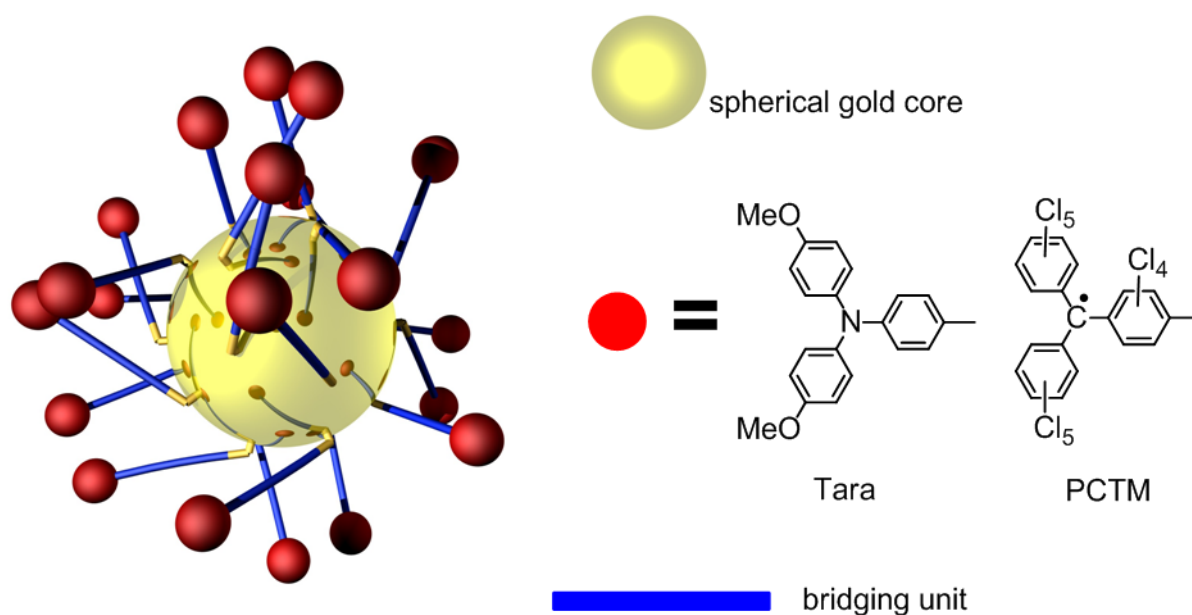
Nanoparticle systems hold tremendous promise in the field of biomedical,^{1, 2} catalytic^{3, 4} and sensing^{5, 6} applications.⁷ Different kinds of metals, such as gold, silver and platinum, were used for the fabrication of nanoparticle systems. But also semiconductor nanoparticles were synthesized, for example CdS,^{8, 9} PbS,¹⁰ Ag₂S,^{4, 11} CdSe,^{12, 13} and TiO₂.^{14, 15} By far the most studied of these are gold nanoparticles. Generally, gold nanoparticle systems are composed of a metal core and a protecting organic layer. The organic layer is introduced to prevent agglomeration of the metal core and to incorporate functionalities into the hybrid system.

The metal core can be used as a template to bring many organic molecules in close contact to form stable mono- or mixed-layers. This concept is also applied in the area of self-assembled monolayers (SAMs) on planar gold surfaces. These structures are e.g. useful to study the heterogeneous electron transfer between the gold surface and an attached redox active molecule.¹⁶⁻¹⁹ However the two dimensional character of these systems limits the methods the chemisorbed molecules can be probed with.^{20, 21} Nanoparticle systems can be adsorbed onto surfaces but are also soluble in many solvents which increases the variety of analytical methods. For example, the optical properties of chromophore-functionalized nanoparticle systems can be studied very well, whereas chromophores attached to planar surfaces have very low absorbance.

The physical properties of the nanoparticle hybrid systems are one of the most fascinating aspects in the field of nanoparticle research. Concerning the metal particle there are size-dependent electronic and optical effects, such as the quantized double layer (QDL) charging,^{22, 23} the characteristic surface plasmon absorption bands (SPB)⁷ or the fluorescence of semiconductor nanoparticles.²⁴ Especially the SPB is very sensitive to the size but also to the shape^{1, 2} and the dielectric function of the components.²⁵ Tuning the three parameters is a very powerful tool in the development of new sensing applications, for example the localized surface plasmon resonance (LSPR) spectroscopy.²⁶⁻²⁹ Also, the attached organic layer offers new features which are only seen in the specific arrangement of the organic molecules on the metal core. This includes mainly optical effects, for example, the surface-enhanced Raman scattering (SERS) effect^{6, 30} and the surface enhanced fluorescence effect.³¹⁻³³ For these surface-enhanced effects generally chromophores are linked to the metal core.

The first part of this work deals with the synthesis of some thiol protected gold nanoparticles (AuNP) and the investigation of the optical, electrochemical and

spectroelectrochemical properties of these hybrid structures. The nanoparticles consist of a redox active chromophore ligand shell attached via a bridging unit to small spherical gold nanoparticles (Scheme 1 left). The intension of the investigations is to study chromophore-chromophore interactions and gold core-chromophore interactions. For this reason the chemical structure and the length of the bridging unit connecting the chromophore and the gold core are varied. Triarylamine (Tara) and perchlorinated triarylmethyl (PCTM)-radical units are used for this purpose as chromophores because of their optical and electrochemical stability (Scheme 1).



Scheme 1. Triarylamine (Tara) and perchlorinated triarylmethyl (PCTM)-radical functionalized gold nanoparticles.

The second part of this work aims at the synthesis of SERS-markers (**SEMA**) for tissue imaging by immuno-SERS microscopy. The SERS-markers are designed to possess a thiol group to bind to the Ag/Au nanoshell, a polar tail-group to make the marker soluble in polar solvents and a Raman-active vibrational band oriented along the molecular axis to generate intense SERS-signals (Chart 1). Molecules with different Raman-active functionalities were synthesized and adsorbed onto Au/Ag nanoshells in order to form SERS-labels. The Raman activity of the SERS-labels was studied via SERS.

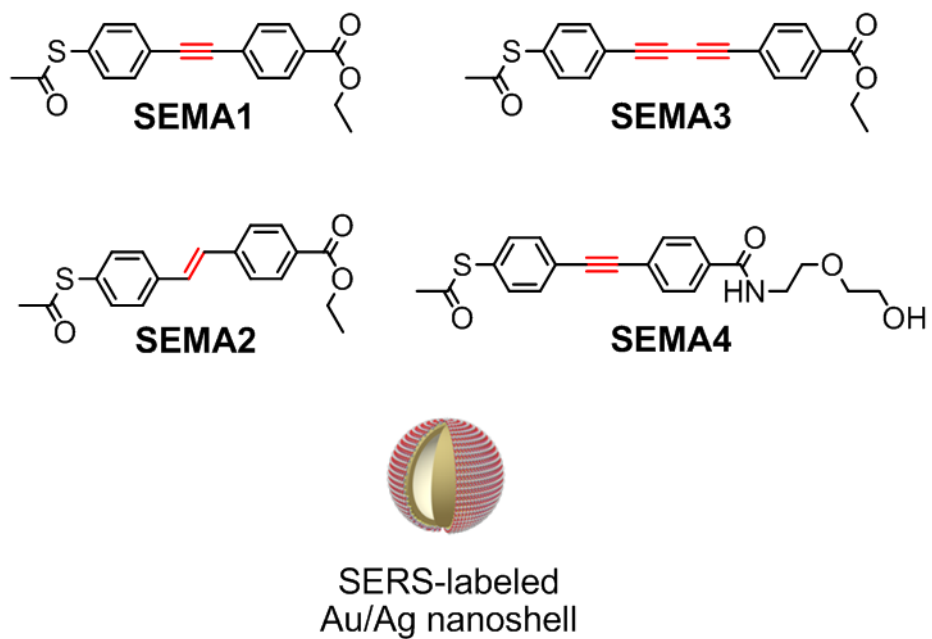


Chart 1.

1.1 Structure of Spherically Shaped Gold Nanoparticles

Gold nanoparticles can be obtained in different shapes and sizes, e.g. nanorods, nanospheres, nanoshells or platonic nanoparticles.³⁴⁻⁴⁴ Tuning the shape and the size is very desirable because both parameters are important factors for the electronic and optical properties of metal particles.

Monolayer protected gold nanospheres can be synthesized in sizes up to 100 nm. Generally the product fractions consist of particles with different sizes. A detailed analysis of these fractions revealed that there are some preferred particle sizes. This fact is illustrated in Figure 1 where the size exclusion chromatography experiment of a nanoparticle sample exhibits several peak maxima which are related to specific particle sizes. This indicates the presence of several main particle fractions which are denoted as “magic-numbers”.

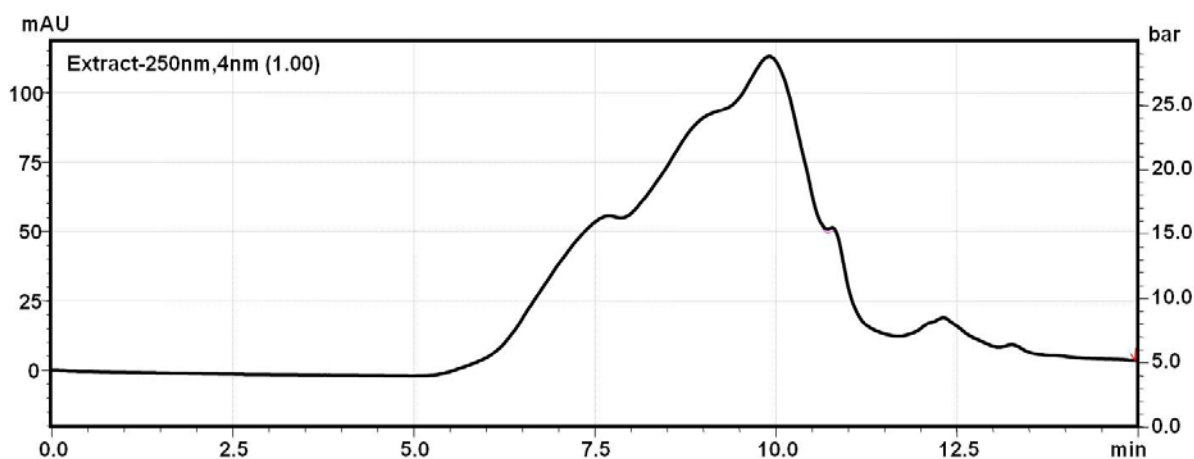


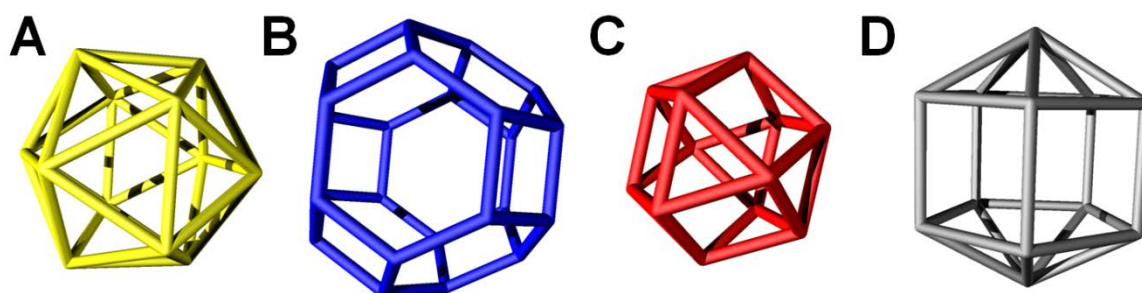
Figure 1. Size exclusion chromatography experiment of a gold nanoparticle (**Au-Tara2**, see Chart 4) sample; detection wavelength 250 nm.

Studying the size of poly(vinylpyrrolidone) stabilized gold nanoparticles via MALDI-MS, Tsunoyama et al. detected gold clusters with 35 ± 1 , 43 ± 1 , 58 ± 1 , 70 ± 3 , 107 ± 4 , 130 ± 1 and 150 ± 2 gold atoms.⁴⁵ Investigations on thiol protected gold cluster have revealed that gold core sizes with 25,⁴⁶⁻⁴⁸ 38,⁴⁹⁻⁵⁴ 102,⁵⁵ 116,⁵⁶ 140,^{50, 56} 225,⁵⁶ 314⁵⁶ and 459⁵⁶ gold atoms were predominately formed.

1.2 Gold Core Structure

In order to study the structure of the gold nanoparticle in more detail, several groups have extracted monodisperse fractions from polydisperse samples. High-resolution electron microscopy HREM and X-ray diffraction measurements combined with theoretical investigations resulted in a detailed picture of the gold core structure.^{46, 54-61} First, the gold core has a crystalline structure. This crystalline structure can be detected in electron microscopy measurements (Figure 2) if the lattice planes are oriented parallel to the electron beam. Therefore a face centered cubic structure of the gold core was observed for cluster sized above a diameter of 1 nm.^{56, 58}

Second, the gold core has a polyhedral shape, for example icosahedral,⁴⁶ truncated octahedral,^{56, 62, 63} cuboctahedral or truncated decahedron^{55, 58} shape (Scheme 2).



Scheme 2. Polyhedral shapes: A) icosahedron, B) truncated octahedron, C) cuboctahedron and D) example for a truncated decahedron.

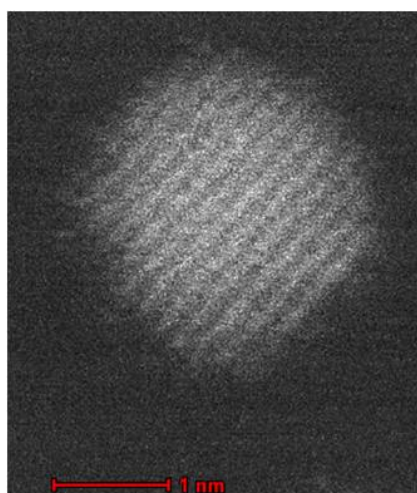


Figure 2. Scanning transmission electron microscopy (STEM) image of **Au-Tara4** (see Chart 4).

The surface of these polyhedral shaped gold cores consists of edge, vertex and face sites. The protecting ligands, e.g. thiols, can bind to all of these sites. Regarding the self-assembled monolayers on flat gold (111) surfaces, the edge and vertex positions are denoted as defect sites. These defect sites combined with the curvature of the gold core lead to a high surface coverage of the ligands. Hostelter et al. have shown that the coverage of aliphatic thiols on gold nanoparticles is much higher than for aliphatic thiols on flat gold surfaces.⁶⁴ Only at very large particle sizes does the coverage

approach the value for flat surfaces (38%).

1.3 Structure of Thiol-Functionalized Gold Nanoparticles

Until now, the X-ray structures of only three thiol-functionalized gold nanoparticles have been determined. The analysis revealed a new view of the gold core structure and the thiol-gold binding motif. Furthermore, the results were used to explain the stability of these clusters with the superatom concept (see chapter 1.3.4).⁶⁰

1.3.1 Au₁₀₂(SR)₄₄

The first total structure determination of a *p*-mercaptobenzoic acid (*p*-MBA) thiol-protected gold nanoparticle was published by the group of Kronberg, based on X-ray diffraction from single crystals (Figure 3 top).⁵⁵ The cluster consists of 102 gold atoms and 44 thiol ligands arranged around the gold core.

The Au₁₀₂ gold core: the gold core can be described as a 49-gold atom Marks decahedral with two 20-gold atom caps with *C*₅ symmetry on opposite poles. Additionally a 13-gold atom band with no apparent symmetry is located on the equator which is responsible for the overall chirality of the particles.⁵⁵ Summing up, the gold core consists of $49 + (2 \times 20) + 13 = 102$ gold atoms.

The gold-thiolate binding motif: X-ray structure analysis combined with a full density functional treatment of the electronic structure of the Au₁₀₂(*p*-MBA)₄₄ resulted in a detailed picture of the gold-thiolate binding motif.^{55, 60, 65} The thiols form 21 RS(AuSR)_{*x*} (*x* = 1, 2) ligand units which consist of two or three thiols connected via one or two gold atoms (see Figure 3 middle, small yellow and brown balls). These ligand units bind in a bridge conformation to two gold atoms (see Figure 3 middle, large brown balls) of an inner gold core. The 21 RS(AuSR)_{*x*} (*x* = 1, 2) ligand units can be divided into 19 units of *x* = 1 and two units of *x* = 2. Consequently there are 23 gold ligand atoms (Au_{ligand}) and $102 - 23 = 79$ gold core atoms (Au_{core}) which form the inner gold core. The inner gold core can be alternatively to the concept above described as a decahedral Au₇₉ core (approximately *D*_{5h}-symmetric, Figure 3 bottom). The 21 ligand units are arranged around the Au₇₉ core in a *staple* motif. Thus, the

nanoparticle is not a thiolate protected Au_{102} core but rather a Au_{79} core protected with gold-thiolate staples and is more accurately described in the formulation $\text{Au}_{79}[\text{Au}_{23}(\text{p-MBA})_{44}]$.

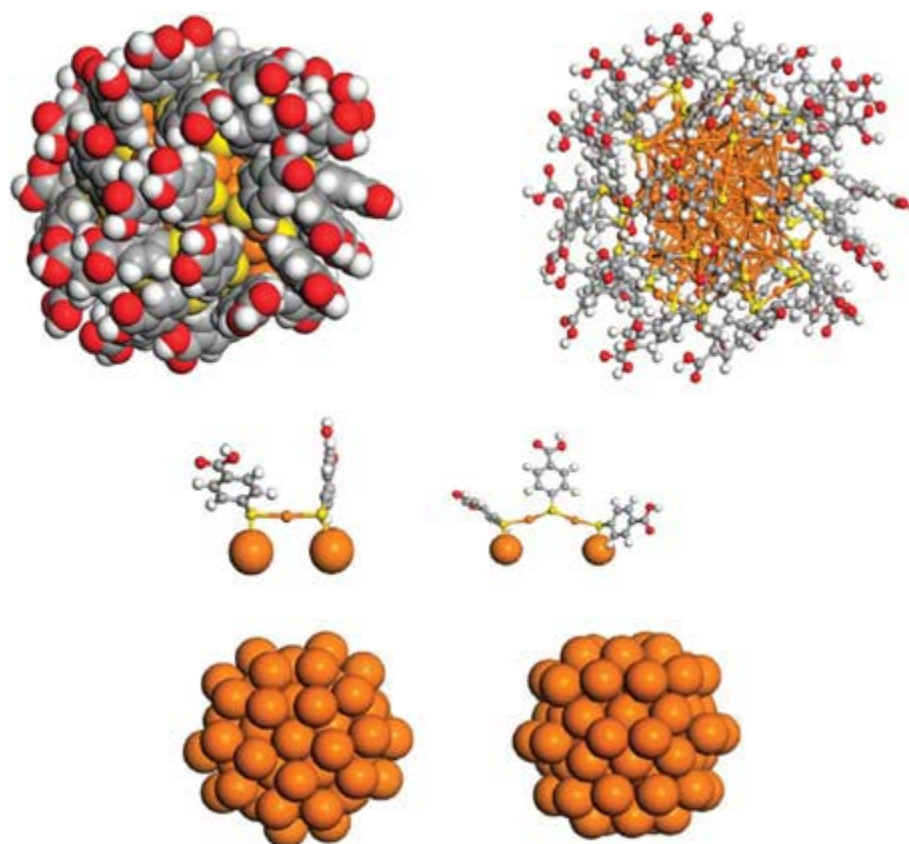


Figure 3. X-ray crystal structure of $\text{Au}_{102}(\text{p-MBA})_{44}$. Top: two views of the $\text{Au}_{102}(\text{p-MBA})_{44}$ cluster. Middle: the protecting RSAuSR and $\text{SR}(\text{AuSR})_2$ staples, bound to core Au atoms (large balls). Bottom: two views of the Au_{79} decahedral core. Legend: Au: brown, S: yellow, C: gray, O: red, H: white.⁶⁰ – Reproduced by permission of [The Royal Society of Chemistry](#).

1.3.2 $[\text{NR}'_4][\text{Au}_{25}(\text{SR})_{18}]$

The composition of nanoparticles with 25 gold atoms has been intensively studied in recent years.^{47, 48, 61} However the first crystal structure of a thiol protected Au_{25} cluster was published by the group of Murray in 2008.⁴⁶ They studied a Au_{25} core passivated with $\text{SCH}_2\text{CH}_2\text{Ph}$ ligands. The unit cell of the crystal also contains a quaternary ammonium counter ion (TOA^+) which indicates that the gold is negatively charged (Figure 4 c). The crystal structure reveals that one central gold atom is surrounded by 12 gold atoms positioned on the vertices of an icosahedron (Figure 4 a). This core is capped with 12 gold atoms that are centered above 12 of the 20 faces of the Au_{13} icosahedron (Figure 4 b, the arrangement is

clarified by the dotted black lines). These 12 gold atoms form six orthogonal semirings of $(\text{Au}_2(\text{SCH}_2\text{CH}_2\text{Ph})_3)$ around the Au_{13} core (Figure 4 b). Hence the structure can be formulated as an Au_{13} core capped with 6 $(\text{Au}_2(\text{SCH}_2\text{CH}_2\text{Ph})_3)$ ligand units and one counter ion. Summing up, the X-ray analysis of the Au_{25} cluster also points out that the nanoparticle is not a thiolate protected Au_{25} core but a *staple-protected* Au_{13} core.^{46, 60}

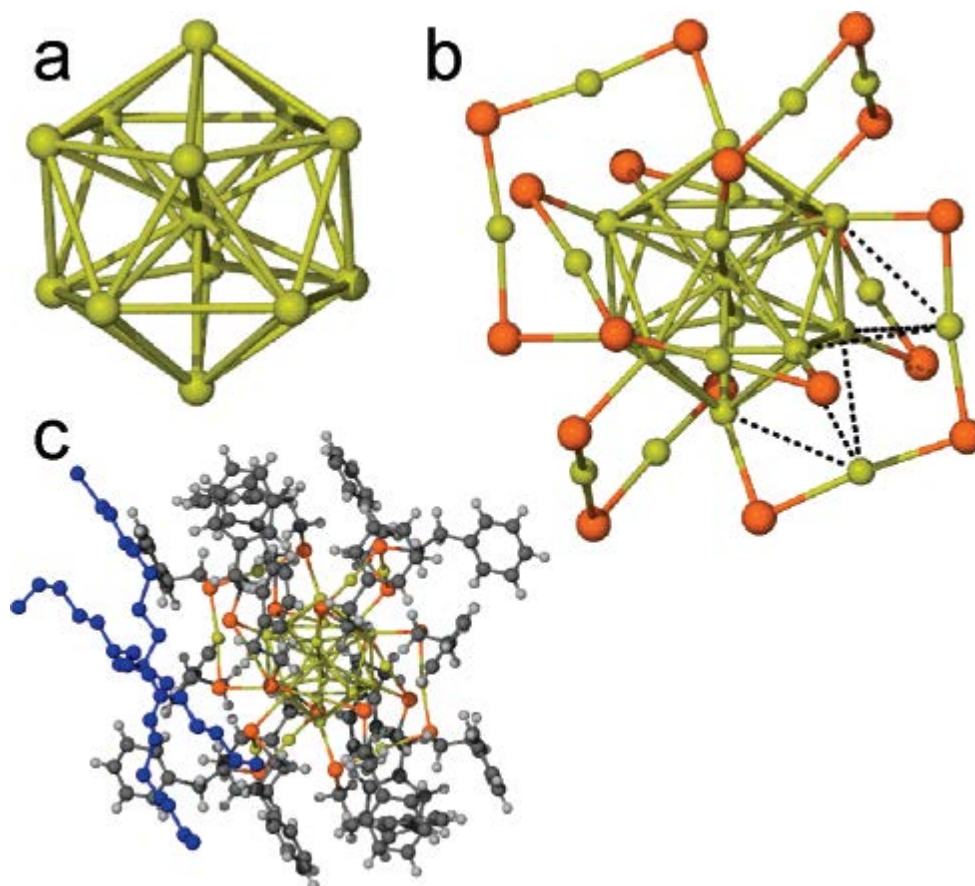


Figure 4. X-ray crystal structure of $[\text{TOA}^+][\text{Au}_{25}(\text{SCH}_2\text{CH}_2\text{Ph})_{18}^-]$. (a) Arrangement of the Au_{13} core, (b) six orthogonal $-\text{Au}_2(\text{SCH}_2\text{CH}_2\text{Ph})_3-$ ligand units surrounding the Au_{13} core, (c) $[\text{TOA}^+][\text{Au}_{25}(\text{SCH}_2\text{CH}_2\text{Ph})_{18}^-]$ structure with the ligands and TOA^+ cation (depicted in blue). Legend: Au: yellow, S: orange, C: gray, H: white. "Reprinted with permission from Ref 46.⁴⁶ Copyright 2008 American Chemical Society."

1.3.3 $\text{Au}_{38}(\text{SR})_{24}$

The synthesis and composition of thiolate-functionalized Au_{38} cluster has been investigated by several groups.⁵¹⁻⁵³ In 2010, Qian et al. presented the first X-ray diffraction

analysis of a Au_{38} cluster passivated with 24 thiol ligands (2-phenylethanethiol, $\text{SCH}_2\text{CH}_2\text{Ph}$).⁵⁴ The analysis revealed that the unit cell contains a pair of enantiomeric nanoparticles. The left handed isomer is shown in Figure 5 (left side).

The cluster is based on a face-fused biicosahedral Au_{23} core. Analyzing the structure in more detail the core consists of two icosahedrons which are fused together via sharing a common Au_3 face (Figure 5 right side). The Au_{23} core is capped by a second shell comprised of the remaining 15 gold atoms. These 15 gold atoms and the 24 thiol ligands form three monomeric $\text{Au}(\text{SR})_2$ ligand units and six dimeric $\text{Au}_2(\text{SR})_3$ ligand units which are arranged around the Au_{23} core in a *staple* motif. Thus the *staple* motif is also seen for $\text{Au}_{38}(\text{SR})_{24}$ nanoparticles.

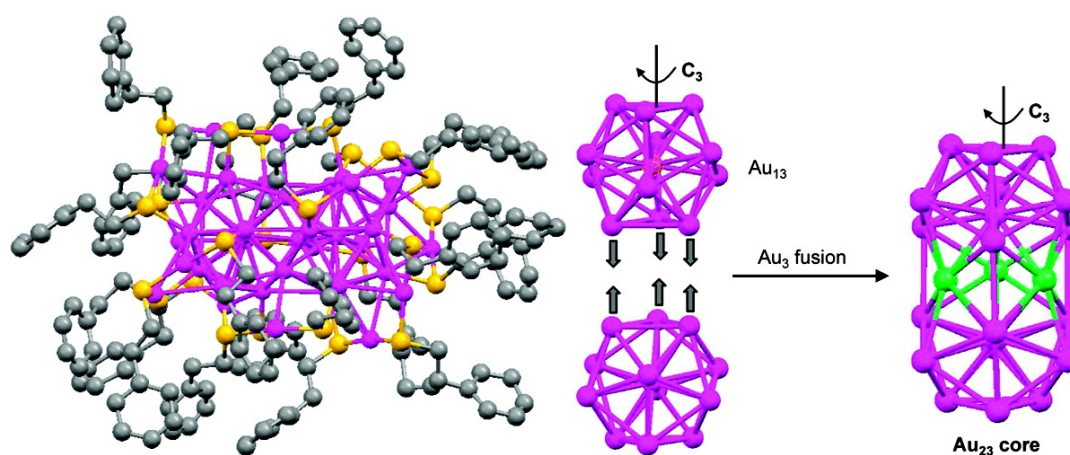


Figure 5. X-ray crystal structure of $\text{Au}_{38}(\text{SCH}_2\text{CH}_2\text{Ph})_{24}$. Left: Total structure of $\text{Au}_{38}(\text{SC}_2\text{H}_4\text{Ph})_{18}$ (L-isomer); Right: biicosahedral Au_{23} core. Legend: Au: magenta, S: yellow, C: grey, H atoms are omitted. "Reprinted with permission from Ref 54.⁵⁴ Copyright 2010 American Chemical Society."

1.3.4 The Superatom Concept

The stability of the noble-gases is due to the closed electron shell and is associated with a count of

$$n^* = 2, 8, 18, 34, 58, 92, \dots \quad (1)$$

valence electrons. The stability of the noble-gas electron configuration is also a reason for the stability of organic as well as many inorganic compounds. The noble-gas electron configuration of the atoms is achieved by the electronic interaction with other atoms.

Analog to the atomic theory, the stability of monolayer protected gold clusters can also be referred to the stability of the noble-gas electron configuration.^{60, 61, 65} Thereby, the gold core is assumed to be a superatom which is stabilized by the adsorption of ligands. The cluster can be formulated as



where the gold core (size N) is protected by M electron withdrawing ligands X and S weak ligands L which do not affect the count of electrons n^* . The overall charge of the nanoparticle is q . Therefore the requirement for an electronically closed shell superatom complex is

$$n^* = N\nu_a - M - q \quad (2)$$

where ν_a is the atomic valence of the gold core atoms. ν_a is assumed to be one because there is only one electron in the 6s orbital of the gold.

For example, the above discussed $\text{Au}_{102}(\text{p-MBA})_{44}$ has 102 gold atoms and 44 withdrawing ligands:

$$n^* = 102 - 44 - 0 = 58. \quad (3)$$

Alternatively, the clusters can also be described as a gold core protected with gold-thiolate staples. In the case of the $\text{Au}_{102}(\text{p-MBA})_{44}$ cluster, the gold core is considered to have 79 Au_{core} atoms and 21 gold-thiolate staples ($\text{Au}_{79}[\text{Au}_{23}(\text{p-MBA})_{44}]$). Assuming that all 21 staples interact with the core, each one of them would attract one electron out of the gold core, resulting in:

$$n^* = 79 - 21 - 0 = 58. \quad (4)$$

electrons. From this point of view the stability of a gold nanoparticle cluster is due to a stable electronic structure.

1.4 Absorption Properties of Metal Nanoparticles

Metal nanoparticles exhibit size related optical effects. Especially the absorption properties of metal particles are of particular interest. A prominent example is the Lycurgos Cup from the Roman times (4th century) which consists of glass doped with gold particles. Light reflected from the cup is green whereas light transmitted through the glass appears red. Both effects are due to the scattering of light on nanoparticles and can be described mathematically by Mie theory (1908).⁶⁶ The optical properties of nanoparticles depend thereby on the dielectric function of the particle and its surrounding medium as well as the

size and the shape of the particles. The influence of the particle size on the optical properties of nanoparticles is illustrated in Figure 6.

The larger particles exhibit an intense absorption band around 520 nm. This band is denoted as surface plasmon band (SPB) and is due to a collective excitation of conduction electrons. As illustrated in Scheme 3, the excitation results in a displacement of the negative and positive charges of the metal. Because the positive charge acts as a restoring force, the excited particle can be considered as an oscillating dipole, resulting in an enhancement of the local light field.⁶⁷

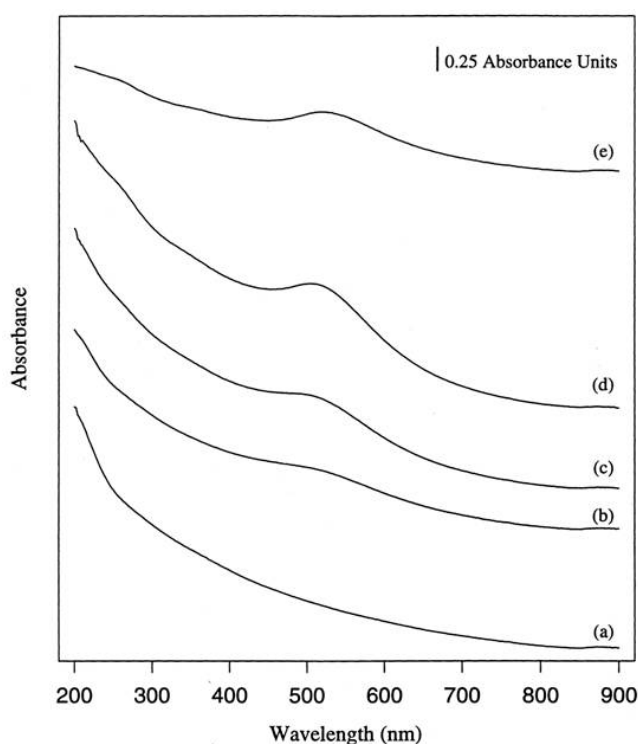
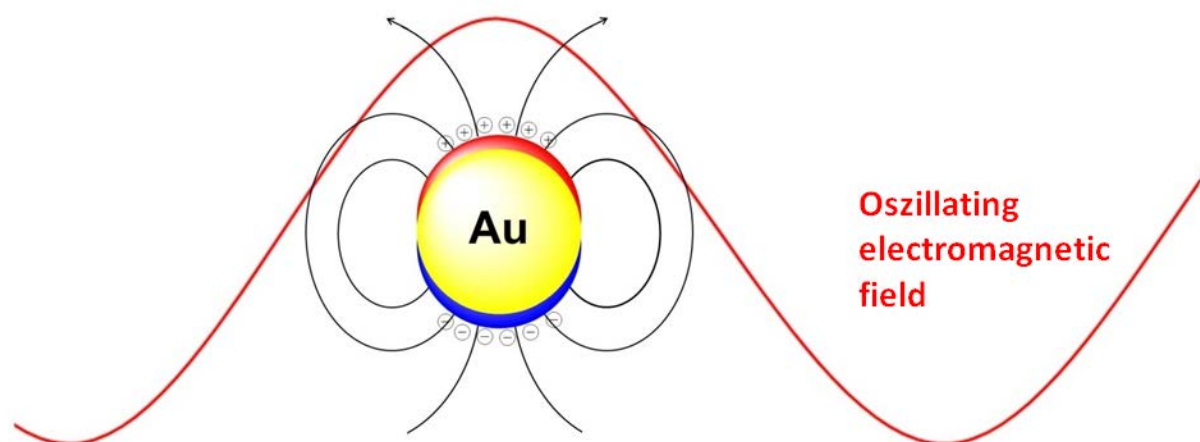


Figure 6. The UV/vis spectra (*n*-hexane) of dodecanethiolate-protected gold nanoparticles with different core radii: (a) 0.76 nm, (b) 1.1 nm, (c) 1.4 nm, (d) 1.7 nm; (e) 2.6 nm. "Reprinted with permission from Ref 64.⁶⁴ Copyright 1998 American Chemical Society."

Furthermore the spectrum of the gold nanoparticles (see Figure 6) exhibits absorption features between 800 and 200 nm which are associated with intraband transitions in the low energy region and with interband transitions above 520 nm.^{68, 69} The intraband transitions can be attributed to transitions within the broad conduction band whereas the interband transitions are due to excitations of conduction band electrons to higher unoccupied states above the

Fermi level. The superimposition of both possible transitions results in an increase of the absorption intensity with the energy of the incident light.



Scheme 3. Light induced excitation of the surface plasmon band.

1.5 Electrochemical Properties of Redox-Center-Functionalized Metal Nanoparticles

The electrochemical behavior of solutions of redox-center-functionalized metal nanoparticles can be partitioned into the electrochemical reactivity of the redox-center-functionalized organic layer and the electrochemical reactivity of the metal core itself. The metal core shows size-related electrochemical behavior which can be divided into three categories: bulk-continuum voltammetry, quantized double-layer charging (QDL) voltammetry and molecule-like voltammetry.²³

Bulk continuum voltammetric behavior is expected for large nanoparticles (diameter > 3 – 4 nm) and is related to an electric double-layer charging at the nanoparticle surface/electrolyte solution interface. The electron charge storage capacity depends on the nanoparticle size (surface area), nanoparticle double layer capacitance C_{DL} and the applied potential (relative to nanoparticle zero charge).²³ In a voltammetry experiment, the capacitive charging currents of dissolved nanoparticles appear as smooth current-potential traces.

Quantized double-layer charging (QDL) is observed if the size (diameter = 1.6 – 2.2, $Au_{140} - Au_{314}$)⁷⁰⁻⁷⁴ and consequently the capacitance C_{DL} of the nanoparticles are very small. Thus, a scan of the electrode potential of a monodisperse nanoparticle-solution leads to a series of evenly spaced current peaks (Figure 7 upper voltammogram).

These current peaks represent single electron transfer processes to/from the nanoparticle, resulting in quantized double layer charging.²² The voltage spacing ΔV between the peaks depends according to equation (5) on the double layer capacitance C_{DL} :

$$\Delta V = \Delta e / C_{DL} \quad (5)$$

where Δe is the electron charge transferred. Therefore ΔV has to be larger than $\sim k_B T$ (25.7 meV at 278 K) to detect discrete QDL peaks. If ΔV is smaller than $\sim k_B T$ the QDL waves are smeared out and double-layer charging falls into the bulk-continuum voltammetric regime. Consequently, an essential requirement is a sufficiently small value of C_{DL} . In order to estimate C_{DL} a concentric sphere capacitor model was introduced:⁷⁵

$$C_{DL} = 4\epsilon\epsilon_0 \frac{r}{d}(r + d) \quad (6)$$

where r is the radius of the core, d is the thickness and ϵ the effective dielectric constant of the organic layer. From equation (5) and (6) it is obvious that both the radius and the dielectric constant should be small to observe discrete QDL peaks.

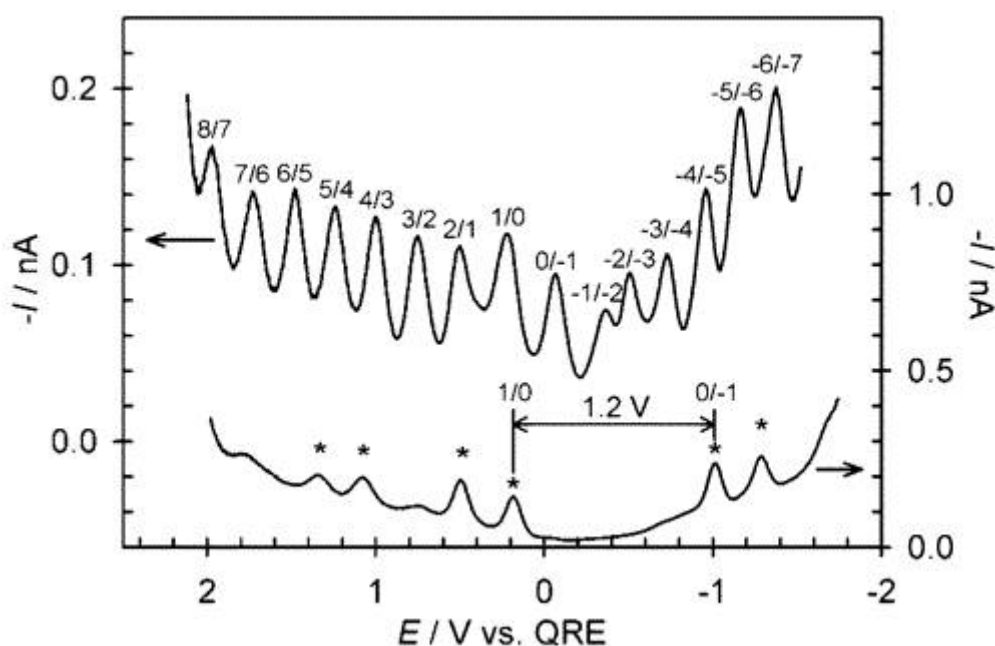


Figure 7. Differential pulse voltammetry (DPV) of monodisperse nanoparticles in 1,2-dichloroethane / 10 mM bis(triphenylphosphoranylidene)ammonium tetrakis(pentafluorophenyl)-borate solution with a platinum working electrode; 177 μM solution of a hexanthiol protected Au_{147} cluster (upper) showing 15 high-resolution QDL peaks and 170 μM solution of a hexanthiol protected Au_{38} cluster (lower) showing a HOMO-LUMO gap. "Reprinted with permission from Ref 76.⁷⁶ Copyright 1998 American Chemical Society."

Following the particle size gradient from large to smaller particles - continuum voltammetry to QDL voltammetry - a *molecule-like voltammetric behavior* is found at very small metal core sizes (diameter < 1.4 nm). Molecule-like voltammetric behavior has been detected for thiol protected gold particles designated as having core sizes of Au₇₅,⁷⁷ Au₅₅,⁷⁸ Au₃₈,⁷⁶ Au₂₅^{49, 79} and Au₁₃.⁸⁰ In contrast to the QDL regime, the evenly spaced core charging peaks diminish and a large spacing between the first one-electron oxidation and the first reduction appears. This spacing is interpreted as the emergence of a “molecule-like” HOMO-LUMO band gap. In the lower voltammogram (Figure 7) the band gap is shown for a hexanethiol protected Au₃₈ particle. The energy gap decreases with particle size and the dielectric constant of the surrounding medium.

Besides the voltammetric reactivity of the metal core, the protecting shell can be functionalized with redox active units. Several redox active units, e.g. ferrocene,^{74, 81-84} anthraquinone,⁸⁵⁻⁸⁷ phenothiazine,⁸⁸ porphyrin,^{89, 90} were introduced to study their electrochemical behavior. The voltammetric behavior of such hybrid systems combines that of the redox reaction of the redox unit and the double layer charging of the gold core.^{83, 91} Investigations on these systems revealed that the electrode reaction is described to be a single electron process ($n = 1$) where all the redox centers react one-at-a-time.^{22, 88} The latter point is very interesting because not all redox centers adsorbed onto the metal core surface are close to the working electrode/solution interface where the redox reaction takes place. Three pathways have been discussed to explain this phenomenon. (1) By the time the particle contacts the working electrode the redox units located directly at the electrode/solution interface become oxidized or reduced. All the other redox units adsorbed onto the same gold core are electrochemically addressed via *electron tunneling* through the core. (2) Another pathway is the *lateral site-site electron hopping* over the nanoparticle circumference. (3) The third possibility involves *rotational diffusion* whereby the rotation of the particles brings each redox unit in contact with the electrode. All three pathways have to be sufficiently faster than the translational diffusion of the particle. Geometrical parameters of the particle and the arrangement of the redox active ligand on the surface determine which pathway is favored.

1.6 General Aspects for the Synthesis of Thiol Protected Spherically Shaped Nanoparticles

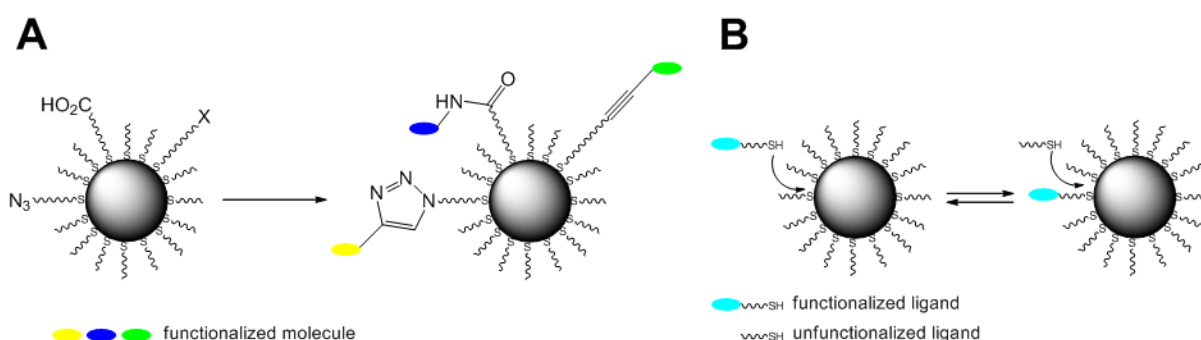
In the past, several synthetic routes have been developed for the synthesis of spherically shaped gold nanoparticles.^{41, 43, 92-94} All these approaches deal with the same strategy: an oxidized gold species is reduced to gold (0) to generate the gold core. The key step is to stabilize the gold core with molecules which adsorb onto the gold surface. The adsorption lowers the free energy of the gold core surface and leads to a steric repulsion between the particles which prevents agglomeration. Stable nanoparticles can only be generated if the molecules form a stable core shell of high density. Ionic surfactants or ligands possessing an anchor group (thiol, disulfide, phosphine, phosphine oxide and amine) are suitable for this purpose.^{41, 95, 96} By far the most widely used is the thiol group due to the soft (HSAB) character of both gold and sulfur.⁷

The first conventional method for the synthesis of spherically shaped gold nanoparticles was published by Turkevich in 1951⁹⁴ who used trisodium citrate in an aqueous medium. In this synthesis the citrate acts as reducing agent and stabilizer. Variation of this synthetic-protocol leads to nanoparticles in the size between 2.3-147 nm.^{43, 97, 98} In a second synthetic step the particle can be functionalized with other stabilizing ligands.⁹⁹⁻¹⁰¹ Due to the aqueous medium, the synthesis is restricted to hydrophilic molecules.

The Brust-Shiffrin method, published 1994, is the most common route for the synthesis of gold nanoparticles functionalized with a variety of organic molecules and can be considered a key step in the research of gold nanoparticle hybrid systems. The advantage of this method is that the synthesis is carried out in an organic medium. Tetrachloroauric acid is thereby first transferred from an aqueous solution to an organic solution (toluene) using surfactants (e.g. tetraoctylammonium bromide). Then a stabilizing reagent, e.g. a thiol, is added, which reduces the gold acid to a colorless gold(I)-thiolate complex, followed by the addition of an aqueous sodium borohydride solution which results in the rapid production of thiolate-protected gold nanoparticles by reduction of Au(I) to Au(0).^{41, 102-105}

The size of the gold core can be adjusted to 1.5-5.2 nm and depends on the reaction conditions, notably the thiol / tetrachloroauric acid ratio, the temperature and the rate of addition.^{7, 64} The limitation of the synthesis is that the ligand has to be soluble in the solvent and has to be inert towards the reducing agent. This problem can be overcome by subsequent derivatization of the attached ligands in a follow up reaction. Chemical reactions like amid

ester couplings, palladium catalyzed couplings, click reactions^{62, 88, 100, 106, 107} as well as place exchange reactions^{21, 62, 81, 108-111} provide the desired functionalized nanoparticle (Scheme 4).



Scheme 4. Derivatization of the organic shell of a nanoparticle by (A) chemical reactions or (B) place exchange reactions.

The disadvantage of the Brust-Shiffrin method is the contamination of the organic shell with surfactants, which are added to render the auric acid soluble in the unpolar solvents.¹¹² In order to produce surfactant-free samples many single phase syntheses were published.

The strategy of surfactant-free synthesis is to dissolve the auric acid in polar solvents and to stabilize the nanoparticle after the addition of the reducing agent *insitu* with thiols. Syntheses in methanol or *N,N*-dimethylformamide are suited to attach very polar thiols to the gold core.^{42, 113-115} Syntheses in tetrahydrofuran or diglyme facilitate the access to less polar thiols. Several different reducing agents are used such as sodium naphthalenide, lithium triethylborohydride or lithium borohydride which are soluble in organic solvents.^{90, 112, 116, 117} These syntheses produce gold nanoparticles in the range of 1 to 10 nm. The size can be adjusted by the stoichiometry of the reactants, the temperature and the rate of addition. The limitation of the synthesis is that the thiol has to be inert towards the reducing agent.

The syntheses discussed above lead to polydisperse nanoparticles. Monodisperse gold nanoparticle can be synthesized via extraction or altering procedures from polydisperse samples.^{50, 118-122}

1.7 Analytical Methods

Many characterization techniques can be used to analyze the geometrical dimension of nanoparticles. The size of the gold core can be determined using transmission electron microscopy (TEM),^{41, 107, 123} atomic force microscopy (AFM),^{20, 124} small angle X-ray scattering (SAXS)²⁰ or X-ray diffraction.^{101, 125} The most common characterization technique, however, is TEM.

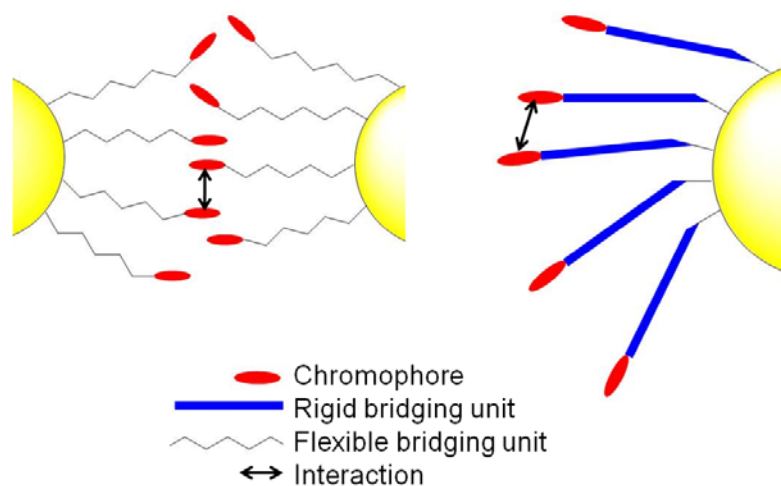
Scanning tunneling microscope (STM),^{20, 126, 127} NMR^{21, 128} or electrochemical methods^{83, 85, 129} can be used to investigate the total size of the particle (gold core + organic shell). The chemical composition of the particle can be analyzed by NMR,^{20, 108, 128, 130} thermogravimetric analysis (TGA),^{20, 117} UV/vis/NIR-spectroscopy,¹³¹ MS-spectroscopy,^{45, 53, 132} IR-spectroscopy^{41, 42} or X-ray photoelectron spectroscopy.^{123, 133-135}

2 Optical and Electrochemical Properties of Triarylamine and Perchlorinated Triarylmethyl Functionalized Gold Nanoparticles

Metal nanoparticles functionalized by an organic layer offer the chance to combine the physical and chemical properties of organic molecules with those of metal nanoparticles. Thus, this class of compounds has been investigated intensively in the last decades^{7, 62, 136} particularly in view of applications in the field of nanobiotechnology, e.g. drug delivery systems for photodynamic and photothermal therapy¹³⁷⁻¹⁴⁰ and the detection, labeling and sensing of biomolecules.^{2, 6, 32, 141-148} The metal core itself exhibits special nanoparticle properties like surface plasmon absorption bands (SPB)^{7, 68, 149} or quantized double layer (QDL) charging.^{22, 23, 150} Concerning the organic layer of these hybrid systems new surface enhanced effects were found and characterized by appropriate spectroscopic methods such as surface-enhanced Raman scattering (SERS) spectroscopy,^{6, 30, 141, 151} surface-enhanced fluorescence spectroscopy^{32, 152} and localized surface plasmon resonance (LSPR) spectroscopy.²⁶⁻²⁹

In recent years many chromophore nanoparticle systems, particularly those based on gold nanoparticles, have been investigated.^{85, 89, 102, 110, 153} The optical properties of the chromophores have been studied by several methods such as absorption, fluorescence or transient absorption spectroscopy.^{26, 109, 114, 121, 131, 154-157} Most frequently, the chromophores were attached *via* an aliphatic thiol-functionalized bridging unit. Focusing on the absorption properties the length of the bridging unit is an important factor. While long units can block electronic interactions between the gold core and the chromophore^{90, 109, 110} short bridging units will facilitate interactions.^{96, 102, 155} Such an interaction may result in a damping or shift of chromophore absorption bands in comparison to the free chromophore.

Chromophores arranged around the gold core can also show chromophore-chromophore interactions which originate from inter- or intraparticle interactions (Scheme 7). Triphenylene-functionalized nanoparticles have shown π - π stacking behavior which is due to interparticle interaction. To allow intercalation, the free space around the chromophore units have to be sufficiently large.¹⁵⁴



Scheme 7. Left: Interparticle interaction; right: intraparticle interaction.

Intraparticle interactions can occur if redox active chromophores attached *via* π -conjugated bridging units are used. Electrochemical measurements of these hybrid particles revealed a splitting of the first redox wave. This was attributed to an intervalence interaction between neighboring redox centers *via* the metal core in case of ferrocene redox centers attached to ruthenium nanoparticles.^{158, 159} In contrast to these examples, porphyrin,⁹⁰ ferrocene²¹ and anthraquinone^{85, 87} linked *via* a long aliphatic chain to the metal core act independently of each other as non-interacting redox centers and, consequently, exhibit one sharp signal for the first redox wave in electrochemical experiments.

While in recent years, electronic interactions of redox functionalized molecules and of redox centers attached to solid gold electrodes have been studied,^{16, 17, 160-178} the goal in this work is to study electronic interactions of redox active chromophores attached to gold nanoparticles. That is, the gold core is used as a template to bring many redox centers in close contact. In this work triarylamine (Tara) and perchlorinated triarylmethyl (PCTM) radical are used for this purpose because of their optical and electrochemical stability (Chart).

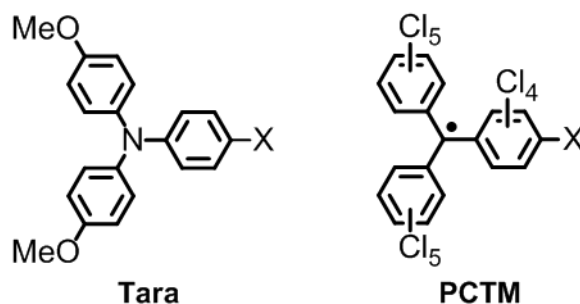


Chart 2.

2.1 Optical and Electrochemical Properties of Triarylamines-Gold-Nanoparticle Conjugates: Short π -Conjugated Bridging Unit

The object of this chapter is the synthesis and investigation of gold nanoparticles that are covered by a relative short π -conjugated bridging unit which is terminated by a triarylamine unit (**Au-Tara1**). The optical and electrochemical properties of the **Au-Tara1** nanoparticles and of their corresponding unbound ligand **Ref1** (Chart 3) were investigated in order to detect triarylamine-triarylamine interactions and gold core-triarylamine interactions. Additionally the size of the gold core template was varied to study how the optical and electrochemical properties depend on the core size.

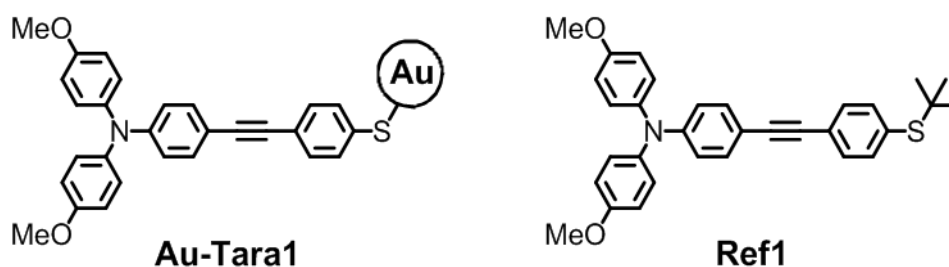
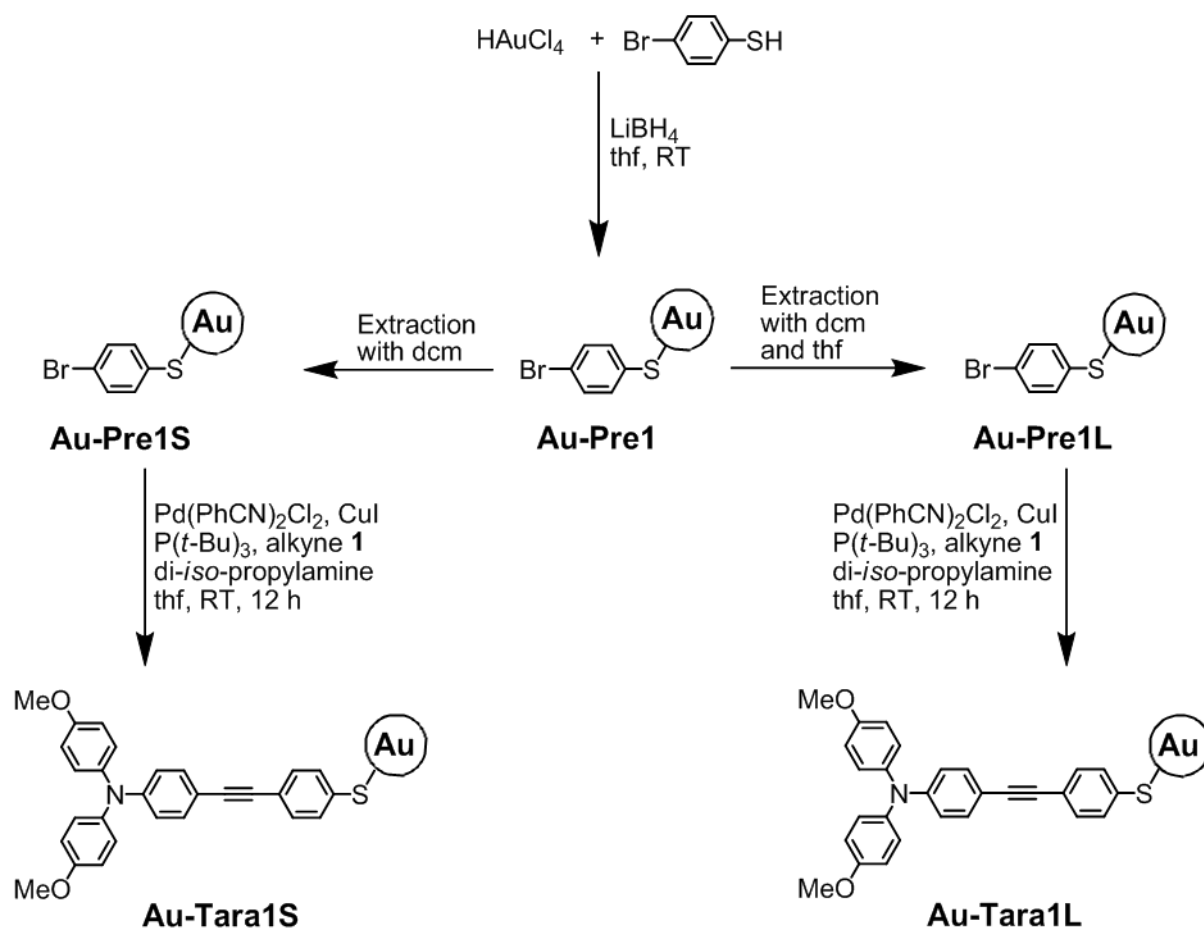


Chart 3.

2.1.1 Synthesis

Gold nanoparticles are accessible via several routes (see Chapter 1). Two synthetic aspects are important for the synthesis of the triarylamine-functionalized gold nanoparticles. First, the samples should not be contaminated with surfactants because the contaminants could affect the electrochemical and optical properties. The surfactant-free single phase synthesis is suited for this purpose. Second, a homogeneous organic shell is required for an accurate analysis. Because the reduction of the auric acid is carried out in the presence of the protecting ligand, the redox active unit has to be introduced in a second step.

The first step to synthesize triarylamine-functionalized gold nanoparticles (**Au-Tara1**) was to generate the precursor **Au-Pre1** by reduction of HAuCl_4 with LiBH_4 in the presence of 4-bromothiophenol (Scheme 5).¹¹⁷ Extraction of the crude product with dichloromethane (dcm) only or with both dcm and tetrahydrofuran (thf) yields particles of different size (**Au-Pre1S** and **Au-Pre1L**, respectively). The two fractions with different



Scheme 5. Synthesis of the gold nanoparticles **Au-Tara1S** and **Au-Tara1L**.

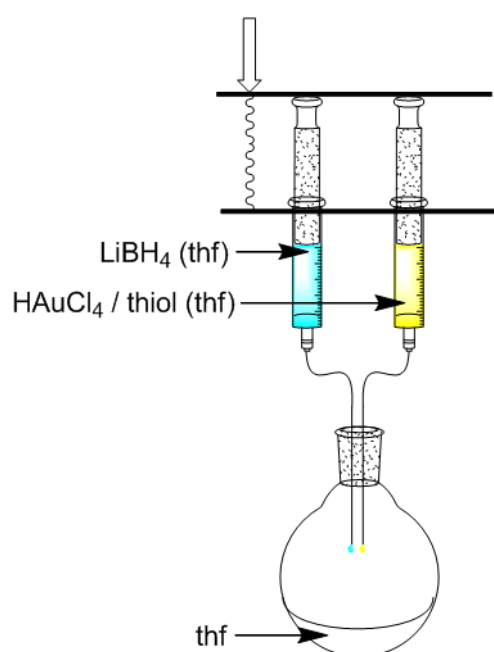


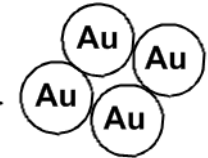
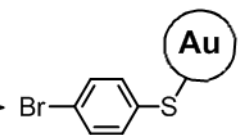
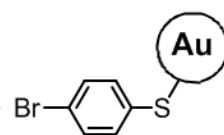
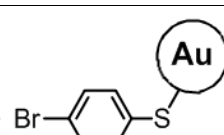
Figure 8. Synthesis of the precursors *via* syringe pump

particle size and the terminal alkyne **1** were then transformed *via* a *Hagihara-Sonogashira* coupling reaction into the desired products **Au-Tara1S** and **Au-Tara1L**.¹⁰⁷

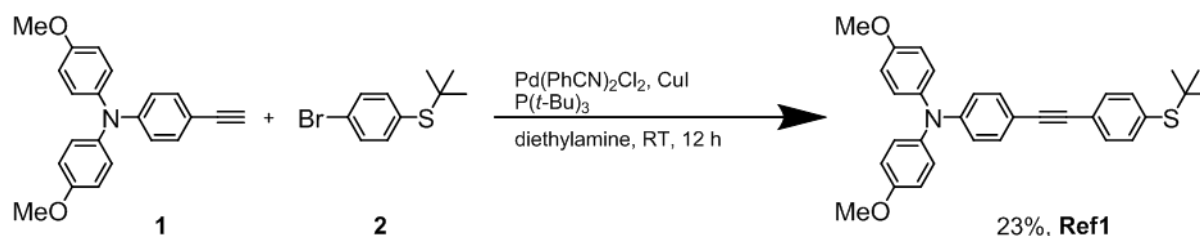
The synthesis of the precursor turned out to be complicated. More than 100 approaches have been necessary to develop an efficient synthetic protocol. Some approaches are exemplarily depicted in Table 1. The reaction is influenced by many parameters, such as reaction temperature, solvent, stoichiometry of the reactants and the rate of addition. However, in entry 4 in Table 1 the conditions which gave stable nanoparticles with good yield are shown. As illustrated in Figure 8

the reducing agent and a mixture of the auric acid and the thiol were simultaneously added via a syringe pump to vigorously stirred thf.

Table 1. Synthetic Approaches for the Synthesis of Au-Pre

Approach	Reaction conditions	Result
1	HAuCl_4 / thiol (methanol) $\xrightarrow[0^\circ\text{C}]{\text{NaBH}_4 \text{ (aq.)}}$ 	agglomeration
2	HAuCl_4 (thf) $\xrightarrow[0^\circ\text{C}]{\text{LiBH}_4 \text{ / thiol (thf)}}$ 	agglomeration or stable nanoparticles with low yield
3	HAuCl_4 / thiol (thf) $\xrightarrow[0^\circ\text{C}]{\text{LiBH}_4 \text{ (thf)}}$ 	agglomeration or stable nanoparticles with low yield
4	HAuCl_4 / thiol (thf) $\xrightarrow[\text{RT}]{\text{LiBH}_4 \text{ (thf)}}$ 	Stable nanoparticles, good yield

In order to compare the ligand properties with and without gold core a reference compound **Ref1** was synthesized by a palladium catalyzed *Hagihara-Sonigashira* coupling reaction of the alkyne **1** with the bromophenyl derivative **2** in 23% yield (Scheme 6).^{123, 179} The sulfur-functionality possibly disrupts the coupling reaction which leads to the low yield.



Scheme 6. Synthesis of **Ref1**.

2.1.2 Analysis

The surface functionalization and the purity of the **Au-Tara1** samples were checked by $^1\text{H-NMR}$ spectroscopy. The NMR spectra of molecules bound to the gold core are generally line broadened. The protons very close to the gold core are tightly packed and the broadening is caused by rapid spin-spin relaxation from dipolar interactions. Additionally, the different S-Au binding sites on the gold core, e.g., attached molecules bound to a face versus an edge,^{50, 132} and the polydispersity of the particles lead to a line broadening.^{64, 128} Any traces of unbound molecules would superimpose these broadened signals with sharp peaks.

However, the spectra of the **Au-Tara1** particles show broadened peaks attributed to the organic layer of the particle (see Figure 9) which proves that the samples are essentially free of unbound triarylamine ligands.

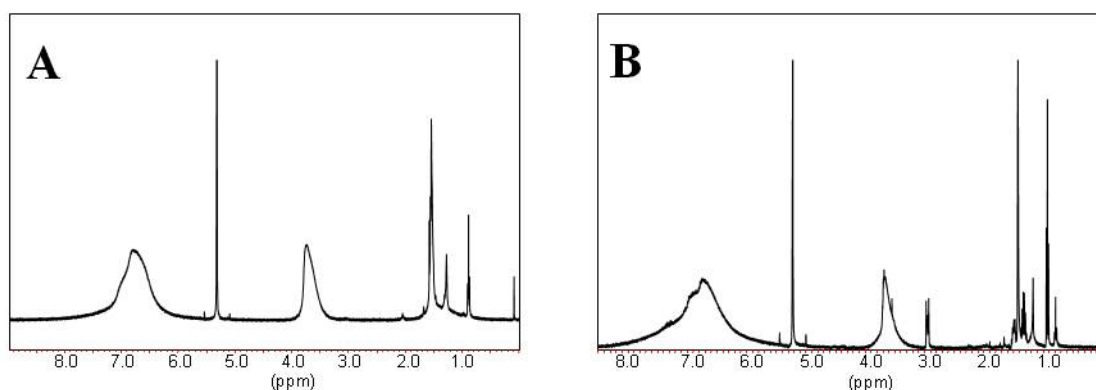


Figure 9. $^1\text{H-NMR}$ of nanoparticle (A) **Au-Tara1S** and (B) **Au-Tara1L** in dichloromethane- d_2 .

The gold core radius distribution of the nanoparticles was measured using dark-field scanning transmission electron microscopy. **Au-Tara1S** has an average radius of $1.12 (\pm 0.24)$ nm and **Au-Tara1L** of $1.36 (\pm 0.28)$ nm (Figure 10-11).

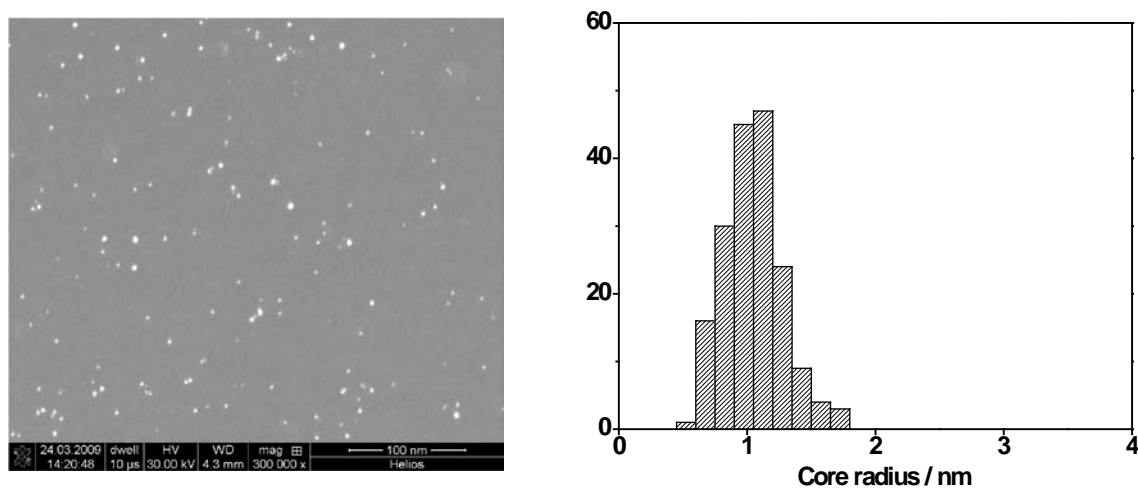


Figure 10. Dark field STEM images of **Au-Tara1S** recorded on a FEI Helios Nanolab and the associated histogram.

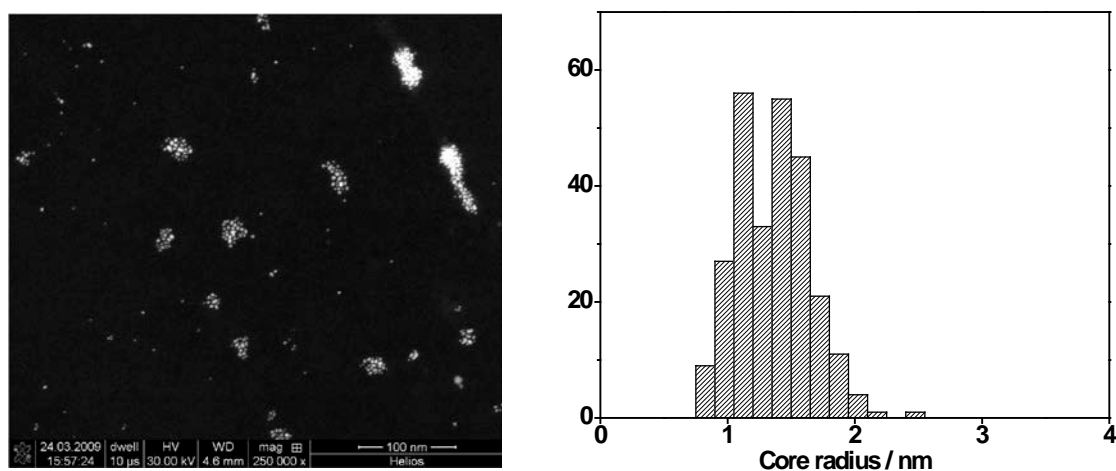


Figure 11. Dark field STEM images of **Au-Tara1L** recorded on a FEI Helios Nanolab and the associated histogram.

The stability of the gold core structure of the **Au-Tara1** particles after *Hagihara-Sonogashira* coupling was checked by UV/vis/NIR-spectroscopy. As can be seen from Figure 12 the characteristic surface plasmon bands of the gold core at ca. 18000 cm^{-1} have similar intensities for the **Au-Pre1** particles and the corresponding **Au-Tara1** particles. Additionally, in the spectra of **Au-Pre1** a band at 39500 cm^{-1} is seen. This band can be attributed to the 4-bromothiophenol ligand and is absent in the spectra of the **Au-Tara1** particles. This analysis demonstrated that the *Hagihara-Sonogashira* reaction does not affect the particle size but it does manipulate the organic layer.

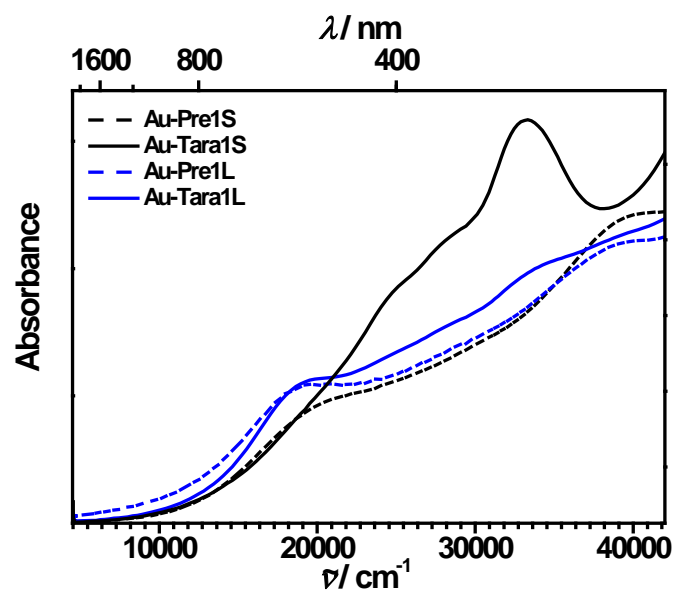


Figure 12. Absorption spectra of the triarylamine-functionalized particles **Au-Tara1S** (black line) and **Au-Tara1L** (blue line) and the corresponding precursors **Au-Pre1S** (dashed black line) and **Au-Pre1L** (dashed blue line).

Additionally, X-ray photoelectron spectroscopy (XPS) measurements were carried out to analyze the composition of the nanoparticles. As can be seen from Figure 13, the features of C1s and O1s and several peaks of the molybdenum substrate as well as the core levels of the Au nanoparticles are clearly visible. In order to verify the absence of traces of the Pd catalyst, we performed detailed measurements in a binding energy range of about 560 eV (see insets of Figure 13) where the 3p_{3/2} level is expected.

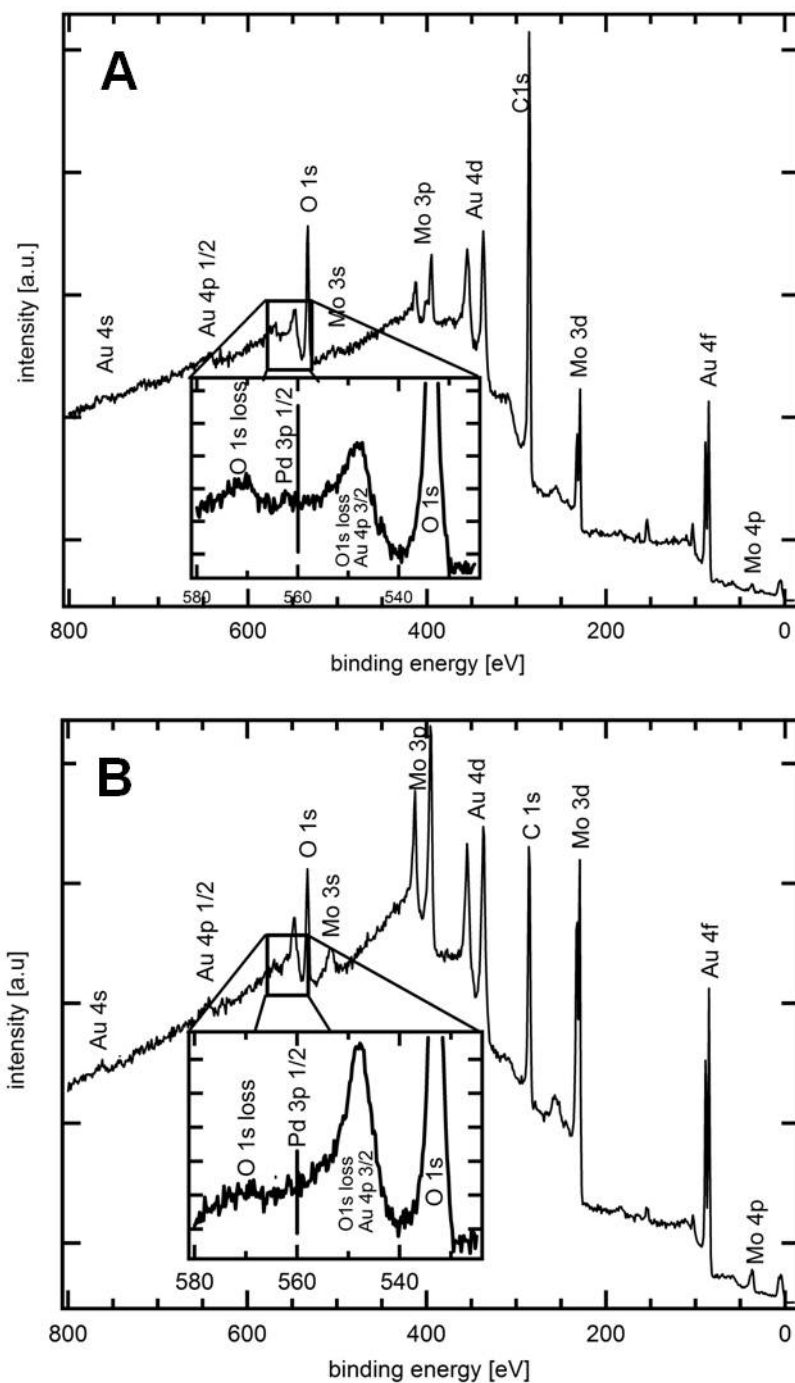


Figure 13. XPS of Au-Tara1S (A) and Au-Tara1L (B).

Within the typical accuracy for the determination of the chemical compositions by core level spectroscopy ($\sim 1\%$) we obtained no evidence for Pd in both the **Au-Tara1S** and **Au-Tara1L** samples. Thus, the palladium catalyzed reaction does not affect the composition of the gold core.

2.1.3 Electrochemical Measurements

Osteryoung square wave voltammetry (OSWV) of **Ref1** in tetrabutylammonium hexafluorophosphate (TBAH) dcm solution shows two peaks ($E_{(Ox1)} = 280$ mV, $E_{(Ox2)} = 950$ mV) which can be assigned to the first and second oxidation of the triarylamine centers (Figure 14 A). Only the first oxidation peak is reversible. The OSWV of **Au-Tara1S** and **Au-Tara1L** reveals a splitting of the first triarylamine oxidation into two reversible oxidation processes (Figure 14 B-C). A fit of the voltammogram with two Voigt-functions reveals a separation (seen as a shoulder) of about 130 mV for **Au-Tara1S** and 140 mV for **Au-Tara1L** (Table 2). This splitting is caused by a very strong coupling between neighboring triarylamine centers (the statistical value for two non-interacting redox centers is 35.6 mV). Such a splitting of the first oxidation is often seen in *bis*(triarylamine) systems^{168, 172, 173, 175, 176} and is also seen for ferrocenes attached to a ruthenium particle via a vinylene unit.¹⁵⁹

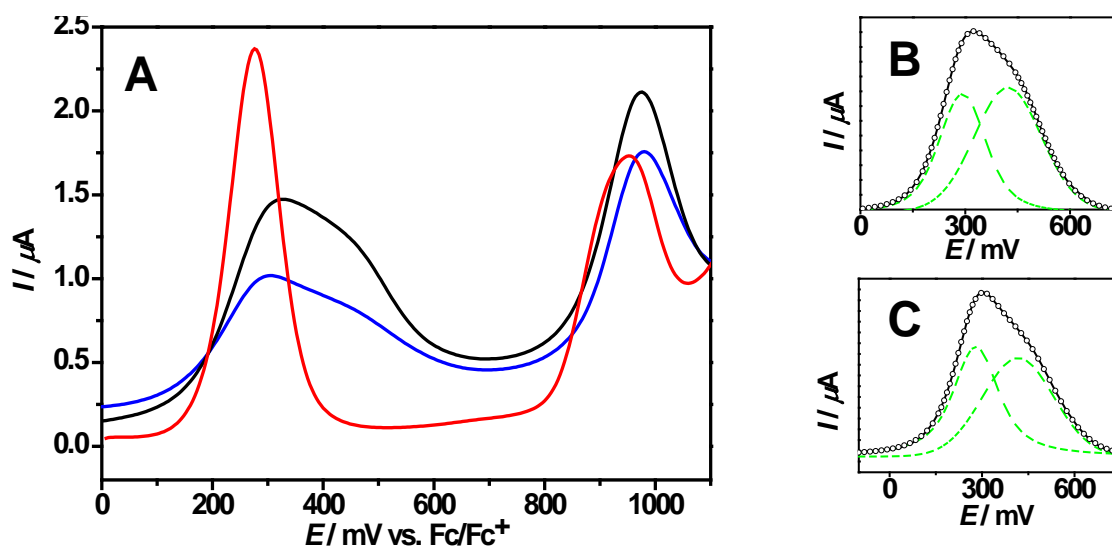


Figure 14. (A) OSWV in dcm (TBAH) of **Au-Tara1S** (black line), **Au-Tara1L** (blue line) and **Ref1** (red line); Fit (black circles) of the OSWV of **Au-Tara1S** (B) and **Au-Tara1L** (C) with two Voigt-functions (dashed green lines) after baseline (capacitive background current) correction with an exponential function.

Table 2. Redox Potentials of Au-Tara1L, Au-Tara1S and Ref1 vs. Ferrocene (Fc/Fc⁺) in dcm/TBAH

	redox potential / mV	
	$E_{(Ox1)}$	$E_{(Ox2)}$
Au-Tara1L	280**, 420**	980*
Au-Tara1S	290**, 420**	980*
Ref1	280*	950*

*measured by OSWV, ** determined by a fit with two Voigt-functions

2.1.4 UV/vis/NIR Absorption Spectroscopy and Fluorescence-Anisotropy Measurements

The absorption spectra of the **Au-Tara1** particles are displayed in Figure 15. Additionally the spectrum of the reference compound **Ref1** is shown to demonstrate the changes by the binding of the triarylamine to the gold core.

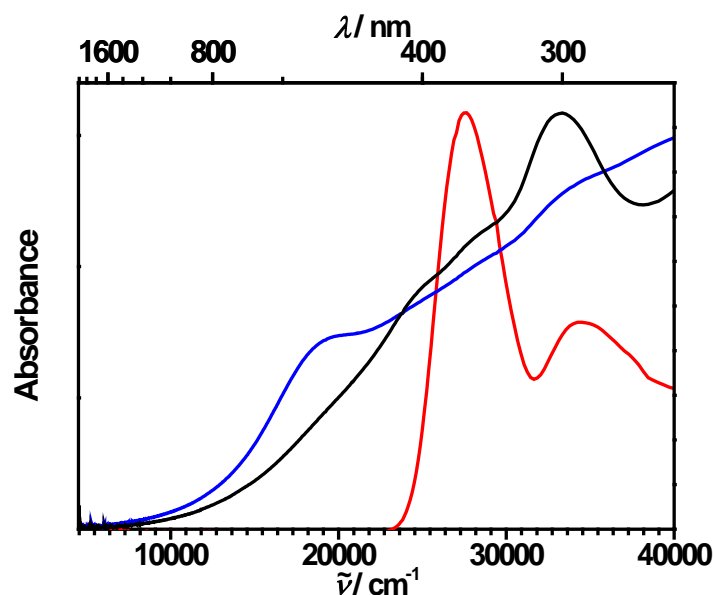


Figure 15. Absorption spectra of the triarylamine-functionalized particles **Au-Tara1S** (black line) and **Au-Tara1L** (blue line) and the reference compound **Ref1** (red line) in dcm.

The absorption spectrum of the reference compound **Ref1** displays two intense bands at 27600 cm^{-1} and 34500 cm^{-1} which are typical of triarylamine systems.^{171, 172, 177} Fluorescence-anisotropy measurements revealed that the low energy band is polarized along the molecular

axis and the high energy band is polarized perpendicularly to the molecular axis. In detail, the excitation and emission-anisotropy spectrum of **Ref1** in a sucrose octaacetate (SOA) matrix and the absorption spectrum in *n*-Bu₂O are shown in Figure 16. The excitation-anisotropy for the low-energy transition at 27700 cm⁻¹ in *n*-Bu₂O is ca. 0.3. In theory a maximum anisotropy value of $r = 0.40$ is obtained for a parallel orientation of the absorption and the emission transition moments and a minimum value of $r = -0.20$ for a perpendicular orientation.¹⁸⁰ Thus, this transition has a parallel oriented transition moment to the emission moment. The deviation from the theoretical maximum value of 0.40 indicates that there is a small contribution from higher energy transitions due to band overlap. For the high-energy transition at 34700 cm⁻¹ in *n*-Bu₂O the anisotropy is at ca. 0.1. Because of the strong decrease in the anisotropy, we assume that transition moments of the absorption and emission for this transition may be oriented perpendicularly. The fact that the anisotropy does not reach the theoretical value of -0.20 is caused by contributions from overlap with lower and higher transitions.

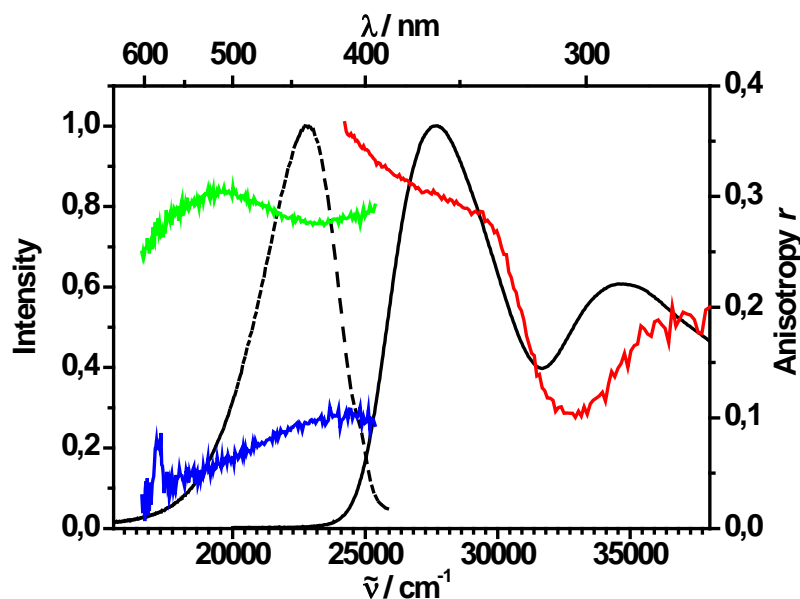


Figure 16. Anisotropy of the excitation (emission wave number 22800 cm⁻¹; red) and the emission (excitation wave number 27700 cm⁻¹ and 34700 cm⁻¹; green and blue) of **Ref1** in a sucrose octaacetate (SOA) matrix at room temperature. The corresponding nonpolarized absorption (solid line) and emission (dashed line) spectra of **Ref1** in *n*-Bu₂O are added for comparison.

The surface plasmon band (SPB) is a characteristic feature in the absorption spectrum of metallic nanoparticles. In the case of spherical particles with the same organic layer, the energy and the intensity of the SPB depend on the size of the gold core.⁷ Consistent

with this fact the larger particle **Au-Tara1L** shows an intense SPB at 19000 cm^{-1} which is practically absent in the smaller particle **Au-Tara1S** (see Figure 15).

In comparison to **Ref1** the higher energy band at 34500 cm^{-1} is also seen with a slight red shift in the spectrum of **Au-Tara1S** but has a very weak intensity in the case of **Au-Tara1L**. Much in contrast, the second characteristic band of **Ref1** at 27600 cm^{-1} is hardly detectable in the spectra of **Au-Tara1L** and **Au-Tara1S**.

The strong damping of the band at 27600 cm^{-1} and the red shift of the band at 34500 cm^{-1} are obviously caused by an interaction between the gold core and the chromophore.^{102, 181, 182} The different degree of damping between the 27600 cm^{-1} band and the 34500 cm^{-1} band might be due to the different relative orientation of the chromophore transition dipole to the surface normal of the gold particle.²⁷ In fact, it is likely that the orientation of the arylthiol units deviates strongly from the gold surface normal.⁵⁵

2.1.5 Spectroelectrochemistry

Further information about the electronic coupling between the triarylamine centers on the particles was obtained by spectroelectrochemistry at a transparent gold-minigrid electrode. Only the oxidation to the triarylamine radical cation is discussed because the oxidation to the dication is irreversible. The SEC of **Ref1** shows that the typical triarylamine absorption band at 27600 cm^{-1} decreases with increasing potential, while at the same time the characteristic band for the monoradical cation at 13000 cm^{-1} and another band at 23000 cm^{-1} increase (Figure 17).^{172, 175, 177} The band at 13000 cm^{-1} is associated with a π - π^* transition of the dianisylphenylamine radical cation.^{168, 173, 175, 176}

The SEC of **Au-Tara1** is shown in Figure 18 A. For a better overview, we divide the spectra into three sequential processes which are grouped according to isosbestic points. The characteristics of the three processes are the increase of the triarylamine radical cation band at 13100 cm^{-1} accompanied by a decrease of the band at 33300 cm^{-1} . During this first process the weak bands at 24900 cm^{-1} and 27900 cm^{-1} decrease. Even more interesting is the observation of a weak band at about 10000 cm^{-1} , which increases during the second process and then decreases during the third process (Figure 18 B). This behavior is indicative of an intervalence charge transfer band (IVCT) which is associated with an optically induced hole transfer between an oxidized and a neutral neighboring triarylamine.

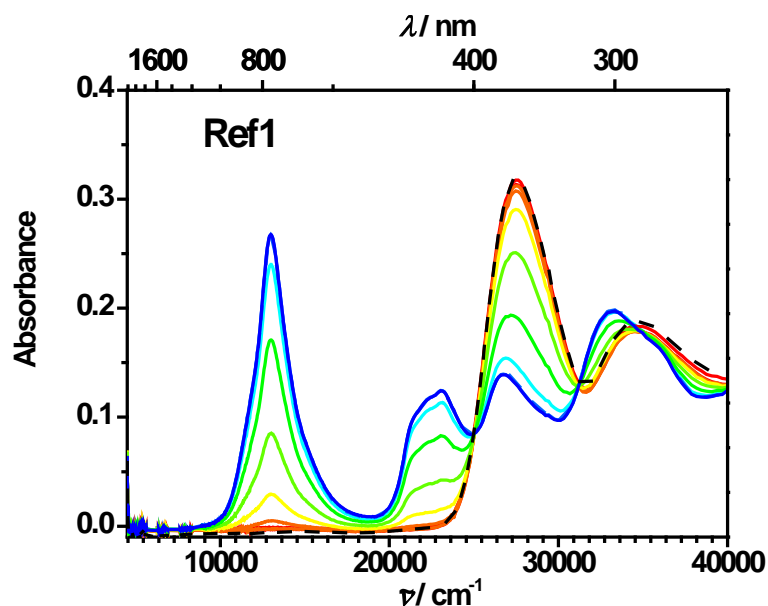


Figure 17. Spectroelectrochemistry of **Ref1** in dcm/TBAH.

The IVCT band should be maximal at 50% oxidation of all triarylamine centers as indeed observed. IVCT bands of similar intensity are seen in many *bis*(triarylamine) radical cation systems^{168, 172, 173, 175, 176} and are also reported for ruthenium particles with attached ferrocenes.¹⁵⁹ In contrast to the mixed valence *bis*(triarylamine) radical cations where hole transfer occurs over the conjugated bridges that connect the two triarylamine moieties, the hole in the partially oxidized triarylamine-gold-nanoparticle conjugates is transferred through space between the triarylamines.

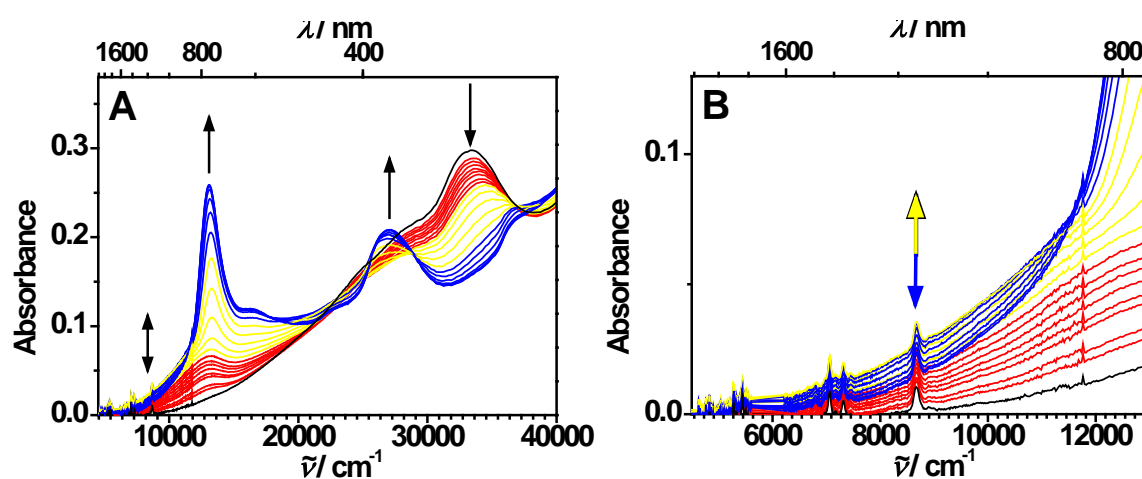


Figure 18. (A) SEC of **Au-Tara1S** (black line) in dcm/TBAH. The SEC is composed of three processes colored with red, yellow and blue. (B) NIR-region of the spectra.

The SEC of **Au-Tara1L** can also be described by three sequential processes. (Figure 19 A). Only the first process is fully reversible. Initial increasing of the potential (first red process) leads to a dramatic decrease of all characteristic gold core band intensities. With further increase of the potential the triarylamine radical cation band at 13100 cm^{-1} rises (second yellow process) and the gold core bands gain more intensity. This process is associated with an increase of a band at ca. 10000 cm^{-1} (Figure 19 B). As the radical cation band continues to increase, the gold core bands and the band at 10000 cm^{-1} decrease (third blue process). Again, as in **Au-Tara1S** the latter band is interpreted to be an IVCT band.

In the first process the gold core gets charged. Such a core-charging alters the electronic structure of the gold core and is known to affect some gold transitions within the gold nanoparticle.^{49, 183} It might also be possible that the electrolyte (TBAH) mediates electrostatic interactions between the charged particles which causes an aggregation of particles. Chandrasekharan et al. found that aggregation of a gold nanoparticle coated with Rhodamine 6G was responsible for a damping and broadening of the SPB.¹⁵⁶ Whatever the reasons may be for this effect, oxidation of the triarylamine centers in the second step disturbs it strongly. In contrast, the smaller particle size of **Au-Tara1S** and/or the superimposition with the more intense triarylamine bands could be the reasons that a damping of the gold core band intensities are not detectable in the SEC of **Au-Tara1S**.

z

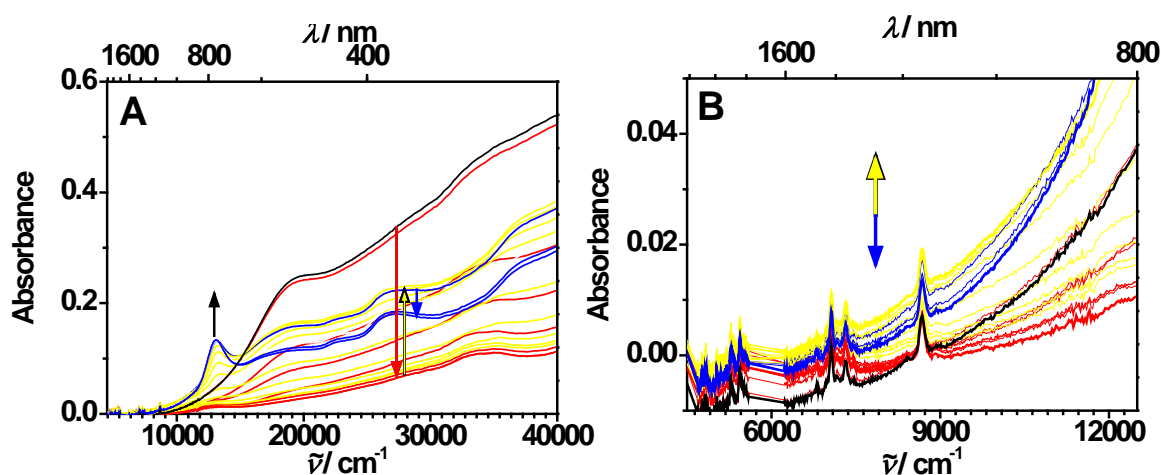


Figure 19. (A) SEC of **Au-Tara1L** (black line) in dcm/TBAH. The SEC is composed of three processes colored with red, yellow and blue. (B) NIR-region of the spectra.

Furthermore, the spectra of the neutral and the oxidized species were used to calculate the density ρ of triarylamine per nanoparticle with equation (7):

$$\rho = \frac{\epsilon_{Au225}^{600\text{ nm}}}{A_{Au-Tara1S}^{600\text{ nm}}} \times \frac{A_{Au-Tara1S^{ox}}^{700\text{ nm}}}{\epsilon_{Ref^{ox}}^{770\text{ nm}}} \quad (7)$$

where $\epsilon_{Au225}^{600\text{ nm}}$ is the extinction coefficient of a $Au_{225}(SC_6H_{13})_{57}$ nanoparticle (radius 1.0 nm)¹⁸⁴ at 600 nm, $A_{Au-Tara1S}^{600\text{ nm}}$ is the absorbance of **Au-Tara1S** at 600 nm, $A_{Au-Tara1S^{ox}}^{700\text{ nm}}$ is the corrected absorbance of the monoradical cation band at 770 nm of the oxidized species of **Au-Tara1S** (eqn (8)) and $\epsilon_{Ref^{ox}}^{770\text{ nm}}$ is the extinction coefficient of the monoradical cation band at 770 nm of the oxidized species of **Ref1**.

$$A_{Au-Tara1S^{ox}}^{700\text{ nm}} = A_{Au-Tara1S}^{770\text{ nm}} - A_{Au-Tara1S^{ox}}^{770\text{ nm}^*} \quad (8)$$

Where $A_{Au-Tara1S}^{770\text{ nm}}$ is the absorbance of the neutral species of **Au-Tara1S** at 770 nm and $A_{Au-Tara1S^{ox}}^{770\text{ nm}^*}$ is the absorbance of the oxidized species at 770 nm. Thus, in **Au-Tara1S** each gold core is covered by ca. 25 chromophores. The density ρ for **Au-Tara1L** was not calculated because we have not found any extinction coefficient for such a large particle.

2.1.6 Conclusion

In summary, we present the first synthesis of triarylamine-functionalized gold nanoparticles of two different sizes. The absorption properties of these two conjugates differ strongly both in the neutral state and in the ligand-oxidized state. In the neutral state this is due to different electric fields emanating from the gold particle which interacts with the transition dipole of the ligands. In the ligand oxidized state, the OSWV and the SEC measurements of the nanoparticles (**Au-Tara1S**, **Au-Tara1L**) revealed a strong coupling between neighboring triarylamine units which is due to through-space intervalence interactions¹⁸⁵ in these metal-organic mixed-valence conjugates. The SEC also showed for the larger particle that by charging the chromophore-nanoparticle system, the gold core transitions are damped. These multi-electron redox-active nanoparticle systems may be interesting building blocks in the field of charge storage (electron sponge) as they can be loaded to a high degree at constant potential.

2.2 Optical and Electrochemical Properties of Triarylamine-Gold-Nanoparticle Conjugates: Varying the Bridging Unit

In chapter 2.1, the optical and electrochemical properties of a triarylamine gold nanoparticle system with a π -conjugated bridging unit (**Au-Tara1**) are presented. This relatively short bridge mediated a strong gold core-chromophore interaction which depends on the relative orientation of the transition dipole moment of the chromophore to the gold surface. Electrochemical and spectroelectrochemical measurements revealed also a strong intraparticle interaction between neighboring triarylamine units which is seen by a sizable intervalence-charge-transfer absorption band (IVCT) in the NIR. In order to study the gold core-chromophore and chromophore-chromophore interactions in more detail, the synthesis and the investigation of triarylamine-gold nanoparticle systems with different bridging units (Chart 4, **Au-Tara2-4**) and the corresponding reference compounds are presented (Chart 4, **Ref2-4**) in this chapter.¹⁸⁶

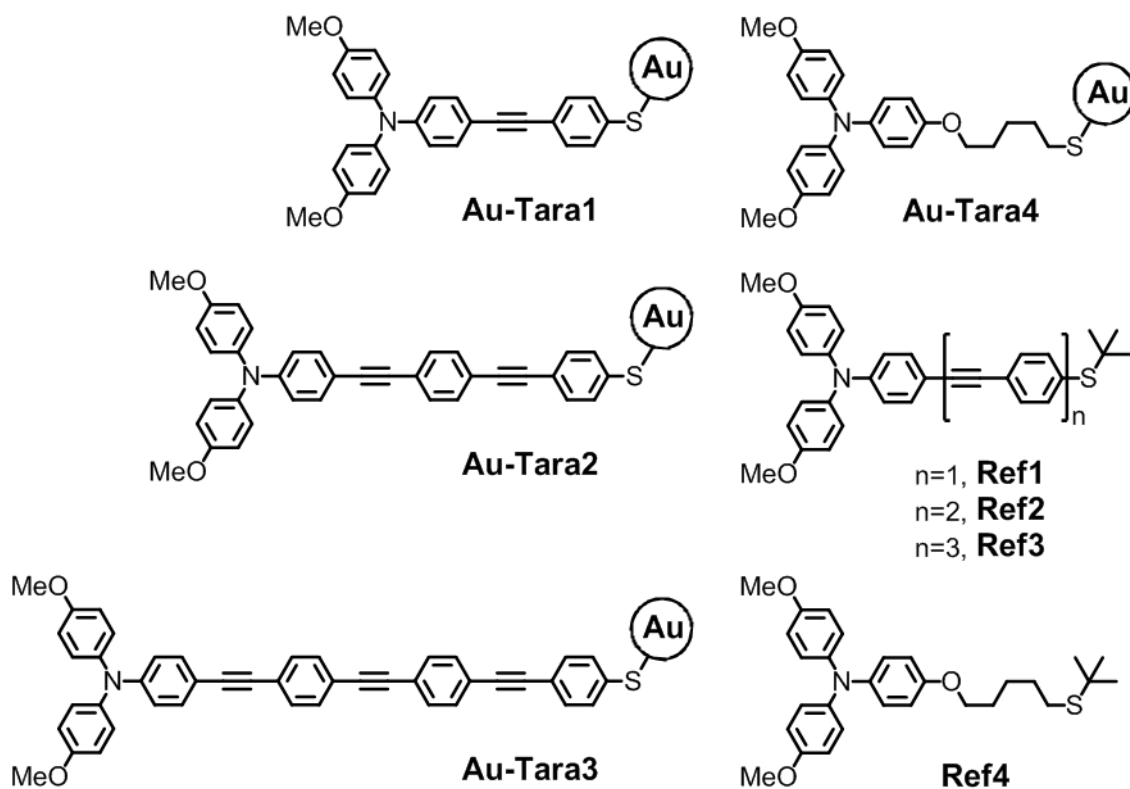
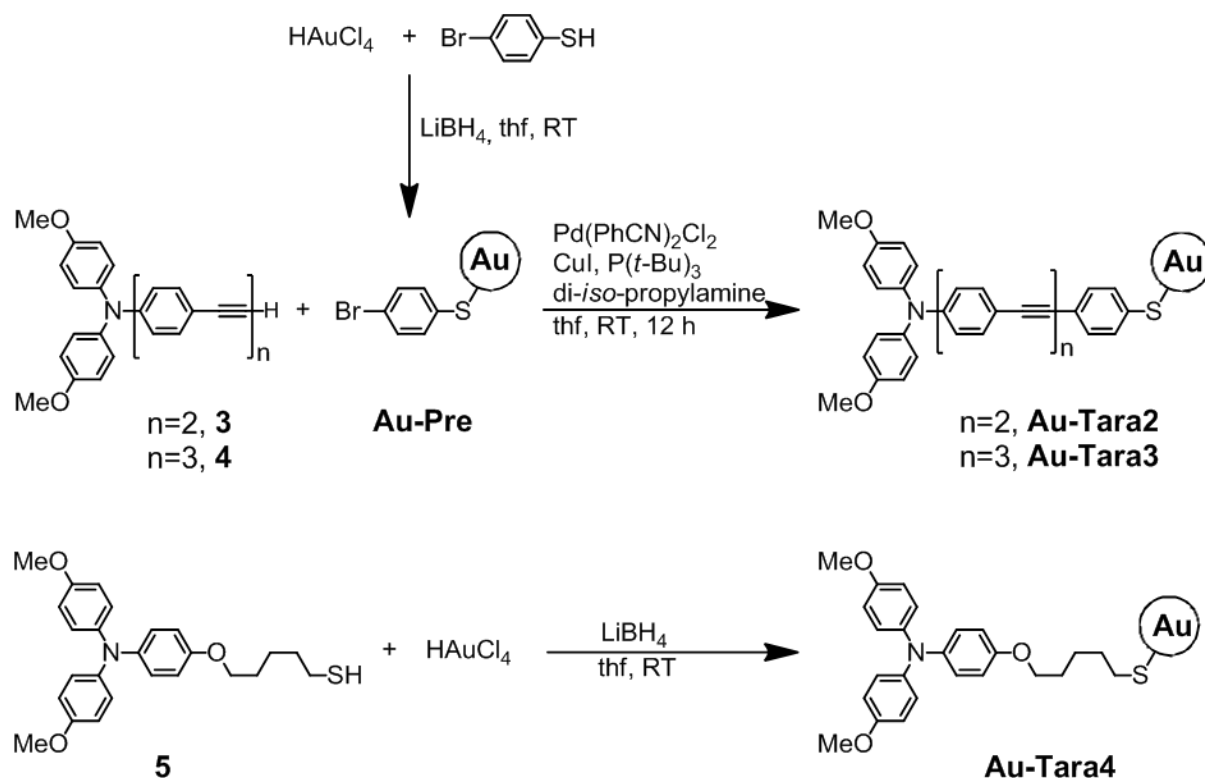


Chart 4.

The length and the chemical structure of the bridging unit were varied to study their influence on the absorption and electrochemical properties of the chromophores. The results are compared with those of **Au-Tara1**. In the interest of clarity, only the results for **Au-Tara1S** are discussed in this chapter.

2.2.1 Synthesis

The synthetic goal was to prepare gold nanoparticles (AuNPs) with comparable gold particle size in order to avoid electronic effects that result from different particle sizes such as surface plasmon resonance effects. Thus, the particles with a π -conjugated bridging unit **Au-Tara2-3** were prepared by the above described synthetic procedure (see Section 2.1.1). This procedure starts from the 4-bromobenzenethiol-functionalized precursor **Au-Pre** which was synthesized by slowly adding concomitantly a mixture of 4-bromobenzenethiol and tetrachloroauric acid in thf and LiBH_4 in thf to a reaction vessel charged with pure thf *via* a syringe pump (see Figure 8).¹²³

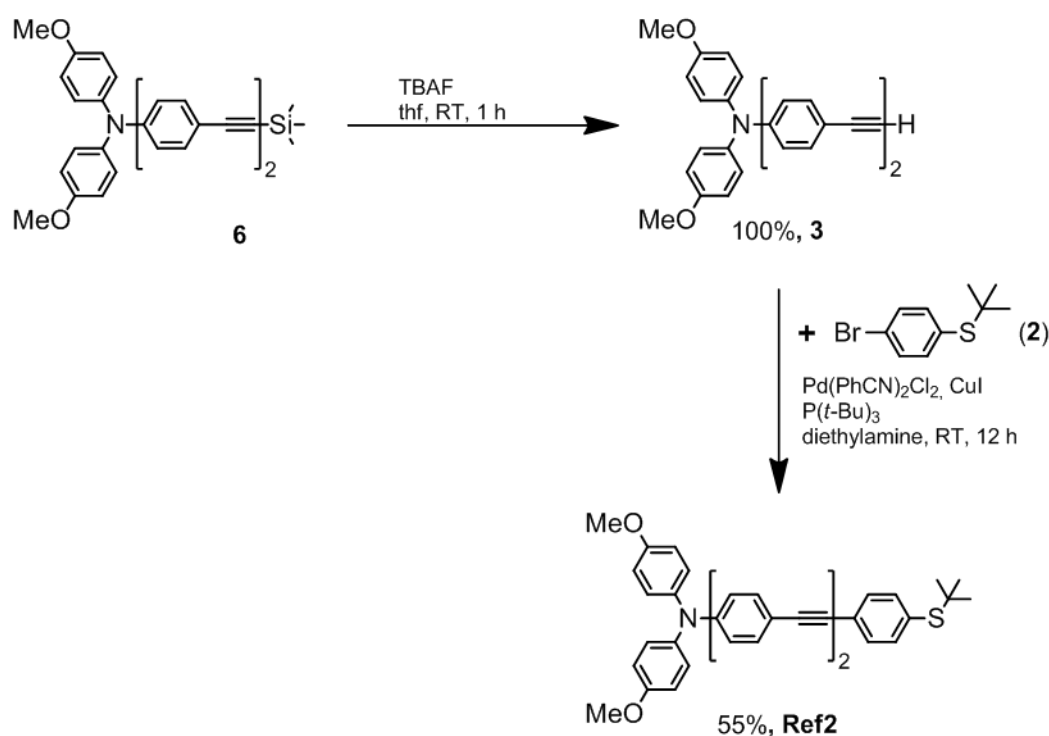


Scheme 8. Synthesis of the **Au-Tara2-4** Particles.

The resulting precursor nanoparticle which is covered by a ligand shell of 4-bromobenzenethiol is then transformed into the desired product by a *Hagihara-Sonogashira* reaction with an appropriate terminal alkyne (**3** or **4**) (Scheme 8).

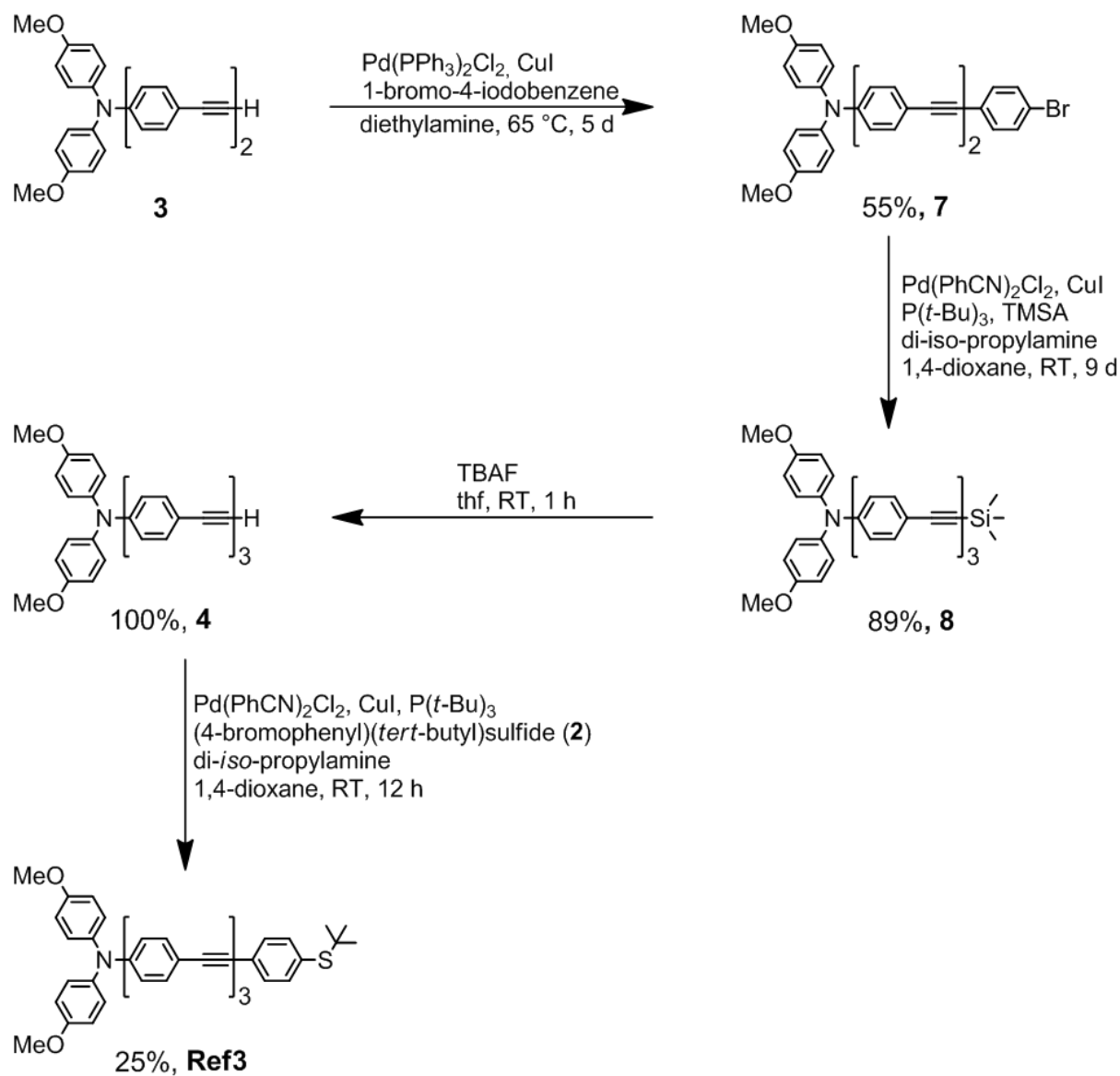
For the synthesis of the nanoparticle with the aliphatic bridging unit **Au-Tara4** a direct procedure by reaction of the functionalized thiol and LiBH_4 was used (Scheme 8).¹¹⁷ The thiol **5** and the tetrachloroauric acid were dissolved in thf and a NaBH_4 -solution in thf was slowly added. It was very important that the thiol was separated from the disulfide derivative carefully because the disulfide is not able to stabilize the nanoparticle and to prevent agglomeration.

The synthesis of **Ref2** is outlined in Scheme 9. The alkyne **3** was obtained from **6**¹⁷² with tetra-*n*-butylammonium fluoride (TBAF) in thf in 100% yield.¹⁶⁴ The reaction of **3** with **2** yielded 55% of **Ref2**.^{123, 179}



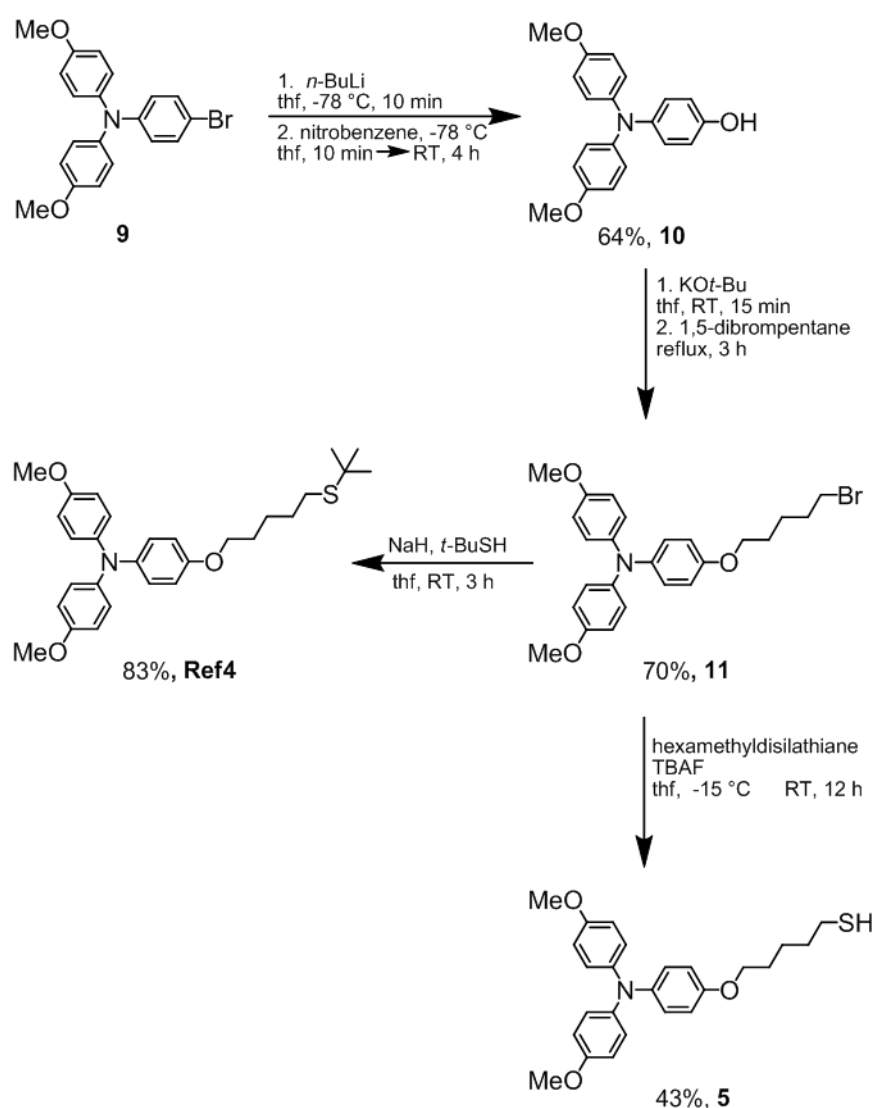
Scheme 9. Synthesis of **Ref2**.

Scheme 10 depicts the synthesis of **Ref3**. The alkyne **3** was converted into **7** via a Hagihara coupling reaction in 55% yield, followed by the same reaction type to obtain **8** in 89% yield.^{123, 179} Removal of the trimethylsilylgroup with TBAF in thf yielded alkyne **4**. **Ref3** was synthesized from **4** in 25% yield.



Scheme 10. Synthesis of **Ref3**.

The thiol ligand **5** and the reference compound **Ref4** were synthesized in three steps starting from the triarylamine **9** (Scheme 11). The aryl bromide was converted into the aryl hydroxide derivative **10** according to Buck et al.¹⁸⁷ in 64%. Compound **11** was obtained by adding KO*t*-Bu and 1,5-dibromopentane to the phenol **10** in 70% yield.¹⁸⁸ From this **Ref4** was synthesized *via* a substitution reaction with *t*-BuSH. According to Hu et al.¹⁸⁹ the alkane bromide **10** was transformed into the thiol ligand **1**. The synthesis of **Au-Tara1**, **Au-Pre1** and **Ref1** are described in chapter 2.1.



Scheme 11. Synthesis of **Ref4** and the thiol **1**.

2.2.2 Analysis

The purity of the **Au-Tara** samples was checked by NMR spectroscopy. Since molecules bound to the gold core exhibit broadened peaks in the $^1\text{H-NMR}$ spectrum^{20, 64, 130} any traces of unbound molecules would superimpose these broadened signals with sharp peaks. However, the spectra of the **Au-Tara** particles show only broadened peaks attributed to the organic layer of the particle (see Figure 20) which proves that the samples are essentially free of unbound ligands.

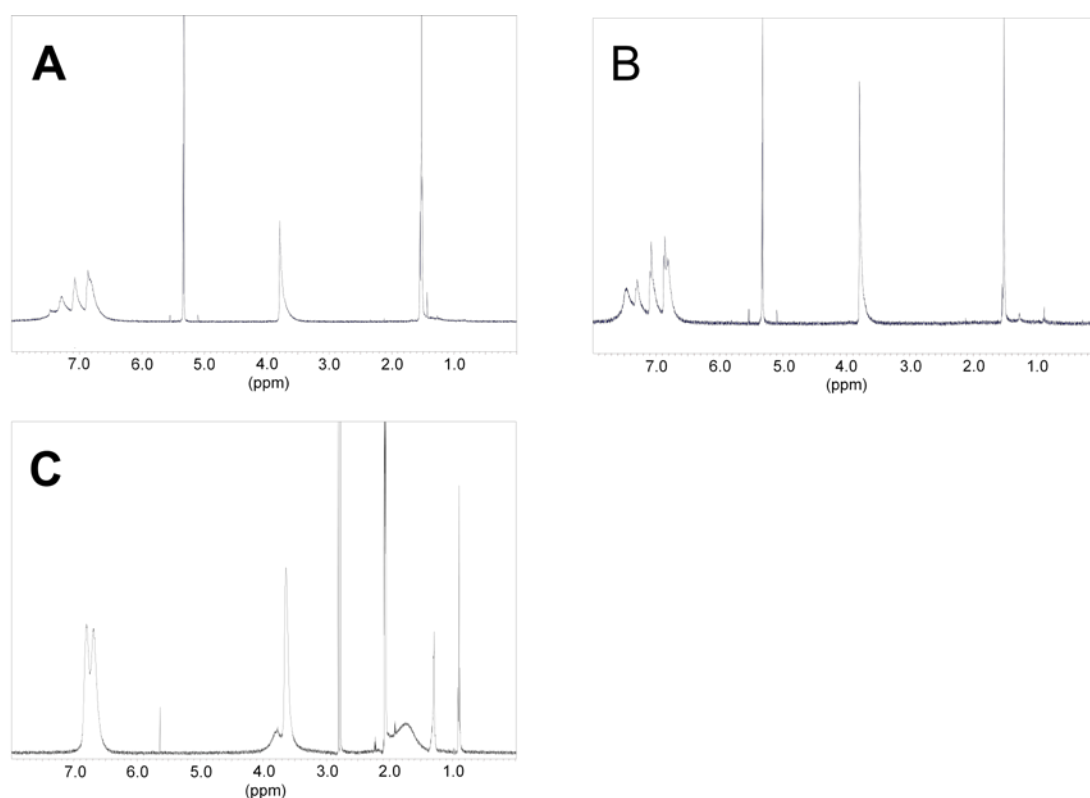


Figure 20. $^1\text{H-NMR}$ spectra of (A) **Au-Tara2** in dichloromethane- d_2 , (B) **Au-Tara3** in dichloromethane- d_2 and (C) **Au-Tara4** in acetone- d_6 .

The particle gold core size was determined by scanning transmission electron microscopy (STEM) measurements. The typical images and the histograms of the size distribution are shown in Figures 21-23 and the results are listed in Table 3. Polydispersity in the core size is seen but the average radii of the **Au-Tara1S** and **Au-Tara2-4** particles are in the same range of ca. 1 nm. Gold particles of this size are expected to have truncated octahedral or cubooctahedral shape^{56, 62, 63} with about 43% of all gold atoms sitting on corners or edges.¹⁹⁰

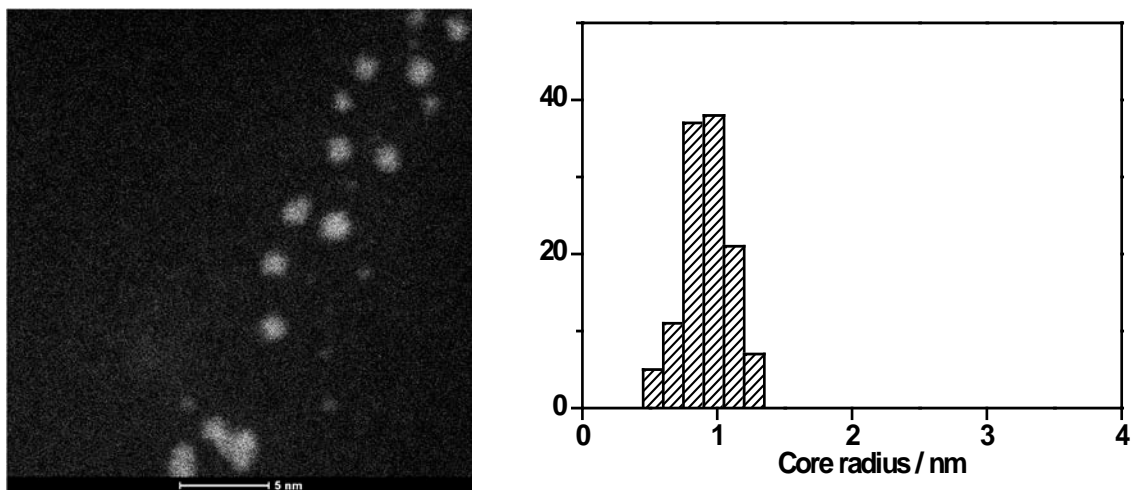


Figure 21. Dark field STEM images of **Au-Tara2** and the associated histogram; recorded using a FEI Titan 80-300 transmission electron microscope.

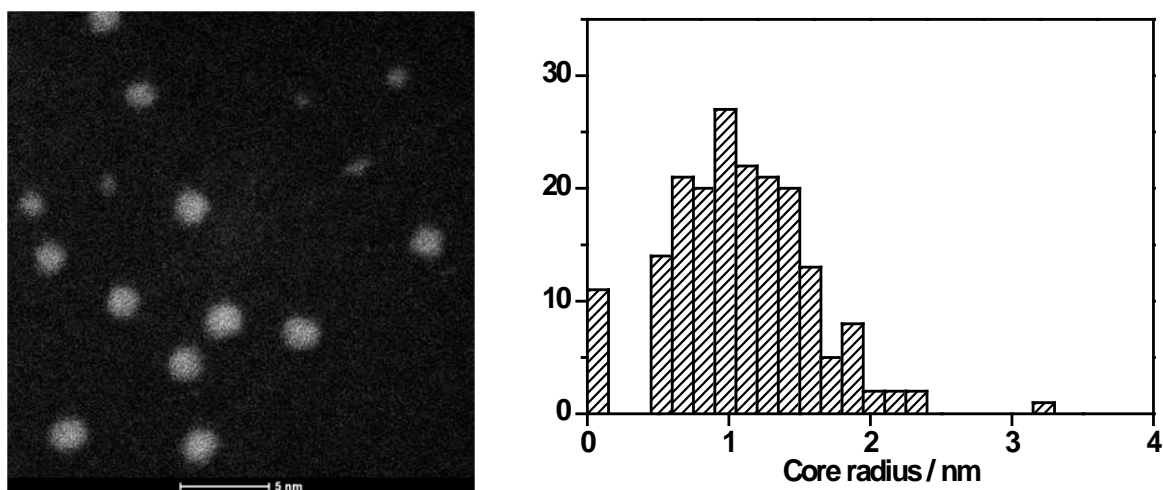


Figure 22. Dark field STEM images of **Au-Tara3** and the associated histogram; recorded on a FEI Titan 80-300 transmission electron microscope.

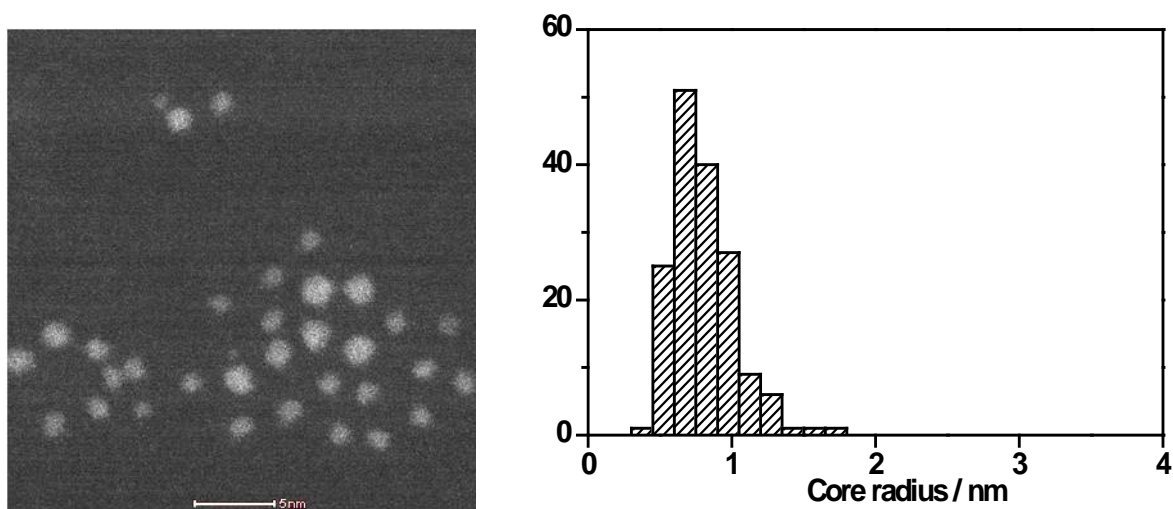


Figure 23. Dark field STEM images of **Au-Tara4** and the associated histogram; recorded using a FEI Titan 80-300 transmission electron microscope.

Table 3. Average Radius R of the Particle Gold Cores

	Au-Tara1S	Au-Tara2	Au-Tara3	Au-Tara4
Particle radius R / nm ^a	1.12±0.24 ^b	0.93±0.17	1.04±0.20	0.80±0.23

^aParticle radii were determined by STEM. ^bsee chapter 2.1.2.

As described in chapter 1.3, the nanoparticles should not be considered as a gold core covered with an organic layer, but rather as a gold core protected with gold thiolate staples. The **Au-Tara** particles are somewhat larger than those discussed in chapter 1.3 but polydisperse. Thus, one can assume that the ligands in **Au-Tara1-4** are attached in a similar fashion as those in refs 46, 54 and 55. However, due to the polydispersity of these samples, we treat the gold core as spherically shaped and do not consider specific binding modes of the ligands.

In order to calculate the hydrodynamic radii of **Au-Tara2-4**, DOSY-NMR measurements were carried out to obtain the diffusion coefficients of the particles in order to calculate the hydrodynamic radii. These experiments were performed at 283 K to suppress flow effects caused by convection. For spherically shaped molecules, the *Stokes-Einstein* equation describes the relationship between the diffusion coefficient D and the hydrodynamic radius R_H :

$$D = \frac{k_B T}{6\pi\eta R_H} \quad (9)$$

in which η is the viscosity of the solvent, k_B the Boltzmann constant and T the absolute temperature.²⁰ R_H is the sum of the gold core radius R and the thickness R_{OS} of the organic ligand shell. The calculated diffusion coefficients of **Au-Tara2-4** are listed in Table 4. Due to altering of the **Au-Tara1S** particle this sample was not analyzed.

Table 4. Dimensions of Particles: Diffusion Coefficient D , Hydrodynamic Radius R_H , Length of Attached Ligand l and Calculated Thickness of the Organic Shell R_{OS}

	Au-Tara2	Au-Tara3	Au-Tara4
D / (m ² /s) ^a	(2.42±0.12)×10 ⁻¹⁰	(2.48±0.08)×10 ⁻¹⁰	(1.88±0.02)×10 ⁻¹⁰
R_H / nm ^b	1.76	1.72	2.26
l / nm ^c	2.47	3.01	1.68
$R_{OS} = R_H - R$	0.83	0.68	1.46

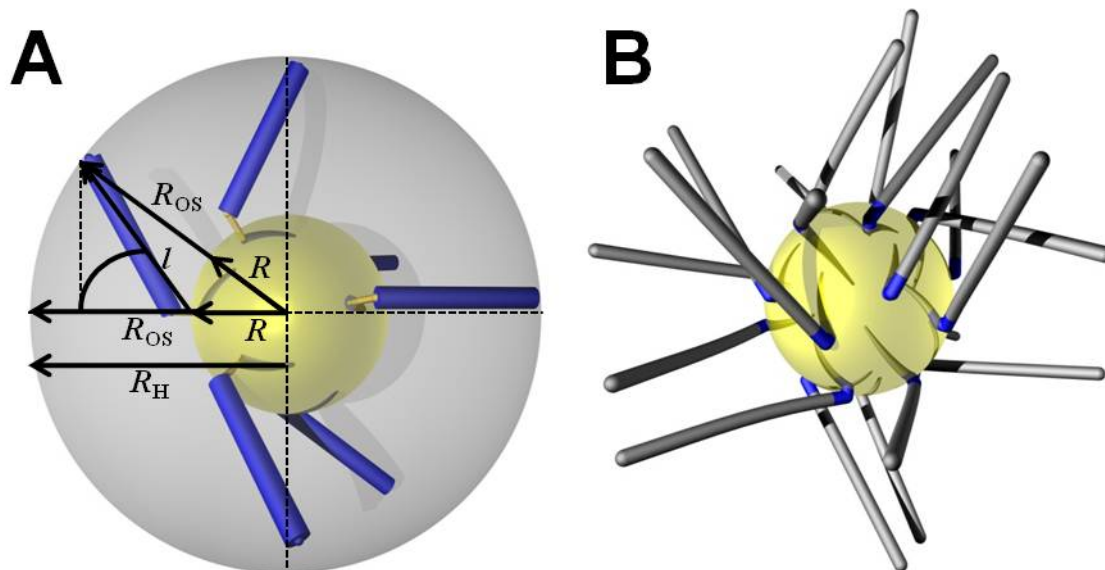
^aDiffusion coefficients D in dichloromethane-d₂ were determined by DOSY-spectra at 283 K.

^bHydrodynamic radii R_H were calculated from the D values with the *Stokes-Einstein* equation. ^cThe length of the ligand was estimated by AM1 computations performed using HyperChem.

Additionally the length l of the ligands was calculated by the AM1 method. If the thickness R_{OS} of the organic shell and the length l of the ligand were about the same size the ligands would be oriented perpendicularly to the surface. As can be seen from Table 4 R_{OS} is smaller than the length l for all nanoparticles. In case of **Au-Tara4** the deviation is only about 0.2 nm. We assume that the deviation is a consequence of the flexibility of the alkyl chain.^{20, 85} The length l of the **Au-Tara4** ligand was calculated for a molecule with a stretched alkyl chain but its flexibility probably shortens the average distance between the triarylamine and the gold surface. In contrast, the **Au-Tara2** and **Au-Tara3** particles possess a rigid π -conjugated bridging unit which fixes the length of the ligands. For these particles, the R_{OS} and l values differ even more strongly. If the attached ligands formed a densely packed and spherically shaped particle, the tilt angle α with respect to the surface normal (see Scheme 12 A) would be:

$$\alpha = 180^\circ - \arccos \left(\frac{l^2 + R^2 - 2R_{OS}^2}{2Rl} \right) \quad (10).$$

This yields an unrealistic angle of about 147° for **Au-Tara2** while α is illdefined for **Au-Tara3**. Average tilt angles for biphenylthiol derivatives self-assembled on polycrystalline gold are about 20° ,^{160, 191, 192} and X-ray structures of *p*-mercaptobenzoic acid protected gold nanoparticles revealed also a strong angular offset (see Figure 3).⁵⁵ However, in principle the angle cannot exceed 90° . Thus, we assume that the calculation of the hydrodynamic radius is incorrect as it rests on the assumption of a densely packed and spherically shaped particle. This assumption is likely to be wrong as will be argued below. Shen *et al.* reported that the free space around triphenylene moieties on the gold core increases with elongating the aliphatic bridging unit.¹⁵⁴ We suppose that this effect also occurs in the case of the rigid π -conjugated bridging unit. The free space around the triarylamine increases with the length of the bridging unit and the outer ligand density decreases. This leads to an urchin-shaped particle (Scheme 12 B) rather than densely packed spherically shaped particle and the calculated values for the hydrodynamic radii would deviate. Even though the orientation of the π -conjugated ligands to the gold surface cannot be determined, the ligands are probably tilted from the surface normal due to the gold thiolate binding motif.^{46, 54, 55, 193}



Scheme 12. A: Geometrical model of the **Au-Tara** particles, R is the radius of the gold core, R_{OS} is the thickness of the organic layer and R_H is the hydrodynamic radius; B: model of the urchin-shaped particles.

The common method for determining the organic weight fraction P_{OL} of gold nanoparticles (AuNP) is thermogravimetric analysis (TGA). By heating the sample, the organic ligands are cleaved from the gold core and the weight loss is detected. Usually, the sample residue of this process is pure gold. Indeed, this is observed for **Au-Tara4**. The weight loss is seen in the TGA-analysis of **Au-Tara4** as a large step (Figure 24).

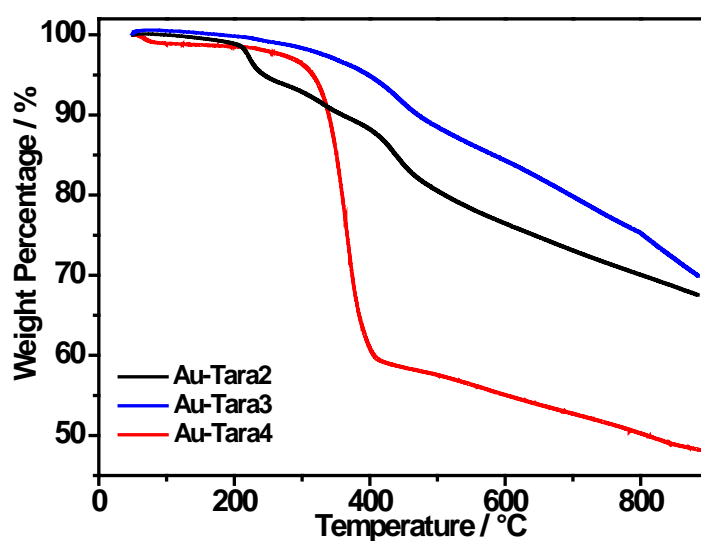


Figure 24. TGA analysis of **Au-Tara2** (solid black line), **Au-Tara3** (solid blue line) and **Au-Tara4** (solid red line).

The weight proportion of the organic layer thus is 40% in this functionalized alkanethiol covered nanoparticle. In contrast, **Au-Tara2** and **Au-Tara3** exhibit a gradual weight loss with much smaller steps over a large temperature range, and the sample residue was slag-like with some “gold-nuggets” inside. Hence, the method is not suitable to evaluate the organic weight fraction for the **Au-Tara2** and **Au-Tara3** particles with arenethiol ligands.

2.2.3 Electrochemistry

The redox potentials $E_{(\text{Ox})}$ of the reference compounds and the redox-center-functionalized nanoparticles were determined by Osteryoung square wave voltammetry (OSWV). These measurements were performed in dcm/TBAH at 298 K. Figure 25 displays the voltammograms of the **Au-Tara** particles. All compounds (nanoparticles **Au-Tara** and reference ligands **Ref**) possess two oxidation peaks, which can be attributed to the first and second oxidation of the triarylamine unit (see Table 5).¹⁷¹ Multi-cycle thin layer cyclic voltammetry experiments show that the first oxidation peak is in all compounds chemically reversible.

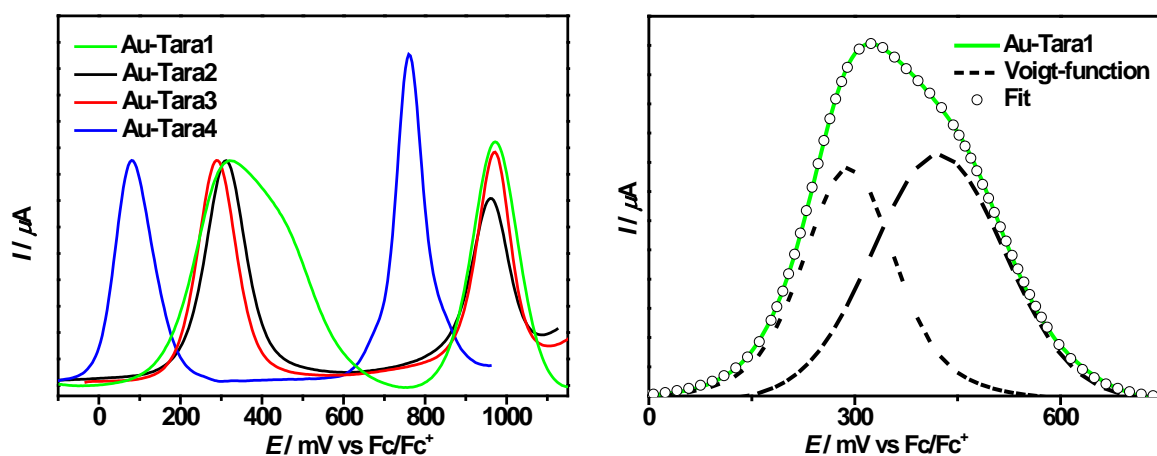


Figure 25. Left: OSWV of **Au-Tara1S** (solid green line, capacitive background currents were subtracted), **Au-Tara2** (solid black line), **Au-Tara3** (solid red line) and **Au-Tara4** (solid blue line) in dcm/0.3 M TBAH solution at 298 K with a platinum working electrode ($A = 3 \text{ mm}^2$). The peak current of the first redox wave is normalized; Right: Fit of the OSWV of **Au-Tara1S** with two Voigt-functions.

The first redox potential $E_{(\text{Ox1})}$ for the particles **Au-Tara1S** and **Au-Tara3** is very similar to that of the corresponding reference compounds (Table 5). In case of **Au-Tara2**, the oxidation peak is shifted by 30 mV to higher values and in case of **Au-Tara4** to lower values than the respective reference compounds. The reason for these minor differences is unknown but may be due to orientation effects of the triarylamine moiety relative to the gold core. The significant difference between **Au-Tara4** and the other **Au-Tara** species is due to the third alkoxy group attached to the triarylamine moiety which lowers the redox potential.^{161, 171, 194} In conclusion, these results show that attaching the ligand to the gold particle *via* a long π -conjugated or an aliphatic bridging unit does not affect the redox potential of the triarylamine units significantly. Therefore, a strong gold core-chromophore interaction cannot be observed by electrochemical methods.

Table 5. Redox Potentials of Au-Tara1S, AuTara2-4 and Ref1-4 Determined by OSWV vs. Ferrocene (Fc/Fc⁺) in dcm/0.3 M TBAH Solution at 298 K with a Platinum Working Electrode ($A = 3 \text{ mm}^2$)

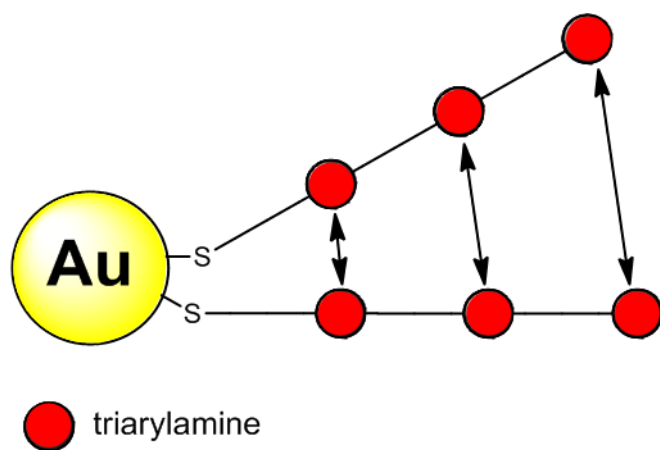
	Redox potential / mV	
	$E_{(\text{Ox1})}$	$E_{(\text{Ox2})}$
Au-Tara1S	290, 420 ^a	980
Ref1	280	950
Au-Tara2	310	960
Ref2	280	980
Au-Tara3	290	970
Ref3	290	960
Au-Tara4	80	760
Ref4	110	860

^aDetermined by a fit with two Voigt-functions (see chapter 2.1.3).¹²³

Unlike **Au-Tara1S**, the shape of the oxidation waves in the OSWV and CV of the **Au-Tara2-4** particles is only slightly broader (peak width at half height 108-116 mV) than the ideal peak width of 90 mV.⁸⁶ This indicates that the triarylaminines react independently of each other as non-interacting redox centers.^{23, 83, 84} In contrast, the OSWV analysis of **Au-Tara1S** exhibits a broadened signal for the first oxidation of the triarylaminines (see Figure 25 left). A fit of the OSWV voltammograms by two Voigt-functions reveals that the broadening is due to a splitting of the oxidation into two peaks (see Figure 25 right and

chapter 2.1.3). This splitting is associated with a strong interligand coupling between neighboring triarylamine centers.¹²³

Two reasons may account for the fact that strong intraparticle coupling of the ligands cannot be detected for the **Au-Tara2-4** particles. First, the distance between the terminal triarylamine units increases with the length of the rigid π -conjugated bridging unit (Scheme 13). This increasing distance possibly diminishes the coupling between neighboring triarylamines. That is why a broadening of the redox signal is not seen for the **Au-Tara2** and **Au-Tara3** particles. Note that in mixed valence *bis*-triarylamine systems the coupling between the triarylamine units also decreases by lengthening the distance between the units.^{168, 172} Furthermore, electrochemical studies on self-assembled monolayers on flat gold surfaces revealed signal broadening for attached redox centers.^{16, 17, 195} It was shown that the broadening depends on the mole fractions of the redox center in the monolayer. At low mole fractions, the oxidation wave becomes symmetric and less broadened.¹⁹⁶ Aside from inhomogeneities of the monolayer the broadening may originate from interactions between the redox centers.^{16, 195, 196} Second, in case of **Au-Tara4**, the redox centers are attached to the gold core *via* a flexible alkyl chain. The flexibility of the bridging unit possibly prevents a strong interaction as was reported for ferrocene-functionalized nanoparticles.⁷⁴



Scheme 13. Model of the **Au-Tara1-3** particles: relation between the distance of neighboring triarylamines and the length of the π -conjugated bridging unit.

Furthermore, we used the redox properties of the triarylamines to analyze the organic layer of the **Au-Tara2-4** particles with cyclic voltammetry. The redox-peak current i_p in a cyclic voltammetry experiment is a function of the square root of the scan rate ν and is described by the *Randles-Sevcik* equation (11):

$$i_p = 0.4463n^{3/2}F^{3/2}AC_0\sqrt{\frac{vD}{RT}} \quad (11)$$

in which n is the stoichiometric number of electrons involved in the electrode reaction, F is Faraday's constant, D is the diffusion coefficient (determined by DOSY, see Table 4), A is the effective electrode area ($A = 0.64 \text{ mm}^2$, determined by ferrocene), T is the temperature ($T = 283 \text{ K}$), and C_0 is the concentration of the electroactive species. The electrode reaction is described to be a single electron process ($n = 1$).^{22, 23, 85} A plot of i_p (in A) versus $v^{1/2}$ results in a straight line. The concentration C_0 (in mol m^{-3}) was evaluated from the slope m of this line by:

$$C_0 = \frac{m}{0.4463 \cdot F^{3/2} A \sqrt{\frac{D}{RT}}} \quad (12)$$

We divided C_0 by the concentration C_{AuNP} (weight per volume) of the cyclic voltammetry (CV)-solution used to obtain the mole of triarylamine units per gram nanoparticle $C_{\text{Tara/AuNP}}$:

$$C_{\text{Tara/AuNP}} = \frac{C_0}{C_{\text{AuNP}}} \quad (13)$$

From this we calculated the triarylamine weight fraction P_{Tara} of the total weight by:

$$P_{\text{Tara}} = \frac{C_0 M_{\text{Tara}}}{C_{\text{AuNP}}} = C_{\text{Tara/AuNP}} M_{\text{Tara}} \quad (14)$$

The CV-measurements of **Au-Tara2-4** at different scan rates and the plot of the redox-peak current i_p versus the square root of the scan rate v are given in Figures 26 and 27. In all cases, the current i_p increases linearly with $v^{1/2}$. This indicates that the particles do not adsorb onto the electrode surface and a linear diffusion controlled redox process can be assumed.^{85, 87, 91, 197} The analysis of the plot with the *Randles-Sevcik* equation and the corresponding calculations are presented in Table 6.

Table 6. Concentration of Redox Active Molecules (Triarylamine)s per Volume C_0 of the CV-Solution, Concentration of the Total Weight of the Particles per Volume C_{AuNP} of the CV-Solution, Number of Redox Active Molecules per Total Weight of the Particles $C_{\text{Tara/AuNP}}$, Triarylamine Weight Fraction P_{Tara} , Organic Weight Fraction P_{OL} , Average Composition of the Particles and Formal Particle Surface Coverage Γ

	Au-Tara2	Au-Tara3	Au-Tara4
$C_0 / (\text{mol L}^{-1})^a$	$(1.03 \pm 0.06) \times 10^{-3}$	$(0.979 \pm 0.06) \times 10^{-3}$	$(0.992 \pm 0.05) \times 10^{-3}$
$C_{\text{AuNP}} / (\text{g L}^{-1})$	1.24×10^{-3}	1.04×10^{-3}	1.09×10^{-3}
$C_{\text{Tara/AuNP}} / (\text{mol g}^{-1})$	$(0.831 \pm 0.048) \times 10^{-3}$	$(0.941 \pm 0.058) \times 10^{-3}$	$(0.910 \pm 0.046) \times 10^{-3}$
P_{Tara}	45%	60%	38%
P_{OL}^b	--	--	40%
Average composition ^c	$\text{Au}_{195}(\text{Tara-ligand})_{59}$	$\text{Au}_{273}(\text{Tara-ligand})_{127}$	$\text{Au}_{124}(\text{Tara-ligand})_{35}$
Γ / nm^{-2}	5.4	9.3	4.4

^aCalculated by the *Randles-Sevcik* equation from a cyclic voltammetry experiment. ^bDetermined by TGA. ^cThe average composition of the nanoparticles was established by the calculated triarylamine weight fraction P_{Tara} and the gold core radius R assuming that the gold core has a tightly-packed spherical structure and the organic layer consists only of the triarylamine ligands.

The triarylamine weight fraction P_{Tara} is calculated to be 38% for **Au-Tara4**. This value is in amazingly good agreement with that from the TGA measurement. Because of the higher molecular weight **Au-Tara2** and **Au-Tara3** show higher values for P_{Tara} . From these data and the average gold core particle size determined by STEM, we evaluated the average composition of the nanoparticles. We used a model published by Terrill *et al.* which assumes a tightly-packed spherical gold core with an atom density of bulk gold ρ_{Au} of 58.01 atoms nm^{-3} .²⁰

We also calculated the surface coverage Γ as the number of ligands per gold particle surface. The surface coverage is 5.4 molecules nm^{-2} for **Au-Tara2** which is much larger than that of very similar triarylamine-thiol ligands on flat gold surfaces which is ca. 1-2 molecules nm^{-2} ,¹⁷ but very similar to the coverage of tolanthiol on Au(111) (4.8 molecules nm^{-2}).¹⁹⁸ A surface coverage of ca. 5 molecules nm^{-2} is well conceivable for the nanoparticles (AuNP) if one takes the urchin-like arrangement of ligands into account which allows a dense packing right at the gold particle surface (where the ligands of **Au-Tara1-3** are more like the above mentioned tolanthiols) but a loose configuration at the bulkier triarylamine termini. The coverage for **Au-Tara3** is 9.3 molecules nm^{-2} which is still below the formal coverage of a *p*-

mercaptobenzoic acid protected gold nanoparticle (102 Au atoms and 44 ligands)²⁰ of 14.5 molecules nm⁻².

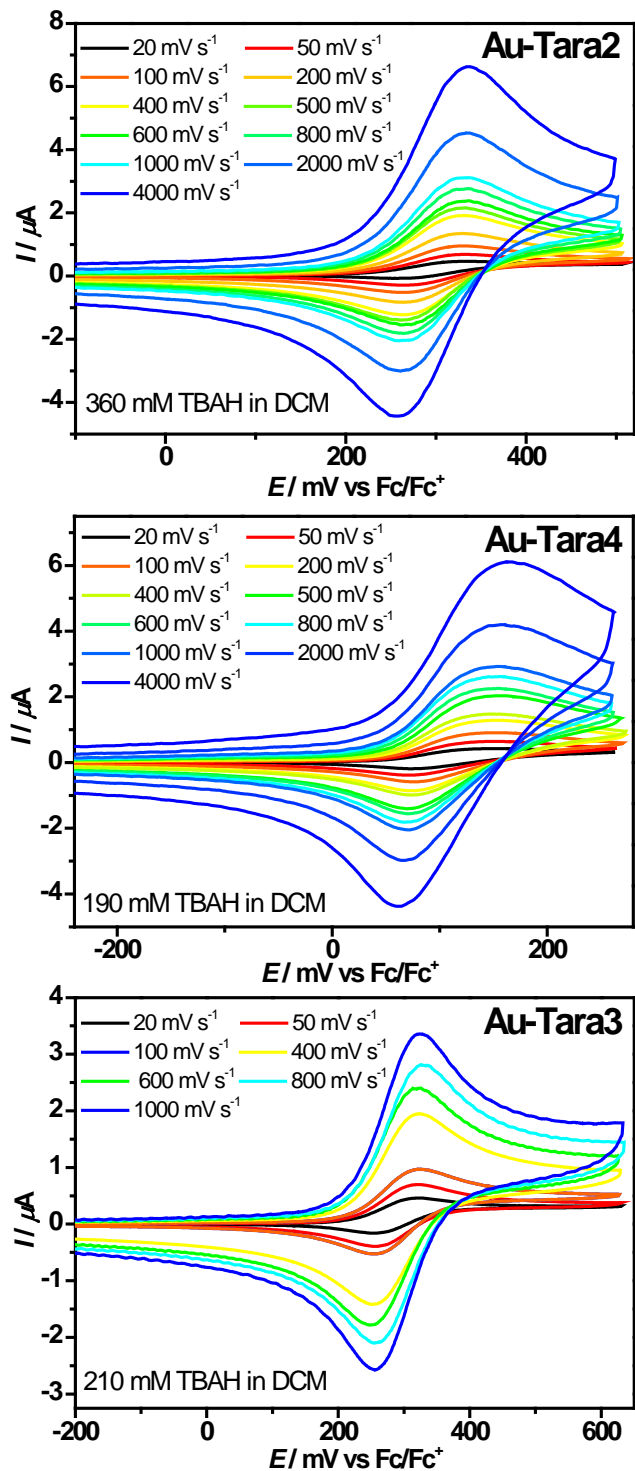


Figure 26. Cyclic voltammograms of Au-Tara2-4 at different scan rates in dcm/TBAH at 283 K with a platinum working electrode ($A = 0.64 \text{ mm}^2$); each voltammogram is referenced against Fc/Fc^+ .

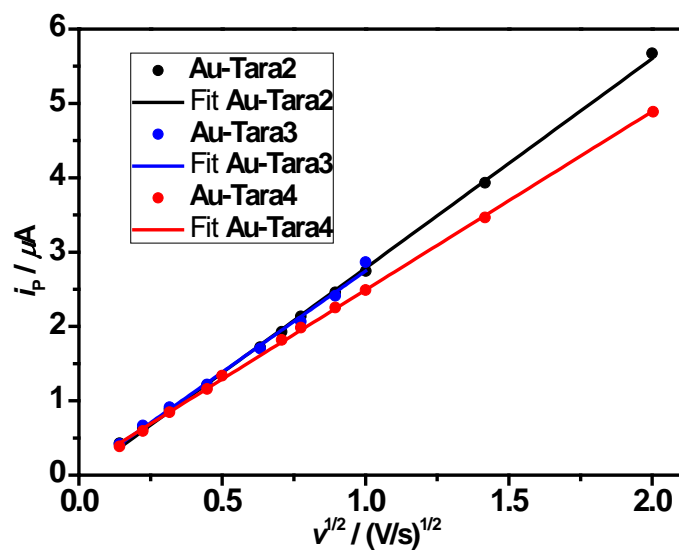


Figure 27. Redox-peak current i_p (filled circles) versus square root of the scan rate v for **Au-Tara2-4**; the capacitive background currents were subtracted for the determination of i_p . The linear correlation is given by solid lines.

2.2.4 UV/vis/NIR Absorption Spectroscopy

The optical properties of the here presented compounds were investigated by UV/vis/NIR absorption spectroscopy (see Figure 28). The reference compounds **Ref2** and **Ref3** exhibit two intense absorption bands at 26000 and 32700 cm^{-1} . In comparison to **Ref1**, which also shows two bands, both bands are bathochromic shifted which is due to the more extended π -system. In contrast to the π -conjugated ligands, **Ref4** shows only one intense band at 33300 cm^{-1} with a weak shoulder to the red edge at 27900 cm^{-1} . The substitution pattern is responsible for this band structure.¹⁷¹

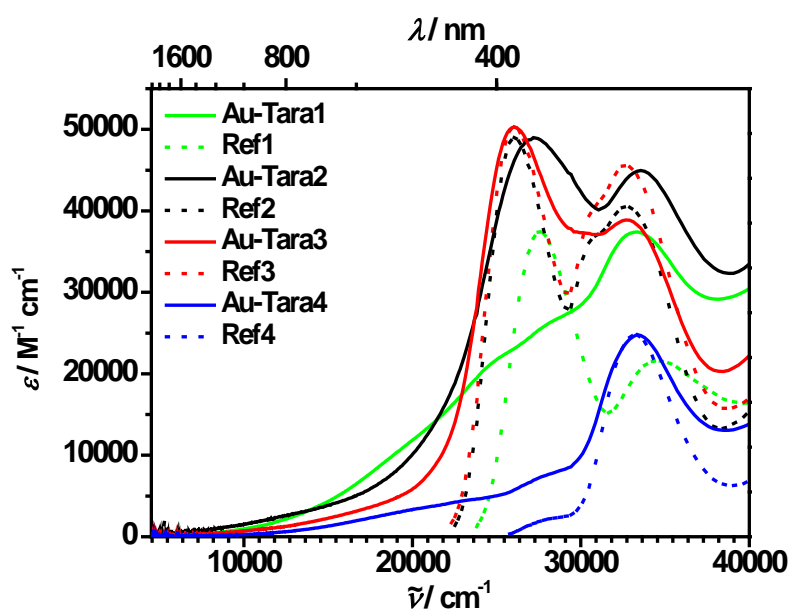


Figure 28. Absorption spectra of the **Au-Tara** nanoparticles (solid lines) and the corresponding reference compounds (dotted lines) in dcm. The extinction coefficients refer to the reference compounds **Ref**. The most intensive band of the nanoparticles is normalized to the most intensive band of the corresponding reference compound.

The spectra of **Au-Tara2** and **Au-Tara3** are characterized by two intense absorption bands at 27200/26000 cm^{-1} and 33600/32700 cm^{-1} . Both can be assigned to the triarylamine ligands. In the case of **Au-Tara3**, the band maxima are at the same position as in the reference compound **Ref3**. The band maxima of the triarylamine ligands in the spectra of **Au-Tara2** are blue shifted both by ca. 1200/900 cm^{-1} in comparison to **Ref2**. The blue shift might either be due to an increased interaction of the chromophore ligand with the emanating electrostatic field of the gold core or is due to an interaction between neighboring ligand

chromophores (excitonic interaction of transition dipole moments). The spectra of **Au-Tara3** do not exhibit such a shift of the triarylamine bands. Although the chromophore density is larger than in **Au-Tara2**, both possible interactions are weakened due to the longer bridging unit. Lengthening of the bridging unit increases the distance between the chromophore termini and the gold core and therefore results in decreasing gold-chromophore interactions. However, lengthening also increases the distance between neighboring ligand chromophores whose inter-chromophore interactions consequently also decrease. Thus, even though the larger chromophore density in **Au-Tara3** than in **Au-Tara2** should lead to a decrease of the chromophore-chromophore distance, we assume that the longer bridging unit in **Au-Tara3** overcompensates this effect.

In the spectrum of **Au-Tara1S** (see also Figure 15), the low energy ligand band of the triarylamine ligand was not observed. This was interpreted to be due to an anisotropic interaction between electromagnetic fields emanating from the gold core with the two differently oriented transition moments of the ligand (see chapter 2.1.4). This interaction affects predominantly the low energy band of the ligand polarized along the long molecular axis.¹²³ Both ligand bands of the **Au-Tara2** and **Au-Tara3** particles are very intense. However, in these systems the bridging unit is too long to mediate a strong gold core-chromophore interaction as in **Au-Tara1S**.

The absorption spectrum of **Au-Tara4** reflects the absorption properties of the reference compound **Ref4** very closely. The transition moments of the ligands do not seem to be affected by the gold core or the adjacent ligands. In this case, the aliphatic bridging unit prevents any intraparticle and ligand-gold interactions. We assume that both the flexibility and the aliphatic character of the bridge are responsible for this observation.

In order to study the ligand-gold interactions in more detail, we have performed gel permeation chromatography (GPC) analysis to fractionate the polydisperse samples of **Au-Tara2-4** by size.¹⁹⁹⁻²⁰¹ In Figure 29, the absorption spectra of the fractions are plotted versus the particle size (the size decreases with the retention time). With decreasing particle size, the band maxima of the chromophores do not shift. In contrast, the optical properties of the gold core change while scanning the particle size. Therefore, we conclude that the size-related optical and electronic effects of the small gold core do not affect the optical properties of the attached chromophores. This indicates that the long π -conjugated and aliphatic bridging units cannot support any interactions between the chromophores and small gold cores.

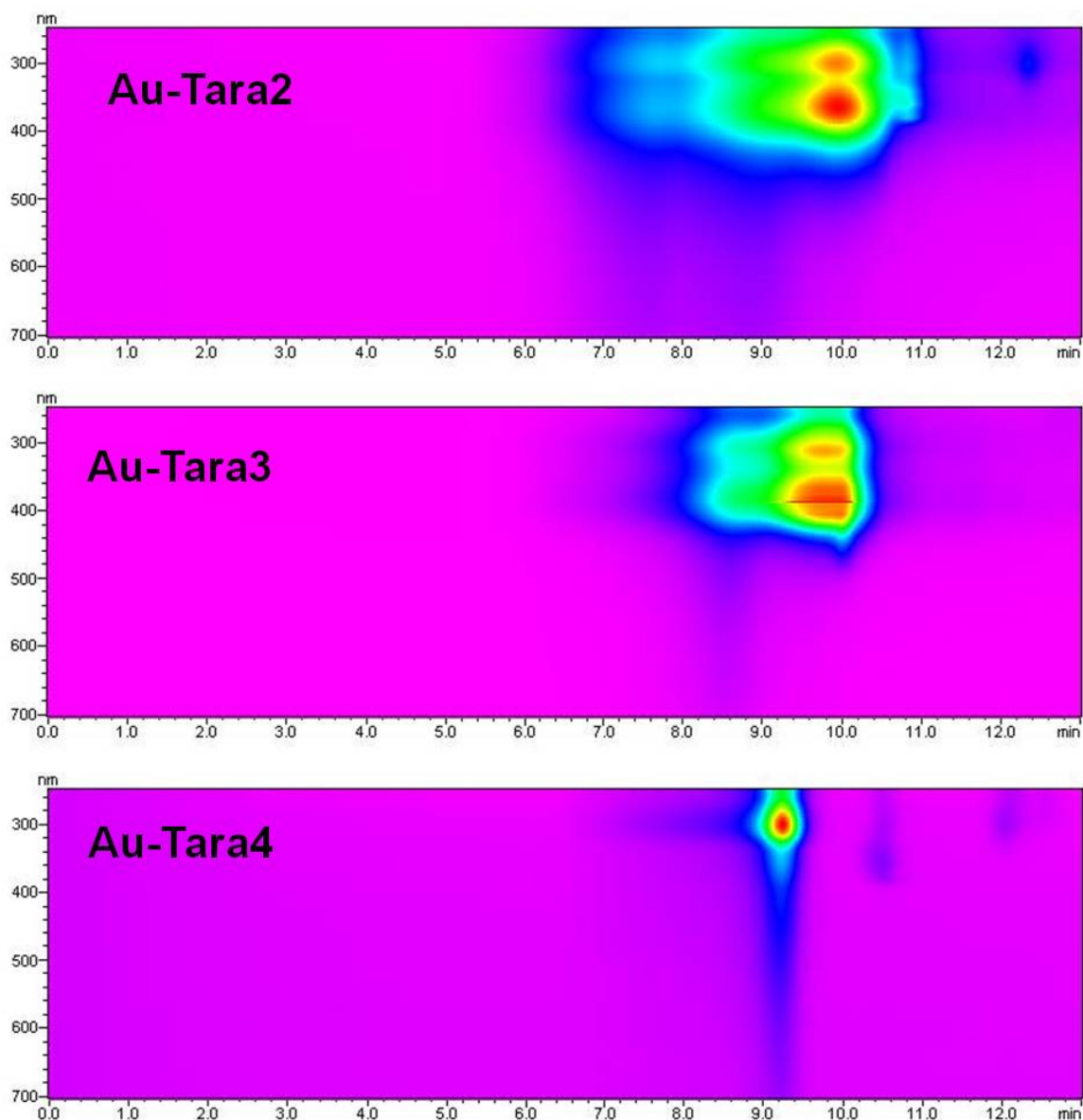


Figure 29. GPC analysis of **Au-Tara2**, **Au-Tara3** and **Au-Tara4**; UV/vis spectra vs. retention time.

We also calculated the molar extinction coefficients of the triarylamine absorption bands via the *Lambert-Beer* law and the concentration of triarylamines in the nanoparticle solution ($C_{\text{Tara}/\text{AuNP}}$, number of redox active molecules per total weight of the particles, see Table 6). The ligand extinction coefficients of the **Au-Tara** compounds are larger than those of the reference compounds (see Table 7). This is due to the ligand bands overlapping with bands of the gold core. The electronic transitions of the gold core have weak intensity in the red and gain intensity with increasing wave number.⁶⁹ The resulting gold core spectrum superimposes the ligand spectra. As a result of the small gold core size, the surface plasmon band, a broad

absorption band in the visible region around 19100 cm^{-1} , is not seen in the spectra of **Au-Tara2-3**.⁷

Table 7. Absorption Maxima $\tilde{\nu}$ and Corresponding Extinction Coefficients ε in dcm

	$\tilde{\nu}/\text{cm}^{-1}(\varepsilon/\text{M}^{-1}\text{cm}^{-1})$	
Ref1	27600 (37700)	34500 (21400)
Ref2	26000 (48800)	32700 (40700)
Au-Tara2	27200 (53600 ^a)	33600 (48900 ^a)
Ref3	26000 (50200)	32700 (45600)
Au-Tara3	26000 (62400 ^a)	32900 (49100 ^a)
Ref4		33300 (24800)
Au-Tara4		33300 (44200 ^a)

^aExtinction coefficient per mole ligand.

2.2.5 Spectroelectrochemistry

Furthermore spectroelectrochemical measurements were carried out in order to monitor the UV/vis/NIR spectral changes of the AuNPs during stepwise oxidation. In principle, both the gold core as well as the triarylamine center can be oxidized. Only the first oxidation was investigated, because the oxidation to the dication of the triarylamine ligands is chemically irreversible on a long timescale. All spectra (see Figure 30) demonstrate that with proceeding oxidation the triarylamine bands lose intensity and simultaneously an intense band between 13000 cm^{-1} and 14100 cm^{-1} rises. This new band is associated with a π - π^* -transition of the triarylamine radical cation. Taking into account that the spectra of **Au-Tara3** and **Au-Tara4** are superimposed by the gold core absorption bands, the spectra of the triarylamine radical cations are very similar to the spectra of the radical cations of the corresponding reference compounds. A comparison of the corresponding difference spectra illustrates this fact in more detail (see Figure 31). In the case of **Au-Tara2**, the progression of the spectra differs from **Ref2**. For a better overview, we partitioned the spectra of **Au-Tara2** in three processes. The first (given in red) process shows an increase of bands in the vis/NIR region and a decrease of bands in the UV region (see also Figure 32A). The next process (in yellow) is characterized by the increase of the π - π^* -transition band at 13100 cm^{-1} of the radical cation and a weak band at 6000 cm^{-1} . The latter one diminishes during the last process (in blue, see inset in Figure 30). In order to point out the dynamic of the three consecutive processes in more detail, the difference spectra of the SEC measurement are shown in Figure 31. The different progression of the individual processes is clearly seen in the NIR region.

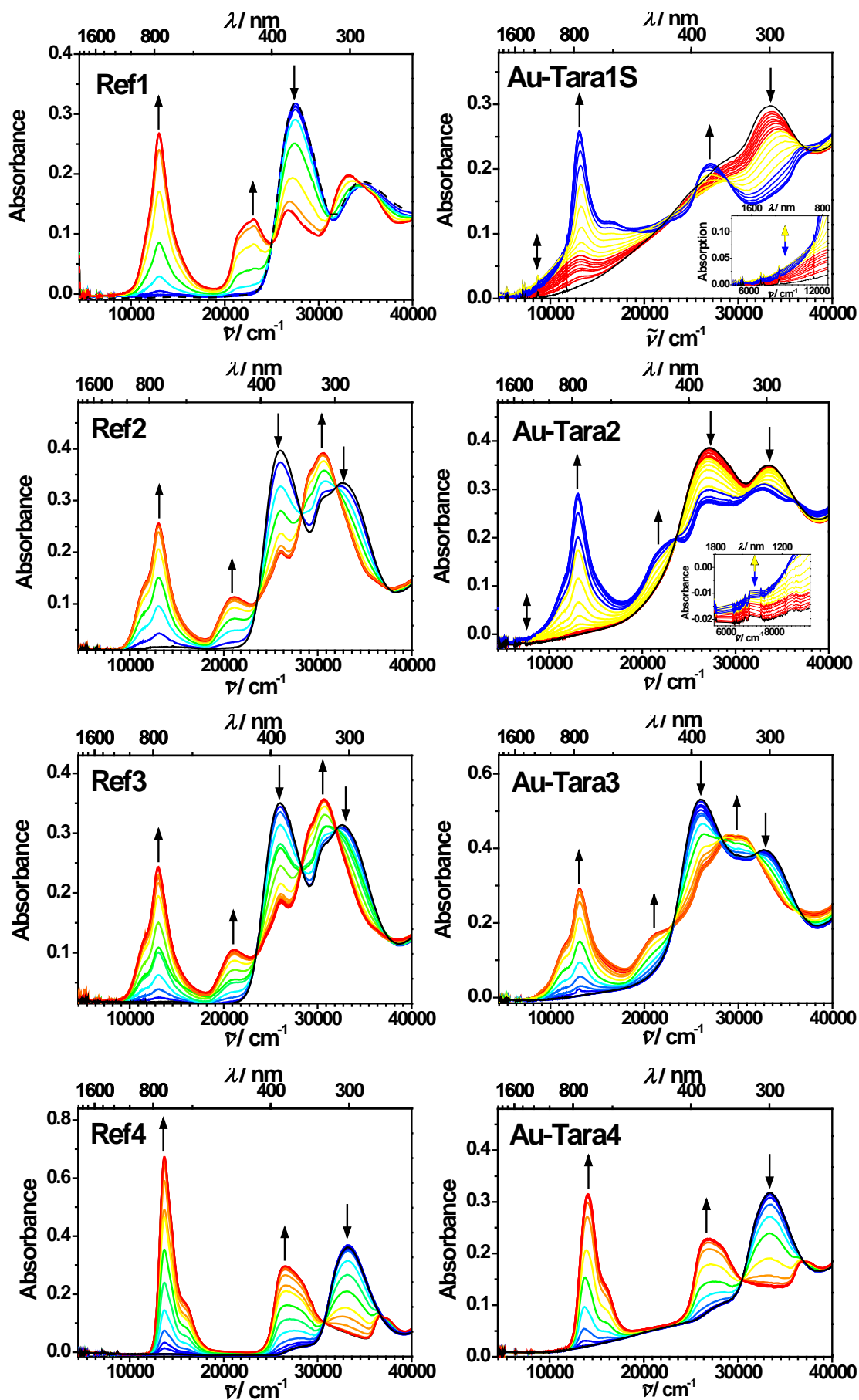


Figure 30. SEC of Au-Tara1S, Au-Tara2-4 and Ref1-4 in dcm/0.3 M TBAH solution at 298 K.

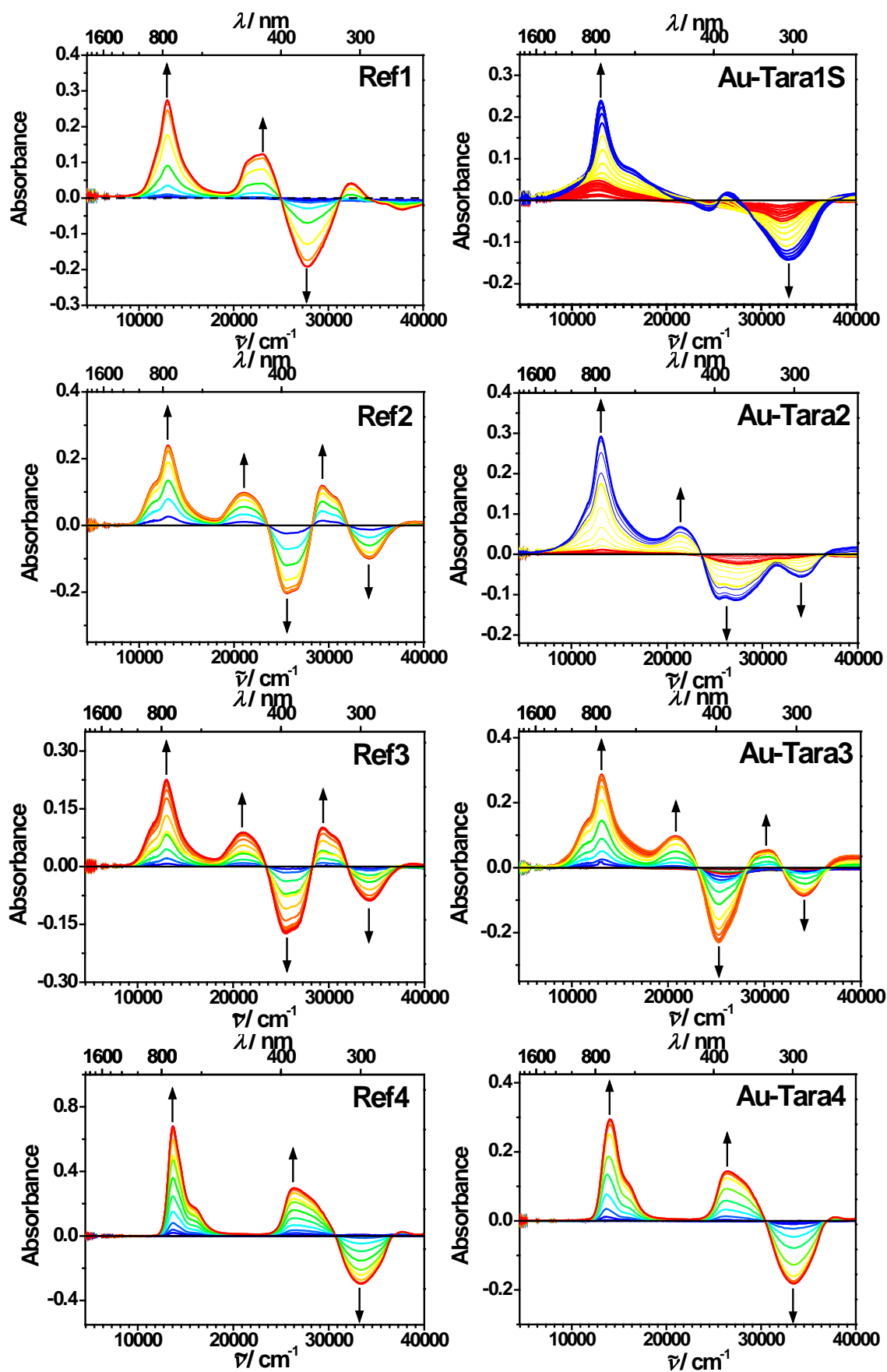


Figure 31. Difference absorption spectra of the SEC measurements with respect to the neutral species.

The increase and decrease of the bands in the first process is probably a result of gold core charging supported by the electrolyte. We assume that the TBAH electrolyte penetrates into the organic layer and mediates the charging of the gold core. It is known that charging the gold core can affect gold core transitions in the UV/vis/NIR region.^{49, 50, 79, 202, 203} The incorporation of electrolyte in the organic layer is possibly a consequence of an inhomogeneous and quite loose arrangement of the ligands in case of **Au-Tara2**.

As has been observed in other *bis*-triarylamine systems,^{168, 172, 177} the weak band at 6000 cm^{-1} that rises and decreases during the oxidation of **Au-Tara2** can be assigned to an intervalence charge transfer band (IVCT) which is associated with a hole transfer from an oxidized triarylamine to a neighboring neutral triarylamine. Thereby the hole is transferred through space between the triarylamines.^{123, 185, 204} The **Au-Tara1S** particle exhibits an even more intense IVCT-band than that of **Au-Tara2** (see also chapter 2.1.5). This is likely due to the larger Tara-Tara distance in **Au-Tara2** than in **Au-Tara1S** (see also Scheme 13), resulting in a lower intraparticle coupling of the ligands. The OSWV measurements confirm this conclusion.

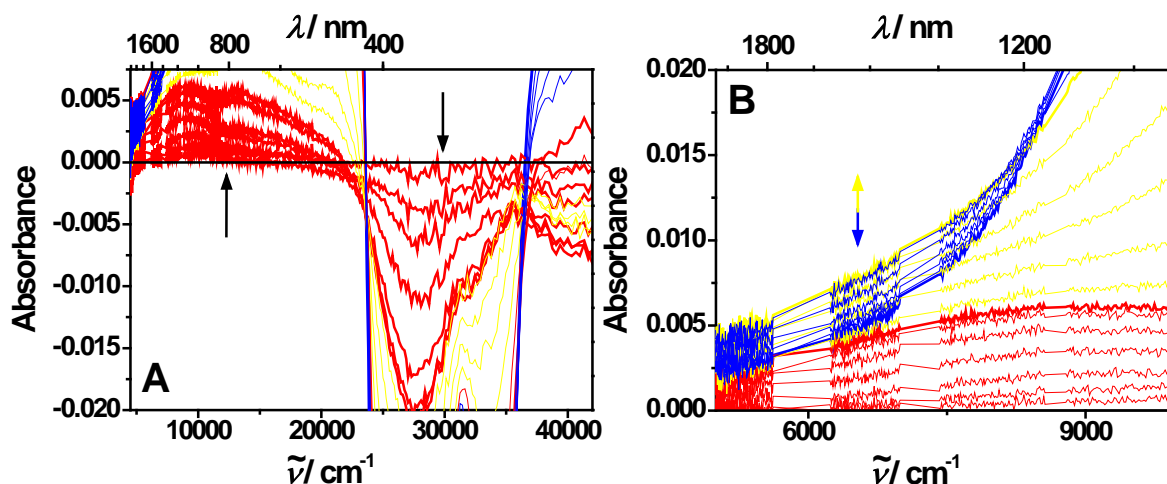


Figure 32. Difference absorption spectra of the SEC measurement of **Au-Tara2**; (A) the first process of the measurement (red), B) NIR-region of the spectra.

2.2.6 Conclusions

In this chapter, we presented the synthesis and the spectroscopic/electrochemical analysis of triarylamine-functionalized gold nanoparticles. We focused on relatively small gold

nanoparticles with an average radius of ca. 1 nm. This avoids strong surface plasmon bands that would otherwise interfere with transitions associated with the chromophore ligands. The triarylamine ligands were attached to the gold core *via* different π -conjugated bridging units that differ in their length and, for comparison, *via* a saturated alkyl chain. A combination of scanning transmission electron microscopy (STEM) measurements and cyclic voltammetry (CV) measurements allowed the determination of the average gold-ligand composition of the gold nanoparticles (AuNP). These data suggest an urchinlike structure with a dense arenethiol packing right at the gold core surface but a much more loose arrangement at the terminal triarylamine moieties.

The absorption and electrochemical properties of the triarylamine ligands attached to the gold core depend on the length and the chemical structure of the bridging unit. For **Au-Tara1S**, strong gold-ligand interactions in the neutral state are visible in the UV/vis spectra as well as interligand interactions in the oxidized state by a splitting of redox potentials and by the observation of an interligand IVCT band.^{49, 50, 79, 202, 203} For **Au-Tara2**, only a very weak IVCT band is visible upon oxidation of the triarylamine ligands. For **Au-Tara3** and **Au-Tara4**, neither gold core-chromophore nor chromophore-chromophore interactions are seen. This is due to the extended length of the π -conjugated bridging unit in **Au-Tara3** and the blocking character of the aliphatic C₅-chain in **Au-Tara4**. Thus, short and π -conjugated character of the bridging unit is essential to facilitate a communication between the gold core and the chromophore and between neighboring chromophores. On the other hand, the fact that there is no interligand interaction present in **Au-Tara3** and **Au-Tara4** leads to an “electron sponge” behavior of these nanoparticles; that is, they can be charged up to an average of 122 positive unit charges in the case of **Au-Tara3** at the same potential, a property that may be used in molecular batteries.²⁰⁵

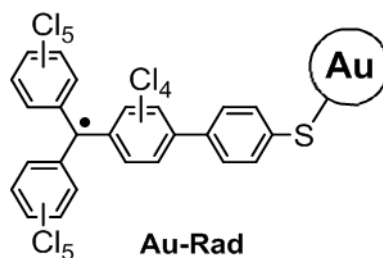
The results presented in this work give a basic insight in the optical and electrochemical properties of triarylaminates, located in the vicinity of a gold nanoparticle. Because the triarylamine nanoparticle system is both redox active and optically excitable, there is considerable potential for using this system in optoelectronic devices.

2.3 Optical and Electrochemical Properties of Perchlorinated Triarylmethyl Radical-Functionalized Gold Nanoparticle Systems

2.3.1 Introduction

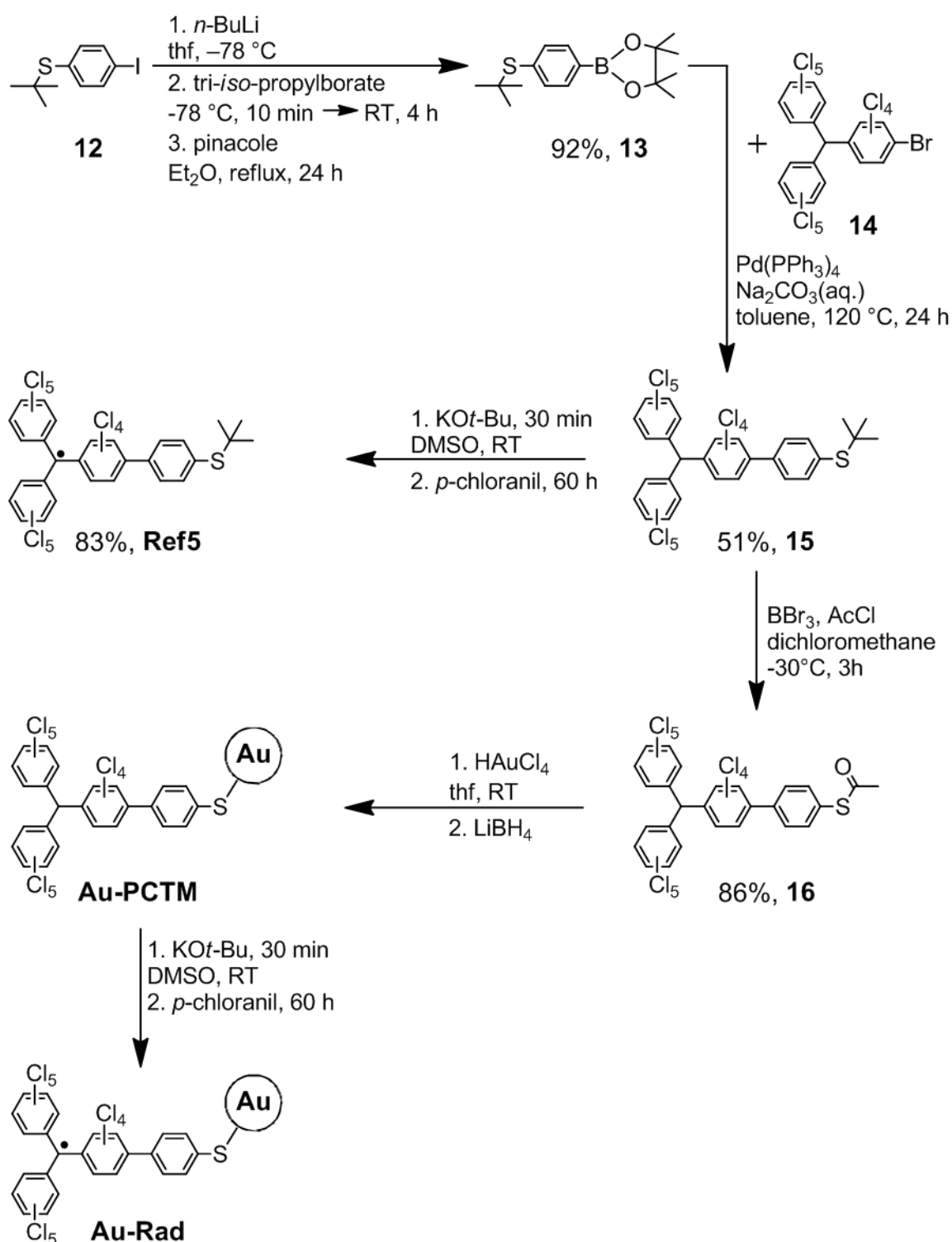
Perchlorinated triarylmethyl (PCTM) compounds are promising molecules in the field of molecular electronic switches and have therefore been studied very intensively in the last two decades.^{162, 166, 178, 206-214} Their suitability for such applications is mainly a result of the chemical and physical properties of the anionic and the neutral species. Both species are chemically stable, due to the electron-withdrawing character of the chlorine substituents and the effective steric shielding of the central carbon by the chlorine atoms in the *ortho* position. Furthermore, the radical species can be electrochemically reduced to the anionic species. Therefore the PCTM-radical was used as an acceptor in donor-bridge-acceptor molecules in order to study the optically induced electron-transfer.^{208, 212} Especially *bis*-PCTM-radical systems and PCTM-radical-triarylamine systems have been investigated.^{162, 166, 178, 209-211} The latter have been demonstrated to be the first neutral organic mixed valence compounds. Another important feature of the PCTM-compounds is that only the radical species exhibits magnetic behavior. The group of Rovira has shown that electroactive PCTMs, self-assembled onto flat gold or SiO₂ surfaces act as molecular switches which are electrochemically switchable between the magnetic on/off states.^{206, 213} These investigations demonstrated the potential of PCTM-compounds for the fabrication of molecular electronic switches.

The object of this work was to generate a soluble nanoswitch. Therefore, a PCTM-radical-functionalized gold nanoparticle (**Au-Rad**) was synthesized and the optical, electrochemical and spectroelectrochemical properties were investigated.



2.3.2 Synthesis

The perchlorinated triarylmethyl radical-functionalized gold particle **Au-Rad** and the reference compound **Ref5** were synthesized starting with compound **12** (Scheme 14). The aryl iodide **12** was transformed into the boron ester **13** in three steps.



Scheme 14. Synthesis of **Ref5** and **Au-Rad**.

Compound **13** was coupled with the perchlorinated triarylmethane derivate **14**¹⁶² via *Suzuki* reaction to yield compound **15** in 51% yield.^{215, 216} The triarylmethane derivative **15** was deprotonated with KO*t*-Bu and then oxidized with *p*-chloranil to the radical **Ref5**.¹⁶⁶ The acetyl protected thiol **16** was synthesized from **15** with BBr₃ and acetyl chloride. Compound **16** was insitu deprotected with LiBH₄ to the thiolate and then added to the auric acid to obtain **Au-PCTM**. Deprotonation of the triarylmethane derivative **Au-PCTM** followed by an oxidation yielded the radical **Au-Rad**.

2.3.3 Analysis

As described above, ¹H-NMR spectroscopy is useful to study the organic layer of gold nanoparticles. The spectrum of the precursor **Au-PCTM** displays broadened signals for the ligands and some aliphatic impurities (Figure 33). Therefore, the sample contains no “free” ligands and a stable organic layer has been formed. Due to the paramagnetic character of the PCTM-radical, the target compound **Au-Rad** could not be characterized by ¹H-NMR spectroscopy.

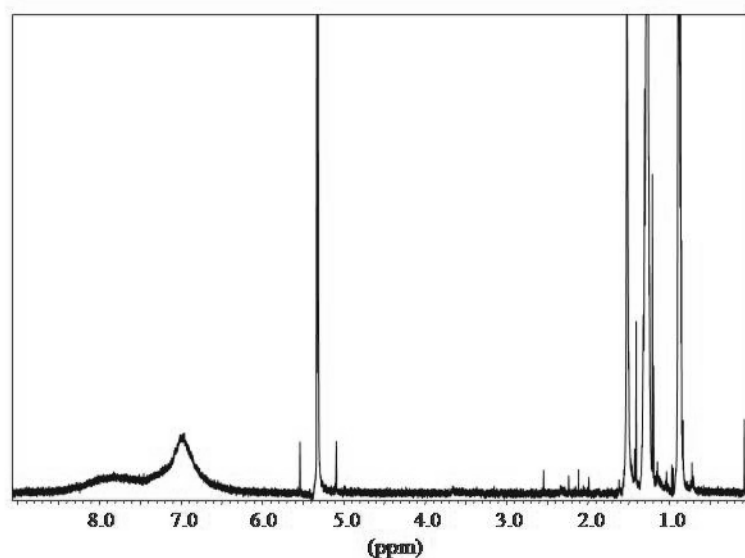


Figure 33. ¹H-NMR spectra of **Au-PCTM** in dichloromethane-d₂.

TEM measurements on a JEOL JEM-2010 at the Fraunhofer-Institut at Würzburg were carried out to determine the particle size. As can be seen from Figure 34 the resolution of the TEM was not high enough to study the particle size accurately. The contrast between the

black balls and the background is very bad, but the particle radius can be estimated to be smaller than 0.5 nm.

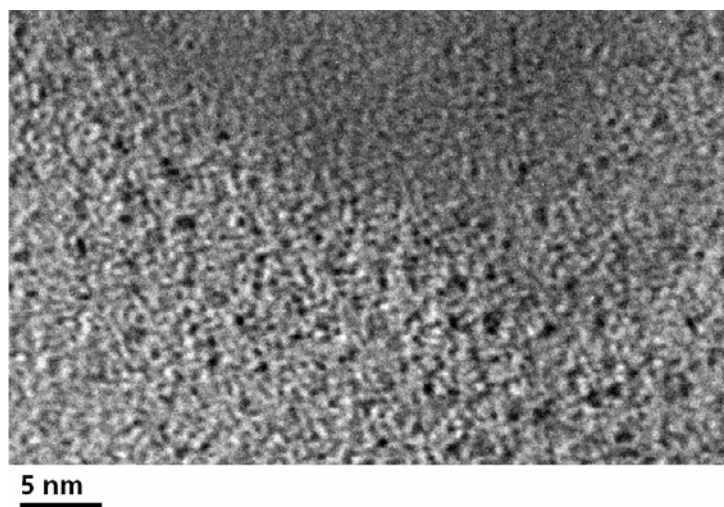


Figure 34. TEM image of Au-PCTM.

2.3.4 Electrochemistry

The redox potentials of the PCTM-radicals **Ref5** and **Au-Rad** were checked by CV (Figure 35). Both compounds show a reversible reduction wave which is at -660 mV for **Au-Rad** and at -650 mV for **Ref5** (Table 8). This wave is associated with a reduction of the PCTM-radical to the anionic derivative.^{162, 166, 217} From the CV it is evident that the radical species of the PCTM-ligand was successfully formed.

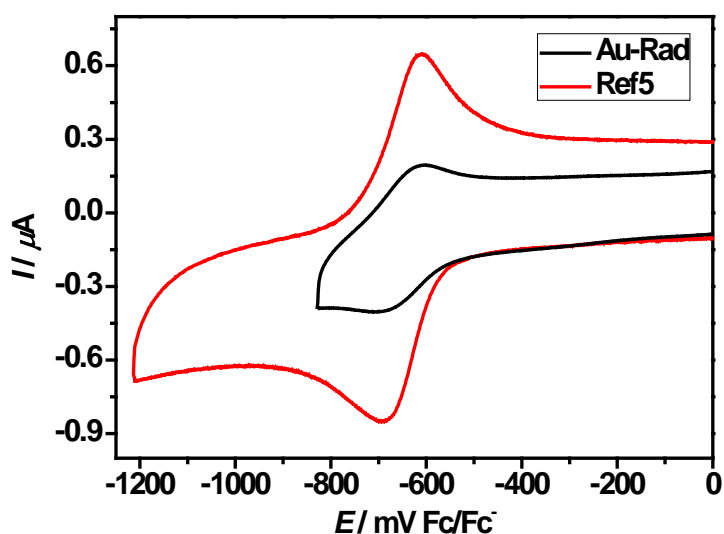


Figure 35. Cyclic voltammograms of **Au-Rad** (solid black line) and **Ref5** (solid red line) in dcm/TBAH (0.3 M) with scan rate of 250 mVs^{-1} at 298 K with a platinum working electrode ($A = 3 \text{ mm}^2$); the voltammograms are referenced against Fc/Fc^+ .

Table 8. Redox Potentials of Au-Rad and Ref5 Determined by CV vs. Ferrocene (Fc/Fc^+) in dcm/0.3 M TBAH Solution with Scan Rate of 250 mVs^{-1} at 298 K with a Platinum Working Electrode ($A = 3 \text{ mm}^2$)

	Redox potential $E_{(\text{red})} / \text{mV}$
Au-Rad	-660 mV
Ref5	-650 mV

The redox potentials of the two PCTM-radicals are very similar. Hence, attaching the PCTM-radical to the gold core does not alter the electrochemical behavior of the radical. The peak separation is about 100 mV for **Au-Rad** and higher than the ideal peak separation for a reversible electrochemical reaction of 59 mV. This broadening could be explained by a weak

interaction between the radical moieties on the gold surface and was already described for self-assembled monolayers of PCTM-radicals on gold.²⁰⁶

2.3.5 UV/vis/NIR Absorption Spectroscopy

The UV/vis spectra of the perchlorinated triarylmethane nanoparticles (**Au-PCTM**, **Au-Rad**) and the corresponding ligands (**15**, **Ref5**) are shown in Figure 36. All PCTM-derivatives have a strong absorption at 43500 cm^{-1} . This band and a very weak absorption band in the section between 32800 cm^{-1} and 35800 cm^{-1} is typical of PCTM-derivatives.²¹³ Only the radicalized compounds show absorption bands around 26000 cm^{-1} , which are characteristic for PCTM-radical compounds.^{166, 212, 213} The radical-band of **Au-Rad** is less intensive than of **Ref5**. This suggests an incomplete radicalization of the PCTM-ligand. In comparison to **Ref5** the radical band of **Au-Rad** is red shifted. This is probably due to interactions between the radical units and the gold core.¹⁸² Interactions between neighboring radicals can be neglected because the density of radicals on the gold surface is very low due to an incomplete radicalization.

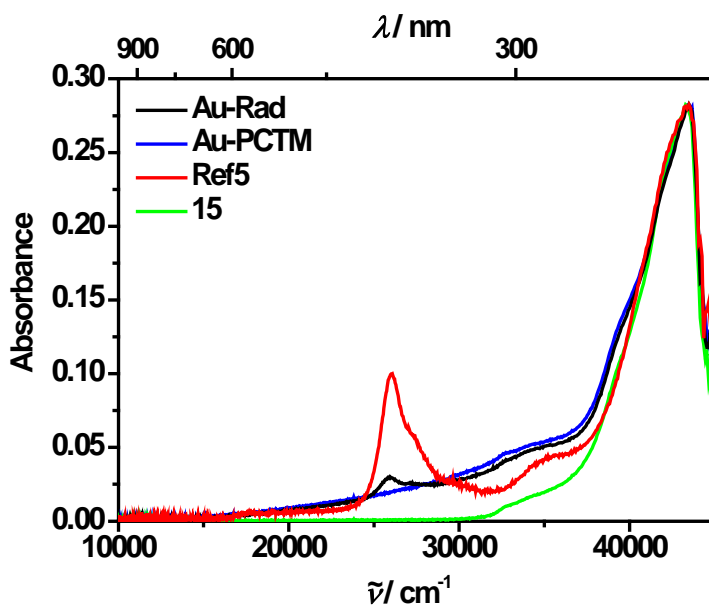


Figure 36. The absorption spectra of **Au-Rad**(black line), **Au-PCTM** (blue line) and the corresponding ligands **Ref5** (red line) and **15** (green line) in dcm.

2.3.6 Spectroelectrochemistry

Spectroelectrochemical measurements were carried out to study intraparticle interactions between neighboring radical and anionic species. Therefore the radical species is successively reduced to the anionic species. The difference spectra of the SEC are displayed in Figure 37.

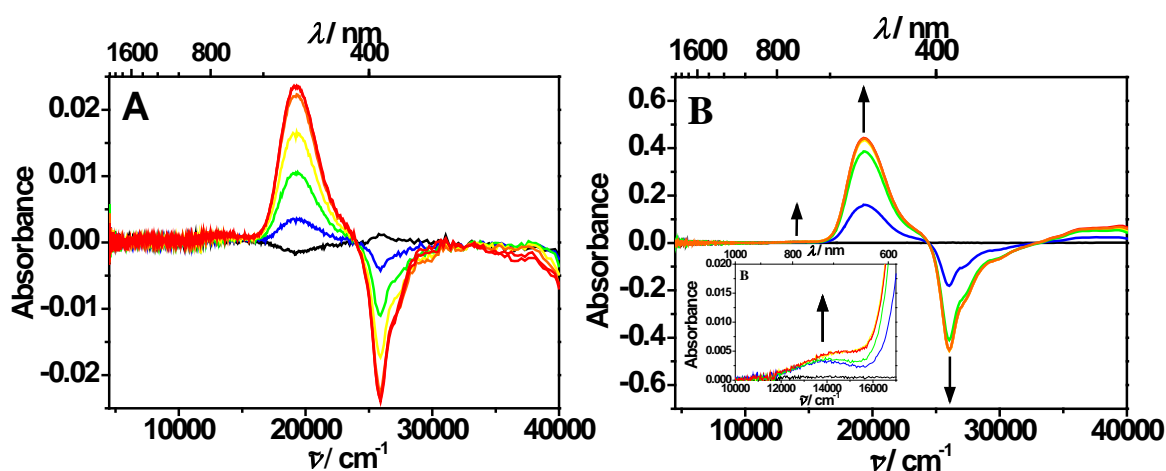


Figure 37. Difference absorption spectra of the SEC measurements with respect to the neutral species: reduction of (A) **Au-Rad** and (B) **Ref5** to the anionic species.

While generating the anionic species, the characteristic radical band loses intensity (negative absorption) and a new band gains intensity. The new absorption bands at 19200 cm^{-1} for **Au-Rad** and at 19300 cm^{-1} for **Ref5** can be assigned to the anionic PCTM-species (Figure 37).^{208, 210, 212, 213} Additionally, a weak band at 14000 cm^{-1} is observed in the spectra of **Ref5** which is caused by an internal electronic transition of the anionic species (Figure 37 B). The reduction process is reversible for both compounds and intervalence charge transfer behavior can not be detected. The interaction between the radical and the anionic species possibly did not occur because of the above-mentioned low density of the radicals on the gold surface.

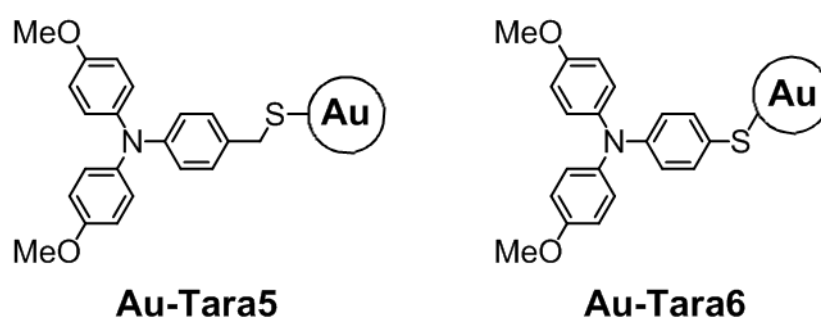
The CV and the SEC experiments revealed that the radical nanoparticle hybrid system behaves like a molecular switch which is electrochemical switchable between the paramagnetic radical and the anionic species. This process is also associated with a change in the optical properties.

2.3.7 Conclusion

Gold nanoparticles functionalized with perchlorinated triarylmethane derivatives were synthesized and the optical and electrochemical properties analyzed. Due to the low resolution of the TEM the radius of the gold core could only be estimated to be smaller than 0.5 nm. The PCTM-ligands of the **Au-PCTM** particle were chemically radicalized to the PCTM-radical. Subsequent electrochemical and UV/vis/NIR absorption measurements were carried out to confirm the presence of the PCTM-radical. The cyclic voltammetry measurements demonstrated that the radical can be reversibly reduced to the anionic species. By comparison with the unbound PCTM-radical **Ref5** one observes that the electrochemical behavior of the radical is marginally perturbed by attaching it to the gold core. The optical investigations have shown that the radicalization of the **Au-PCTM** particle was incomplete and the density of radicals on the gold surface is reduced. That is why only weak interactions between neighboring PCTM-radicals are detected in the electrochemical and optical investigations. The radical and the corresponding anionic species were also detected in the SEC. The CV and the SEC experiments revealed that the **Au-PCTM** particle is electrochemically switchable between two magnetic on/off states. This behavior could be useful in the field of molecular switches as described for self-assembled radical monolayers on Au(111) surfaces.^{206, 207}

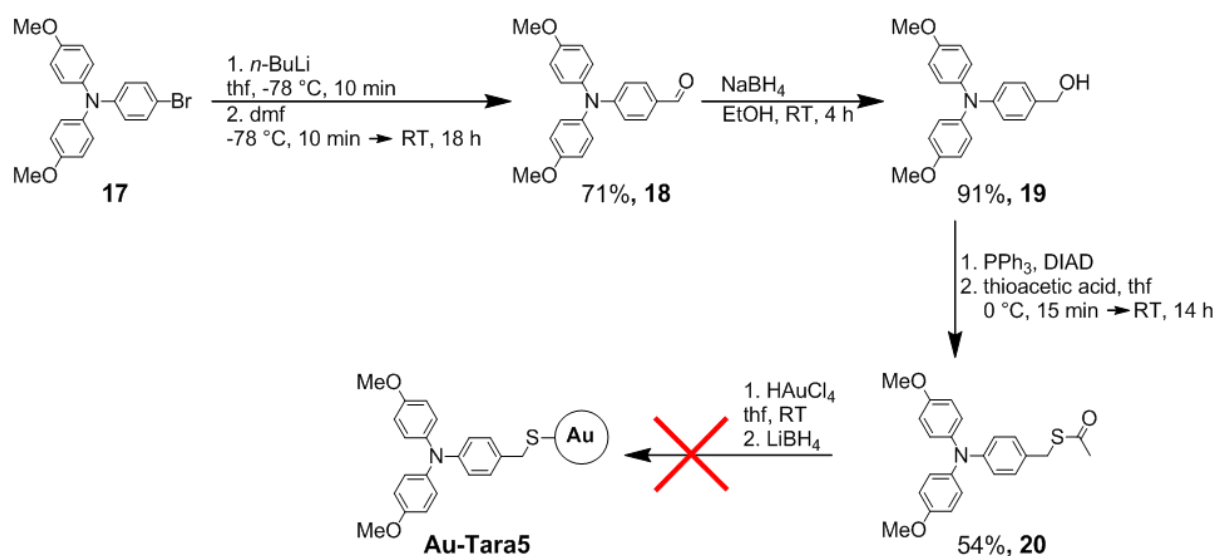
2.4 Synthesis of Au-Tara Systems with Short Bridging Units

Triarylamine-functionalized gold nanoparticles with very short bridging units (**Au-Tara5**, **Au-Tara6**) were thought to exhibit strong interligand and ligand-gold core interactions. The short bridge should facilitate both, a strong intervalence charge transfer behavior between neighboring triarylamines and possibly interfacial charge transfer behavior between the adsorbed triarylamines and the gold core.



2.4.1 Synthesis of Au-Tara5

In order to synthesize the nanoparticle **Au-Tara5** the precursor **20** was generated in three steps (Scheme 15). The triarylamine derivative **17** was treated with *n*-butyllithium and *N,N*-dimethylformamide to give the aldehyde **18** in 71% yield.

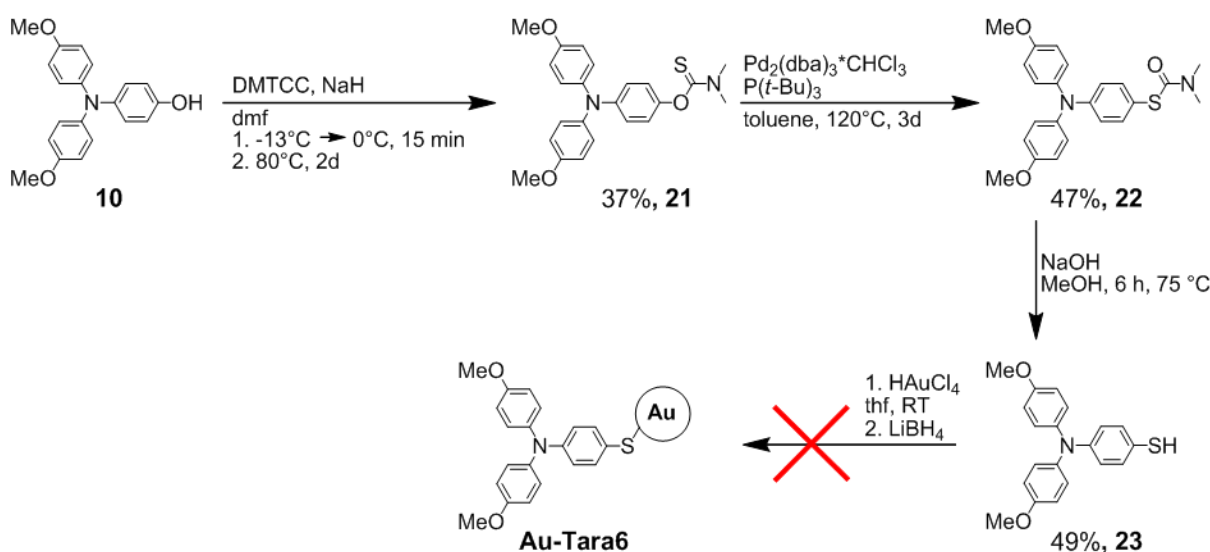


Scheme 15. Synthesis of **20** and attempted synthesis of **Au-Tara5**.

The aldehyde was reduced with sodium borohydride to the alcohol **19**. Compound **19** was converted into the thioester **20** via a Mitsunobu reaction in 54% yield.²¹⁸ Several attempts were made to synthesize the nanoparticle **Au-Tara5** but it was not possible due to agglomeration. When the triarylamine **20** was added to the auric acid the yellowish solution turned deep black. This indicates that the auric acid was reduced by the triarylamine to generate gold nanoparticles. The addition of lithium borohydride yielded agglomerated products. Probably the short C₁-bridging unit leads to a steric hindrance between the bulky triarylamine units. This prevents a homogeneous assembling of the ligands around the gold core to produce stable nano particles.

2.4.2 Synthesis of Au-Tara6

The synthetic path to the thiol **23** is outlined in Scheme 16. Compound **10** was converted into the triarylamine **21** with dimethylthiocarbamoyl chloride (DMTCC) and sodium hydride in 37% yield.^{219, 220} A palladium catalyzed Newman-Kwart rearrangement was used to transform the *O*-thiocarbamide **21** into the *S*-thiocarbamide **22** in 47% yield.²²¹ The reaction of **22** with sodium hydroxide yielded 49% of **23**. The synthesis of **Au-Tara6** also failed. Exactly the same observations were made as described for **Au-Tara5** and the same reasons can be assumed.



Scheme 16. Synthesis of **23** and attempted synthesis of **Au-Tara6**.

2.4.3 Concluding Remarks

The synthesis of the **Au-Tara** systems with short bridging units was not successful. Despite this fact an important conclusion can be drawn: the bridging unit seems to be short enough to facilitate a strong triarylamine gold interaction. Normally, the addition of a thiol derivative to auric acid results in the formation of a colorless gold(I)-thiolate complex as observed for the synthesis of **Au-Tara4**. Instead, in case of **20** and **23** the yellowish solution turned deep black. This indicates that the auric acid is immediately reduced to gold(0) after the formation of the gold(I)-triarylamine thiolate complex, resulting in the generation of small nanoparticles. This redox reaction can probably be assumed to result from an electron transfer from the triarylamine to the gold(I) species resulting in the formation of unstable gold nanoparticles.

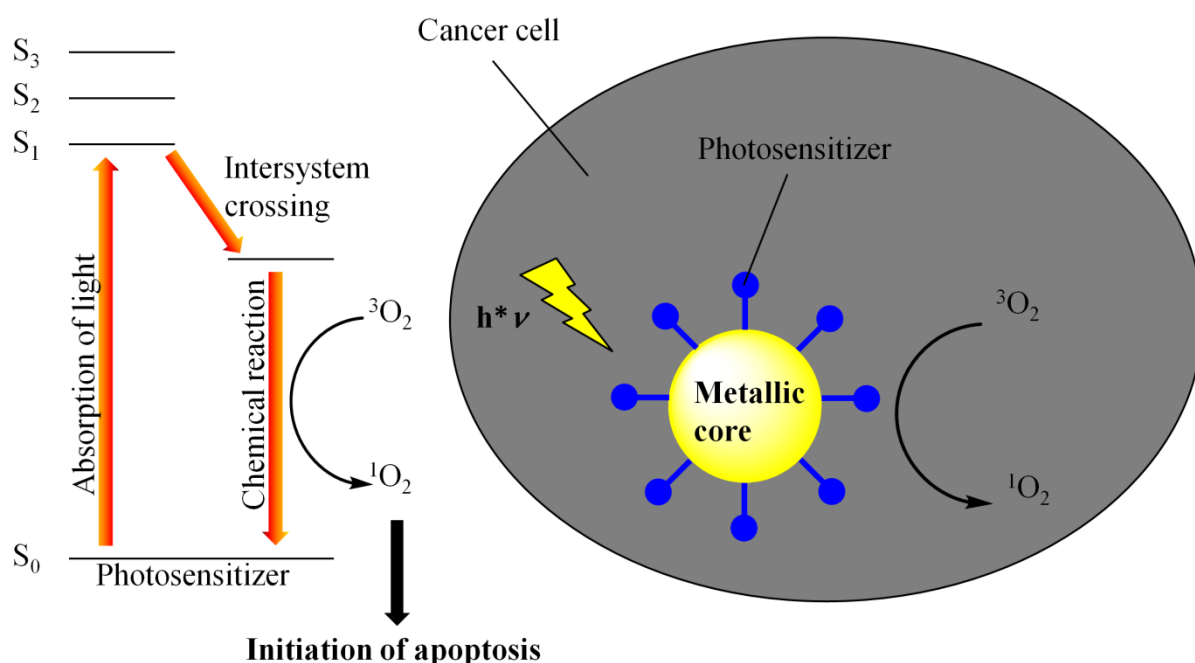
3 Raman-Reporter Molecules for SERS Application

3.1 Introduction

An impressive application of nanoparticle systems is their use in the field of nanobiotechnology. Nanoparticles are attractive candidates for biodiagnostic assays and drug delivery systems because of their structural robustness, small size and correspondingly large surface-to-volume ratio as well as their size-related physical properties.

3.1.1 Drug Delivery Systems

In the biomedical research area, nanoparticle systems can be used as drug delivery systems for photodynamic therapies (PDT).^{138, 140, 222} In these therapeutic methods the particles are functionalized with photosensitizers and transferred into cancer cells. When such photosensitizers are irradiated with an appropriate wavelength of light, the excited molecule can transfer the energy to molecular oxygen to form singlet oxygen ($^1\text{O}_2$) (Scheme 17). The reactive oxygen species is cytotoxic and is able to destroy cancerous tissue.²²³



Scheme 17. Photodynamic process involved in photodynamic therapy.

The photosensitizing agents should absorb light in the far-red region of the electromagnetic spectrum, because these wavelengths exhibit a greater penetration depth into human tissue.^{137, 223} Phthalocyanines are a class of compounds that fulfill this need. In order to infiltrate the sensitizer into the cancer cells a drug delivery system is required. For this reason phthalocyanine-functionalized gold nanoparticles have been developed^{137, 140, 223} because the gold core is chemically inert and has a minimum toxicity.¹⁴⁰

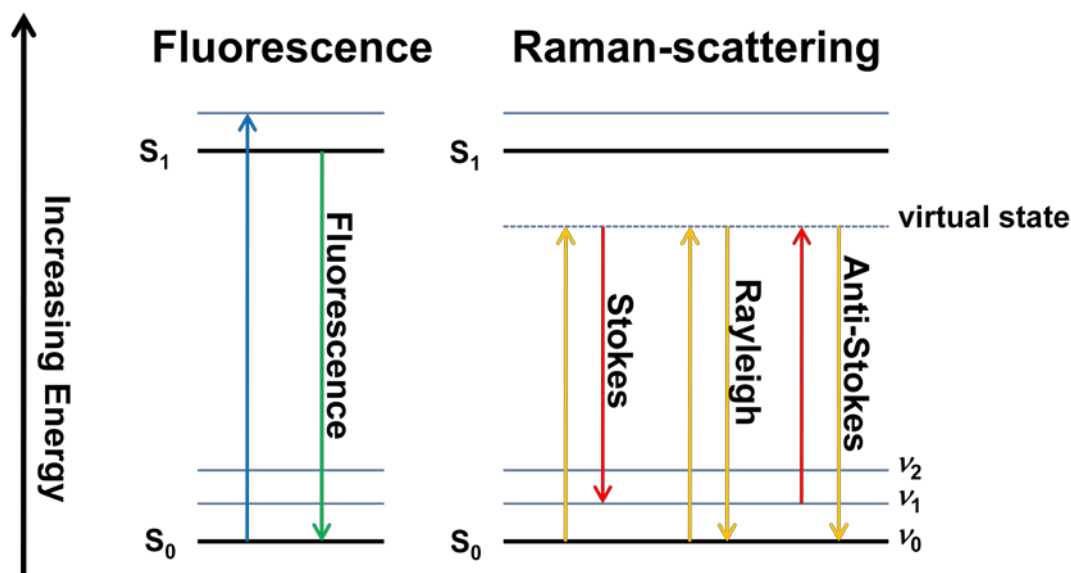
3.1.2 Tuning the Absorption Properties

The absorption properties of nanoparticles can be influenced by the physical properties of the surrounding medium. Especially the surface plasmon absorption band is very sensitive to changes of the index of refraction.²²⁴ This effect was examined intensively for dye-nanoparticle structures^{26, 27, 225, 226} and was used for sensing applications.^{227, 228} For example, Frederix *et al.* have developed a method for the detection of human serum albumin (HSA). Therefore, the attachment of the complementary anti-HSA antibody to a HAS-functionalized nanoparticle results in a shift and an increase of the SPB and inter band transitions.²²⁹ Furthermore, several groups have shown that also aggregation effects of nanoparticle structures can be used to detect biomolecules.²³⁰⁻²³² The aggregation can be induced by anionic molecules (Concanavalin A)²³¹ or by linking molecules (DNA strains).²³² The decrease of the SPB intensity signals the recognition of the biomolecule. Another approach was to initiate aggregation by dipole-dipole interactions.²³³ For this strategy, nanoparticles were functionalized with azobenzene to take advantage of the light-induced switch in between the trans and cis state.²³⁴ The isomerisation gives rise to a significant increase of the dipole moment and consequently the particles aggregate. This concept was used by Grzybowski *et al.* to develop a self-erasable “ink”.²³⁵

3.1.3 Light Emitting and Scattering Probes

Nanoparticle systems have also been developed for the detection, labeling and sensing of biomolecules with fluorescence and Raman spectroscopy. The energy level diagram of the fluorescence and the Raman scattering are illustrated in Scheme 18. Concerning the

fluorescence, the absorption of a photon results in an excitation of the molecule into a higher electronic and vibrational state S_1 . After molecular vibrational relaxations a photon is emitted and the molecule returns to the ground state. The emitted light is shifted to lower energy due to the vibrational relaxation (e.g. $\nu_1 \rightarrow \nu_0$) in the excited electronic state. Generally, the fluorescence signal is related to the electronic structure of the molecule.



Scheme 18. Energy level diagrams for fluorescence and Raman scattering; S are electronic and ν are vibrational states of the molecule; arrow-up represents the incident exciting light whereas arrow-down represents the emitted or scattered light.

In contrast, Raman spectroscopy is directly associated with the structure of the molecule because vibrational and rotational states of the molecule are detected. Again a photon is absorbed but the energy of the photon is related to the gap between the ground (S_0) and a virtual state. Instantaneously a photon is emitted.¹⁴¹ The emitted wavelength predominately corresponds to a relaxation of the virtual state into the electronic and vibrational ground state ($S_0-\nu_0$), called Rayleigh scattering. Additionally a weak emission to lower energy is detected and corresponds to a relaxation into the $S_0-\nu_1$ state, called Stokes scattering. Also anti-Stokes scattering can be seen which is related to an excitation from higher vibrational states into the virtual state. The emitted photon is shifted to higher energy but the intensity is very low due to the small population of the higher vibrational states. Because both the Stokes and anti-Stokes scattering is very weak compared to most fluorescence events a signal enhancement must be used to increase the sensitivity.

The crucial impetus for the research in this field was given by the exploration of surface enhanced effects on metal surfaces, for example surface-enhanced Raman scattering (SERS) effect^{6, 30} and the surface enhanced fluorescence effect.³¹⁻³³

3.1.4 Fluorescent Probes

The assembling of dyes onto a metal nanoparticle can enhance the emission by a factor of 10 up to a few hundred.³³ This effect is caused by dipole-dipole coupling of the excited fluorophore to metal plasmons.³² The surface enhanced fluorescence effect was used to develop metal-enhanced fluorescent probes^{32, 143, 145, 146} which can be applied in a biological detection assay.^{33, 152} Mostly dyes, e.g. rhodamine or indocyanine green, attached to silver nanoparticles or silver island films are used in this field of research.

On the other hand, gold nanoparticles are also excellent quenchers of fluorescence. This quenching is due to nanosurface energy transfer (NSET)^{148, 236} and the quenching effect can be reduced by distancing the fluorophores from the gold core. The distance dependence of surface energy transfer behavior over distances more than 100 Å, i.e. quenching efficiency, is proportional to $1/d^4$ whereas the Förster resonance energy transfer (distance < 100 Å) is proportional to $1/d^6$.²³⁶⁻²³⁸ Nie and co-workers used this quenching effect to detect specific DNA strains. A gold core was attached with oligonucleotide molecules labeled with a thiol group at one end and a fluorophore at the other. The oligonucleotide chemisorbs onto the gold core via the thiol. Additionally the fluorophore binds nonspecifically to the gold surface. In this loop structure the gold core quenches the emission of the fluorophore. Binding a target molecule to the oligonucleotide breaks the loop structure, resulting in a measurable fluorescence.²³⁹

Furthermore, Rotello and Bunz have investigated indicator displacement assays (IDAs). These assays consist of a gold core coated with a positively charged oligo(ethylene glycol) side chain and a negatively charged dye. In this “supramolecular” arrangement, the fluorescence of the dye is quenched by the gold core. A negatively charged analyte can displace the dye, resulting in a fluorescence signal of the free dye.²⁴⁰ The signal intensity depends on the level of displacement determined by the relative nanoparticle-dye binding strength and the analyte-nanoparticle interaction. The authors have shown that the IDA system is able to identify bacteria and to detect different proteins.^{147, 148, 241, 242}

3.1.5 Surface Enhanced Raman Spectroscopy (SERS) Probes

Even though fluorescent probes have shown their potential in applications for biological detection assays, these probes are not suited for multiplexed detection of target molecules (multiplexing). This is due to the line width of the fluorescence signal. In contrast, SERS signals possess a small line width of vibrational Raman bands (Figure 38). This is a very important benefit for applications in multiplexing experiments.

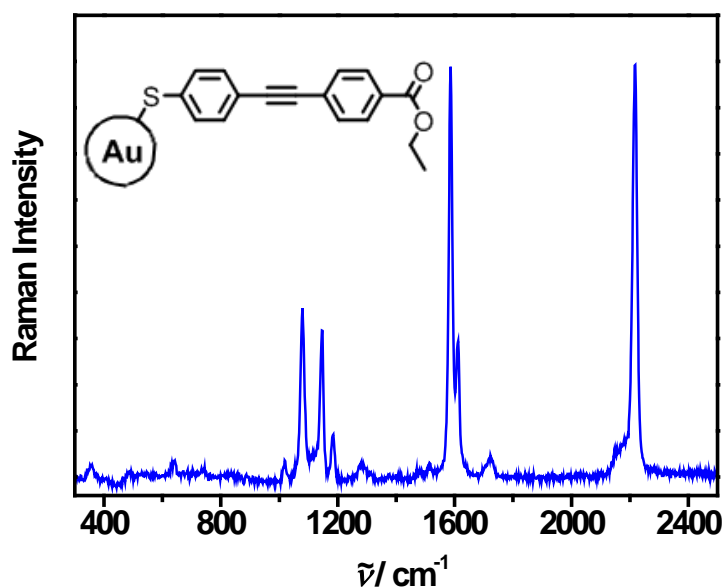


Figure 38. The SERS spectrum of an alkyne derivative, adsorbed as a self-assembled monolayer on the surface of Au nanospheres in ethanol.

As mentioned above Stokes-Raman bands are normally very weak. However the intensity of these bands increases if the Raman-active molecule is in very close proximity to specific metal surfaces (Figure 38). Under these conditions enhancement of the Raman signal by factor 10^6 can be served.¹⁴¹ The enhancement is due to the increased size of the electromagnetic field at the metal surface (see Scheme 3). When the conduction electrons are excited by an incident photon, the particle acts as an antenna which amplifies the scattered light. The enhancement efficiency thereby decreases with the distance between the Raman-active molecule and the metal surface, for example, a metal nanoparticle. Furthermore, only vibrations with a molecular polarizability tensor oriented parallel to the surface normally experience the largest enhancement.²⁴³

Due to the tunable surface plasmon absorption bands (SPB) of metal nanospheres and nanoshells, these structures are most often used as SERS probes. Kneipp et al. demonstrated that SERS approaches may be used for the characterization of changing cellular environments and are useful for intracellular applications.²⁴⁴ In this study, unfunctionalized gold nanoparticles were injected into rat and mouse cells and SERS spectra were recorded. Adenosine phosphate was thereby detected on the basis of the characteristic SERS spectra. The disadvantage of this label-free method is that all molecules close to the gold surface are detected. In order to detect and label specific biomolecules, nanoparticles were functionalized with both a Raman-reporter molecule and a specific recognition molecule for biomolecules (antibody). This approach was used by Hu et al.²⁴⁵ to mark HeLa cells (cervical cancer cells). In this work, nanoparticles were labeled with a benzonitrile derivative and a terminal hydrazine unit. The intense $C\equiv N$ Raman vibration was used to detect the SERS probe and to show that the hydrazine unit binds selectively to ketone-functionalized cell proteins.

A similar approach was reported by Jehn et al. who attached a SERS-marker to a gold/silver nanoshell. The shell was then functionalized with prostate specific antigen (PSA) (Scheme 19). The authors demonstrated selective imaging of PSA in prostate biopsies by Raman microscopy.³⁹



Scheme 19. Model of a biofunctionalized SERS-label. Left: Gold/Silver nanoshell. Middle: SERS-marker. Right: monoclonal antibody for antigen recognition (e.g. PSA).

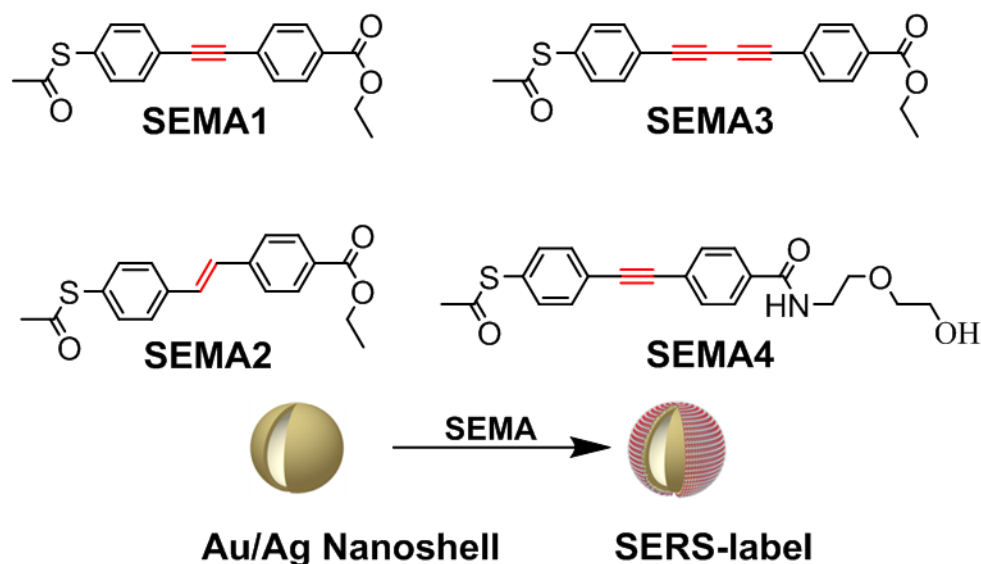
A disadvantage of SAM-only protected nanoparticles is that other molecules of the solution can penetrate into the organic shell and replace the SERS-marker or the antibody. Encapsulation of the SERS-label can completely eliminate this issue by avoiding the adsorption and desorption of molecules attached to the surface. Several groups have developed methods to protect the organic layer via a protective shell. Organic polymers or silica can be used for this purpose.¹⁴¹ Silica-encapsulated Raman-labeled nanoparticles have

many useful features, for example physical robustness, optical robustness and an excellent surface for biomolecule attachment.¹⁴¹ An encapsulation can be achieved by the deposition of SiO₂ precursors on the organic layer via the Stöber method.²⁴⁶⁻²⁵¹ Hence, the organic layer has to be functionalized with a coupling agent (alkoxy silane functionalized ligand) or prepared with a polyelectrolyte layer.^{6, 247-253}

Küstner et al. have used this concept to build up silica-encapsulated SAMs on tunable gold/silver nanoshells.⁶ The SERS spectrum of the samples revealed very intensive Raman bands corresponding to the encapsulated Raman-reporters. Afterwards the silica shell was functionalized with prostate specific antigen (PSA) and SERS microscopic experiments demonstrated the specific binding of the samples in the epithelium of prostate.

The high-sensitivity and high-selectivity of SERS probes combined with the small line width of the enhanced Raman bands can be used for multiplexing experiments. Due to the broad emission band of fluorescent probes, the multiplexing capacity of these probes is limited to approximately 1-3. In contrast, the SERS technique can detect 10-30 analytes simultaneously. Mirkin¹⁴⁴ and Graham²⁵⁴ demonstrated the use of SERS probes to detect DNA strains in a multiplexing approach. Mirkin and co-workers functionalized gold particles with Raman dye-labeled oligonucleotides to monitor the presence of specific target DNA strands.¹⁴⁴ These experiments have shown the potential of SERS-labels as the next-generation labeling technology for biodiagnostic research.

This chapter deals with the synthesis and characterization of new Raman-reporter molecules, denoted as SERS-marker (**SEMA1-4**). In cooperation with the group of Schlücker (University of Osnabrück) the Raman-active molecules are adsorbed onto Ag/Au nanoshells to generate SERS-labels (Scheme 20) which are characterized by SERS. The use of the Ag/Au nanoshells was important, because the surface plasmon band (SPB) of these nanoshells can be adjusted to the far-red region of the electromagnetic spectrum.^{6, 40, 255} In this region the absorbance of tissue is minimized and the SERS-label can be employed for immune-SERS experiments.^{137, 223}

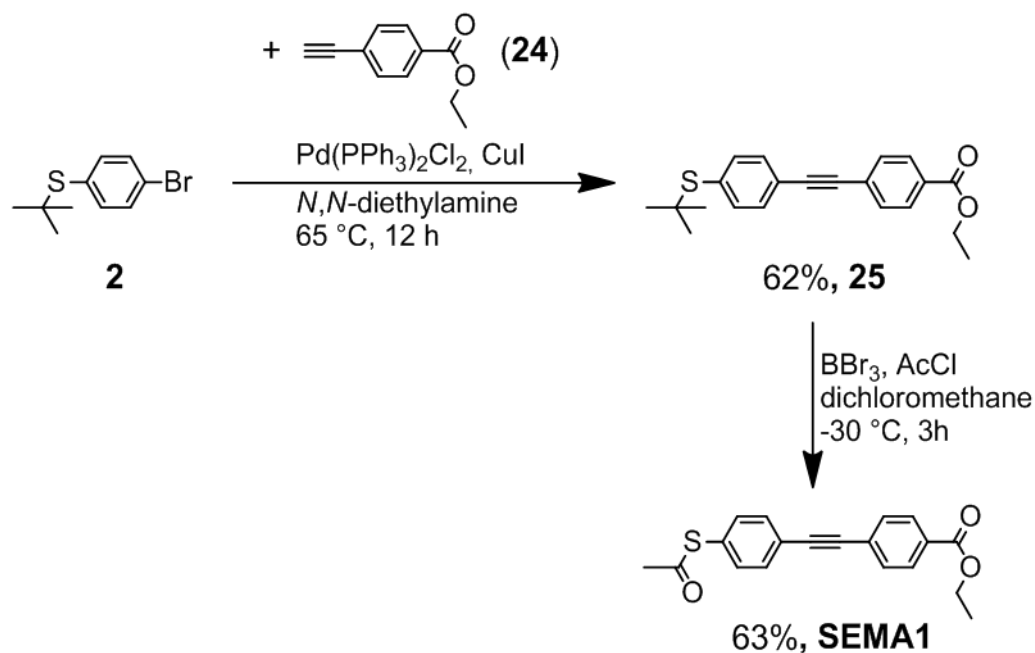


Scheme 20. SERS-markers **SEMA1-4** and a SERS-label.

In order to detect intense SERS signals the SERS-markers are designed to have Raman-active vibrational bands oriented along the molecular axis. Additionally the SERS markers possess a hydrophilic group to make the marker soluble in polar solvents and a thiol group for attachment onto the surface of the Ag/Au nanoshell. A high coverage of the SERS-marker onto the surface should thereby ensure that all markers are uniformly oriented to the surface. Furthermore, the application of these hybrid structures for tissue imaging in prostate biopsies is demonstrated.

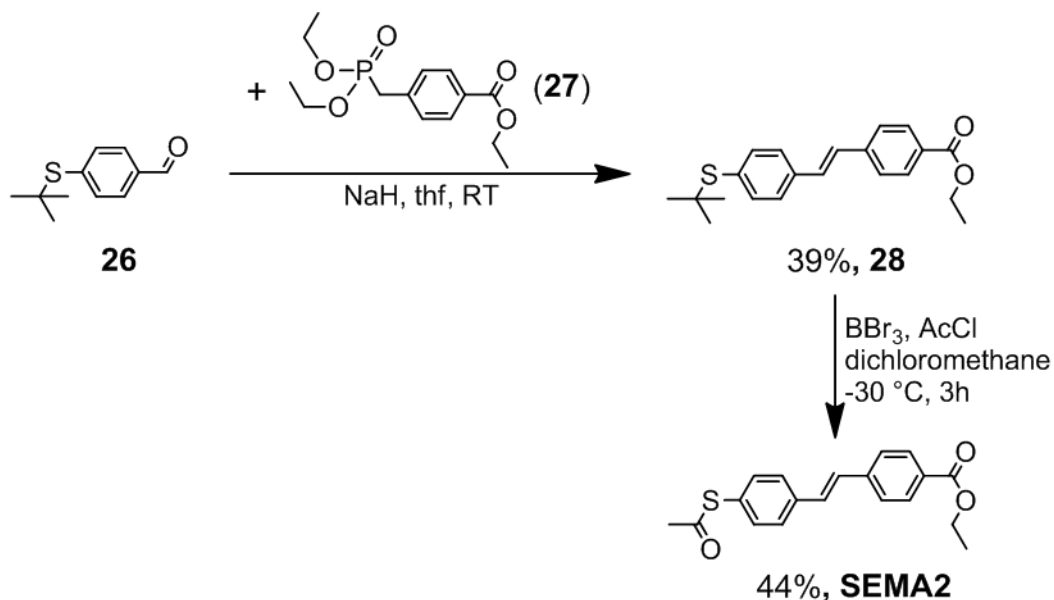
3.2 Synthesis

The synthesis of the SERS-marker **SEMA1** is outlined in Scheme 21. The alkyne **25** is accessible by a palladium catalyzed *Hagihara-Sonogashira* coupling of the aryl bromide **2** with the terminal alkyne **24**. The *t*-butyl protected thiol **25** was converted into the acetyl protected thiol **SEMA1** with boron tribromide and acetyl chloride in 63% yield.^{256, 257}



Scheme 21. Synthesis of SEMA1.

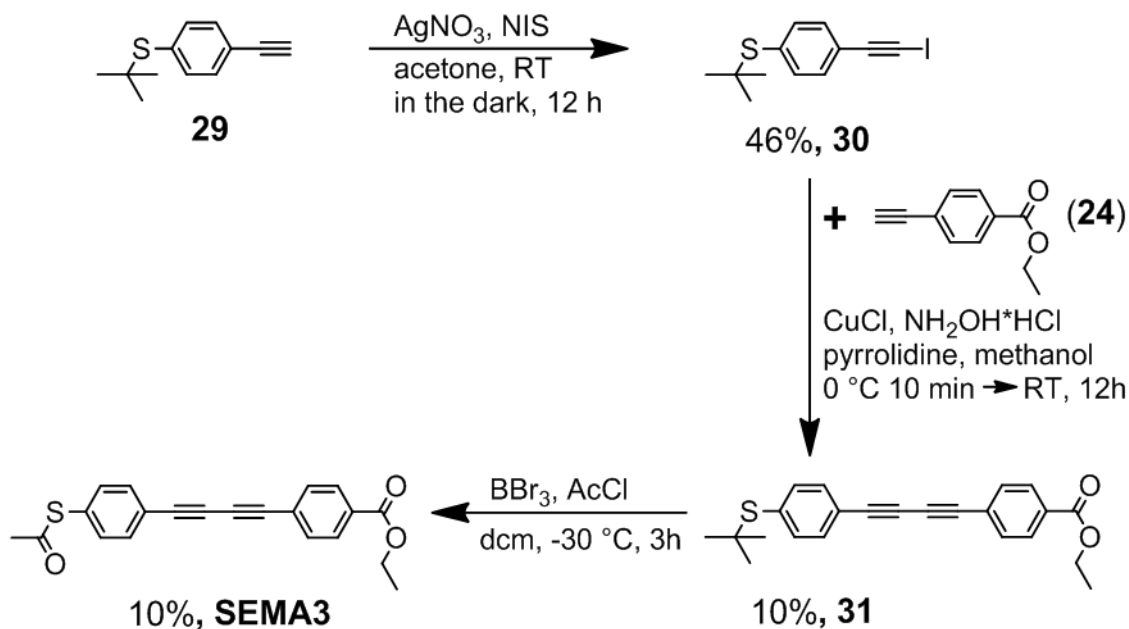
The stilbene **28** was synthesized via a *Wittig-Horner* reaction of the aldehyde **26**²⁵⁶ with the phosphonate **27**²⁵⁸ and yielded 39% of the *trans* isomer (Scheme 22).^{259, 260} Compound SEMA2 was obtained by the reaction of **28** with boron tribromide and acetyl chloride.



Scheme 22. Synthesis of SEMA2.

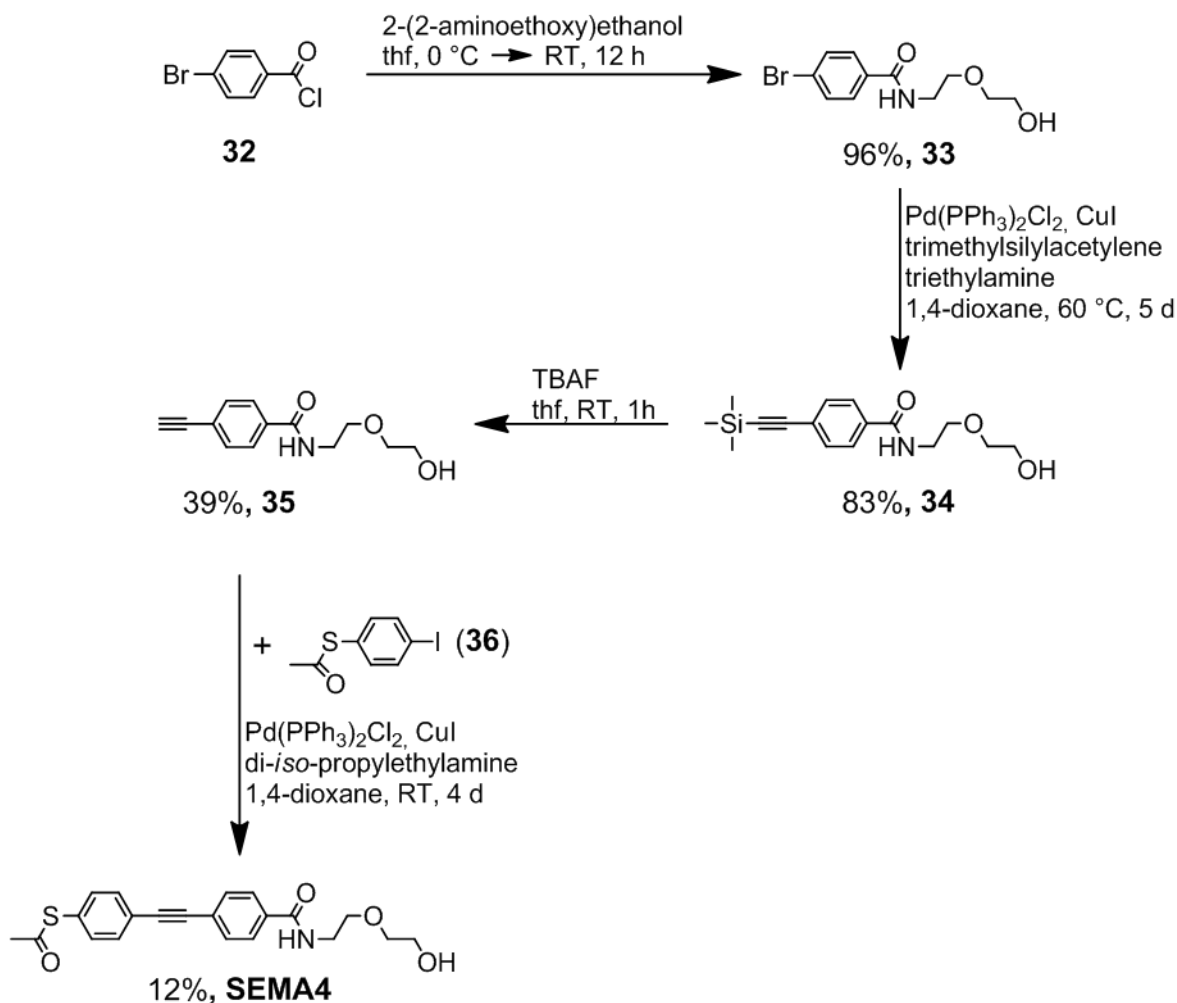
SEMA3 was synthesized in three steps (Scheme 23). Compound **30** was generated from the terminal alkyne **29** with silver nitrate and *N*-iodosuccinimide in 46% yield.²⁶¹ A copper

catalyzed *Codiot-Chodkiewicz* reaction was used to obtain the diacetylene **31** by reaction of iodoacetylene **30** with the terminal alkyne **24**.²⁶¹ Reaction of **31** with boron tribromide and acetyl chloride yielded the thioester **SEMA3**.



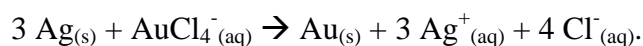
Scheme 23. Synthesis of **SEMA3**.

The synthesis of the SERS-marker **SEMA4** is outlined in Scheme 24. The acyl chloride **32** was transformed into the acyl amide **33** by a reaction with 2-(2-aminoethoxy)ethanol. Compound **34** was synthesized by a palladium catalyzed *Hagihara-Sonogashira* reaction of **33** and trimethylsilylacetylene. The protecting trimethylsilyl group was removed with TBAF to obtain compound **35**.¹⁶⁴ A *Hagihara-Sonogashira* reaction of **35** with **36** yielded **SEMA4** in 12% yield.



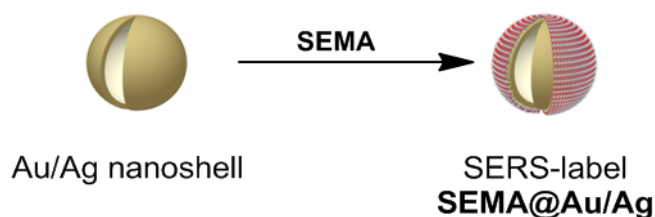
Scheme 24. Synthesis of **SEMA4**.

The adsorption of the SERS-marker onto the surface of Au/Ag nanoshells and the subsequent silica encapsulation were carried out by the group of Schlücker (University of Osnabrück). The Au/Ag nanoshells were synthesized following a method published by Xia and coworkers.⁴⁰ A spherical silver nanoparticle is thereby used as a template to fabricate a gold nanoshell. Silver particles were prepared by the reduction of silver nitrate in ethylene glycol, used as solvent and as reducing agent, and polyvinylpyrrolidone, used as protecting agent.^{262, 263} Due to the difference of the standard potential ($AuCl_4^- / Au > Ag^+ / Ag$) the silver core can be oxidized by $HAuCl_4$ according to the following redox reaction:



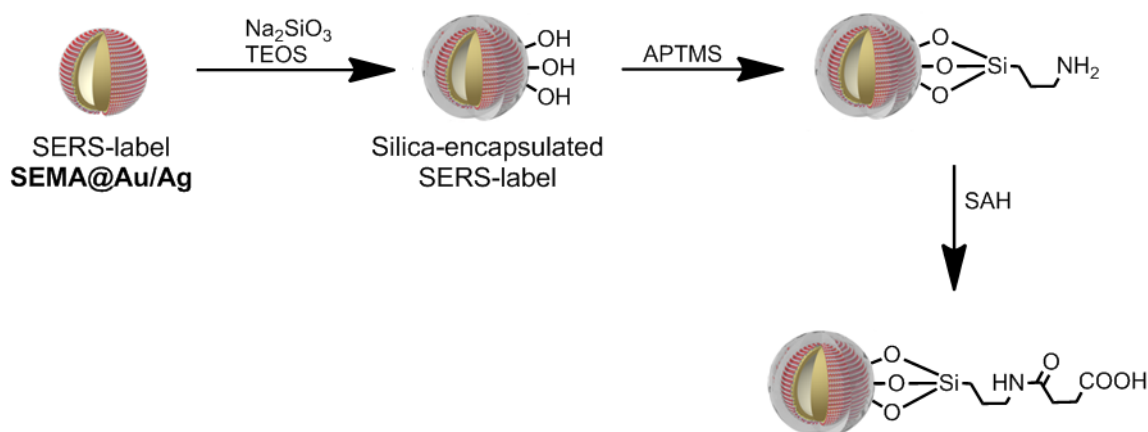
The elemental gold atoms produced in this redox reaction merge to very small nanoparticles, resulting in the growth of a gold shell around the silver particle. The morphology of the shell is very similar to that of the silver template. Afterwards a self-assembled monolayer of the

SERS-marker is adsorbed onto the nanoshells via the thiol unit to generate a **SERS-label** (Scheme 25).



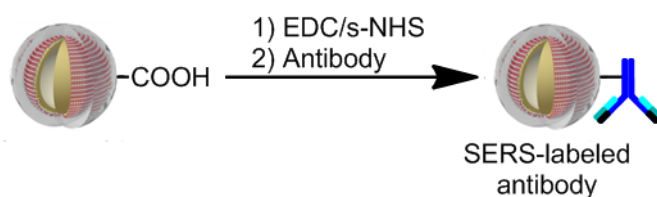
Scheme 25. Synthesis of **SERS-labels**.

The hydrophilic ethylene glycol unit of **SEMA4** was used to fabricate a silica-encapsulated SERS-label. The encapsulation was achieved in two steps. First, the SAM was coated with an ultrathin silica shell by adding sodium silicate (Na_2SiO_3).²⁵⁰ In a second step, the silica shell was enlarged by the hydrolysis and condensation of tetraethoxyorthosilicate (TEOS).^{6, 246} Then, the silica-encapsulated nanoshell was treated with 3-amino-*n*-propyltrimethoxysilane (APTMS) and succinic anhydride (SAH) in order to activate the silica surface for chemical reactions (Scheme 26).²⁶⁴



Scheme 26. Synthesis of the silica-encapsulated SERS label and the activation of the silica surface with APTMS and SAH.

Finally EDC/s-NHS (ethyl dimethyl-aminopropyl carbodiimide / N-hydroxysulfosuccinimide sodium salt) chemistry was used to conjugate an anti-p63 antibody to the activated carboxy surface (Scheme 27).²⁶⁵ The SERS-labeled antibody was used for imaging experiments of the tumor suppressor p63.



Scheme 27. Synthesis of a SERS-labeled antibody.

3.3 SERS-Measurements

The synthesized SERS-labels consist of a Au/Ag nanoshell with a diameter of ~ 70 nm and a self-assembled monolayer of one of the SERS-marker **SEMA1-4**. The nanoshell possesses an intense surface plasmon band at $\lambda_{\max} \sim 620$ nm which was employed for excitation with the 632.8 nm-line from a HeNe laser. The SERS-spectra of the SERS-labels were recorded and are shown in Figure 39. In all spectra an intense Raman band around 1580 cm^{-1} is seen which can be assigned to a phenyl ring bending vibration.

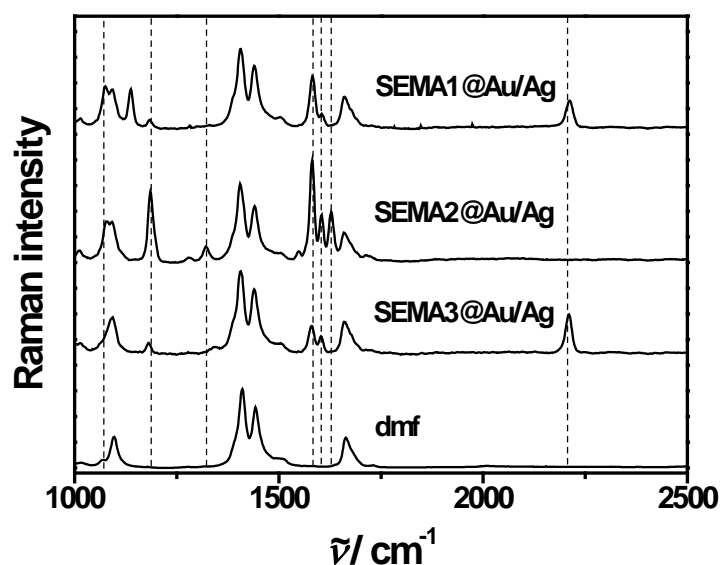


Figure 39. The SERS spectra of the SERS-labels **SEMA1@Au/Ag**, **SEMA2@Au/Ag** and **SEMA3@Au/Ag** in dmf are displayed. For comparison the Raman spectrum of dmf is also shown.

The spectra also reflect the structural difference of the SERS-marker. For example, the C=C stretching vibration at 1628 cm^{-1} is only seen in the spectra of **SEMA2@Ag/Au**. In contrast, the C≡C stretching vibration at 2213 cm^{-1} and 2210 cm^{-1} is only detected in the spectra of **SEMA1@Ag/Au** and **SEMA3@Ag/Au**. The slight band shift of the C≡C stretching vibrations in **SEMA3@Ag/A** is due to the dialkyne structure. The analysis revealed two important aspects. First, the detection of the characteristic stretching vibrations demonstrates that the SERS-markers are uniformly oriented parallel to the surface normal. Second, the discrimination between the alkene- and alkyne-functionalized marker is sufficient for multiplexing experiments whereas the shift of C≡C stretching vibrations is too small for such applications.

3.4 Immuno-SERS Microscopy

The combination of SERS-labeled antibodies and their localization by Raman microscopy in cellular and tissue specimens is termed immuno-SERS microscopy.^{151, 243} In this study, p63 was chosen as a target protein for diagnostic imaging studies. p63 is a tumor suppressor and abundant in benign prostate.²⁶⁶ The SERS-labeled antibody consists of a Au/Ag nanoshell with a diameter of $\sim 70\text{ nm}$ which was functionalized with **SEMA4** and encapsulated with silica. In Figure 40 the TEM images of the encapsulated metal nanoshells exhibit dark central spots (metal shell) which are surrounded by a brighter shell (silica shell). Anti-p63 antibody was bound to the silica surface to generate the SERS-labeled antibody.

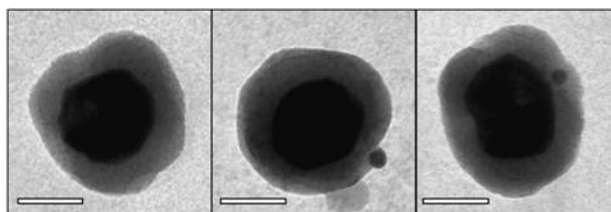


Figure 40. TEM images of silica-encapsulated Au/Ag nanoshells with a self-assembled monolayer of **SEMA4**. Scale bar 50 nm.

For immuno-SERS microscopy applications the SERS-labeled antibodies were incubated in a $5\ \mu\text{m}$ tissue section from prostate biopsies. The intense phenyl ring bending vibration at

1582 cm^{-1} of **SEMA4** Raman-marker was chosen for the detection of the SERS-labeled antibody in a mapping experiment with a confocal Raman microscope (WITec, Alpha300R). Figure 41 A displays the white light image of the incubated prostate tissue together with a superimposed false color SERS image based on the integrated Raman intensity of the marker band. High intensities in the SERS false color image correspond to high concentration of the SERS-labeled antibody and consequently to high expression levels of the tumor suppressor p63. Additionally five representative SERS spectra from different regions in the tissue, marked with white crosses in Figure 41 B are shown. This analysis illustrates that the tumor depressor p63 is only abundant in the basal epithelium (Figure 41 A, crosses 1-3) but not in the secretory epithelium or stroma.

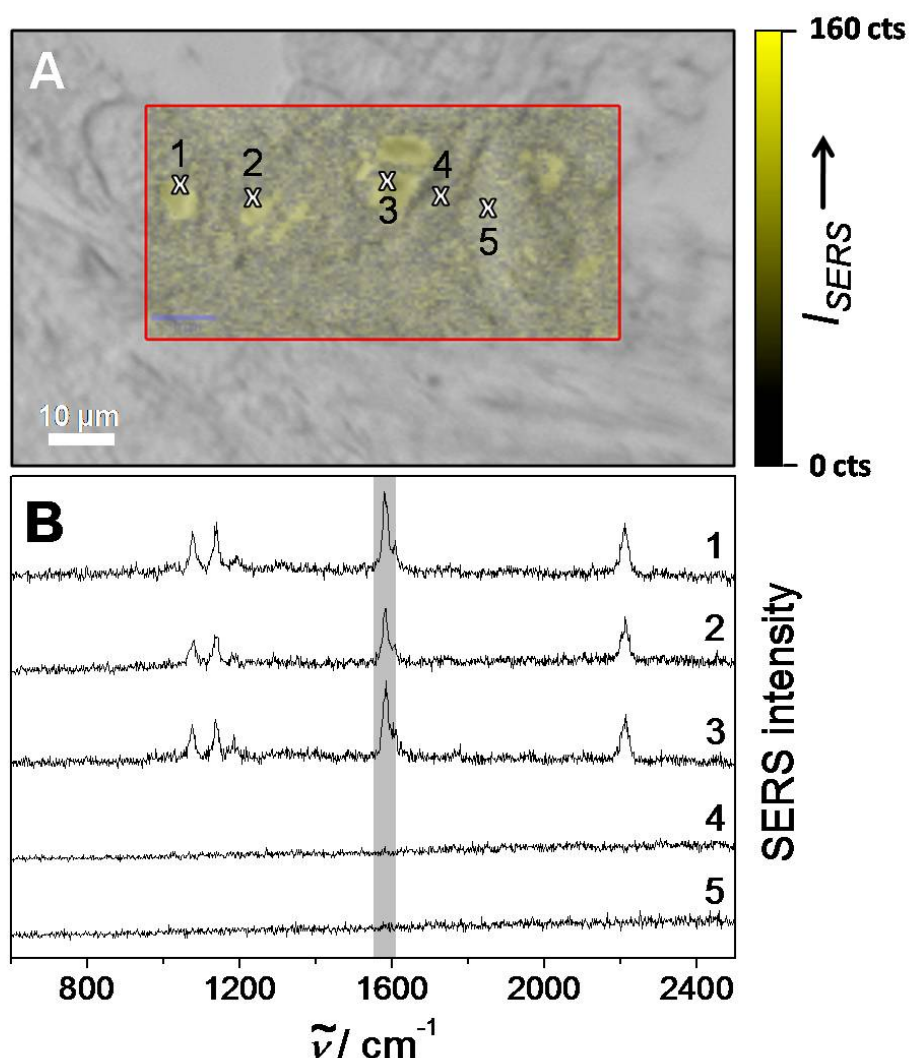


Figure 41. (A) White light image of prostate tissue with overlaid SERS false color image based on the intensity of the 1580 cm^{-1} Raman-marker band (**SEMA4**). (B) Five representative SERS spectra from different locations in (A), indicated by white crosses (from left to right).

3.5 Conclusion

In this chapter the synthesis and characterization of new SERS-markers for immuno-SERS application is presented. Each SERS-marker was designed to have characteristic Raman vibrations and a thiol group for chemisorptions to Au/Ag nanoshells. The adsorption of the specifically designed SERS-marker to Au/Ag nanoshells yields SERS-labels. Each SERS-label revealed a characteristic SERS spectrum with intense Raman bands. The discrimination of the SERS-labels due to the different Raman-active units opens the possibility for SERS-multiplexing experiments.

Furthermore, the intense characteristic Raman bands were used for the detection of the tumor suppressor p63 in benign prostate tissue via immuno-SERS microscopy. The hydrophobic SERS-label **SEMA4@Au/Ag** was thereby silica-encapsulated and the silica shell afterwards functionalized with anti-p63 antigen. Immuno-SERS imaging of prostate tissue incubated with SERS-labeled anti-p63 antibodies demonstrated the selective detection of p63 in the basal epithelium. The results show the potential of the method for the detection of several biomolecules in a multiplexing SERS experiment.

4 Summary

In this work the synthesis and analysis of chromophore functionalized spherical gold nanoparticles is presented. The optical, electrochemical and spectroelectrochemical properties of these hybrid materials are furthermore studied. The work therefore is divided into two parts.

The first part deals with triarylamine and PCTM-radical functionalized gold nanoparticles. The focus thereby was on the synthesis and on the investigations of chromophore-chromophore interactions and gold core-chromophore interactions. The chromophores, especially triarylamines, were attached to the gold core via different bridging units and were studied with optical and electrochemical methods.

Although the synthesis of chromophore functionalized gold nanoparticles was a great challenge, syntheses for stable nanoparticles have been developed. The use of a syringe pump was very useful to control the rate of reactant addition.

The purity and dimensions of the nanoparticles was determined by $^1\text{H-NMR}$ spectroscopy, diffusion ordered NMR spectroscopy (DOSY), TGA, XPS and STEM. Furthermore a cyclic voltammetry technique was used to determine the composition of the particles *via* the *Randles-Sevcik* equation. An analysis of these parameters led to a model of a sea urchin-shaped nanoparticle.

Optical measurements of the particles revealed an anisotropic absorption behavior of the triarylamine units due to gold core-chromophore interaction. However this behavior depends strongly on the relative orientation of the transition dipole moment of the chromophore to the gold surface and the distance of the chromophore to the surface. Hence, the anisotropic behavior was exclusively detected in the spectra of the **Au-Tara1** particles. The short and rigid π -conjugated bridging unit thereby facilitates this gold core-chromophore interaction.

It was shown from electrochemical investigations that the triarylamine units can be chemically reversibly oxidized to the triarylamine monoradical cation. Furthermore, the measurements revealed a strong interligand triarylamine-triarylamine interaction which was only seen for the **Au-Tara1** particles. The long π -conjugated bridging units of the **Au-Tara2** and **Au-Tara3** particles as well as the aliphatic bridging unit of **Au-Tara4** prevent any detectable interligand interactions. One may conclude that both the gold core-chromophore

and the interligand triarylamine-triarylamine interaction depend on the length and the rigidity of the bridging unit.

The electron transfer behavior of the triarylamine units adsorbed onto the gold core was additionally studied via spectroelectrochemical (SEC) measurements which are able to reveal weaker interactions. The investigations of **Au-Tara1** and **Au-Tara2** revealed a significant strong coupling between neighboring triarylamine units which is due to through-space intervalence interactions. This behavior was not detected for **Au-Tara3** or for **Au-Tara4**. The SEC analysis also revealed that these observed interligand interactions depend on the length and the rigidity of the bridging unit. Thus, the systematic variation of the bridging unit gave a basic insight in the optical and electrochemical properties of triarylamines, located in the vicinity of a gold nanoparticle.

Further attempts were made to synthesize and radicalize perchlorinated triarylmethane (PCTM) functionalized gold particles. The PCTM-radical gold particle was analyzed, but the size could only be estimated to be smaller than 1 nm. Due to an incomplete radicalization of the PCTM-ligand, the optical and electrochemical properties of the radical are only slightly influenced by adsorption onto the gold core. Spectroelectrochemical measurements demonstrated that the **Au-Rad** nanoparticle can be reversibly switched between the magnetic on-state of the radical species and the magnetic off-state of the anionic species. The PCTM-radical functionalized gold nanoparticle can thus be considered as a “freely diffusing nanoswitch”.

The second part of this work aimed at the synthesis of new molecules, denoted as SERS-markers, for immuno SERS applications. For this purpose, the SERS-markers were designed to have a Raman-active unit and a thiol group for chemisorptions to Au/Ag nanoshells. The Raman vibrations should thereby be polarized along the molecular axis, to obtain intense SERS signals. In cooperation with the group of Schlücker (University of Osnabrück) the SERS-markers were absorbed onto Au/Ag nanoshells, denoted as SERS-labels, and characterized. The SERS spectra of the SERS-labels exhibited intense and characteristic SERS-signals for each marker.

For immuno SERS investigations **SEMA3** was functionalized with a hydrophilic end unit. This marker was adsorbed onto an Au/Ag nanoshell and encapsulated with silica. An anti-p63 antibody was bound to the silica surface in order to generate a SERS-labeled antibody for the detection of the tumor suppressor p63 in benign prostate. Immuno-SERS

imaging of prostate tissue incubated with SERS-labeled anti-p63 antibodies demonstrated the selective detection of p63 in the basal epithelium. The results show the potential of the method for the detection of several biomolecules in a multiplexing SERS experiment.

5 Experimental Section

5.1 Analytical Methods

5.1.1 General Analytical Methods

All reagents were obtained from commercial suppliers and were used without further purification. Diethylamine, 1,4-dioxane, tetrahydrofuran (thf) and pyrrolidine were purified and dried by standard procedures and kept under inert gas atmosphere (nitrogen, dried with Sicapent from MERCK, oxygen was removed by copper oxide catalyst R3-11 from BASF). Thin-layer chromatography was carried out on Merck silica gel plates (60 F254). Merck silica gel (32-63 μm) was used for flash chromatography. Column chromatography was carried out using neutral alumina with activity V (63-200 μm).

5.1.2 NMR Spectroscopy

- Bruker AC 250 FT-Spectrometer (250 MHz)
- Bruker Avance 400 FT-Spectrometer (400 MHz)
- Bruker Avance DMX 600 FT-Spectrometer (600 MHz)

All NMR spectra were recorded at room temperature unless otherwise indicated. The signal of the respective solvent was used as the internal reference and the chemical shifts are given in ppm (δ -scale) versus TMS. Multiplicities were denoted as s (singlet), d (doublet), t (triplet) and m (multiplet). Coupling constants are given in Hz. NMR-Spectroscopy data are quoted as follows: chemical shift (multiplicity, coupling constants, number of protons).

DOSY spectra were measured with the 600 MHz spectrometer and a cryprobe. Because of small temperature gradients in the sample we used a double-stimulated-echo to suppress convection artefacts.²⁶⁷ The DOSY-NMR data were fitted with a mono exponential function²⁶⁷ with the assumption that all particles have the same size.

5.1.3 Mass Spectroscopy

- Finnigan MAT 90
- Bruker Daltonik microTOF focus

Mass spectra were recorded at the Institute of Organic Chemistry, University of Würzburg. For ESI-spectra 10 μM solutions of the sample in chloroform or dichloromethane were prepared.

5.1.4 Osteryoung Square Wave Voltammetry and Cyclic Voltammetry

- Electrochemical workstation BAS CV-50 W including software version 2.0

Osteryoung square wave voltammograms and cyclic voltammograms were recorded on an electrochemical workstation BAS CV-50 W including software version 2.0. The square wave amplitude was 25 mV, the frequency was 15 Hz and the potential step height for base staircase wave form was 4 mV. The electrochemical experiments were performed in dry, argon-saturated dichloromethane with tetrabutylammonium hexafluorophosphate (TBAH) as the supporting electrolyte using a conventional three-electrode set-up with a platinum disk electrode (3 mm², 0.64 mm², active surface determined by CV experiments with ferrocene). The potentials are referenced against ferrocene (Fc/Fc⁺). The electrochemical reversibility of the redox process was checked by multi-cycle thin layer cyclic voltammetry and by plotting the anodic current against the scan rate (*Randles-Sevcik* equation). In order to check the long-term chemical reversibility we performed measurements under thin-layer conditions in which the working electrode was placed onto a polished mobile glass hemisphere.²⁶⁸

5.1.5 UV/vis/NIR Spectroscopy

- JASCO V-570 UV/vis/NIR spectrometer

Dichloromethane was of spectroscopic grade and was used without any further purification. Absorption spectra were recorded in 1 cm quartz cuvettes (Hellma).

5.1.6 Spectroelectrochemistry

- JASCO V-570 UV/vis/NIR spectrometer
- EG & G potentiostat/galvanostat model 363

The solutions of the voltammetry experiments were transferred by a syringe into a spectroelectrochemical optical transparent thin-layer cell (optical path length of 100 μm with a gold minigrid working electrode) as described by Salbeck.²⁶⁹ UV/vis/NIR spectra were recorded while applying a constant potential (EG & G potentiostat/galvanostat model 363) to the solution in the thin-layer arrangement referenced against a Pt electrode. The potential was increased in 50 mV steps. Spectra were recorded until the first oxidative process was fully covered. Back reduction was also performed in order to prove reversibility of the whole process in all cases.

5.1.7 Polarised Steady-State Fluorescence Spectroscopy

- Photon Technology International QuantaMasterTM Model QM-2000-4 including a cooled photomultiplier (type R928P) and a 75 W xenon short arc lamp (type UXL-75XE, Ushio)

Fluorescence-anisotropy measurements were carried out in a sucrose octaacetate (SOA) matrix at room temperature. Two Glan–Thompson polarisers from Photon Technology International were used in an L-format setup. SOA was purchased from Acros Organics and recrystallised twice from ethanol. Sample preparation was done according to a procedure

reported in literature.²⁷⁰ Compound **Ref1** and SOA were dissolved in dichloromethane (Merck, Uvasol). The solution was filtered through a 0.1 μm filter in order to remove any traces of lint and dust and purged with dry and oxygen-free argon for 10 min. Dichloromethane was partially removed *in vacuo* until a viscous oil resulted, which was filled into a 1 cm fluorescence quartz cuvette. The cuvette was then kept in an oven at 100 °C for about 1 h and at 130 °C for 5 h to remove the remaining dichloromethane.

5.1.8 Scanning Transmission Electron Microscopy (STEM)

- FEI Helios Nanolab equipped with an insertable multi-segment solid-state detector (acceleration voltage of 30 kV and a beam current of 170 pA)
- FEI Titan 80-300 transmission electron microscope (acceleration voltage of 300kV, a beam convergence angle of 9.5 mrad and a current of 125 pA)

STEM measurements were carried out by Prof. M. Kamp at the Department of Physics, University of Würzburg. Samples for STEM analysis were prepared from a 20 $\mu\text{g}/\text{mL}$ solution of the nanoparticles in dichloromethane. A single drop was transferred on a carbon coated copper grid. The solvent was evaporated at room temperature.

5.1.9 X-ray Photoelectron Spectroscopy (XPS)

- Scienta R4000 electron analyser using a monochromatic Al K α light source²⁷¹

XPS measurements were carried out by the group of Prof. F.Reinert at the Department of Physics, University of Würzburg. Molybdenum substrates have been coated with a solution of **Au-Tara1** in thf and were transferred into the UHV measuring chamber ($p = 10^{-10}$ mbar). Since the samples are mainly dominated by carbon and oxygen from both the residua of the solvent and the organic shell of the Au nanoparticles the samples were slightly sputtered by Ar⁺-ion bombardment. This process permitted a reduction of the amount of light elements like carbon and oxygen without destroying the metal core of the nanoparticle. Figure S5 shows the photoemission results of **Au-Tara1S** and **Au-Tara1L**, respectively.

5.1.10 Thermogravimetric Analysis (TGA)

- TGA measurements were performed with a Perkin Elmer STA 6000 on accurately weighed, carefully dried nanoparticle samples at 10 °C/min. Nitrogen was used as purge gas.

TGA measurements were performed at the Institute of Organic Chemistry, University of Würzburg.

5.1.11 Recycling-GPC

- Gel permeation chromatography (GPC) measurements were carried out on an instrument from Shimadzu (diode array detector SPD-M20A, system controller CBM-20A, solvent delivery unit LC-20AD, on-line degasser DGU 20A).

The chromatography was carried out at 20 °C on two Phenogel[®]-columns (600 x 20.8 mm, pore size 100 Å) from Phenomenex and on an analytic SDV (styrene-divinylbenzene copolymer network) column “linear S” from PSS.

5.1.12 IR-Spectroscopy

Infrared spectra were recorded using a JASCO 410 FT-IR spectrophotometer fitted with an attenuated total reflectance (ATR) attachment. Positions of the absorption bands are given in reciprocal centimetres (cm⁻¹), signal intensities are described by w (weak), m (medium) and s (strong).

5.2 Synthesis

GP1: Hagihara-Sonogashira Coupling with Pd(PhCN)₂Cl₂, P(*t*-Bu)₃ and CuI in diethylamine

Under a nitrogen atmosphere the alkyne, the aryl bromide, Pd(PhCN)₂Cl₂ (0.05 equiv.*), CuI (0.025 equiv.*) and P(*t*-Bu)₃ (0.01 equiv.*, 1.0 M solution in toluene) were dissolved in diethylamine and degassed. The reaction mixture was stirred in the dark. The solvent was removed *in vacuo*. The residue was dissolved in dichloromethane and was washed with water. The organic phase was dried with MgSO₄ and the solvent removed *in vacuo*. The crude product was purified by chromatography.

*The data are referenced to the reactant with the lowest quantity.

GP2: Hagihara-Sonogashira Coupling with Pd(PPh₃)₂Cl₂ and CuI in diethylamine

Under a nitrogen atmosphere the alkyne, the aryl bromide, Pd(PPh₃)₂Cl₂ (0.05 equiv.*) and CuI (0.025 equiv.*) were dissolved in diethylamine and degassed. The reaction mixture was stirred at 65 °C in the dark. The solvent was removed *in vacuo*. The residue was dissolved in dichloromethane and was washed with water. The organic phase was dried with MgSO₄ and the solvent removed *in vacuo*. The crude product was purified by chromatography.

*The data are referenced to the reactant with the lowest quantity.

GP3: Hagihara-Sonogashira Coupling with Pd(PhCN)₂Cl₂, P(*t*-Bu)₃, CuI and di-*iso*-propylamine in 1,4-dioxane

Under a nitrogen atmosphere the alkyne, the aryl halide, Pd(PhCN)₂Cl₂ (0.05 equiv.*), CuI (0.025 equiv.*), di-*iso*-propylamine (1.5 equiv.*) and P(*t*-Bu)₃ (0.01 equiv.*, 1.0 M solution in toluene) were dissolved in 1,4-dioxane and degassed. The mixture was stirred at room temperature in the dark. The solvent was removed *in vacuo*. The residue was dissolved in dichloromethane and was washed with water. The organic phase was dried with MgSO₄ and the solvent removed *in vacuo*. The crude product was purified by chromatography.

*The data are referenced to the reactant with the lowest quantity.

GP4: Hagihara-Sonogashira Coupling with Pd(PPh₃)₂Cl₂ and CuI in 1,4-dioxane

To the alkyne, the aryl bromide, Pd(PPh₃)₂Cl₂ (0.05 equiv.*), CuI (0.025 equiv.*) and a base under nitrogen atmosphere was added 1,4-dioxane and degassed. The reaction mixture was stirred in the dark. The solvent was removed *in vacuo*. The residue was dissolved in dichloromethane and was washed with water. The organic phase was dried with MgSO₄ and the solvent removed *in vacuo*. The crude product was purified by chromatography.

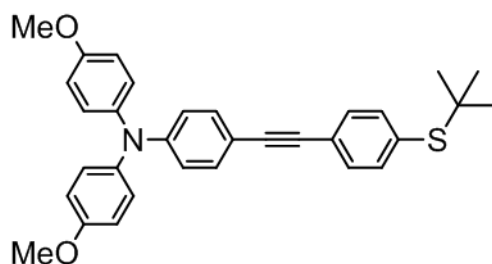
*The data are referenced to the reactant with the lowest quantity.

GP5: Synthesis of the Nanoparticle Precursors

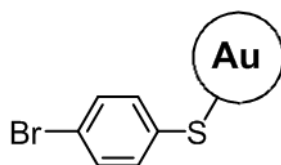
Under a nitrogen atmosphere tetrachloroauric acid trihydrate and 4-bromobenzenethiol were dissolved together in dry thf and added simultaneously with a LiBH₄-solution (thf) into a Schlenk tube with stirred dry thf *via* a syringe pump (2.5 mL / min). The black solution was stirred for 1 min before water (1 mL) was added. The mixture was concentrated to 4 mL, dichloromethane (15 mL) was added and filtered through a glass frit (pore 3). The residue was extracted with dichloromethane (20 mL) and the organic phase was washed with water (3 x 20 mL). The organic phase was concentrated to 4 mL and added to *n*-hexane (30 mL). This mixture was centrifuged and the black residue was washed with *n*-hexane.

GP6: Transformation of the *t*-butylthiol group into the acetyl thiol group

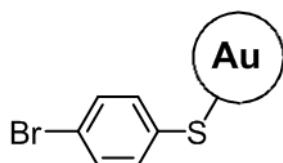
Under nitrogen atmosphere a solution of the *t*-butylthiol functionalized molecule in dry dichloromethane was cooled to -20 °C. After the addition of BBr₃ (1 equiv.) and acetyl chloride (19 equiv.) the solution was stirred for 3 h at -20 °C and then allowed to warm to room temperature. The solvent was removed *in vacuo* and the residue was redissolved in dichloromethane (15 mL). The organic phase was washed with water (3 x 20 mL) and then dried with MgSO₄. The solvent was removed *in vacuo*.

**Synthesis of 4-((4-*t*-butylthiophenyl)ethynyl)-*N,N*-bis(4-methoxyphenyl)benzene-amine
Ref1**

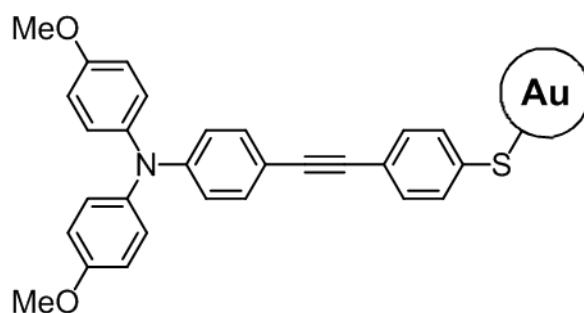
Compound **Ref1** was synthesised from the alkynes **1** (400 mg, 1.21 mmol) and the aryl bromide **2** (426 mg, 1.74 mmol) in diethylamine (14 mL) at room temperature according to general procedure **GP1** (reaction time 12 h). Flash chromatography on silica gel with petroleum ether / dichloromethane (3:1 \rightarrow 2:1) as eluent yielded 140 mg (284 μ mol, 23%) of an orange solid. $^1\text{H-NMR}$ (400 MHz, acetone- d_6 , 295 K): δ/ppm = 7.55 (AA', 2H), 7.50 (BB', 2H), 7.35 (AA', 2H), 7.13 (AA', 4H), 6.96 (BB', 4H), 6.80 (BB', 2H), 3.82 (s, 6H), 1.30 (s, 9H). $\{^1\text{H}\}^{13}\text{C-NMR}$ (100 MHz, acetone- d_6 , 295 K): δ/ppm = 157.1 (quart.), 149.6 (quart.), 140.4 (quart.), 137.6 (tert.), 133.1 (quart.), 132.7 (tert.), 131.5 (tert.), 127.7 (tert.), 124.6 (quart.), 119.0 (tert.), 115.2 (tert.), 113.6 (quart.), 92.0 (quart.), 87.8 (quart.), 55.8 (prim.), 46.7 (quart.), 31.1 (prim.). MS (ESI pos, high resolution): calc. for $\text{C}_{32}\text{H}_{31}\text{NO}_2\text{S}$: m/z = 493.20700, exp.: m/z = 493.20732 (Δ = 0.65 ppm).

Synthesis of 4-bromothiophenol protected gold nanoparticle Au-Pre1S

Following **GP5**: Tetrachloroauric acid trihydrate (140 mg, 355 μ mol) and 4-bromobenzenethiol (Aldrich) (134 mg, 711 μ mol) were solved in dry thf (14 mL). This solution and LiBH_4 (14 mL, 1.40 mmol, 0.1 M in thf) were both added to thf (8 mL). The yield was 60 mg of a black solid.

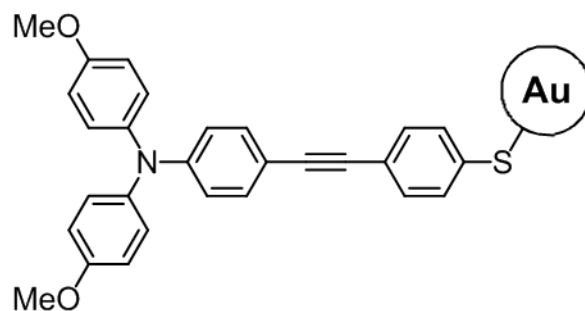
Synthesis of 4-bromothiophenol protected gold nanoparticle Au-Pre1L

Tetrachloroauric acid trihydrate (144 mg, 366 μmol) and 4-bromobenzenethiol (Aldrich) (138 mg, 731 μmol) were dissolved in dry thf (14 mL) and added simultaneously with a LiBH_4 -solution (14 mL, 1.40 mmol, 0.1 M in thf) to stirred dry thf (8 mL) *via* a syringe pump (2.5 mL/min). The black solution was stirred for 1 min before water (1 mL) was added. The mixture was concentrated to 4 mL, dichloromethane (20 mL) was added and filtered through a glass frit (pore 3). The residue was extracted with dichloromethane (20 mL) and thf (20 mL) and the organic phase was washed with water (3 x 20 mL). The organic phase was concentrated to 4 mL and added to *n*-hexane (30 mL). This mixture was centrifuged and the black residue was washed with *n*-hexane. The yield was 59 mg of a black solid.

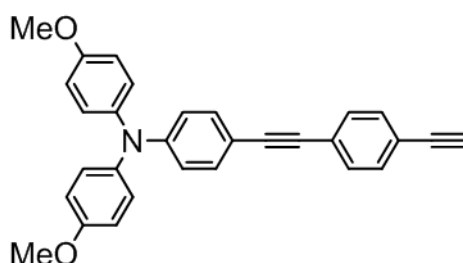
Synthesis of the gold nanoparticle Au-Tara1S

Under a nitrogen atmosphere alkyne **1** (100 mg, 304 μmol), $\text{P}(t\text{-Bu})_3$ (30 μL , 1.0 M in toluene, 30 μmol) and di-*iso*-propylamine (51 μL , 364 μmol) were added to a solution of nanoparticle **Au-Pre1S** (60 mg) in dry thf (6 mL). The mixture was degassed and $\text{Pd}(\text{PhCN})_2\text{Cl}_2$ (9.3 mg, 24 μmol) and CuI (2.9 mg, 15 μmol) were added. The mixture was stirred for 12 h at room temperature. The solvent was removed *in vacuo*, and the residue was dissolved in dichloromethane and filtered (glass frit; pore 3). The solution was washed with a saturated aqueous solution of NaCl and water. The organic phase was concentrated to 4 mL

and *n*-hexane (30 mL) was added. This mixture was centrifuged. The black residue was dissolved in dichloromethane (4 mL) and dropped into *n*-hexane (30 mL) and again centrifuged. This purification step was repeated at least seven times. The yield was 30 mg of a black solid. ¹H-NMR (400 MHz, dichloromethane-d₂, 295 K): δ /ppm = 8.50-5.50 (16H), 4.20-3.10 (6H). STEM: radius 1.12 (\pm 0.24) nm.

Synthesis of the gold nanoparticle Au-Tara1L

Under a nitrogen atmosphere alkyne **1** (39 mg, 118 μmol), $\text{P}(t\text{-Bu})_3$ (12 μL , 1.0 M in toluene, 12 μmol) and di-*iso*-propylamine (20 μL , 142 μmol) were added to a solution of nanoparticle **Au-PreL** (59 mg) in dry thf (6 mL). The mixture was degassed and $\text{Pd}(\text{PhCN})_2\text{Cl}_2$ (3.6 mg, 9.5 μmol) and CuI (1.1 mg, 5.9 μmol) were added. The mixture was stirred for 3 d at room temperature. The solvent was removed *in vacuo*, and the residue was dissolved in dichloromethane and filtered (glass frit; pore 3). The solution was washed with a saturated aqueous solution of NaCl and water. The organic phase was concentrated to 4 mL and *n*-hexane (30 mL) was added. This mixture was centrifuged. The black residue was dissolved in dichloromethane (4 mL) and dropped into *n*-hexane (30 mL) and again centrifuged. This purification step was repeated at least seven times. The yield was 35 mg of a black solid. $^1\text{H-NMR}$ (400 MHz, dichloromethane- d_2 , 295 K): δ/ppm = 8.50-5.50 (16H), 4.20-3.10 (4H). STEM: radius 1.36 (\pm 0.28) nm.

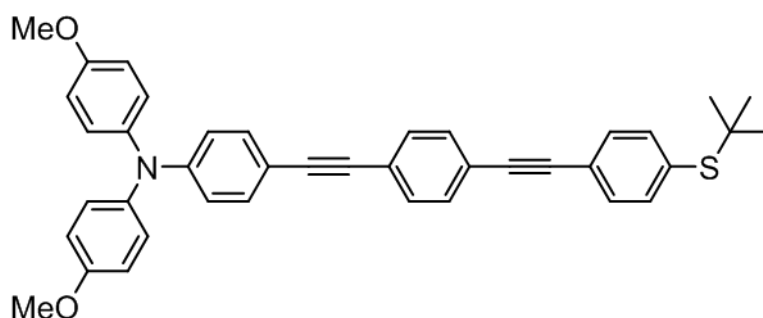
Synthesis of 4-((4-ethynylphenyl)ethynyl)-*N,N*-bis(4-methoxyphenyl)aniline 3

Compound **6** (410 mg, 817 μmol) was dissolved in thf (10 mL) and a solution of tetra-*n*-butylammonium fluoride (TBAF) (1.1 mL, 1.10 mmol, 1.0 M in thf) was added. After stirring for 1 h at room temperature the solvent was removed *in vacuo*. The residue was dissolved in

dichloromethane. The organic phase was washed with water and dried with MgSO_4 . The solvent was removed *in vacuo* to afford 351 mg (817 μmol , 100%) of a black solid. $^1\text{H-NMR}$ (400 MHz, chloroform- d_1 , 295 K): δ/ppm = 7.43 (-, 4H), 7.29 (AA', 2H), 7.07 (AA', 4H), 6.86-6.83 (-, 6H), 3.80 (s, 6H), 3.15 (s, 1H). $\{^1\text{H}\}^{13}\text{C-NMR}$ (100 MHz, chloroform- d_1 , 295 K): δ/ppm = 157.1 (quart.), 149.6 (quart.), 140.3 (quart.), 132.8 (tert.), 132.4 (tert.), 131.5 (tert.), 127.8 (tert.), 124.8 (quart.), 121.6 (quart.), 118.9 (tert.), 115.2 (tert.), 113.4 (quart.), 92.7 (quart.), 87.8 (quart.), 83.6 (quart.), 78.9 (tert.), 55.8 (prim.).* MS (EI pos, high resolution): calc. for $\text{C}_{30}\text{H}_{23}\text{NO}_2^{*+}$: m/z = 429.17233, exp: m/z = 429.17208 (Δ = 0.58 ppm).

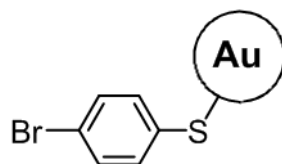
*The multiplicity were determined by varying the optimized H-C coupling constant (J = 50 Hz, 145 Hz, 250 Hz) in the DEPT135 experiment.

Synthesis of 4-((4-((4-(*t*-butylthio)phenyl)ethynyl)phenyl)ethynyl)-*N,N*-bis(4-methoxyphenyl)aniline Ref2



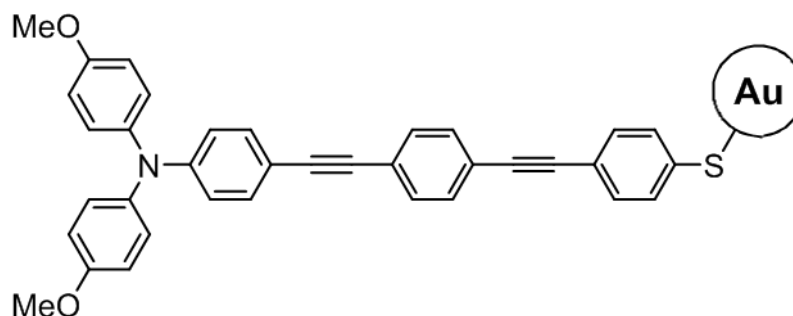
Compound **Ref2** was synthesized from **3** (252 mg, 587 μmol) and **2** (158 mg, 645 μmol) in diethylamine (8 mL) at 75 °C according to general procedure **GP1** (reaction time 12 h). Flash chromatography on silica gel with petroleum ether / dichloromethane (3:1 \rightarrow 2:1) as eluent yielded 190 mg (320 μmol , 55%) of a yellow solid. $^1\text{H-NMR}$ (400 MHz, chloroform- d_1 , 295 K): δ/ppm = 7.53-7.46 (-, 8H), 7.31 (AA', 2H), 7.08 (AA', 4H), 6.86-6.83 (-, 6H), 3.81 (s, 6H), 1.30 (s, 9H). $\{^1\text{H}\}^{13}\text{C-NMR}$ (150 MHz, dichloromethane- d_2 , 295 K): δ/ppm = 157.0 (quart.), 149.5 (quart.), 140.2 (quart.), 137.6 (tert.), 134.0 (quart.), 132.7 (tert.), 131.9 (tert.), 131.7 (tert.), 131.5 (tert.), 127.7 (tert.), 124.3 (quart.), 123.7 (quart.), 122.5 (quart.), 118.8 (tert.), 115.1 (tert.), 113.3 (quart.), 92.6 (quart.), 90.8 (quart.), 90.7 (quart.), 87.9 (quart.), 55.8 (prim.), 46.7 (quart.), 31.1 (prim.). MS (EI pos, high resolution): calc. for $\text{C}_{40}\text{H}_{35}\text{NO}_2\text{S}^{*+}$: m/z = 593.23830, exp: m/z = 593.23826 (Δ = 0.07 ppm).

Synthesis of 4-bromothiophenol protected gold nanoparticle Au-Pre2



Following **GP5**: Tetrachloroauric acid trihydrate (138 mg, 350 μmol) and 4-bromobenzenethiol (Alfa Aesar) (199 mg, 1.05 mmol) were solved in dry thf (14 mL). This solution and LiBH_4 (14 mL, 1.40 mmol, 0.1 M in thf) were both added to thf (8 mL). The yield was 50 mg of a black solid.

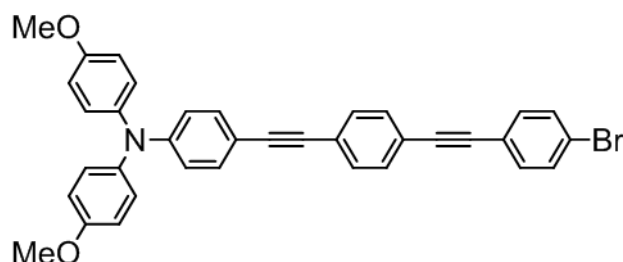
Synthesis of Au-Tara2



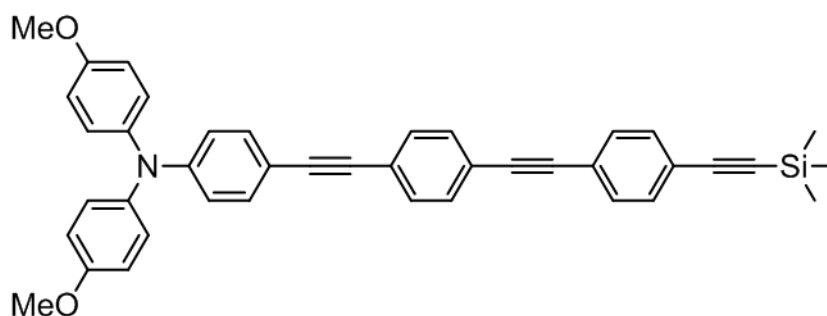
Under a nitrogen atmosphere a solution of **Au-Pre2** (50 mg), alkyne **2** (32.7 mg, 76.2 μmol), $\text{P}(t\text{-Bu})_3$ (190 μL , 192 μmol , 1.0 M in toluene), di-*iso*-propylamine (44 μL , 317 μmol), $\text{Pd}(\text{PhCN})_2\text{Cl}_2$ (20 mg, 51 μmol) and CuI (6.0 mg, 32 μmol) in dry thf (6 mL) were degassed and stirred for 12 h at room temperature. The solvent was removed *in vacuo*, and the residue was dissolved in dichloromethane and filtered (glass frit; pore 3). The filtrate was washed with a saturated aqueous solution of NaCl (2 x 30 mL) and water (30 mL). The organic phase was concentrated to 4 mL and *n*-hexane (30 mL) was added. This mixture was centrifuged. The black residue was further purified in three steps. First, the nanoparticle was dissolved in dichloromethane (4 mL), dropped into *n*-hexane (30 mL) and again centrifuged (repeated at least seven times). This step was followed by an extraction of the impurities with cyclohexane in a Soxhlet extractor. The residue was dissolved in little dichloromethane and precipitated by adding the concentrated solution into *n*-hexane to obtain 28 mg of a black solid. $^1\text{H-NMR}$

(400 MHz, dichloromethane- d_2 , 298 K): δ /ppm = 8.50-6.00 (20H), 3.90-3.40 (6H). STEM: radius 0.93 (\pm 0.17) nm.

Synthesis of 4-((4-((4-bromophenyl)ethynyl)phenyl)ethynyl)-*N,N*-bis(4-methoxyphenyl)aniline **7**

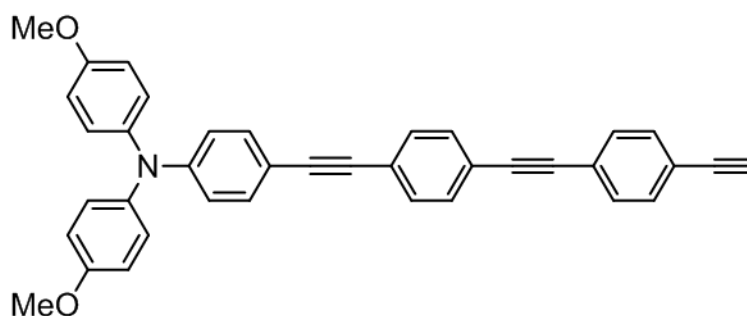


According to general procedure **GP2**, compound **7** was synthesized from **3** (590 mg, 1.37 mmol) and 1-bromo-4-iodobenzene (700 mg, 2.47 mmol) in diethylamine (15 mL) at 65 °C (reaction time 5 d). Flash chromatography on silica gel (petroleum ether / dichloromethane 3:2) yielded 440 mg (753 μ mol, 55%) of an orange solid. $^1\text{H-NMR}$ (400 MHz, chloroform- d_1 , 295 K): δ /ppm = 7.49-7.46 (-, 6H), 7.38 (BB', 2H), 7.31 (AA', 2H), 7.08 (AA', 4H), 6.87-6.83 (-, 6H), 3.81 (s, 6H). $\{^1\text{H}\}^{13}\text{C-NMR}$ (150 MHz, chloroform- d_1 , 295 K): δ /ppm = 156.6 (quart.), 149.2 (quart.), 140.3 (quart.), 133.2 (tert.), 132.6 (tert.), 131.8 (tert.), 131.6 (tert.), 131.5 (tert.), 127.3 (tert.), 124.2 (quart.), 122.8 (quart.), 122.3 (quart.), 122.2 (quart.), 119.2 (tert.), 115.0 (tert.), 113.6 (quart.), 92.5 (quart.), 90.6 (quart.), 90.0 (quart.), 88.0 (quart.), 55.6 (prim.). MS (EI pos, high resolution): calc. for $\text{C}_{36}\text{H}_{26}\text{BrNO}_2^{*+}$: m/z = 583.11414, exp: m/z = 583.11468 (Δ = 0.93 ppm).

Synthesis of bis(4-methoxyphenyl)-*N,N*-(4-((4-((4-((trimethylsilyl)ethynyl)phenyl)ethynyl)phenyl)ethynyl)phenyl)ethynyl)-phenyl)aniline **8**

Following **GP3**, compound **7** (440 mg, 753 μmol) and trimethylsilylacetylene (170 μL , 1.21 mmol) were converted into **8** in 1,4-dioxane (10 mL) at room temperature (reaction time 9 d). Flash chromatography on silica gel (petroleum ether / dichloromethane 3:2) yielded 402 mg (668 μmol , 89%) of an orange solid. $^1\text{H-NMR}$ (400 MHz, chloroform- d_1 , 295 K): δ/ppm = 7.475-7.458 (-, 4H), 7.456-7.438 (-, 4H), 7.31 (AA', 2H), 7.08 (AA', 4H), 6.87-6.83 (-, 6H), 3.81 (s, 6H), 0.26 (s, 9H). $\{^1\text{H}\}^{13}\text{C-NMR}$ (100 MHz, chloroform- d_1 , 295 K): δ/ppm = 156.5 (quart.), 149.2 (quart.), 140.3 (quart.), 132.6 (tert.), 132.1 (tert.), 131.6 (tert.), 131.5 (tert.), 131.45 (tert.), 127.3 (tert.), 124.2 (quart.), 123.3 (quart.), 123.2 (quart.), 122.3 (quart.), 119.2 (tert.), 115.0 (tert.), 113.7 (quart.), 104.8 (quart.), 96.5 (quart.), 92.5 (quart.), 91.4 (quart.), 90.8 (quart.), 88.0 (quart.), 55.6 (prim.), 0.06 (prim.). MS (EI pos, high resolution): calc. for $\text{C}_{41}\text{H}_{35}\text{NO}_2\text{Si}^+$: m/z = 601.24316, exp: m/z = 601.24339 (Δ = 0.38 ppm).

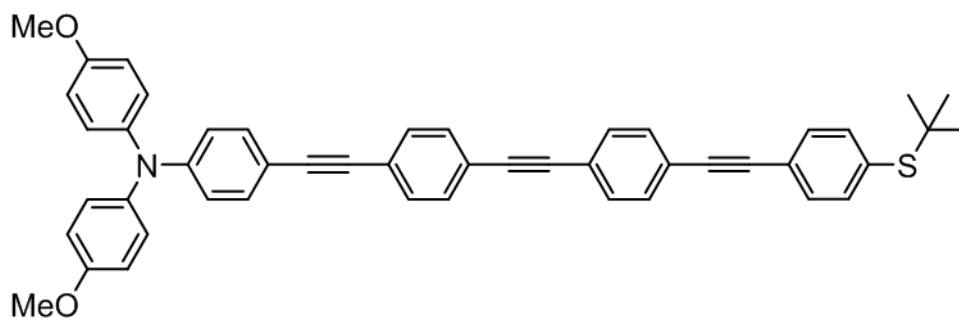
Synthesis of 4-((4-((4-ethynylphenyl)ethynyl)phenyl)ethynyl)-*N,N*-bis(4-methoxyphenyl)aniline **4**



Compound **8** (402 mg, 668 μmol) was dissolved in thf (10 mL) and a solution of TBAF (800 μL , 800 μmol , 1.0 M in thf) was added. After stirring for 1 h at room temperature the solvent was removed *in vacuo*. The residue was dissolved in dichloromethane. The organic phase was washed with water (3 x 15 mL) and dried with MgSO_4 . The solvent was removed *in vacuo* to obtain 353 mg (667 μmol , 100%) of a black solid. $^1\text{H-NMR}$ (400 MHz, chloroform- d_1 , 295 K): δ/ppm = 7.49-7.45 (-, 8H), 7.31 (AA', 2H), 7.08 (AA', 4H), 6.87-6.83 (-, 6H), 3.81 (s, 6H), 3.18 (s, 1H). $\{^1\text{H}\}^{13}\text{C-NMR}$ (150 MHz, chloroform- d_1 , 295 K): δ/ppm = 156.5 (quart.), 149.2 (quart.), 140.3 (quart.), 132.6 (tert.), 132.2 (tert.), 131.7 (tert.), 131.6 (tert.), 131.5 (tert.), 127.3 (tert.), 124.2 (quart.), 123.8 (quart.), 122.2 (quart.), 122.1 (quart.), 119.2 (tert.), 115.0 (tert.), 113.6 (quart.), 92.5 (quart.), 91.4 (quart.), 90.6 (quart.), 88.0 (quart.), 83.4 (quart.), 79.1 (tert.), 55.6 (prim.)* MS (ESI pos, high resolution): calc. for $\text{C}_{38}\text{H}_{27}\text{NO}_2^{*+}$: m/z = 529.20363, exp.: m/z = 529.20361 (Δ = 0.04 ppm).

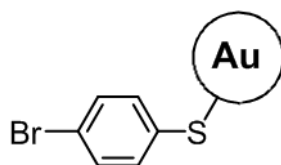
*The multiplicity were determined by varying the optimized H-C coupling constant (J = 50 Hz, 145 Hz, 250 Hz) in the DEPT experiment.

Synthesis of 4-((4-((4-((4-(*t*-butylthio)phenyl)ethynyl)phenyl)ethynyl)phenyl)ethynyl)-*N,N*-bis(4-methoxyphenyl)aniline Ref3



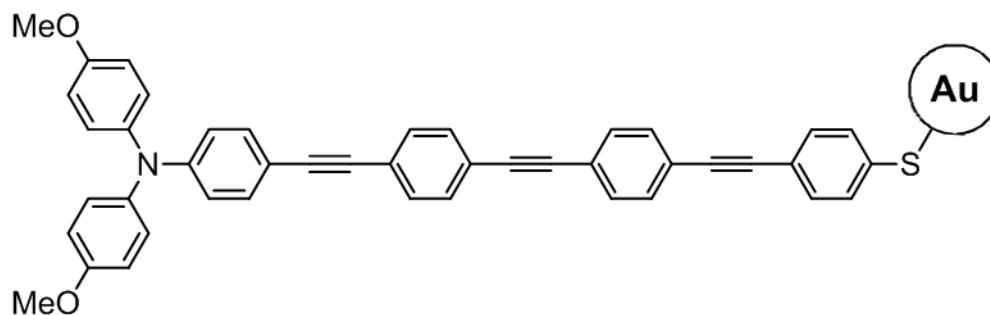
Following **GP3**, compound **4** (60.0 mg, 113 μmol) and compound **2** (44.4 mg, 181 μmol) were transformed into **Ref3** in 1,4-dioxane (5 mL) at room temperature (reaction time 9 d). Flash chromatography on silica gel (petroleum ether / dichloromethane 3:1) yielded 20.0 mg (28.8 μmol , 25%) of a yellow solid. $^1\text{H-NMR}$ (600 MHz, acetone- d_6 , 295 K): δ/ppm = 7.58-7.57 (-, 4H), 7.56-7.53 (-, 6H), 7.51 (BB', 2H), 7.31 (AA', 2H), 7.09 (AA', 4H), 6.91 (BB', 4H), 6.79 (BB', 2H), 3.77 (s, 6H), 1.26 (s, 9H). $\{^1\text{H}\}^{13}\text{C-NMR}$ (150 MHz, acetone- d_6 , 295 K): δ/ppm = 157.9 (quart.), 150.4 (quart.), 140.6 (quart.), 138.2 (tert.), 134.8 (quart.), 133.3 (tert.), 132.58 (tert.), 132.55 (tert.), 132.52 (tert.), 132.4 (tert.), 132.2 (tert.), 128.5 (tert.), 125.1 (quart.), 124.1 (quart.), 124.0 (quart.), 123.9 (quart.), 122.9 (quart.), 118.9 (tert.), 115.8 (tert.), 113.6 (quart.), 93.3 (quart.), 91.8 (quart.), 91.5 (quart.), 91.3 (quart.), 91.1 (quart.), 88.3 (quart.), 55.7 (prim.), 46.8 (quart.), 31.2 (prim.). MS (ESI pos, high resolution): calc. for $\text{C}_{48}\text{H}_{39}\text{NO}_2\text{S}^+$: m/z = 693.26960, exp.: m/z = 693.26999 (Δ = 0.56 ppm).

Synthesis of 4-bromothiophenol protected gold nanoparticle Au-Pre3



Following **GP5**: Tetrachloroauric acid trihydrate (159 mg, 404 μmol) and 4-bromobenzenethiol (Alfa Aesar) (299 mg, 1.21 mmol) were solved in dry thf (16 mL). This solution and LiBH_4 (16 mL, 1.61 mmol, 0.1 M in thf) were both added to thf (8 mL). The yield was 107 mg of a black solid.

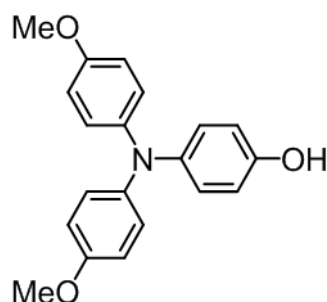
Synthesis of Au-Tara3



Under a nitrogen atmosphere a solution of **Au-Pre3** (107 mg), alkyne **3** (168 mg, 317 μmol), $\text{P}(t\text{-Bu})_3$ (63 μL , 63.0 μmol , 1.0 M in toluene), di-*iso*-propylamine (67 μL , 476 μmol), $\text{Pd}(\text{PhCN})_2\text{Cl}_2$ (12 mg, 32 μmol) and CuI (3.0 mg, 16 μmol) in dry thf (7 mL) were degassed and stirred for 12 h at room temperature. The working-up procedure was the same as reported for **Au-Tara2** and 24 mg of a black solid were obtained. $^1\text{H-NMR}$ (400 MHz, dichloromethane- d_2 , 298 K): δ/ppm = 8.50-6.10 (20H), 3.85-3.55 (6H)*. STEM: radius 1.04 (± 0.20) nm.

*Proton signal next to the gold nanoparticles are missing due to spin relaxation phenomena, see ref. 64.

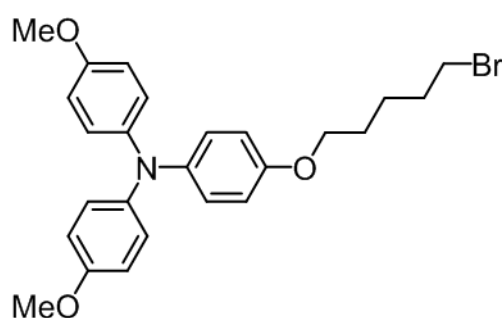
Synthesis of 4-(*N,N*-di-*p*-anisylamino)phenol **10** (CAS 221171-37-5)



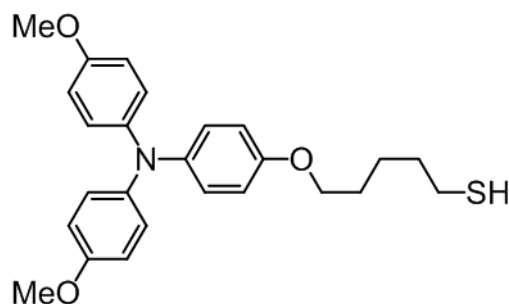
Under a nitrogen atmosphere triarylamine **9** (1.03 g, 2.68 mmol) was dissolved in dry thf (14 mL) and was cooled to $-78\text{ }^\circ\text{C}$. After the dropwise addition of *n*-butyllithium (1.34 mL, 3.22 mmol, 2.4 M in toluene) the mixture was stirred for 10 min. Then dry nitrobenzene (0.61 mL, 5.90 mmol) was added. The mixture was allowed to warm up to room temperature and was stirred for 4 h. Water (2 mL) was added and the organic solvent was removed *in vacuo*.

The residue was dissolved in dichloromethane (20 mL) and was washed with water (3 x 30 mL). The organic phase was dried with MgSO₄ and the solvent was removed *in vacuo*. The crude product was purified by flash chromatography on silica gel (petroleum ether / dichloromethane 2:1 → 1:1 → petroleum ether / ethyl acetate 4:1) to obtain 550 mg (1.71 mmol, 64%) of a brown solid. ¹H-NMR (400 MHz, acetone-d₆, 295 K): δ/ppm = 8.07 (s, 1H), 6.90 (AA', 4H), 6.86 (AA', 2H), 6.82 (BB', 4H), 6.76 (BB', 2H), 3.75 (s, 6H).

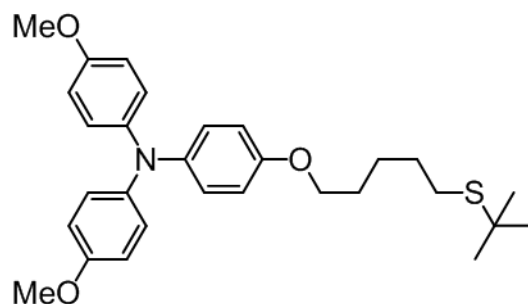
Synthesis of 4-((5-bromopentyl)oxy)-*N,N*-bis(4-methoxyphenyl)aniline **11**



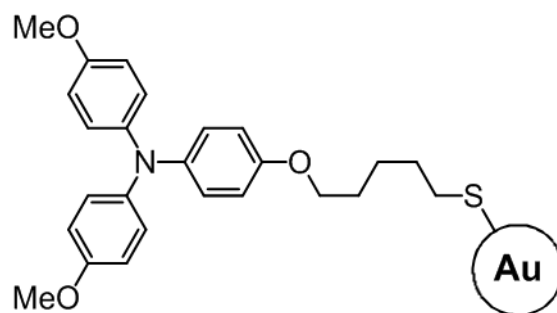
Under a nitrogen atmosphere the triarylamine **10** (200 mg, 622 μmol) was dissolved in dry thf (10 mL) and KO^t-Bu (83.8 mg, 747 μmol) was added. The suspension was stirred for 15 min and 1,5-dibromopentane (430 μl, 3.14 mmol) was added slowly. The mixture was heated for 3 h to reflux. Water (5 mL) and dichloromethane (20 mL) were added. The organic phase was washed with water (3 x 30 mL) and dried with MgSO₄. The solvent was removed *in vacuo*. and the crude product was purified by flash chromatography on silica gel (petroleum ether / dichloromethane 1:1) to obtain 206 mg (438 μmol, 70%) of a colorless oil. ¹H-NMR (400 MHz, acetone-d₆, 295 K): δ/ppm = 6.94-6.88 (-, 6H), 6.87-6.82 (-, 6H), 3.98 (t, ³J_{HH} = 6.3 Hz, 2H), 3.76 (s, 6H), 3.54 (t, ³J_{HH} = 6.78 Hz, 2H), 1.99-1.90 (m, 2H), 1.85-1.76 (m, 2H), 1.68-1.59 (m, 2H). {¹H}¹³C-NMR (100 MHz, acetone-d₆, 295 K): δ/ppm = 156.3 (quart.), 155.7 (quart.), 143.05 (quart.), 143.02 (quart.), 125.78 (tert.), 125.74 (tert.), 116.2 (tert.), 115.6 (tert.), 68.8 (sec.), 55.9 (prim.), 34.8 (sec.), 33.5 (sec.), 29.4 (sec.), 25.7 (sec.). MS (ESI pos, high resolution): *m/z* calc. for C₂₅H₂₈BrNO₃⁺: *m/z* = 469.12471, exp.: *m/z* = 469.12472 (Δ = 0.02 ppm).

Synthesis of 5-(4-(bis(4-methoxyphenyl)amino)phenoxy)pentane-1-thiol 5

Under a nitrogen atmosphere compound **11** (285 mg, 606 μmol) was dissolved in dry thf (12 mL) and cooled to $-15\text{ }^{\circ}\text{C}$. A solution of hexamethyldisilathiane (130 mg, 727 μmol) and TBAF (220 mg, 698 μmol) in dry thf (3 mL) was slowly added and the mixture was stirred for 12 h at room temperature. The solvent was removed *in vacuo* and the residue was dissolved in dichloromethane (20 mL). The organic phase was washed with water (3 x 20 mL) and dried with MgSO_4 . The solvent was removed *in vacuo* and the crude product was purified by flash chromatography on silica gel (petroleum ether / ethyl acetate 8:1) to obtain 110 mg (260 μmol , 43%) of a colorless oil. $^1\text{H-NMR}$ (400 MHz, acetone- d_6 , 295 K): δ/ppm = 6.95-6.88 (-, 6H), 6.86-6.79 (-, 6H), 3.95 (t, $^3J_{\text{HH}}$ = 6.32 Hz, 2H), 3.75 (s, 6H), 3.64 (t, $^3J_{\text{HH}}$ = 6.65 Hz, 1H), 2.59-2.50 (m, 2H), 1.81-1.63 (-, 4H), 1.62-1.52 (m, 2H). $\{^1\text{H}\}^{13}\text{C-NMR}$ (100 MHz, acetone- d_6 , 295 K): δ/ppm = 156.1 (quart.), 155.6 (quart.), 142.9 (quart.), 142.8 (quart.), 125.6 (2 x tert.), 116.0 (tert.), 115.4 (tert.), 68.6 (sec.), 55.7 (prim.), 34.6 (sec.), 29.6 (sec.), 25.6 (sec.), 24.8 (sec.). MS (ESI pos, high resolution): calc. for $\text{C}_{25}\text{H}_{29}\text{NO}_3\text{S}^{*+}$: m/z = 423.18672, exp.: m/z = 423.18627 (Δ = 1.06 ppm).

Synthesis of 4-((5-(*t*-butylthio)pentyl)oxy)-*N,N*-bis(4-methoxyphenyl)aniline Ref4

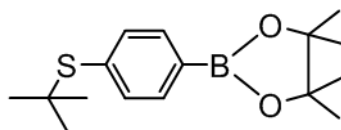
Under a nitrogen atmosphere *t*-butylthiol (24 μL , 213 μmol) and NaH (9.6 mg, 400 μmol) were dissolved in dry thf (7 mL) and the suspension was stirred for 15 min at room temperature. A solution of triarylamine **11** (100 mg, 213 μmol) in thf (3 mL) was added and the mixture was stirred for 3 h at room temperature. After the organic solvent was removed *in vacuo*, the residue was dissolved in dichloromethane (20 mL) and washed with water (2 x 20 mL). The organic phase was dried with MgSO_4 and the crude product was purified by flash chromatography on silica gel (petroleum ether / dichloromethane 1:1) to obtain 102 mg (177 μmol , 83%) of a colorless oil. $^1\text{H-NMR}$ (400 MHz, acetone- d_6 , 295 K): δ/ppm = 6.95-6.88 (-, 6H), 6.87-6.81 (-, 6H), 3.96 (t, $^3J_{\text{HH}}$ = 5.6 Hz, 2H), 3.76 (s, 6H), 2.58 (t, $^3J_{\text{HH}}$ = 7.1 Hz, 2H), 1.84-1.73 (m, 2H), 1.68-1.53 (-, 4H), 1.30 (s, 9H). $\{^1\text{H}\}^{13}\text{C-NMR}$ (100 MHz, dichloromethane- d_2 , 295 K): δ/ppm = 156.2 (quart.), 155.6 (quart.), 142.9 (quart.), 142.8 (quart.), 125.6 (2 x tert.), 116.1 (tert.), 115.4 (tert.), 68.7 (sec.), 55.7 (prim.), 42.0 (quart.), 31.3 (prim.), 30.5 (sec.), 29.8 (sec.), 28.7 (sec.), 26.5 (sec.). MS (ESI pos, high resolution): calc. for $\text{C}_{29}\text{H}_{37}\text{NO}_3\text{S}^+$: m/z = 479.24887, exp.: m/z = 479.24885 (Δ = 0.04 ppm).

Synthesis of Au-Tara4

Under a nitrogen atmosphere tetrachloroauric acid trihydrate (71 mg, 366 μmol) and compound **1** (138 mg, 731 μmol) were dissolved in dry thf (14.4 mL). A solution of LiBH_4 (14.6 mL, 0.1 M in thf, 1.46 mmol) was added (within 3.5 min) and the black solution was stirred for 4 min. The solution was concentrated to 2 mL with a rotary evaporator (the temperature of the water bath should not exceed 35 $^\circ\text{C}$). Dichloromethane was added and the suspension was filtered through a glass frit (pore 3). The residue was extracted with dichloromethane (20 mL). The combined organic phases were washed with water. The organic phase was concentrated to 4 mL and *n*-hexane (30 mL) was added. This mixture was centrifuged and the black residue was washed with *n*-hexane to yield 30 mg of a black solid. $^1\text{H-NMR}$ (400 MHz, dichloromethane- d_2 , 298 K): δ/ppm = 6.94-6.40 (12H), 3.98-3.69 (2H), 3.67-3.51 (6H), 2.00-1.38 (5H)*. TGA: organic weight fraction 40%. STEM: radius 0.80 (± 0.23) nm.

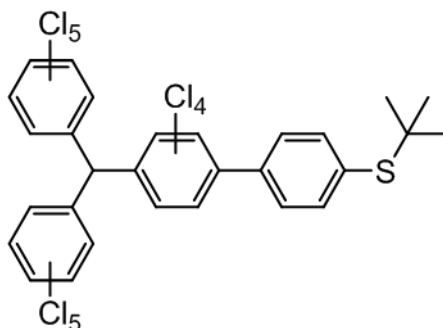
*Proton signal next to the gold nanoparticles are missing due to spin relaxation phenomena, see ref. 64.

Synthesis of 2-(4-(*t*-butylthio)phenyl)-4,4,5,5-tetramethyl-1,3,2-dioxaborolane **13 (CAS 909255-87-4)**



To a solution of 1-bromo-4-(*t*-butylthio)benzene (**12**) (800 mg, 3.26 mmol) in anhydrous thf (10 mL) was added *n*-butyllithium (2.2 mL, 1.6 M in thf, 3.59 mmol) dropwise over 3 min at -78 °C under nitrogen. After 10 min tri-*iso*-propyl borate (1.23 g, 6.53 mmol) was added and the reaction was stirred for 20 min at -78 °C. The reaction was allowed to warm to room temperature within 1 h, quenched with HCl (aq) (4 M, 10 mL) and the resulting mixture was extracted with dichloromethane (3 x 20 mL). The combined extracts were concentrated *in vacuo* and the residue was dissolved in ether (15 mL). Pinacol (1.35 g, 11.4 mmol) was added, and the solution was refluxed under rigorous stirring. After 12 h the solvent was removed and the crude product was purified by flash column chromatography on silica gel (petroleum ether / dichloromethane 5:2) to obtain 768 mg (2.63 mmol, 92%) of a colorless solid. ¹H-NMR (400 MHz, acetone-*d*₆, 295 K): δ /ppm = 7.76 (AA', 2H), 7.53 (BB', 2H), 1.35 (s, 12H), 1.28 (s, 9H).

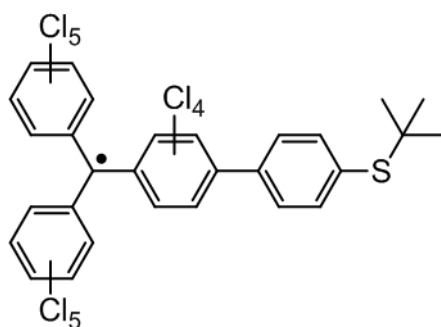
Synthesis of the perchlorinated triarylmethane derivative **15**



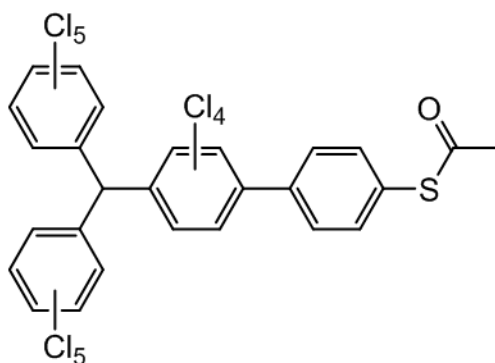
Under a nitrogen atmosphere, compound **14**¹⁶² (550 mg, 680 μ mol) and the pinacol borane **13** (200 mg, 684 μ mol) were dissolved in dry toluene (12 mL). Tetrakis(triphenylphosphine)palladium (23.7 mg, 1.92 μ mol) and sodium carbonate (1.92 mL,

1.00 M in H₂O, 1.92 mmol) were added and then stirred for 24 h at 120 °C. The solvent was removed *in vacuo*, and the residue was dissolved in dichloromethane and was washed with water. The crude product was purified by flash chromatography on silica gel (petroleum ether) to obtain 310 mg (348 μmol, 51%) of a yellow solid. ¹H-NMR (600 MHz, dichloromethane-d₂, 295 K): δ/ppm = 7.65 (AA', 2H), 7.22 (BB', 2H), 7.08 (s, 1H), 1.33 (s, 9H). {¹H} ¹³C-NMR (150 MHz, dichloromethane-d₂, 295 K): δ/ppm = 141.6 (quart.), 138.1 (quart.), 137.7 (2 x tert.), 137.4 (quart.), 136.9 (2 x quart.), 135.5 (quart.), 135.4 (2 x quart.), 135.0 (quart.), 134.4 (quart.), 134.2 (quart.), 134.07 (quart.), 134.04 (quart.), 133.94 (quart.), 133.91 (quart.), 133.84 (quart.), 133.82 (quart.), 133.2 (quart.), 132.81 (quart.), 132.80 (quart.) 129.4 (tert.), 129.2 (tert.), 57.0 (tert.), 46.4 (quart.), 31.1 (prim.). MS (ESI neg, high resolution): calc. for C₂₉H₁₃Cl₁₄S⁻: *m/z* = 888.62975, exp.: *m/z* = 888.63041 (Δ = 0.74 ppm).

Synthesis of the perchlorinated triarylmethyl radical Ref5

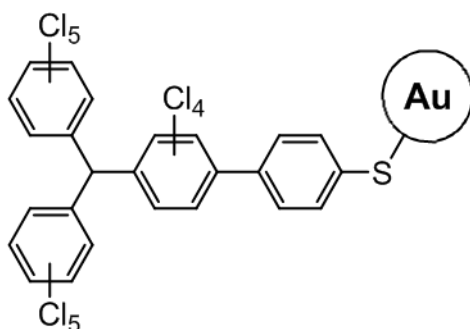


Under a nitrogen atmosphere **15** (120 mg, 135 μmol) was dissolved in dry DMSO (10 mL). Potassium *t*-butoxide (30.2 mg, 269 μmol) was added and the reaction mixture was stirred for 30 min at room temperature in the dark. *p*-chloranil (33.1 mg, 135 μmol) was added, and the mixture was stirred for 60 h in the dark. Dichloromethane (30 mL) was added, and the resulting mixture was washed with water (3 x 30 mL). After removal of the organic solvent under reduced pressure, the residue was purified by flash column chromatography on silica gel (petroleum ether / dichloromethane 2:1). The crude product was washed with aqueous sodium hydroxide (6 x 20 mL, 0.13 M). The organic solvent was removed *in vacuo* to obtain 100 mg (112 μmol, 83%) of a red solid. MS (APCI neg, high resolution): calc. for C₂₉H₁₃Cl₁₄S⁻: *m/z* = 888.62975, exp.: *m/z* = 888.63152 (Δ = 1.99 ppm).

Synthesis of the perchlorinated triarylmethane derivative **16**

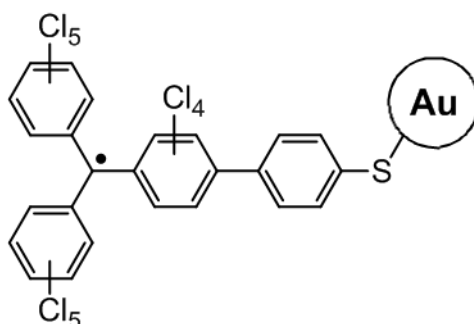
Following **GP6**, BBr_3 and acetyl chloride were added to a solution of **15** (300 mg, 337 μmol) in dry dichloromethane (6 mL). The reaction mixture was quenched with water (20 mL), and extracted with dichloromethane (3x 30 mL). The organic solvent was removed *in vacuo*. The crude product was precipitated twice by addition of a concentrated dichloromethane solution to *n*-hexane. Crystallization from *n*-hexane at $-32\text{ }^\circ\text{C}$ yielded 255 mg (291 μmol , 86%) of a brownish solid. $^1\text{H-NMR}$ (600 MHz, dichloromethane- d_2 , 295 K): $\delta/\text{ppm} = 7.56$ (AA', 2H), 7.31 (BB', 2H), 7.08 (s, 1H), 2.45 (s, 3H). $\{^1\text{H}\}^{13}\text{C-NMR}$ (150 MHz, dichloromethane- d_2 , 295 K): $\delta/\text{ppm} = 193.6$ (quart.), 141.2 (quart.), 138.6 (quart.), 137.6 (quart.), 136.831 (quart.), 136.827 (quart.), 135.5 (quart.), 135.4 (quart.), 135.1 (quart.), 134.82 (tert.), 134.81 (tert.), 134.4 (2 x quart.), 134.2 (quart.), 134.1 (quart.), 134.0 (quart.), 133.9 (quart.), 133.85 (quart.), 133.84 (quart.), 133.2 (quart.), 132.82 (quart.), 133.81 (quart.), 130.1 (tert.), 129.9 (tert.), 129.4 (quart.), 57.0 (tert.), 30.5 (prim.). MS (APCI neg, high resolution): calc. for $\text{C}_{27}\text{H}_7\text{Cl}_{14}\text{OS}^-$: $m/z = 868.58625$, exp.: $m/z = 868.58431$ ($\Delta = 2.23$ ppm).

Synthesis of Au-PCTM



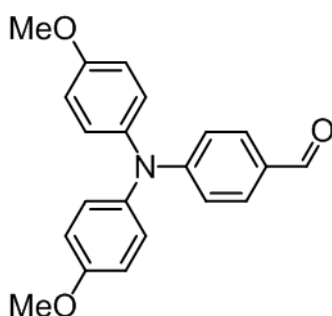
Lithium boron hydride (18.3 mg, 838 μmol) was added to dry thf (6 mL) under a nitrogen atmosphere. The suspension was added to the thioester **16** (134 mg, 152 μmol) and warmed to 30 °C to allow complete dissolution. Two-thirds of the solution (4 mL) were added dropwise to a solution of gold(III) chloride trihydrate (60.0 mg, 152 μmol) in thf (7.6 mL) within 90 sec at room temperature. After stirring for a 60 sec the remaining solution of lithium boron hydride and the thioester **6** (2 mL) was added within 30 sec. The dark colored suspension was stirred for 5 min at 0 °C and then for 11 min at room temperature. Toluene was added (1 mL) and the mixture was concentrated *in vacuo* to 1 mL. The remaining solution was transferred into *n*-hexane (20 mL) and stored at -32 °C overnight. The black precipitate was filtered off and washed with *n*-hexane (6 x 10 mL) to yield 75 mg of a black solid. $^1\text{H-NMR}$ (400 MHz, dichloromethane- d_2 , 295 K): $\delta/\text{ppm} = 9.07 - 7.37$ (bm, 2H), 7.25 - 5.96 (bm, 3H), 7.07 (s, 1H). IR (ATR): $\nu/\text{cm}^{-1} = 2930$ (w), 1590 (w), 1530 (w), 1490 (w), 1360 (s), 1330 (s), 1295 (s), 1020 (s), 805 (s), 730 (s), 580 (s).

Synthesis of Au-Rad



The nanoparticle **Au-PCTM** (40.0 mg) was dissolved in dry DMSO (5 mL) under nitrogen and potassium *t*-butoxide (4.44 mg, 39.6 μmol) was added. After stirring for 2 h in the dark *p*-chloranil (19.5 mg, 79.2 μmol) was added and the mixture was stirred for 1.5 h at room temperature in the dark. Dichloromethane (20 mL) was added and the resulting mixture was washed with aqueous sodium hydroxide (4 x 20 mL, 0.13 M). The organic layer was separated and the solvent was removed under reduced pressure to obtain 30 mg of a brown solid. IR (ATR): ν/cm^{-1} = 2930 (w), 1490 (w), 1360 (s), 1330 (s), 1295 (s), 1020 (s), 850 (s), 805 (s), 580 (s).

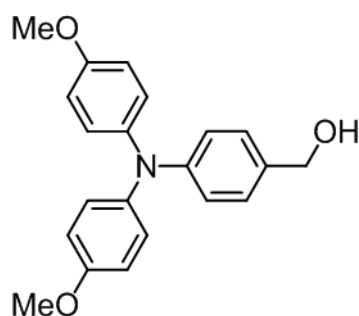
Synthesis of 4-(bis(4-methoxyphenyl)amino)benzaldehyde **18** (CAS 89115-20-8)



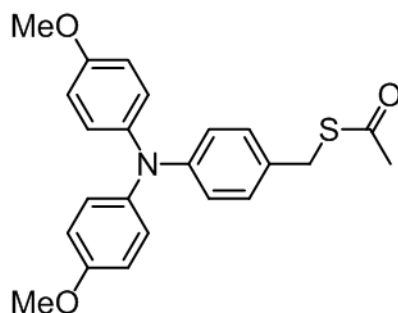
The triarylamine derivative **14** (600 mg, 1.56 mmol) was dissolved in thf and *n*-butyllithium (1.07 mL, 1.72 mmol, 1.6 M in toluene) was added at $-78\text{ }^{\circ}\text{C}$. After 10 min *N,N*-dimethylformamide (240 μL , 3.12 mmol) was added. The reaction mixture was stirred for 10 min at $-78\text{ }^{\circ}\text{C}$ and then for 18 h at room temperature. The solvent was removed *in vacuo* and the crude product was purified by flash chromatography on silica gel (petroleum ether / dichloromethane 8:1 \rightarrow dichloromethane) to obtain an orange solid (370 mg, 1.11 mmol,

71%). $^1\text{H-NMR}$ (400 MHz, chloroform- d_1 , 295 K): δ/ppm = 9.76 (s, 1H), 7.62 (AA', 2H), 7.13 (AA', 4H), 6.89 (BB', 4H), 6.85 (BB', 2H), 3.82 (s, 6H).

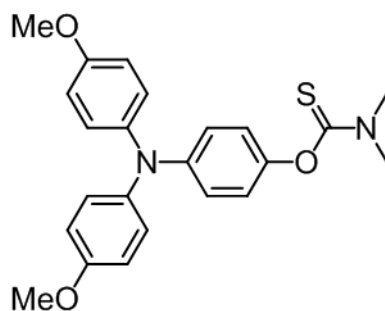
Synthesis of (4-(bis(4-methoxyphenyl)amino)phenyl)methanol **19** (CAS 392662-43-0)



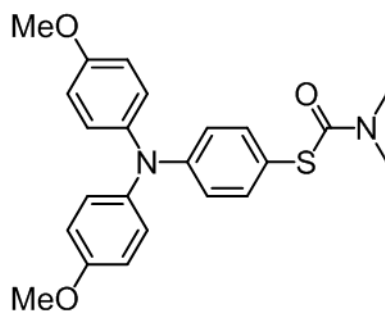
Following lit.²⁷² compound **18** (270 mg, 810 μmol) was converted to **19** with NaBH_4 (61.3 mg, 1.62 mmol) in EtOH (10 mL) at room temperature (reaction time 4 h). The solvent was removed *in vacuo* and the residue was dissolved in dichloromethane (20 mL). The organic phase was washed with water (3x 20 mL) and dried with MgSO_4 . The solvent was removed *in vacuo* to yield (246 mg, 734 μmol , 91%) of a yellow solid. $^1\text{H-NMR}$ (400 MHz, chloroform- d_1 , 295 K): δ/ppm = 7.18 (AA', 2H), 7.00 (BB', 4H), 6.90-6.82 (-, 6H), 5.63 (s, 1H), 4.52 (s, 2H), 3.78 (s, 6H).

Synthesis of S-4-(bis(4-methoxyphenyl)amino)benzyl ethanethioate 20

Di-*iso*-propyl azodicarboxylate (573 mg, 2.83 mmol) and PPh₃ (743 mg, 2.83 mmol) were dissolved in thf (6 mL) and stirred for 20 min at 0 °C. Thioacetic acid (216 mg, 2.83 mmol) and compound **19** (190 mg, 566 μmol) were separately dissolved in thf (6 mL) and slowly added to the di-*iso*-propyl azodicarboxylate / PPh₃ solution. The mixture was stirred for 15 min at 0 °C and then for 14 h at room temperature. The solvent was removed *in vacuo*. The crude product was purified by flash chromatography on silica gel (petroleum ether / dichloromethane 5:4 → 1:1) to obtain a yellow solid (120 mg, 305 μmol, 54%). ¹H-NMR (400 MHz, dichloromethane-d₂, 295 K): δ/ppm = 7.06 (AA', 2H), 7.01 (AA', 4H), 6.83-6.79 (-, 6H), 4.03 (s, 2H), 3.77 (s, 6H), 2.32 (s, 3H). {¹H}¹³C-NMR (100 MHz, dichloromethane-d₂, 295 K): δ/ppm = 195.5 (quart.), 156.4 (quart.), 148.4 (quart.), 141.2 (quart.), 129.73 (tert.), 129.67 (quart.), 126.9 (tert.), 120.7 (tert.), 115.0 (tert.), 55.8 (prim.), 33.4 (sek.), 30.6 (prim.). MS (EI pos, high resolution): calc. for C₂₃H₂₃NO₃S⁺: *m/z* = 393.13932, exp: *m/z* = 393.13924 (Δ = 0.20 ppm).

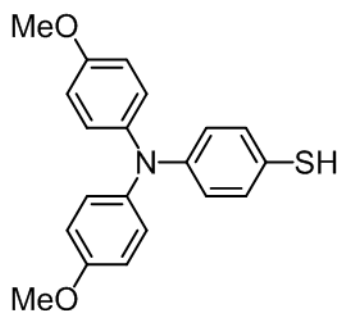
Synthesis of *O*-(4-(bis(4-methoxyphenyl)amino)phenyl) dimethylcarbamothioate 21

The triarylamine **10** (530 mg, 1.65 mmol) was dissolved in dimethylformamide (8 mL) and NaH (79.2 mg, 3.30 mmol) was added. The mixture was cooled to -13 °C and a dimethylthiocarbamoyl chloride-solution (2.0 mL, 2.47 mmol, 1.2 M in *N,N*-dimethylformamide) was added drop wise. The mixture was stirred for 15 min at 0 °C and then for 2 d at 80 °C. Water was added and a yellowish precipitate was isolated by centrifugation. The solid was dissolved in dichloromethane and the organic phase was washed with water and dried with MgSO₄. The solvent was removed *in vacuo* and the crude product was purified by flash chromatography on silica gel (petroleum ether / ethyl acetate 6.5:1 → 6:1) to obtain a yellow oil (250 mg, 612 μmol, 37%). ¹H-NMR (400 MHz, dichloromethane-d₂, 295 K): δ/ppm = 7.05 (AA', 4H), 6.90-6.81 (-, 8H), 3.78 (s, 6H), 3.41 (s, 3H), 3.29 (s, 3H). {¹H}¹³C-NMR (100 MHz, dichloromethane-d₂, 295 K): δ/ppm = 188.4 (quart.), 156.4 (quart.), 148.1 (quart.), 146.9 (quart.), 141.4 (quart.), 126.9 (tert.), 123.4 (tert.), 120.9 (tert.), 115.1 (tert.), 55.8 (prim.), 43.4 (prim.), 38.8 (prim.). MS (ESI pos, high resolution): calc. for C₂₃H₂₄N₂O₃S⁺: *m/z* = 408.15021, exp.: *m/z* = 408.15020 (Δ = 0.02 ppm).

Synthesis of *S*-(4-(bis(4-methoxyphenyl)amino)phenyl) dimethylcarbamothioate **22**

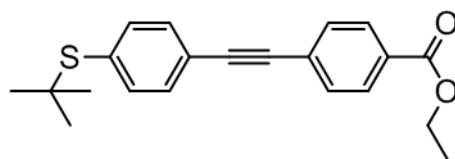
Compound **21** (140 mg, 343 μmol) was dissolved in toluene and $\text{P}(t\text{-Bu})_3$ (79 μL , 78.5 μmol , 1.0 M in toluene) and $\text{Pd}_2(\text{dba})_3 \cdot \text{CHCl}_3$ (36 mg, 34 μmol) were added. The mixture was purged with N_2 for 5 min and stirred at 120 $^\circ\text{C}$ for 2 d. Because compound **21** was not complete converted into the product $\text{Pd}_2(\text{dba})_3 \cdot \text{CHCl}_3$ (20 mg, 19.3 μmol) was added and the mixture was stirred at 120 $^\circ\text{C}$ for 1 d. The solvent was removed *in vacuo* and the residue was redissolved in dichloromethane. The organic phase was washed with water and then dried with MgSO_4 . The solvent was removed *in vacuo* and the crude product was purified by chromatography on alumina (petroleum ether / ethyl acetate 8:1) to obtain a yellow oil (67 mg, 160 μmol , 47%). $^1\text{H-NMR}$ (400 MHz, acetone- d_6 , 295 K): δ/ppm = 7.20 (AA', 2H), 7.10 (AA', 4H), 6.93 (BB', 4H), 6.76 (BB', 2H), 3.80 (s, 6H), 3.28-2.85 (-, 6H). $\{^1\text{H}\}^{13}\text{C-NMR}$ (100 MHz, dichloromethane- d_2 , 295 K): δ/ppm = 167.1 (quart.), 157.9 (quart.), 150.8 (quart.), 141.0 (quart.), 137.6 (tert.), 128.5 (tert.), 119.5 (tert.), 119.0 (quart.), 115.9 (tert.), 55.9 (prim.), 36.9 (prim.). MS (ESI pos, high resolution): calc. for $\text{C}_{23}\text{H}_{24}\text{N}_2\text{O}_3\text{S}^{*+}$: m/z = 408.15021, exp.: m/z = 408.15017 (Δ = 0.10 ppm).

Synthesis of 4-(bis(4-methoxyphenyl)amino)benzenethiol **23**



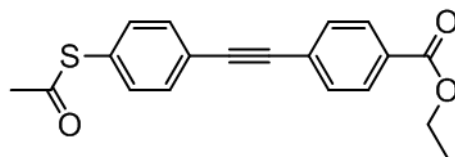
Compound **22** (20 mg, 49 μmol) and NaOH (6 mg, 150 μmol) in MeOH (4 mL) were stirred at 80 °C for 6 h. 1 M hydro chloride (1 mL) and dichloromethane (10 mL) were added. The organic phase was washed with water (3 x 20 mL) and then dried with MgSO_4 . The solvent was removed *in vacuo* and the crude product was purified by chromatography on alumina (petroleum ether / dichloromethane 3:1) to obtain a yellow oil (8 mg, 24 μmol , 49%). $^1\text{H-NMR}$ (600 MHz, acetone- d_6 , 295 K): δ/ppm = 7.30 (AA', 2H), 7.08 (AA', 4H), 6.92 (BB', 4H), 6.75 (BB', 2H), 3.79 (s, 6H). $\{^1\text{H}\}^{13}\text{C-NMR}$ (150 MHz, acetone- d_6 , 295 K): δ/ppm = 157.7 (quart.), 150.4 (quart.), 140.8 (quart.), 133.1 (tert.), 128.4 (tert.), 127.2 (quart.), 119.9 (tert.), 115.7 (tert.), 55.7 (prim.). MS (ESI pos, high resolution): calc. for $\text{C}_{20}\text{H}_{18}\text{NO}_2\text{S}^{*+}$: m/z = 336.10528, exp.: m/z = 336.10522 (Δ = 0.18 ppm).

Synthesis of ethyl 4-((4-(*t*-butylthio)phenyl)ethynyl)benzoate **25** (CAS 149398-19-6)



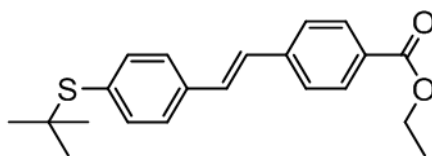
Following **GP2** compound **2** (180 mg, 718 μmol) and **24** (125 mg, 718 μmol) in 1,4-dioxane (8 mL) were transformed into **25** (reaction time 12 h). Flash chromatography on silica gel (petroleum ether / dichloromethane 2:1 \rightarrow 1:1 \rightarrow 1:2) yielded 150 mg (443 μmol , 62%) of a brownish solid. $^1\text{H-NMR}$ (250 MHz, chloroform- d_1 , 295 K): δ/ppm = 8.03 (AA', 2H), 7.58 (BB', 2H), 7.51 (-, 4H), 4.39 (q, 2H, $^3J_{\text{HH}}$ = 7.10 Hz), 1.41 (t, 3H, $^3J_{\text{HH}}$ = 7.17 Hz), 1.30 (s, 9H).

Synthesis of ethyl 4-((4-(acetylthio)phenyl)ethynyl)benzoate SEMA1



According to **GP6** a solution of **25** (80 mg, 240 μmol) in dry dichloromethane (6 mL) was converted into **SEMA1** (50 mg, 150 μmol , 63%) to obtain a brownish solid. $^1\text{H-NMR}$ (400 MHz, chloroform- d_1 , 295 K): δ/ppm = 8.03 (AA', 2H), 7.60-7.55 (-, 4H), 7.42 (BB', 2H), 4.39 (q, 2H, $^3J_{\text{HH}}$ = 7.17 Hz), 2.44 (s, 3H), 1.41 (t, 3H, $^3J_{\text{HH}}$ = 7.15 Hz). $\{^1\text{H}\}^{13}\text{C-NMR}$ (150 MHz, chloroform- d_1 , 295 K): δ/ppm = 193.4 (quart.), 166.2 (quart.), 134.4 (tert.), 132.4 (tert.), 131.7 (tert.), 130.3 (quart.), 129.7 (tert.), 128.8 (quart.), 127.6 (quart.), 124.1 (quart.), 91.5 (quart.), 90.4 (quart.), 61.3 (sec.), 30.5 (prim.), 14.5 (prim.). MS (EI pos, high resolution): calc. for $\text{C}_{19}\text{H}_{16}\text{O}_3\text{S}^+$: m/z = 324.08147, exp.: m/z = 324.08145 (Δ = 0.06 ppm).

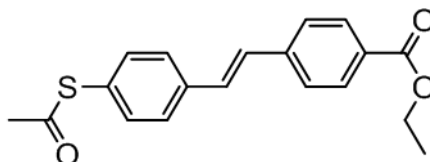
Synthesis of (*E*)-ethyl 4-(4-(*t*-butylthio)styryl)benzoate **28**



Under nitrogen atmosphere NaH (65 mg, 2.7 mmol) was added to a solution of the alkyl phosphonate **27** (440 mg, 1.47 mmol) in dry thf (5 mL) at room temperature. A solution of the aldehyde **26** (280 mg, 1.44 mmol) in thf (5 mL) was added and the mixture was stirred for 10 h. After removal of solvent *in vacuo* the residue was dissolved in dichloromethane (15 mL) and the organic phase was washed with water (3 x 20 mL). Flash chromatography on silica gel (petroleum ether / dichloromethane 5:4 \rightarrow 1:1 \rightarrow 2.5:3 \rightarrow dichloromethane) yielded 190 mg (558 μmol , 39%) of a yellow solid. $^1\text{H-NMR}$ (400 MHz, chloroform- d_1 , 295 K): δ/ppm = 8.04 (AA', 2H), 7.60-7.45 (-, 6H), 7.21 (d, 1H, $^3J_{\text{HH}}$ = 16.3 Hz), 7.15 (d, 1H, $^3J_{\text{HH}}$ = 16.4 Hz), 4.39 (q, 2H, $^3J_{\text{HH}}$ = 7.1 Hz), 1.41 (t, 3H, $^3J_{\text{HH}}$ = 7.1 Hz), 1.31 (s, 9H). $\{^1\text{H}\}^{13}\text{C-NMR}$ (100 MHz, Chloroform- d_1 , 295 K): δ/ppm = 166.5 (quart.), 141.6 (quart.), 137.9 (tert.), 137.3 (quart.), 133.0 (quart.), 130.5 (tert.), 130.2 (tert.), 129.7 (quart.), 128.7 (tert.), 126.8 (tert.),

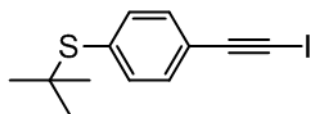
126.5 (tert.), 61.1 (sec.), 46.5 (quart.), 31.1 (prim.), 14.5 (prim.). MS (EI pos, high resolution): calc. for $C_{21}H_{24}O_2S^+$: $m/z = 340.14915$, exp.: $m/z = 340.14931$ ($\Delta = 0.47$ ppm).

Synthesis of (*E*)-ethyl 4-(4-(acetylthio)styryl)benzoate SEMA2



According to **GP6**, compound **28** (190 mg, 558 μ mol) was converted into **SEMA2** (80.0 mg, 245 μ mol, 44%) to obtain a yellow solid. 1H -NMR (400 MHz, chloroform- d_1 , 295 K): $\delta/ppm = 8.04$ (AA', 2H), 7.58-7.55 (-, 4H), 7.42 (BB', 2H), 7.23-7.14 (-, 2H), 4.39 (q, 2H, $^3J_{HH} = 7.1$ Hz), 2.44 (s, 3H), 1.41 (t, 3H, $^3J_{HH} = 7.1$ Hz). $\{^1H\}^{13}C$ -NMR (100 MHz, chloroform- d_1 , 295 K): $\delta/ppm = 194.1$ (quart.), 166.5 (quart.), 141.4 (quart.), 138.1 (quart.), 134.9 (tert.), 130.22 (tert.), 130.18 (tert.), 129.8 (quart.), 129.3 (tert.), 127.7 (quart.), 127.6 (tert.), 126.6 (tert.), 61.1 (sec.), 30.4 (prim.), 14.5 (prim.). MS (EI pos, high resolution): calc. for $C_{19}H_{18}O_3S^+$: $m/z = 326.09766$, exp.: $m/z = 326.09712$ ($\Delta = 1.7$ ppm).

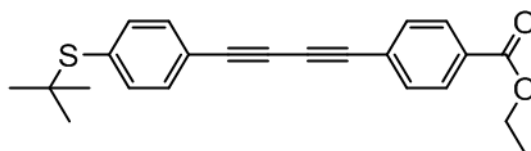
Synthesis of *t*-butyl(4-(iodoethynyl)phenyl)sulfane **30**



In the dark $AgNO_3$ (118 mg, 694 μ mol) and *N*-Iodosuccinimide (286 mg, 1.27 mmol) were added to a solution of the alkyne **29** (220 mg, 1.16 mmol) in acetone (11 mL) at room temperature and stirred for 12 h. The solvent was removed *in vacuo* and the residue dissolved in dichloromethane (10 mL). The organic phase was washed with water (3 x 20 mL) and then dried with $MgSO_4$. After removal of the solvent *in vacuo* the crude product was recrystallized from methanol to obtain 167 mg (528 μ mol, 46%) of a yellow solid. 1H -NMR (400 MHz, acetone- d_6 , 295 K): $\delta/ppm = 7.53$ (AA', 2H), 7.45 (BB', 2H), 1.27 (s, 9H). $\{^1H\}^{13}C$ -NMR (100 MHz, acetone- d_6 , 295 K): $\delta/ppm = 138.1$ (tert.), 135.1 (quart.), 133.2 (tert.), 124.9

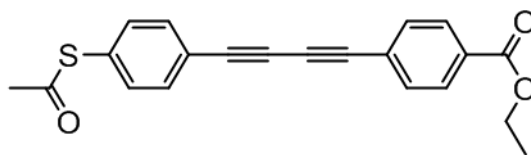
(quart.), 93.9 (quart.), 47.0 (quart.), 31.4 (prim.), 13.4 (quart.). MS (EI pos, high resolution): calc. for $C_{12}H_{13}IS^{+}$: $m/z = 315.97772$, exp.: $m/z = 315.97731$ ($\Delta = 1.30$ ppm).

Synthesis of ethyl 4-((4-(*t*-butylthio)phenyl)buta-1,3-diyne)benzoate **31**



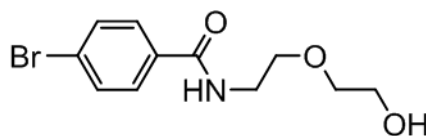
According to lit.,²⁷³ to a stirred solution of the alkyne **24** (92.0 mg, 528 μ mol), CuCl (6.2 mg, 63 μ mol), hydroxylammonium chloride (73.4 mg, 1.06 mmol) and pyrrolidine (11 mL, 1.3 mmol) in dry methanol (8 mL) under nitrogen atmosphere at 0 °C in the dark was added a degassed suspension of the iodoacetylene **30** (167 mg, 528 μ mol) in dry methanol. The mixture was stirred at 0 °C for 10 min and then at room temperature for 12 h. The solvent was removed *in vacuo* and the residue redissolved in dichloromethane (10 mL). The organic phase was washed with water (3 x 20 mL) and the solvent was removed *in vacuo*. The crude product was purified by flash chromatography on silica gel (petroleum ether / dichloromethane 1:1 \rightarrow 3:4) and then recrystallized from acetone to obtain a colorless solid (20.0 mg, 55.2 μ mol, 10%). $^1\text{H-NMR}$ (400 MHz, dichloromethane- d_2 , 295 K): $\delta/\text{ppm} = 8.00$ (AA', 2H), 7.60 (BB', 2H), 7.53-7.49 (-, 4H), 4.36 (q, 2H, $^3J_{\text{HH}} = 7.13$ Hz), 1.38 (t, 3H, $^3J_{\text{HH}} = 7.14$ Hz), 1.29 (s, 9H). $\{^1\text{H}\}^{13}\text{C-NMR}$ (100 MHz, dichloromethane- d_2 , 295 K): $\delta/\text{ppm} = 165.9$ (quart.), 137.5 (tert.), 135.7 (quart.), 132.73 (tert.), 132.70 (tert.), 131.3 (quart.), 129.8 (tert.), 126.3 (quart.), 121.8 (quart.), 82.6 (quart.), 81.4 (quart.), 76.4 (quart.), 74.9 (quart.), 61.6 (sec.), 47.0 (quart.), 31.1 (prim.), 14.4 (prim.).

Synthesis of ethyl 4-((4-(acetylthio)phenyl)buta-1,3-diyne-1-yl)benzoate SEMA3



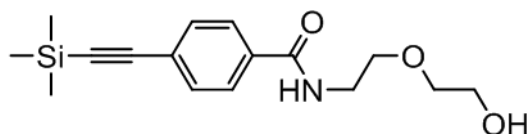
As described in **GP6**, compound **31** (20.0 mg, 55.2 μmol) was converted into **SEMA3** (2.0 mg, 5.7 μmol , 10%) to obtain a yellow solid. $^1\text{H-NMR}$ (400 MHz, dichloromethane- d_2 , 295 K): δ/ppm = 8.01 (AA', 2H), 7.62-7.57 (-, 4H), 7.42 (BB', 2H), 4.36 (q, 2H, $^3J_{\text{HH}}$ = 7.13 Hz), 2.43 (s, 3H), 1.38 (t, 3H, $^3J_{\text{HH}}$ = 7.12 Hz). $\{^1\text{H}\}^{13}\text{C-NMR}$ (100 MHz, dichloromethane- d_2 , 295 K): δ/ppm = 193.2 (quart.), 165.9 (quart.), 134.7 (tert.), 133.3 (tert.), 132.8 (tert.), 131.5 (quart.), 130.5 (quart.), 129.8 (tert.), 126.3 (quart.), 122.8 (quart.), 82.2 (quart.), 81.6 (quart.), 76.3 (quart.), 75.2 (quart.), 61.7 (sec.), 30.6 (prim.), 14.4 (prim.). MS (EI pos, high resolution): calc. for $\text{C}_{21}\text{H}_{16}\text{O}_3\text{S}^+$: m/z = 348.08147, exp.: m/z = 348.08159 (Δ = 0.34 ppm).

Synthesis of 4-bromo-*N*-(2-(2-hydroxyethoxy)ethyl)benzamide **33** (CAS 710330-97-5)



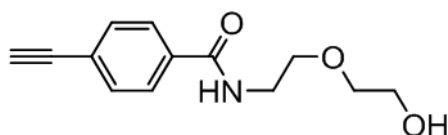
To a solution of 4-bromobenzoyl chloride (**32**) (400 mg, 1.82 mmol) in dry thf (10 mL) under nitrogen atmosphere at 0 °C was added 2-(2-aminoethoxy)ethanol (2.18 mL, 21.9 mmol). After stirring for 12 h at room temperature the solvent was removed *in vacuo*. The crude product was dissolved in dichloromethane and the organic phase washed with water (3 x 20 mL). The solvent was removed *in vacuo* and the crude product was purified by flash chromatography on silica gel (petroleum ether / ethyl acetate 4:1 \rightarrow 1:1 \rightarrow 1:5 \rightarrow ethyl acetate / methanol 5:1) to obtain a colorless solid (500 mg, 1.74 mmol, 96%). $^1\text{H-NMR}$ (400 MHz, chloroform- d_1 , 295 K): δ/ppm = 7.72 (AA', 2H), 7.49 (BB', 2H), 7.06-6.89 (-, 1H), 3.78-3.70 (m, 2H), 3.67-3.54 (-, 6H), 2.81-2.52 (-, 1H).

Synthesis of *N*-(2-(2-hydroxyethoxy)ethyl)-4-((trimethylsilyl)ethynyl)benzamide **15**



According to general procedure **GP4**, compound **34** was synthesized from **33** (250 mg, 868 μmol) and ethynyl-trimethyl-silane (240 μL , 1.70 mmol) with triethylamine (250 μL , 1.80 mmol) (reaction time 5 d). Flash chromatography on silica gel (petroleum ether / ethyl acetate 1:5 \rightarrow petroleum ether / ethyl acetate / methanol 2:4:0.5) yielded 220 mg (720 μmol , 83%) of a colorless oil. $^1\text{H-NMR}$ (400 MHz, chloroform- d_1 , 295 K): δ/ppm = 7.71 (AA', 2H), 7.47 (BB', 2H), 6.96-6.83 (-, 1H), 3.74-3.68 (m, 2H), 3.68-3.57 (-, 6H), 2.17-2.08 (-, 1H), 0.26 (s, 9H). $\{^1\text{H}\}^{13}\text{C-NMR}$ (100 MHz, dichloromethane- d_2 , 295 K): δ/ppm = 166.8 (quart.), 134.7 (quart.), 132.3 (tert.), 127.3 (tert.), 126.6 (quart.), 104.3 (quart.), 97.2 (quart.), 72.7 (sec.), 70.1 (sec.), 62.1 (sec.), 40.2 (sec.), -0.13 (prim.). MS (ESI pos, high resolution): calc. for $\text{C}_{16}\text{H}_{24}\text{NO}_3\text{Si}^+$: m/z = 306.15200, exp.: m/z = 306.15196 (Δ = 0.13 ppm).

Synthesis of 4-ethynyl-*N*-(2-(2-hydroxyethoxy)ethyl)benzamide **35**

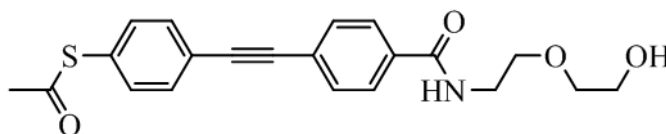


Compound **34** (210 mg, 688 μmol) was dissolved in thf (10 mL) and a solution of tetra-*n*-butylammonium fluoride (TBAF) (830 μL , 830 μmol , 1.0 M in thf) was added. After stirring for 1 h at room temperature the solvent was removed *in vacuo* and the residue was dissolved in dichloromethane. The organic phase was washed with water and dried with MgSO_4 . The solvent was removed *in vacuo* and the crude product was purified by flash chromatography on silica gel (ethyl acetate \rightarrow ethyl acetate / methanol 5:1) to afford 62.0 mg (266 μmol , 39%) of a black oil. $^1\text{H-NMR}$ (400 MHz, chloroform- d_1 , 295 K): δ/ppm = 7.72 (AA', 2H), 7.49 (BB', 2H), 7.06-6.89 (-, 1H), 3.78-3.70 (m, 2H), 3.67-3.54 (-, 6H), 2.81-2.52 (-, 1H). $\{^1\text{H}\}^{13}\text{C-NMR}$ (150 MHz, dichloromethane- d_2 , 295 K): δ/ppm = 167.1 (quart.), 135.1 (quart.), 132.5 (tert.), 127.4 (tert.), 125.4 (quart.), 83.0 (quart.), 79.6 (tert.), 72.7 (sec.), 70.1 (sec.), 61.9 (sec.), 40.3

(sec.)* MS (ESI pos, high resolution): calc. for $C_{13}H_{16}NO_3^+$: $m/z = 234.11247$, exp.: $m/z = 234.11244$ ($\Delta = 0.13$ ppm).

*The multiplicity were determined by varying the optimized H-C coupling constant ($J = 50$ Hz, 145 Hz, 250 Hz) in the DEPT135 experiment.

Synthesis of S-4-((4-(2-(2-hydroxyethoxy)ethylcarbamoyl)phenyl)ethynyl)phenyl ethanethioate SEMA4



As described in **GP4**, **SEMA4** was synthesized from **35** (70.0 mg, 300 μ mol) and **36** (92 mg, 330 μ mol) with di-*iso*-propylethylamine (60 μ L, 360 μ mol) (reaction time 4 d). The solvent was removed *in vacuo* and the crude product was purified by GPC to obtain 14.0 mg (36.5 μ mol, 12%) of a yellow solid. $^1\text{H-NMR}$ (250 MHz, chloroform- d_1 , 295 K): δ /ppm = 7.78 (AA', 2H), 7.61 (BB', 2H), 7.59 (AA', 2H), 7.37 (BB', 2H), 6.74-6.62 (m, 1H), 3.75-3.70 (m, 2H), 3.69-3.62 (-, 4H), 3.61-3.59 (m, 2H), 2.43 (s, 3H), 2.12-2.04 (m, 1H). $\{^1\text{H}\}^{13}\text{C-NMR}$ (150 MHz, dichloromethane- d_2 , 295 K): δ /ppm = 193.6 (quart.), 166.7 (quart.), 134.73 (tert.), 134.71 (quart.), 132.5 (tert.), 132.0 (tert.), 129.2 (quart.), 127.4 (tert.), 126.2 (quart.), 124.4 (quart.), 90.9 (quart.), 90.4 (quart.), 72.6 (sec.), 70.1 (sec.), 62.1 (sec.), 40.2 (sec.), 30.5 (prim.). MS (ESI pos, high resolution): calc. for $C_{21}H_{22}NO_4S^+$: $m/z = 384.12641$, exp.: $m/z = 384.12636$ ($\Delta = 0.13$ ppm).

6 Literature

1. Hu, M.; Chen, J. Y.; Li, Z. Y.; Au, L.; Hartland, G. V.; Li, X. D.; Marquez, M.; Xia, Y. N., *Chem. Soc. Rev.* **2006**, 35, 1084-1094.
2. Murphy, C. J.; Gole, A. M.; Stone, J. W.; Sisco, P. N.; Alkilany, A. M.; Goldsmith, E. C.; Baxter, S. C., *Acc. Chem. Res.* **2008**, 41, 1721-1730.
3. Maye, M. M.; Lou, Y.; Zhong, C.-J., *Langmuir* **2000**, 16, 7520-7523.
4. Kryukov, A. I.; Stroyuk, A. L.; Zin'chuk, N. N.; Korzhak, A. V.; Kuchmii, S. Y., *J. Mol. Catal. A: Chem.* **2004**, 221, 209-221.
5. Katz, E.; Willner, I.; Wang, J., *Electroanalysis* **2004**, 16, 19-44.
6. Küstner, B.; Gellner, M.; Schutz, M.; Schöppler, F.; Marx, A.; Ströbel, P.; Adam, P.; Schmuck, C.; Schlucker, S., *Angew. Chem. Int. Ed.* **2009**, 48, 1950-1953.
7. Daniel, M. C.; Astruc, D., *Chem. Rev.* **2004**, 104, 293-346.
8. Hirai, T.; Okubo, H.; Komasaawa, I., *J. Phys. Chem. B* **1999**, 103, 4228-4230.
9. Hickey, S. G.; Riley, D. J., *J. Phys. Chem. B* **1999**, 103, 4599-4602.
10. Zhu, J.; Liu, S.; Palchik, O.; Koltypin, Y.; Gedanken, A., *J. Solid State Chem.* **2000**, 153, 342-348.
11. Gao, F.; Lu, Q.; Zhao, D., *Nano Lett.* **2002**, 3, 85-88.
12. Lifshitz, E.; Dag, I.; Litvin, I.; Hodes, G.; Gorer, S.; Reisfeld, R.; Zelner, M.; Minti, H., *Chem. Phys. Lett.* **1998**, 288, 188-196.
13. Talapin, D. V.; Shevchenko, E. V.; Kornowski, A.; Gaponik, N.; Haase, M.; Rogach, A. L.; Weller, H., *Adv. Mater.* **2001**, 13, 1868-1871.
14. Bessekhoud, Y.; Robert, D.; Weber, J. V., *J. Photochem. Photobiol., A* **2003**, 157, 47-53.
15. Li, X.; Chen, W.; Bian, C.; He, J.; Xu, N.; Xue, G., *Appl. Surf. Sci.* **2003**, 217, 16-22.
16. Lambert, C.; Kriegisch, V.; Terfort, A.; Zeysing, B., *J. Electroanal. Chem.* **2006**, 590, 32-36.
17. Lambert, C.; Kriegisch, V., *Langmuir* **2006**, 22, 8807-8812.
18. Brevnov, D. A.; Finklea, H. O.; Van Ryswyk, H., *J. Electroanal. Chem.* **2001**, 500, 100-107.
19. Creager, S. E.; Yu, C. J.; Bamdad, C.; O'Conner, S.; MacLean, T.; Lam, E.; Chong, Y.; Olsen, G. T.; Luo, J.; Gozin, M.; Kayyem, J. F., *J. Am. Chem. Soc.* **1999**, 121, 1059.
20. Terrill, R. H.; Postlethwaite, T. A.; Chen, C.-H.; Poon, C.-D.; Terzis, A.; Chen, A.; Hutchison, J. E.; Clark, M. R.; Wignall, G.; Londono, J. D.; Superfine, R.; Falvo, M.; Johnson Jr., C. S.; Samulski, E. T.; Murray, R. W., *J. Am. Chem. Soc.* **1995**, 117, 12537-12548.
21. Hostetler, M. J.; Green, S. J.; Stokes, J. J.; Murray, R. W., *J. Am. Chem. Soc.* **1996**, 118, 4212-4213.
22. Murray, R. W., *Chem. Rev.* **2008**, 108, 2688-2720.
23. Sardar, R.; Funston, A. M.; Mulvaney, P.; Murray, R. W., *Langmuir* **2009**, 25, 13840-13851.
24. Bruchez, M.; Moronne, M.; Gin, P.; Weiss, S.; Alivisatos, A. P., *Science* **1998**, 281, 2013-2016.
25. Mulvaney, P., *Langmuir* **1996**, 12, 788-800.
26. Zhao, J.; Jensen, L.; Sung, J.; Zou, S.; Schatz, G. C.; Van Duyne, R. P., *J. Am. Chem. Soc.* **2007**, 129, 7647-7656.
27. Haes, A. J.; Zou, S.; Zhao, J.; Schatz, G. C.; Van Duyne, R. P., *J. Am. Chem. Soc.* **2006**, 128, 10905-10914.

28. Kottmann, J. P.; Martin, O. J. F.; Smith, D. R.; Schultz, S., *New J. Phys.* **2000**, 2, 27.1-27.9.
29. Ambjörnsson, T.; Mukhopadhyay, G.; Apell, S. P.; Käll, M., *Phys. Rev. B* **2006**, 73, 085412.
30. Nie, S.; Emory, S. R., *Science* **1997**, 275, 1102-1106.
31. Lakowicz, J. R.; Geddes, C. D.; Gryczynski, I.; Malicka, J.; Gryczynski, Z.; Aslan, K.; Lukomska, J.; Matveeva, E.; Zhang, J.; Badugu, R.; Huang, J., *J. Fluoresc.* **2004**, 14, 425-441.
32. Resch-Genger, U.; Grabolle, M.; Cavaliere-Jaricot, S.; Nitschke, R.; Nann, T., *Nat. Meth.* **2008**, 5, 763-775.
33. Zhang, J. A.; Fu, Y.; Lakowicz, J. R., *J. Phys. Chem. C* **2007**, 111, 1955-1961.
34. Grzelczak, M.; Perez-Juste, J.; Mulvaney, P.; Liz-Marzan, L. M., *Chem. Soc. Rev.* **2008**, 37, 1783-1791.
35. Gou, L.; Murphy, C. J., *Chem. Mater.* **2005**, 17, 3668-3672.
36. Nikoobakht, B.; El-Sayed, M. A., *Chem. Mater.* **2003**, 15, 1957-1962.
37. Nikoobakht, B.; Wang, J.; El-Sayed, A. M., *Chem. Phys. Lett.* **2002**, 366, 17-23.
38. Khanal, B. P.; Zubarev, E. R., *J. Am. Chem. Soc.* **2008**, 130, 12634-12635.
39. Jehn, C.; Kustner, B.; Adam, P.; Marx, A.; Strobel, P.; Schmuck, C.; Schlucker, S., *Phys. Chem. Chem. Phys.* **2009**, 11, 7499-7504.
40. Sun, Y.; Mayers, B. T.; Xia, Y., *Nano Lett.* **2002**, 2, 481-485.
41. Brust, M.; Walker, M.; Bethell, D.; Schiffrin, D. J.; Whyman, R., *J. Chem. Soc., Chem. Commun.* **1994**, 801-802.
42. Brust, M.; Fink, J.; Bethell, D.; Schiffrin, D. J.; Kiely, C., *J. Chem. Soc., Chem. Commun.* **1995**, 1655-1656.
43. Frens, G., *Nature: Phys. Sci.* **1973**, 241, 20-22.
44. Graber, K. C.; Freeman, R. G.; Hommer, M. B.; Natan, M. J., *Anal. Chem.* **1995**, 67, 735-743.
45. Tsunoyama, H.; Tsukuda, T., *J. Am. Chem. Soc.* **2009**, 131, 18216-18217.
46. Heaven, M. W.; Dass, A.; White, P. S.; Holt, K. M.; Murray, R. W., *J. Am. Chem. Soc.* **2008**, 130, 3754-3755.
47. Negishi, Y.; Chaki, N. K.; Shichibu, Y.; Whetten, R. L.; Tsukuda, T., *J. Am. Chem. Soc.* **2007**, 129, 11322-11323.
48. Tracy, J. B.; Kalyuzhny, G.; Crowe, M. C.; Balasubramanian, R.; Choi, J.-P.; Murray, R. W., *J. Am. Chem. Soc.* **2007**, 129, 6706-6707.
49. Jimenez, V. L.; Georganopoulou, D. G.; White, R. J.; Harper, A. S.; Mills, A. J.; Lee, D.; Murray, R. W., *Langmuir* **2004**, 20, 6864-6870.
50. Song, Y.; Harper, A. S.; Murray, R. W., *Langmuir* **2005**, 21, 5492-5500.
51. Toikkanen, O.; Ruiz, V.; Rönnholm, G.; Kalkkinen, N.; Liljeroth, P.; Quinn, B. M., *J. Am. Chem. Soc.* **2008**, 130, 11049-11055.
52. Qian, H.; Zhu, M.; Andersen, U. N.; Jin, R., *J. Phys. Chem. A* **2009**, 113, 4281-4284.
53. Chaki, N. K.; Negishi, Y.; Tsunoyama, H.; Shichibu, Y.; Tsukuda, T., *J. Am. Chem. Soc.* **2008**, 130, 8608-8610.
54. Qian, H.; Eckenhoff, W. T.; Zhu, Y.; Pintauer, T.; Jin, R., *J. Am. Chem. Soc.* **2010**, 132, 8280-8281.
55. Jadzinsky, P. D.; Calero, G.; Ackerson, C. J.; Bushnell, D. A.; Kornberg, R. D., *Science* **2007**, 318, 430-433.
56. Whetten, R. L.; Houry, J. T.; Alvarez, M. M.; Murthy, S.; Vezmar, I.; Wang, Z. L.; Stephens, P. W.; Cleveland, C. L.; Luedtke, W. D.; Landman, U., *Adv. Mater.* **1996**, 8, 428-433.
57. Barnard, A. S.; Curtiss, L. A., *ChemPhysChem* **2006**, 7, 1544-1553.

58. Barnett, R. N.; Cleveland, C. L.; Hakkinen, H.; Luedtke, W. D.; Yannouleas, C.; Landman, U., *Eur. Phys. J. D* **1999**, 9, 95-104.
59. Cleveland, C. L.; Landman, U.; Schaaff, T. G.; Shafigullin, M. N.; Stephens, P. W.; Whetten, R. L., *Phys. Rev. Lett.* **1997**, 79, 1873-1876.
60. Hakkinen, H., *Chem. Soc. Rev.* **2008**, 37, 1847-1859.
61. Akola, J.; Walter, M.; Whetten, R. L.; Häkkinen, H.; Grönbeck, H., *J. Am. Chem. Soc.* **2008**, 130, 3756-3757.
62. Templeton, A. C.; Wuelfing, W. P.; Murray, R. W., *Acc. Chem. Res.* **2000**, 33, 27-36.
63. Luedtke, W. D.; Landman, U., *J. Phys. Chem. B* **1998**, 102, 6566-6572.
64. Hostetler, M. J.; Wingate, J. E.; Zhong, C.-J.; Harris, J. E.; Vachet, R. W.; Clark, M. R.; Londono, J. D.; Green, S. J.; Stokes, J. J.; Wignall, G. D.; Glish, G. L.; Porter, M. D.; Evans, N. D.; Murray, R. W., *Langmuir* **1998**, 14, 17-30.
65. Walter, M.; Akola, J.; Lopez-Acevedo, O.; Jadzinsky, P. D.; Calero, G.; Ackerson, C. J.; Whetten, R. L.; Grönbeck, H.; Häkkinen, H., *Proc. Natl. Acad. Sci. U. S. A.* **2008**, 105, 9157-9162.
66. Mie, G., *Ann. Phys.* **1908**, 25, 377-445.
67. Slistan-Grijalva, A.; Herrera-Urbina, R.; Rivas-Silva, J. F.; Ávalos-Borja, M.; Castellón-Barraza, F. F.; Posada-Amarillas, A., *Phys. E* **2005**, 27, 104-112.
68. Kreibig, U.; Vollmer, M., *Optical Properties of Metal Clusters*. Springer: Berlin, 1995.
69. Alvarez, M. M.; Houry, J. T.; Schaaff, T. G.; Shafigullin, M. N.; Vezmar, I.; Whetten, R. L., *J. Phys. Chem. B* **1997**, 101, 3706-3712.
70. Miles, D. T.; Murray, R. W., *Anal. Chem.* **2003**, 75, 1251-1257.
71. Hicks, J. F.; Templeton, A. C.; Chen, S.; Sheran, K. M.; Jasti, R.; Murray, R. W., *Anal. Chem.* **1999**, 71, 3703-3711.
72. Wolfe, R. L.; Murray, R. W., *Anal. Chem.* **2006**, 78, 1167-1173.
73. Kim, Y.-G.; Garcia-Martinez, J. C.; Crooks, R. M., *Langmuir* **2005**, 21, 5485-5491.
74. Wolfe, R. L.; Balasubramanian, R.; Tracy, J. B.; Murray, R. W., *Langmuir* **2007**, 23, 2247-2254.
75. Chen, S.; Murray, R. W.; Feldberg, S. W., *J. Phys. Chem. B* **1998**, 102, 9898-9907.
76. Quinn, B. M.; Liljeroth, P.; Ruiz, V.; Laaksonen, T.; Kontturi, K., *J. Am. Chem. Soc.* **2003**, 125, 6644-6645.
77. Chen, S.; Ingram, R. S.; Hostetler, M. J.; Pietron, J. J.; Murray, R. W.; Schaaff, T. G.; Houry, J. T.; Alvarez, M. M.; Whetten, R. L., *Science* **1998**, 280, 2098-2101.
78. Balasubramanian, R.; Guo, R.; Mills, A. J.; Murray, R. W., *J. Am. Chem. Soc.* **2005**, 127, 8126-8132.
79. Lee, D.; Donkers, R. L.; Wang, G.; Harper, A. S.; Murray, R. W., *J. Am. Chem. Soc.* **2004**, 126, 6193-6199.
80. Menard, L. D.; Gao, S.-P.; Xu, H.; Twisten, R. D.; Harper, A. S.; Song, Y.; Wang, G.; Douglas, A. D.; Yang, J. C.; Frenkel, A. I.; Nuzzo, R. G.; Murray, R. W., *J. Phys. Chem. B* **2006**, 110, 12874-12883.
81. Labande, A.; Ruiz, J.; Astruc, D., *J. Am. Chem. Soc.* **2002**, 124, 1782-1789.
82. Daniel, M.-C.; Ruiz, J.; Nlate, S.; Palumbo, J.; Blais, J.-C.; Astruc, D., *Chem. Commun.* **2001**, 2000-2001.
83. Green, S. J.; Stokes, J. J.; Hostetler, M. J.; Pietron, J.; Murray, R. W., *J. Phys. Chem. B* **1997**, 101, 2663-2668.
84. Qu, X.; Peng, Z.; Jiang, X.; Dong, S., *Langmuir* **2004**, 20, 2519-2522.
85. Ingram, R. S.; Murray, R. W., *Langmuir* **1998**, 14, 4115-4121.
86. Miles, D. T.; Murray, R. W., *Anal. Chem.* **2001**, 73, 921-929.
87. Yamada, M.; Tadera, T.; Kubo, K.; Nishihara, H., *Langmuir* **2001**, 17, 2363-2370.

88. Templeton, A. C.; Hostetler, M. J.; Warmoth, E. K.; Chen, S.; Hartshorn, C. M.; Krishnamurthy, V. M., *J. Am. Chem. Soc.* **1998**, 120, 4845.
89. Imahori, H.; Kashiwagi, Y.; Endo, Y.; Hanada, T.; Nishimura, Y.; Yamazaki, I.; Araki, Y.; Ito, O.; Fukuzumi, S., *Langmuir* **2004**, 20, 73-81.
90. Imahori, H.; Kashiwagi, Y.; Hanada, T.; Endo, Y.; Nishimura, Y.; Yamazaki, I.; Fukuzumi, S., *J. Mater. Chem.* **2003**, 13, 2890-2898.
91. Green, S. J.; Pietron, J. J.; Stokes, J. J.; Hostetler, M. J.; Vu, H.; Wuelfing, W. P.; Murray, R. W., *Langmuir* **1998**, 14, 5612-5619.
92. Schmid, G.; Pfeil, R.; Boese, R.; Bandermann, F.; Meyer, S.; Calis, G. H. M.; van der Velden, J. W. A., *Chem. Ber.* **1981**, 114, 3634-3642.
93. Briant, C. E.; Theobald, B. R. C.; White, J. W.; Bell, L. K.; Mingos, D. M. P.; Welch, A. J., *J. Chem. Soc., Chem. Commun.* **1981**, 201-202.
94. Turkevich, J.; Stevenson, P. C.; Hillier, J., *Discuss. Faraday Soc.* **1951**, 11, 55-75.
95. Weare, W. W.; Reed, S. M.; Warner, M. G.; Hutchison, J. E., *J. Am. Chem. Soc.* **2000**, 122, 12890-12891.
96. Thomas, K. G.; Kamat, P. V., *J. Am. Chem. Soc.* **2000**, 122, 2655-2656.
97. Ji, X.; Song, X.; Li, J.; Bai, Y.; Yang, W.; Peng, X., *J. Am. Chem. Soc.* **2007**, 129, 13939-13948.
98. Yonezawa, T.; Kunitake, T., *Colloids Surf., A* **1999**, 149.
99. Tshikhudo, T. R.; Demuru, D.; Wang, Z.; Brust, M.; Secchi, A.; Arduini, A.; Pochini, A., *Angew. Chem. Int. Ed.* **2005**, 44, 2913-2916.
100. Brennan, J. L.; Hatzakis, N. S.; Tshikhudo, T. R.; Dirvianskyte, N.; Razumas, V.; Patkar, S.; Vind, J.; Svendsen, A.; Nolte, R. J. M.; Rowan, A. E.; Brust, M., *Bioconjugate Chem.* **2006**, 17, 1373-1375.
101. Jang, S.; Kim, S. I.; Shin, S.; Joo, S.-W., *Surf. Interface Anal.* **2004**, 36, 43-48.
102. Ipe, B. I.; Thomas, K. G., *J. Phys. Chem. B* **2004**, 108, 13265-13272.
103. Pucci, A.; Tirelli, N.; Willneff, E. A.; Schroeder, S. L. M.; Galembeck, F.; Ruggeri, G., *J. Mater. Chem.* **2004**, 14, 3495-3502.
104. Li, D.; Li, J., *New J. Chem.* **2003**, 27, 498-501.
105. Badia, A.; Demers, L.; Dickinson, L.; Morin, F. G.; Lennox, R. B.; Reven, L., *J. Am. Chem. Soc.* **1997**, 119, 11104-11105.
106. Shon, Y.-S.; Choo, H., *Chem. Commun.* **2002**, 2560-2561.
107. Xue, C.; Arumugam, G.; Palaniappan, K.; Hackney, S. A.; Liu, H.; Liu, J., *Chem. Commun.* **2005**, 1055-1057.
108. Hostetler, M. J.; Templeton, A. C.; Murray, R. W., *Langmuir* **1999**, 15, 3782-3789.
109. Gu, T.; Whitesell, J. K.; Fox, M. A., *Chem. Mater.* **2003**, 15, 1358-1366.
110. Nerambourg, N.; Werts, M. H. V.; Charlot, M.; Blanchard-Desce, M., *Langmuir* **2007**, 23, 5563-5570.
111. Pramod, P.; Sudeep, P. K.; Thomas, K. G.; Kamat, P. V., *J. Phys. Chem. B* **2006**, 110, 20737-20741.
112. Schulz-Dobrick, M.; Sarathy, K. V.; Jansen, M., *J. Am. Chem. Soc.* **2005**, 127, 12816-12817.
113. Umeda, R.; Awaji, H.; Nakahodo, T.; Fujihara, H., *J. Am. Chem. Soc.* **2008**, 130, 3240-3241.
114. Busby, M.; Chiorboli, C.; Scandola, F., *J. Phys. Chem. B* **2006**, 110, 6020-6026.
115. Yamada, M.; Shen, Z.; Miyake, M., *Chem. Commun.* **2006**, 2569-2571.
116. Yee, C. K.; Jordan, R.; Ulman, A.; White, H.; King, A.; Rafailovich, M.; Sokolov, J., *Langmuir* **1999**, 15, 3486-3491.
117. Rowe, M. P.; Plass, K. E.; Kim, K.; Kurdak, C.; Zellers, E. T.; Matzger, A. J., *Chem. Mater.* **2004**, 16, 3513-3517.
118. Price, R. C.; Whetten, R. L., *J. Am. Chem. Soc.* **2005**, 127, 13750-13751.

119. Hicks, J. F.; Miles, D. T.; Murray, R. W., *J. Am. Chem. Soc.* **2002**, 124, 13322-13328.
120. Wu, Z.; Suhan, J.; Jin, R., *J. Mater. Chem.* **2009**, 19, 622-626.
121. Devadas, M. S.; Kwak, K.; Park, J. W.; Choi, J. H.; Jun, C. H.; Sinn, E.; Ramakrishna, G.; Lee, D., *J. Phys. Chem. Lett.* **2010**, 1, 1497-1503.
122. Jana, N. R.; Peng, X., *J. Am. Chem. Soc.* **2003**, 125, 14280-14281.
123. Müller, C. I.; Lambert, C.; Steeger, M.; Forster, F.; Wiessner, M.; Schöll, A.; Reinert, F.; Kamp, M., *Chem. Commun.* **2009**, 6213-6215.
124. Mulvaney, P.; Giersig, M., *J. Chem. Soc. Faraday Trans.* **1996**, 92, 3137-3143.
125. Leff, D. V.; O'Hara, P. C.; Heath, J. R.; Gelbart, W. M., *J. Phys. Chem.* **1995**, 99, 7036-7041.
126. Brust, M.; Kiely, C. J., *Colloids Surf., A* **2002**, 202, 175-186.
127. Reetz, M. T.; Helbig, W.; Quaiser, S. A.; Stimming, U.; Breuer, N.; Vogel, R., *Science* **1995**, 267, 367-369.
128. Kohlmann, O.; Steinmetz, W. E.; Mao, X.-A.; Wuelfing, W. P.; Templeton, A. C.; Murray, R. W.; Johnson Jr., C. S., *J. Phys. Chem. B* **2001**, 105, 8801-8809.
129. Chaki, N. K.; Kakade, B.; Vijayamohan, K. P.; Singh, P.; Dharmadhikari, C. V., *Phys. Chem. Chem. Phys.* **2006**, 8, 1837-1844.
130. Badia, A.; Cuccia, L.; Demers, L.; Morin, F.; Lennox, R. B., *J. Am. Chem. Soc.* **1997**, 119, 2682-2692.
131. Kotiaho, A.; Lahtinen, R.; Efimov, A.; Lehtivuori, H.; Tkachenko, N. V.; Kanerva, T.; Lemmetyinen, H., *J. Photochem. Photobiol., A* **2010**, 212, 129-134.
132. Schaaff, T. G.; Shafiqullin, M. N.; Khoury, J. T.; Vezmar, I.; Whetten, R. L., *J. Phys. Chem. B* **2001**, 105, 8785-8796.
133. Wu, M. L.; Chen, D. H.; Huang, T. C., *Langmuir* **2001**, 17, 3877-3883.
134. Woehrlé, G. H.; Brown, L. O.; Hutchison, J. E., *J. Am. Chem. Soc.* **2005**, 127, 2172-2183.
135. Brown, L. O.; Hutchison, J. E., *J. Am. Chem. Soc.* **1997**, 119, 12384-12385.
136. Love, J. C.; Estroff, L. A.; Kriebel, J. K.; Nuzzo, R. G.; Whitesides, G. M., *Chem. Rev.* **2005**, 105, 1103-1170.
137. Wieder, M. E.; Hone, D. C.; Cook, M. J.; Handsley, M. M.; Gavrilovic, J.; Russell, D. A., *Photochem. Photobiol. Sci.* **2006**, 5, 727-734.
138. Hone, D. C.; Walker, P. I.; Evans-Gowing, R.; FitzGerald, S.; Beeby, A.; Chambrier, I.; Cook, M. J.; Russell, D. A., *Langmuir* **2002**, 18, 2985-2987.
139. Kim, J.; Piao, Y.; Hyeon, T., *Chem. Soc. Rev.* **2009**, 38, 372-390.
140. Cheng, Y.; Samia, A. C.; Meyers, J. D.; Panagopoulos, I.; Fei, B.; Burda, C., *J. Am. Chem. Soc.* **2008**, 130, 10643-10647.
141. Doering, W. E.; Piotti, M. E.; Natan, M. J.; Freeman, R. G., *Adv. Mater.* **2007**, 19, 3100-3108.
142. Shanmukh, S.; Jones, L.; Driskell, J.; Zhao, Y. P.; Dluhy, R.; Tripp, R. A., *Nano Lett.* **2006**, 6, 2630-2636.
143. Aslan, K.; Gryczynski, I.; Malicka, J.; Matveeva, E.; Lakowicz, J. R.; Geddes, C. D., *Curr. Opin. Biotechnol.* **2005**, 16, 55-62.
144. Cao, Y. W. C.; Jin, R. C.; Mirkin, C. A., *Science* **2002**, 297, 1536-1540.
145. Malicka, J.; Gryczynski, I.; Geddes, C. D.; Lakowicz, J. R., *J. Biomed. Opt.* **2003**, 8, 472-478.
146. Aslan, K.; Lakowicz, J. R.; Szmajcinski, H.; Geddes, C. D., *J. Fluores.* **2004**, 14, 677-679.
147. You, C.-C.; Miranda, O. R.; Gider, B.; Ghosh, P. S.; Kim, I.-B.; Erdogan, B.; Krovi, S. A.; Bunz, U. H. F.; Rotello, V. M., *Nat. Nanotechnol.* **2007**, 2, 318-323.
148. Bunz, U. H. F.; Rotello, V. M., *Angew. Chem. Int. Ed.* **2010**, 49, 3268-3279.

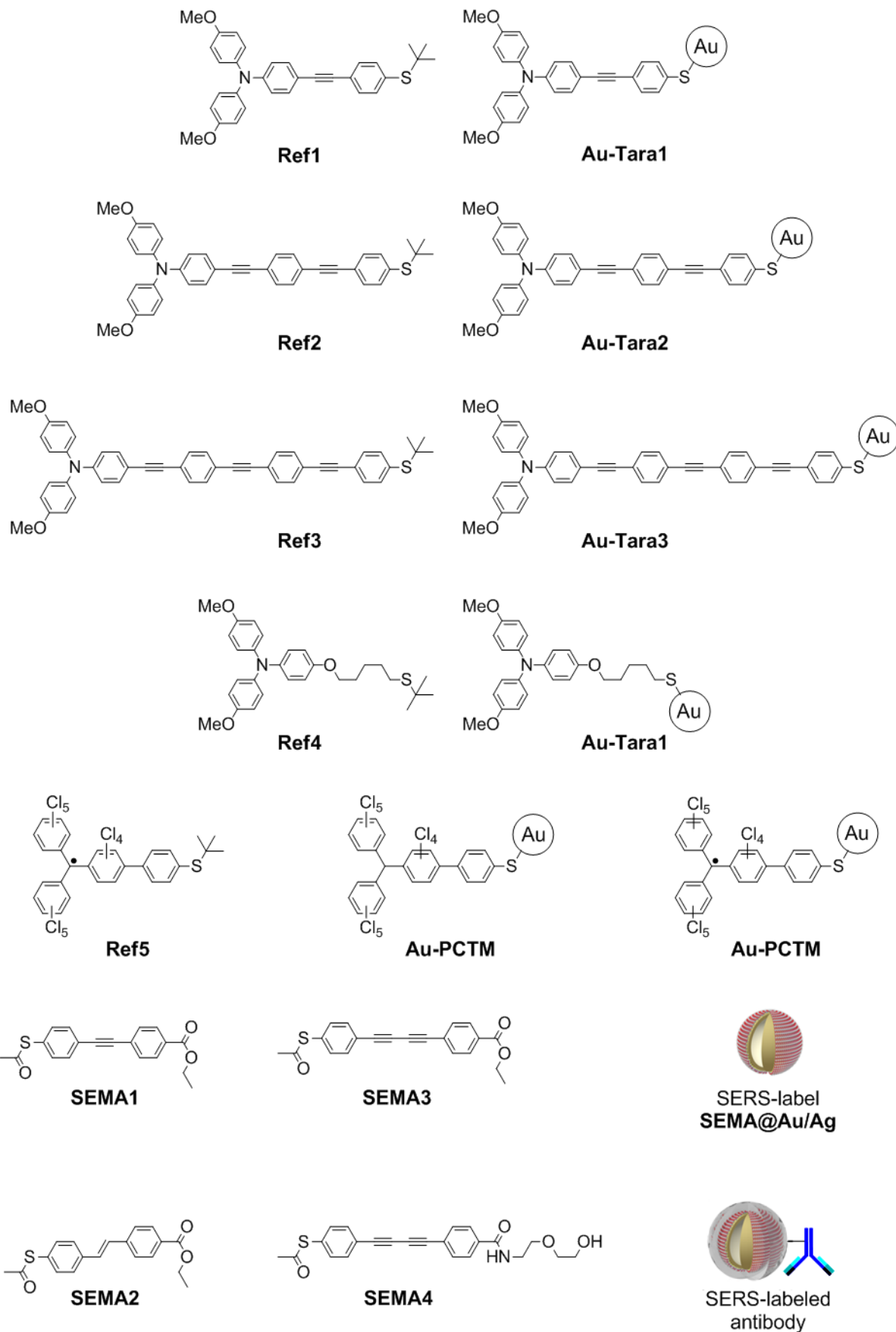
149. Myroshnychenko, V.; Rodriguez-Fernandez, J.; Pastoriza-Santos, I.; Funston, A. M.; Novo, C.; Mulvaney, P.; Liz-Marzan, L. M.; Garcia de Abajo, F. J., *Chem. Soc. Rev.* **2008**, *37*, 1792-1805.
150. Zabet-Khosousi, A.; Dhirani, A.-A., *Chem. Rev.* **2008**, *108*, 4072-4124.
151. Schütz, M.; Müller, C. I.; Salehi, M.; Lambert, C.; Schlücker, S., *J. Biophotonics* **2010**, DOI: 10.1102/.
152. Zhang, J.; Malicka, J.; Gryczynski, I.; Lakowicz, J. R., *J. Phys. Chem. B* **2005**, *109*, 7643-7648.
153. Fukuzumi, S.; Hanazaki, R.; Kotani, H.; Ohkubo, K., *J. Am. Chem. Soc.* **2010**, *132*, 11002-11003.
154. Shen, Z.; Yamada, M.; Miyake, M., *J. Am. Chem. Soc.* **2007**, *129*, 14271-14280.
155. Kanehara, M.; Takahashi, H.; Teranishi, T., *Angew. Chem. Int. Ed.* **2008**, *47*, 307-310.
156. Chandrasekharan, N.; Kamat, P. V.; Hu, J.; Il, G. J., *J. Phys. Chem. B* **2000**, *104*, 11103-11109.
157. Cai, X.; Anyaogu, K. C.; Neckers, D. C., *J. Am. Chem. Soc.* **2007**, *129*, 11324-11325.
158. Chen, W.; Zuckerman, N. B.; Kang, X.; Ghosh, D.; Konopelski, J. P.; Chen, S., *J. Phys. Chem. C* **2010**, *114*, 18146-18152.
159. Chen, W.; Chen, S.; Ding, F.; Wang, H.; Brown, L. E.; Konopelski, J. P., *J. Am. Chem. Soc.* **2008**, *130*, 12156-12162.
160. Kriegisch, V.; Lambert, C., *Top. Curr. Chem.* **2005**, *258*, 257-313.
161. Holzappel, M.; Lambert, C.; Selinka, C.; Stalke, D., *J. Chem. Soc., Perkin Trans. 2* **2002**, 1553-1561.
162. Heckmann, A.; Lambert, C., *J. Am. Chem. Soc.* **2007**, *129*, 5515-5527.
163. Lambert, C.; Noll, G.; Schmalzlin, E.; Meerholz, K.; Brauchle, C., *Chem.-Eur. J.* **1998**, *4*, 2129-2135.
164. Holzappel, M.; Lambert, C.; Selinka, C.; Stalke, D., *J. Chem. Soc.-Perkin Trans. 2* **2002**, 1553-1561.
165. Dümmler, S.; Roth, W.; Fischer, I.; Heckmann, A.; Lambert, C., *Chem. Phys. Lett.* **2005**, *408*, 264-268.
166. Heckmann, A.; Lambert, C.; Goebel, M.; Wortmann, R., *Angew. Chem. Int. Ed.* **2004**, *43*, 5851-5856.
167. Lambert, C.; Nöll, G., *Angew. Chem.* **1998**, *110*, 2239.
168. Lambert, C.; Nöll, G., *J. Am. Chem. Soc.* **1999**, *121*, 8434-8442.
169. Lambert, C.; Nöll, G.; Hampel, F., *J. Phys. Chem. A* **2001**, *105*, 7751.
170. Coropceanu, V.; Lambert, C.; Nöll, G.; Brédas, J. L., *Chem. Phys. Lett.* **2003**, *153*.
171. Amthor, S.; Noller, B.; Lambert, C., *Chem. Phys.* **2005**, *316*, 141-152.
172. Heckmann, A.; Amthor, S.; Lambert, C., *Chem. Commun.* **2006**, 2959-2961.
173. Lambert, C.; Amthor, S.; Schelter, J., *J. Phys. Chem. A* **2004**, *108*, 6474-6486.
174. Lambert, C.; Noll, G.; Schelter, J., *Nature Materials* **2002**, *1*, 69-73.
175. Kattinig, D. R.; Mladenova, B.; Grampp, G.; Kaiser, C.; Heckmann, A.; Lambert, C., *J. Phys. Chem. C* **2009**, *113*, 2983-2995.
176. Amthor, S.; Lambert, C., *J. Phys. Chem. A* **2006**, *110*, 1177-1189.
177. Lambert, C.; Nöll, G., *Angew. Chem. Int. Ed.* **1998**, *37*, 2107-2110.
178. Heckmann, A.; Dümmler, S.; Pauli, J.; Margraf, M.; Köhler, J.; Stich, D.; Lambert, C.; Fischer, I.; Resch-Genger, U., *J. Phys. Chem. C* **2009**, *113*, 20958-20966.
179. Takahashi, S.; Kuroyama, Y.; Sonogashira, K.; Hagihara, N., *Synthesis* **1980**, 627-630.
180. Lakowicz, J. R., *Principles of Fluorescence Spectroscopy*. 3rd ed.; Springer Science+Business Media: New York, 2006.
181. Li, D.; Zhang, Y.; Jiang, J.; Li, J., *J. Colloid Interface Sci.* **2003**, *264*, 109-113.
182. Ohyama, J.; Hitomi, Y.; Higuchi, Y.; Shinagawa, M.; Mukai, H.; Kodera, M.; Teramura, K.; Shishido, T.; Tanaka, T., *Chem. Commun.* **2008**, 6300-6302.

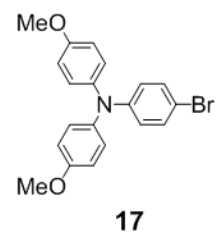
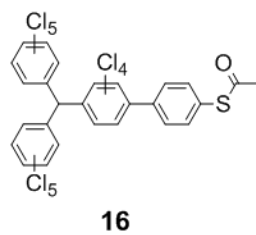
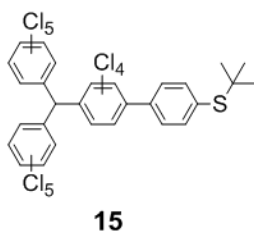
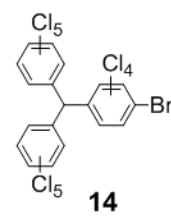
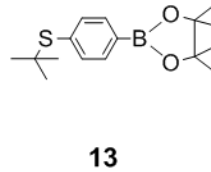
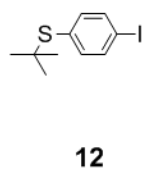
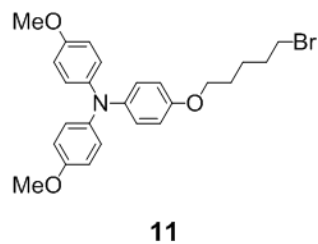
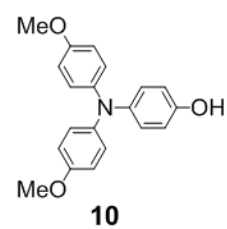
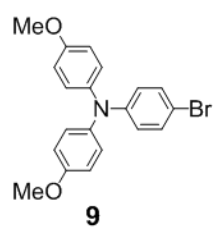
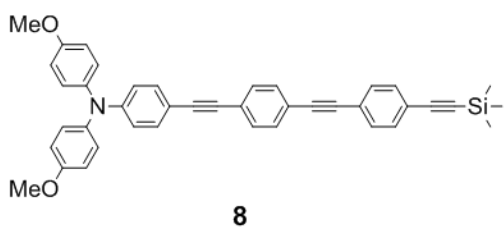
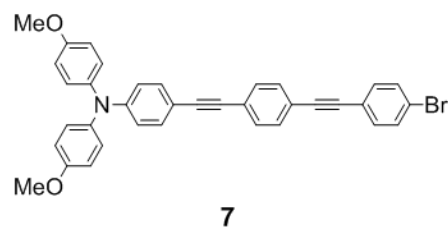
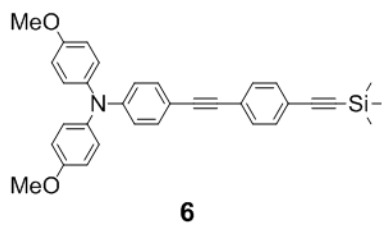
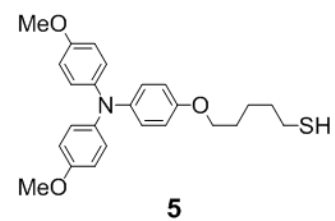
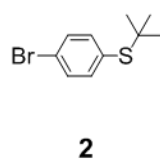
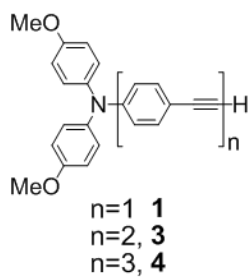
183. Lica, G. C.; Zelakiewicz, B. S.; Constantinescu, M.; Tong, J. *Phys. Chem. B* **2004**, 108, 19896-19900.
184. Cheng, P. P. H.; Silvester, D.; Wang, G. L.; Kalyuzhny, G.; Douglas, A.; Murray, R. W., *J. Phys. Chem. B* **2006**, 110, 4637-4644.
185. Sun, D.-L.; Rosokha, S. V.; Lindeman, S. V.; Kochi, J. K., *J. Am. Chem. Soc.* **2003**, 125, 15950-15963.
186. Müller, C. I.; Lambert, C., *Langmuir* **2011**, DOI: 10.1021/la1051244.
187. Buck, P.; Kobrich, G., *Tetrahedron Letters* **1967**, 1563-&.
188. Bonhote, P.; Moser, J. E.; Humphry-Baker, R.; Vlachopoulos, N.; Zakeeruddin, S. M.; Walder, L.; Gratzel, M., *J. Am. Chem. Soc.* **1999**, 121, 1324-1336.
189. Hu, J.; Fox, M. A., *J. Org. Chem.* **1999**, 64, 4959-4961.
190. Hostetler, M. J.; Stokes, J. J.; Murray, R. W., *Langmuir* **1996**, 12, 3604-3612.
191. Frey, S.; Stadler, V.; Heister, K.; Eck, W.; Zharnikov, M.; Grunze, M.; Zeysing, B.; Terfort, A., *Langmuir* **2001**, 17, 2408-2415.
192. Leung, T. Y. B.; Schwartz, P.; Scoles, G.; Schreiber, F.; Ulman, A., *Surf. Sci.* **2000**, 458, 34-52.
193. Lopez-Acevedo, O.; Akola, J.; Whetten, R. L.; Grönbeck, H.; Häkkinen, H., *J. Phys. Chem. C* **2009**, 113, 5035-5038.
194. Dapperheld, S.; Steckhan, E.; Grosse Brinkhaus, K.-H.; Esch, T., *Chem. Ber.* **1991**, 124, 2557-2567.
195. Dudek, S. P.; Sikes, H. D.; Chidsey, C. E. D., *J. Am. Chem. Soc.* **2001**, 123, 8033-8038.
196. Chidsey, C. E. D.; Bertozzi, C. R.; Putvinski, T. M.; Mujsce, A. M., *J. Am. Chem. Soc.* **1990**, 112, 4301-4306.
197. Horikoshi, T.; Itoh, M.; Kurihara, M.; Kubo, K.; Nishihara, H., *J. Electroanal. Chem.* **1999**, 473, 113-116.
198. Dhirani, A.-A.; Zehner, R. W.; Hsung, R. P.; Guyot-Sionnest, P.; Sita, L. R., *J. Am. Chem. Soc.* **1996**, 118, 3319-3320.
199. Watson, K.; Zhu, J.; Nguyen, S. T.; Mirkin, C. A., *Pure Appl. Chem.* **2000**, 72, 67-72.
200. Wei, G.-T.; Liu, F.-K.; Wang, C. R. C., *Anal. Chem.* **1999**, 71, 2085-2091.
201. Wilcoxon, J. P.; Martin, J. E.; Provencio, P., *Langmuir* **2000**, 16, 9912-9920.
202. Ruiz, V.; Colina, A.; Heras, A.; López-Palacios, J., *Small* **2006**, 2, 56-58.
203. Templeton, A. C.; Pietron, J. J.; Murray, R. W.; Mulvaney, P., *J. Phys. Chem. B* **2000**, 104, 564-570.
204. Rosokha, S. V.; Neretin, I. S.; Sun, D.; Kochi, J. K., *J. Am. Chem. Soc.* **2006**, 128, 9394-9407.
205. Kusamoto, T.; Ruiz, J.; Astruc, D., *New J. Chem.* **2009**, 33, 2204-2207.
206. Crivillers, N.; Mas-Torrent, M.; Vidal-Gancedo, J.; Veciana, J.; Rovira, C., *J. Am. Chem. Soc.* **2008**, 130, 5499-5506.
207. Mas-Torrent, M.; Crivillers, N.; Mugnaini, V.; Ratera, I.; Rovira, C.; Veciana, J., *Journal of Materials Chemistry* **2009**, 19, 1691-1695.
208. Chopin, S.; Cousseau, J.; Levillain, E.; Rovira, C.; Veciana, J.; Sandanayaka, A. S. D.; Araki, Y.; Ito, O., *J. Mater. Chem.* **2006**, 16, 112-121.
209. Lloveras, V.; Vidal-Gancedo, J.; Ruiz-Molina, D.; Figueira-Duarte, T. M.; Nierengarten, J.-F.; Veciana, J.; Rovira, C., *Faraday Discuss.* **2006**, 131, 291-305.
210. Domingo, V. M.; Castaner, J.; Riera, J.; Brillas, E.; Molins, E.; Martinez, B.; Knight, B., *Chem. Mater.* **1997**, 9, 1620-1629.
211. Bonvoisin, J.; Launay, J.-P.; Rovira, C.; Veciana, J., *Angew. Chem.* **1994**, 106, 2190-2193.
212. Sporer, C.; Ratera, I.; Ruiz-Molina, D.; Gancedo, J. V.; Wurst, K.; Jaitner, P.; Rovira, C.; Veciana, J., *J. Phys. Chem. Sol.* **2004**, 65, 753-758.

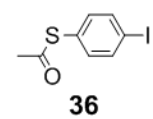
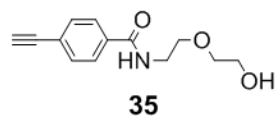
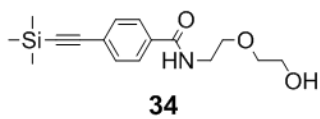
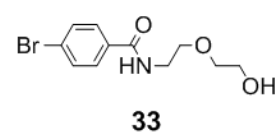
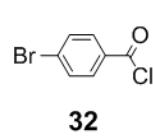
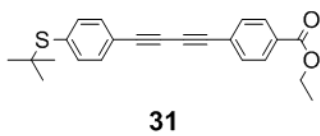
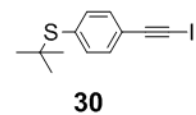
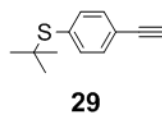
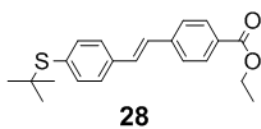
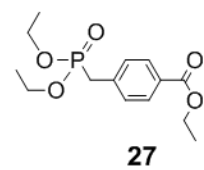
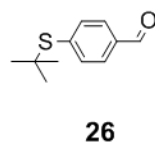
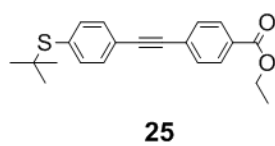
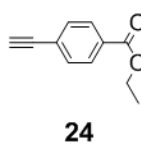
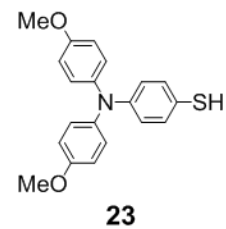
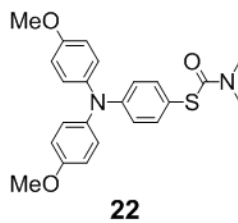
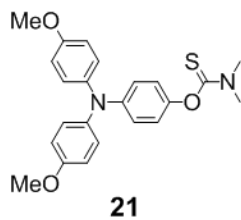
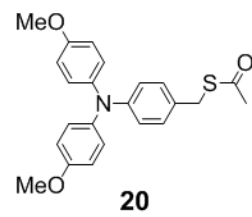
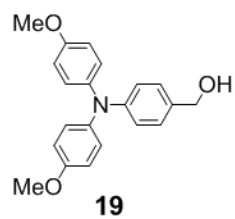
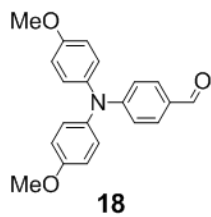
213. Crivillers, N.; Mas-Torrent, M.; Perruchas, S.; N, R.; Vidal-Gancedo, J.; Vecaina, J.; Rovira, C.; Basabe-Desmonts, L.; Ravoo, B. J.; Crego-Calama, M.; Reinhoudt, D. N., *Angew. Chem. Int. Ed.* **2007**, 46, 2215-2219.
214. Ribas, X.; Maspoch, D.; Wurst, K.; Veciana, J.; Rovira, C., *Inorg. Chem.* **2006**, 45, 5383-5392.
215. Miyaura, N.; Suzuki, A., *Chem. Rev.* **1995**, 95, 2457-2483.
216. Suzuki, A., *J. Organomet. Chem.* **1999**, 576, 147-168.
217. Rovira, C.; Bonvoisin, J.; Launay, J.-P.; Veciana, J., *Chem. Eur. J.* **2001**, 7, 240.
218. Armstrong, F. A.; Barlow, N. L.; Burn, P. L.; Hoke, K. R.; C, J. L. J., *Chem. Commun.* **2004**, 316-317.
219. Moseley, J. D.; Sankey, R. F.; Tang, O. N.; Gilday, J. P., *Tetrahedron* **2006**, 62, 4685-4689.
220. Hatano, M.; Maki, T.; Moriyama, K.; Arinbo, M.; Ishihara, K., *J. Am. Chem. Soc.* **2008**, 130, 16858-16860.
221. Harvey, J. N.; Jover, J.; Lloyd-Jones, G. C.; Moseley, J. D.; Murray, P.; Renny, J. S., *Angew. Chem. Int. Ed.* **2009**, 48, 7612-7615.
222. Roy, I.; Ohulchanskyy, T. Y.; Pudavar, H. E.; Bergey, E. J.; Oseroff, A. R.; Morgan, J.; Dougherty, T. J.; Prasad, P. N., *J. Am. Chem. Soc.* **2003**, 125, 7860-7865.
223. Camerin, M.; Magaraggia, M.; Soncin, M.; Jori, G.; Moreno, M.; Chambrier, I.; Cook, M. J.; Russell, D. A., *Eur. J. Cancer* **2010**, 46, 1910-1918.
224. Underwood, S.; Mulvany, P., *Langmuir* **1994**, 10, §427-3430.
225. Ni, W.; Yang, Z.; Chen, H.; Li, L.; Wang, J., *J. Am. Chem. Soc.* **2008**, 130, 6692-6693.
226. Zheng, Y. B.; Yang, Y. W.; Jensen, L.; Fang, L.; Juluri, B. K.; Flood, A. H.; Weiss, P. S.; Stoddart, J. F.; Huang, T. J., *Nano Lett.* **2009**, 9, 819-825.
227. Englebienne, P.; Van Hoonacker, A.; Verhas, M., *Analyst* **2001**, 126, 1645-1651.
228. Hutter, E.; Fendler, J. H., *Adv. Mater.* **2004**, 16, 1685-1706.
229. Frederix, F.; Friedt, J.-M.; Choi, K.-H.; Laureyn, W.; Campitelli, A.; Mondelaers, D.; Maes, G.; Borghs, G., *Anal. Chem.* **2003**, 75, 6894-6900.
230. Chah, S.; Hammond, M. R.; Zare, R. N., *Chem. Biol.* **2005**, 12, 323-328.
231. Watanabe, S.; Yoshida, K.; Shinkawa, K.; Kumagawa, D.; Seguchi, H., *Colloids Surf., B* **2010**, 81, 570-577.
232. Storhoff, J. J.; Lazarides, A. A.; Mucic, R. C.; Mirkin, C. A.; Letsinger, R. L.; Schatz, G. C., *J. Am. Chem. Soc.* **2000**, 122, 4640-4650.
233. Klajn, R.; Bishop, K. J. M.; Grzybowski, B. A., *Proc. Natl. Acad. Sci. U. S. A.* **2007**, 104, 10305-10309.
234. Klajn, R.; Wesson, P. J.; Bishop, K. J. M.; Grzybowski, B. A., *Angew. Chem. Int. Ed.* **2009**, 48, 7035-7039.
235. Klajn, R.; Stoddart, J. F.; Grzybowski, B. A., *Chem. Soc. Rev.* **2010**, 39, 2203-2237.
236. Yun, C. S.; Javier, A.; Jennings, T.; Fisher, M.; Hira, S.; Peterson, S.; Hopkins, B.; Reich, N. O.; Strouse, G. F., *J. Am. Chem. Soc.* **2005**, 127, 3115-3119.
237. Chhabra, R.; Sharma, J.; Wang, H.; Zou, S.; Lin, S.; Yan, H.; Lindsay, S.; Liu, Y., *Nanotechnology* **2009**, 20, 485201.
238. Persson, B. N. J.; Lang, N. D., *Phys. Rev. B* **1982**, 26, 5409-5415.
239. Maxwell, D. J.; Taylor, J. R.; Nie, S., *J. Am. Chem. Soc.* **2002**, 124, 9606-9612.
240. Phillips, R. L.; Miranda, O. R.; Mortenson, D. E.; Subramani, C.; Rotello, V. M.; Bunz, U. H. F., *Soft Matter* **2009**, 5, 607-612.
241. Phillips, R. L.; Miranda, O. R.; You, C.-C.; Rotello, V. M.; Bunz, U. H. F., *Angew. Chem. Int. Ed.* **2008**, 47, 2590-2594.
242. De, M.; Rana, S.; Akpınar, H.; Miranda, O. R.; Arvizo, R. R.; Bunz, U. H. F.; Rotello, V. M., *Nat. Chem.* **2009**, 1, 461-465.
243. Schlücker, S., *ChemPhysChem* **2009**, 10, 1344-1354.

244. Kneipp, J.; Kneipp, H.; McLaughlin, M.; Brown, D.; Kneipp, K., *Nano Letters* **2006**, 6, 2225-2231.
245. Hu, Q.; Tay, L.-L.; Noestheden, M.; Pezacki, J. P., *J. Am. Chem. Soc.* **2006**, 129, 14-15.
246. Stöber, W.; Fink, A.; Bohn, E., *J. Colloid Interface Sci.* **1968**, 26, 62-69.
247. García-Santamaría, F.; Salgueiriño-Maceira, V.; López, C.; Liz-Marzán, L. M., *Langmuir* **2002**, 18, 4519-4522.
248. Chen, M. M. Y.; Katz, A., *Langmuir* **2002**, 18, 8566-8572.
249. Pastoriza-Santos, I.; Pérez-Juste, J.; Liz-Marzán, L. M., *Chem. Mater.* **2006**, 18, 2465-2467.
250. Li, J. F.; Huang, Y. F.; Ding, Y.; Yang, Z. L.; Li, S. B.; Zhou, X. S.; Fan, F. R.; Zhang, W.; Zhou, Z. Y.; WuDe, Y.; Ren, B.; Wang, Z. L.; Tian, Z. Q., *Nature* **2010**, 464, 392-395.
251. Makarova, O. V.; Ostafin, A. E.; Miyoshi, H.; Norris, J. R.; Meisel, D., *J. Phys. Chem. B* **1999**, 103, 9080-9084.
252. Mulvaney, S. P.; Musick, M. D.; Keating, C. D.; Natan, M. J., *Langmuir* **2003**, 19, 4784-4790.
253. Doering, W. E.; Nie, S., *Anal. Chem.* **2003**, 75, 6171-6176.
254. Faulds, K.; McKenzie, F.; Smith, W. E.; Graham, D., *Angewandte Chemie International Edition* **2007**, 46, 1829-1831.
255. Sun, Y.; Xia, Y., *Anal. Chem.* **2002**, 74, 5297-5305.
256. Stuhr-Hansen, N.; Christensen, J. B.; Harrit, N.; Bjornholm, T., *J. Org. Chem.* **2003**, 68, 1275-1282.
257. Mayor, M.; Weber, H. B.; Reichert, J.; Elbing, M.; v. Hänisch, C.; Beckmann, D.; Fischer, M., *Angew. Chem. Int. Ed.* **2003**, 42, 5834-5838.
258. Chaplais, G.; Le Bideau, J.; Leclercq, D.; Vioux, A., *Chem. Mater.* **2003**, 15, 1950-1956.
259. Iwase, Y.; Kamada, K.; Ohta, K.; Kondo, K., *J. Mater. Chem.* **2003**, 13, 1575-1581.
260. Viau, L.; Maury, O.; Le Bozec, H., *Tetrahedron Lett.* **2004**, 45, 125-128.
261. Mu, Z. C.; Shu, L. J.; Fuchs, H.; Mayor, M.; Chi, L. F., *J. Am. Chem. Soc.* **2008**, 130, 10840-10841.
262. Silvert, P.-Y.; Herrera-Urbina, R.; Tekaiia-Elhsissen, K., *J. Mater. Chem.* **1997**, 7, 293-299.
263. Silvert, P.-Y.; Herrera-Urbina, R.; Duvauchelle, N.; Vijayakrishnan, V.; Elhsissen, K. T., *J. Mater. Chem.* **1996**, 6, 573-577.
264. Padmanabhan, S.; Coughlin, J. E.; Iyer, R. P., *Tetrahedron Lett.* **2005**, 46, 343-347.
265. Hermanson, G. T.; Mallia, A. K.; Smith, P. K., *Immobilized Affinity Ligand Techniques*. Academic Press: London, 1992.
266. Signoretti, S.; Waltregny, D.; Dilks, J.; Isaac, B.; Lin, D.; Garraway, A.; Yang, A.; Montironi, R.; McKeon, F.; Loda, M., *Am. J. Pathol.* **2000**, 157, 1769-1775.
267. Jerschow, A.; Müller, N., *J. Magn. Reson. A* **1997**, 125, 372-375.
268. Carlier, R.; Simonet, J., *Bull. Soc. Chim. Fr.* **1988**, 5, 831-833.
269. Salbeck, J., *Anal. Chem.* **1993**, 65, 2169-2173.
270. Dorfman, R. C.; Lin, Y.; Fayer, M. D., *J. Phys. Chem.* **1989**, 93, 6388-6396.
271. Klein, M.; Kroha, J.; Lohneysen, H. V.; Stockert, O.; Reinert, F., *Phys. Rev. B* **2009**, 79, 075111.
272. Zheng, S.; Barlow, S.; Risko, C.; Kinnibrugh, T. L.; Khrustalev, V. N.; Jones, S. C.; Antipin, M. Y.; Tucker, N. M.; Timofeeva, T. V.; Coropceanu, V.; Brédas, J.-L.; Marder, S. R., *J. Am. Chem. Soc.* **2006**, 128, 1812-1817.
273. Bandyopadhyay, A.; Varghese, B.; Sankararaman, S., *J. Org. Chem.* **2006**, 71, 4544-4548.

7 Table of Formulas







8 Zusammenfassung

In dieser Arbeit wurde die Synthese und Analyse von neuen Nanopartikel-Hybrid-Strukturen gezeigt. Darüber hinaus wurden die optischen, elektrochemischen und spektroelektrochemischen Eigenschaften dieser Materialien untersucht. Die Arbeit gliederte sich dabei in zwei Teile.

Der erste Teil beschäftigt sich mit Triarylamin- und PCTM-Radikal-funktionalisierten Gold-Nanopartikeln. Im Zentrum dieser Untersuchung stand neben der Synthese vor allem die Untersuchung von Chromophor-Chromophor Wechselwirkungen und Goldkern-Chromophor Wechselwirkungen. Dazu wurden in erster Linie Triarylamine mit verschiedenen Brückeneinheiten an den Goldkern angeknüpft und mit optischen und elektrochemischen Methoden untersucht.

Obwohl die Synthese von Chromophor-funktionalisierten Gold-Nanopartikeln eine große Herausforderung darstellte, konnten Syntheserouten zu stabilen Nanopartikeln entwickelt werden. Dabei hat sich vor allem der Einsatz einer Spritzenpumpe zur genauen Regelung der Zugabe-Geschwindigkeiten der einzelnen Reaktanden als nützlich erwiesen.

Im Weiteren konnten die Reinheit und die Abmessungen der Nanopartikel mit $^1\text{H-NMR}$ Spektroskopie, diffusion-ordered-NMR Spektroskopie-(DOSY), TGA, XPS und STEM genau bestimmt werden und die Zusammensetzung der Partikel mit einer elektrochemischen Analysemethode errechnet werden. Aus diesen Parametern wurde dann die Seeigel-artige Struktur der Partikel abgeleitet.

Die optischen Untersuchungen der Partikel zeigte ein anisotropes Absorptionsverhalten der Triarylamine, welches eine Folge von Goldkern-Chromophor Wechselwirkungen ist. Dieses Verhalten war allerdings sehr stark von der Orientierung des Übergangsdipolmoments des Chromophors zur Goldoberfläche abhängig und vom Abstand des Chromophors zur Goldoberfläche. So war das anisotrope Verhalten nur bei **Au-Tara1** zu beobachten. Die kurze und starre π -konjugierte Brückeneinheit begünstigte dabei die Chromophor-Goldkern Wechselwirkung.

In elektrochemischen Untersuchungen konnte gezeigt werden, dass die Triarylamin-Einheiten chemisch reversibel zum Monoradikal-Kation oxidiert werden können. Darüber hinaus konnte in den Messungen eine starke Interligand-Triarylamin-Triarylamin-Wechselwirkung für die **Au-Tara1** Partikel beobachtet werden. Die längeren

Brückeneinheiten der **Au-Tara2** und **Au-Tara3** Partikel als auch die aliphatische Brücke des **Au-Tara4** Partikels verhinderten eine elektronische Interligand-Wechselwirkung. Somit zeigt sich, dass nicht nur die Triarylamin-Goldkern-Wechselwirkung sondern auch die Interligand-Wechselwirkung sehr sensitiv auf die Länge und Starrheit der Brücke reagieren.

In einer weiteren Untersuchung wurde das Elektronentransferverhalten der Triarylamin-Einheiten auf dem Partikel untersucht. In den dafür durchgeführten spektroelektrochemischen Untersuchungen wurde eine starke Kopplung zwischen benachbarten Triarylamin-Einheiten beobachtet. Dieses Verhalten wurde den Intervalenz-Wechselwirkungen durch den Raum zugeordnet und war weder für **Au-Tara3** noch für **Au-Tara4** zu beobachten. Diese Analyse zeigte, dass auch diese interligand Wechselwirkung stark von dem Abstand und der Orientierung der Triarylamin-Einheiten zueinander abhängt. Somit konnte durch die systematische Variierung der Brückeneinheit ein detaillierter Einblick in die optischen und elektrochemischen Eigenschaften von Triarylaminen adsorbiert auf kleinen runden Gold-Nanopartikeln gegeben werden.

Des Weiteren wurden Goldpartikel mit einem perchlorierten Triarylmethan (PCTM)-Derivat funktionalisiert und dann chemisch radikalisiert. Der resultierende PCTM-Radikal-Gold-Nanopartikel wurde anschließend analysiert. Die Größe des Goldkerns wurde auf kleiner als 1 nm abgeschätzt. Es zeigte sich, dass die optischen und elektrochemischen Eigenschaften des Radikals durch die Anbindung an die Goldoberflächen nur in geringem Maße beeinflusst werden. Hierfür war vor allem die unvollständige Radikalisierung verantwortlich. Anhand von spektroelektrochemischen Messungen konnte gezeigt werden, dass zwischen den beiden magnetischen on/off Zuständen des Radikals und des Anions reversibel geschaltet werden kann. Der PCTM-Radikal-funktionalisierte-Gold-Nanopartikel stellt somit einen frei diffundierenden Nanoschalter da.

Im zweiten Teil dieser Arbeit wurden neue Moleküle, sogenannte SERS-Marker, für den Einsatz in immuno-SERS-Mikroskopie Experimenten synthetisiert. Zu diesem Zweck wurden die Moleküle mit verschiedenen Raman-aktiven Einheiten und einer Thiol-Funktion ausgestattet. Dabei sollte die Raman Schwingung des Markers entlang der Molekül-Achse polarisiert sein, um ein intensives SERS-Signal zu bekommen. In Zusammenarbeit mit der Arbeitsgruppe von Prof. S. Schlücker (Universität Osnabrück) wurden die Marker mittels Thiol-Einheit auf Au/Ag-Hohlkugeln aufgebracht (SERS-Label) und dann untersucht. Die SERS-Spektren der SERS-Label zeigten intensive und für jeden Marker charakteristische SERS-Signale.

Für immuno-SERS-Experimente wurde dann **SEMA3** mit einer hydrophilen Schwanzeinheit versehen. Dieser Marker wurde wiederum auf eine Au/Ag-Hohlkugel aufgebracht und an den hydrophilen Schwanzeinheiten mit einer Silikatschicht überzogen. Anschließend wurde zusätzlich ein anti-p63 Antikörper aufgebracht, um den Tumorsuppressor p63 zu detektieren, der vor allem in gutartigen Prostata-Gewebe vorkommt. Mit dem SERS-markierten Antikörper konnte an Prostata-Gewebe p63 im Basal-Epithel nachgewiesen werden. Diese Untersuchungen zeigen das Potential dieser Methode zum gleichzeitigen Nachweis verschiedener Biomoleküle in einem Multiplexing Experiment.

Appendix

Poster

Optical and Electrochemical Properties of Triarylamine Attached via π -Conjugated Bridges to Gold-Nanoparticles. Christian Müller, Christoph Lambert. *ICP2007*, Köln 2007.

Optical and Electrochemical Properties of Triarylamine and Perchlorotriphenylmethyl Radicals Attached to Gold-Nanoparticles via π -Conjugated Bridges. Christian Müller, Christoph Lambert. *Symposium on Photochemistry*, Göteborg 2008.

Optical and Electrochemical Properties of Mixed-Valence Triarylamine-Gold-Nanoparticle Conjugates. Christian Müller, Christoph Lambert. *ICP2009*, Toledo 2009.

Publikations

Mixed-Valence Interactions in Triarylamine-Gold-Nanoparticle Conjugates. Müller, C. I.; Lambert, C.; Steeger, M.; Forster, F.; Wiessner, M.; Schöll, A.; Reinert, F.; Kamp, M. *Chem. Commun.* **2009**, *41*, 6213-6215.

Design and synthesis of Raman reporter molecules for tissue imaging by immuno-SERS microscopy. Schütz, M.; Müller, C. I.; Salehi, M.; Lambert, C.; Schlücker, S. *J. Biophotonics* **2011**, DOI: 10.1102/.

Electrochemical and optical characterization of triarylamine functionalized gold nanoparticles. Müller, C. I.; Lambert, C. *Langmuir* **2010**, DOI: 10.1021/la1051244.

Danksagung

An dieser Stelle möchte ich mich bei allen bedanken, die zum Gelingen dieser Arbeit beigetragen haben. Mein besonderer Dank gilt dabei:

Herrn Dr. M. Grüne und Frau E. Ruckdeschel für die Aufnahme der NMR Spektren.

Herrn Dr. M. Büchner, Herrn F. Dadrich und Frau A. Hautzinger für die Aufnahme der Massenspektren.

Herrn M. Ramold für sämtliche Sonderanfertigungen für verschiedene Messungen.

Herrn M. Braun für die gut gelaunte und jederzeit bereitwillige Unterstützung bei technischen Problemen.

Allen Angestellten des Instituts für Organische Chemie: *Herrn Dr. C. Stadler, Frau P. Leckert, Frau A. Krug, Frau A. Dreher, Frau U. Rüppel, Herrn M. Fromm, Herrn M. Ludwig, Herrn F. Förtsch und Herrn B. Brunner.*

Der Arbeitsgruppe von *Prof. Dr. F. Reinert* (Physik - Würzburg) danke ich für die XPS Messungen. Mein besonderer Dank gilt dabei *Dr. F. Forster* und *M. Wiessner* für die praktische und kurzfristige Durchführung der Messungen.

Prof. Dr. M. Kamp (Physik - Würzburg) möchte ich für die STEM Messungen danken und seine aufgeschlossenen Art und Weise dem „Chemiker“ gegenüber.

Dr. C. Gellermann (Fraunhofer ISC Würzburg) und *Frau Schindler* (Fraunhofer ISC Würzburg) danke ich für die Probemessungen am TEM.

Prof. Dr. G. Krohne (Biologie - Würzburg) und *C. Gehrig* (Biologie - Würzburg) möchte ich dafür danken, dass sie mir die Möglichkeit gegeben haben selbstständig am TEM zu messen. Eine besondere Erfahrung an einem besonderen Gerät.

Prof. Dr. S. Schlücker (Physik - Osnabrück) und seinem Team möchte ich für die sehr gute und interessante Kooperation danken. Besonders möchte ich hierbei *M. Schütz* danken, der die SERS-Messungen durchgeführt hat und ein sehr aufgeschlossener Planungspartner war.

G. Jarre (IOC - Würzburg) und *T. Meinhardt* (IOC - Würzburg) für die Kooperation und die lustige Zeit während den TGA Messungen.

Christian Rewitz (AK Brixner) möchte ich für die Diskussionbereitschaft über das Mysterium Surface-Plasmon-Band danken. „Es hat was gebracht.“

Ein besonderer Dank gilt natürlich den Mitarbeitern des AK Lamberts.

Fabian Zieschang: Ich kenne keinen der so gerne ein Bier trinkt. ☺ Außerdem waren die Diskussionen im Caferaum immer schön. Auch wenn wir musikalisch nicht ganz auf einer Linie waren, so war die Zeit im Labor doch schön. Dienstag Reu? Ich bin da. ☺

Sebastian Völker: Die Zeit in Spanien wird mir unvergessen bleiben: „1 Euro das Pils und dazu Tapas umsonst. Verrückt.“ Am Buffet bleiben wir ungeschlagen. ☺ Neben den Aktivitäten nach 18 Uhr war auch die Zeit im Lab immer angenehm. Bis auf... (Siehe Fabi letzter Teil. ☺). Danke auch für die Kooperation bei der Organisation der Trikots und anderer Feste.

Johannes Klein: Danke nochmal für deine Kurrierdienste während des OP2s. Du weist schon. ☺ Außerdem kenne ich keinen, der eine solch Gute Laune an den Tag legt. Die Zeit im AK war schon schön, vorallem dein Siegeslauf am ChemCup 2010. ☺

Markus Steeger: Danke für deine Bereitschaft mit mir über synthetische und messtechnische Probleme zu diskutieren. Deinen Wissens-Support wusste ich immer zu schätzen. Außerdem warst du mein einziger Verbündeter im Lab gegen das PURE Grauen. ☺ Außerdem danke für die schöne Zeit nach der Uni und auf den Tagungen. Werde den Abend mit dem „Schmetterling und dem mp3 Player in Göteborg“ niemals vergessen. ☺
P.S.: „Es kann nur ein Törchen24 Team geben.“ ☺

Nina Dürrbeck: Danke für die Korrekturen und die musikalischen und die „Gott-und-die-Welt“ Gespräche. Ich glaube du kannst Rubens Bodycheck als einzige bezeugen. ☺ Eine schöne Zeit.

Dr. Dörte Reitzenstein: Danke, dass du mich mit in den Monteverdichor gezerrt hast. Eine sehr gute Entscheidung. ☺ Außerdem möchte ich dir für deine offene Art danken und das Trocknen der CV-Lömis.

Conrad Kaiser: Dir Conny danke ich für die sarkastischen und lebensbedrohlichen Situationen am Abzug. Unvergessen. ☺ Außerdem danke ich dir für die schöne Zeit während des Studiums und neben der Uni (Klingenberg, USA, FC Bayern : Manu).

Alexander Schmiedel: Danke für die Diskussionsbereitschaft bei physikalischen Fragestellungen und für das Wodka Seminar. ☺

Michael Moos: So lange bist du noch nicht dabei, aber ich schätze jetzt schon deine ruhige und lustige Art. ☺

Harald Ceymann: Der dritte Enkel vom Heckmann. ☺ Danke für deine Arbeiten während des F-Praktikums und dafür, dass du bis morgens in der Kälte ausgeharrst hast, nur um das Geschirr abzuspülen. ☺

Christl Wendinger: Danke für deine direkten Bemerkungen am Cafetisch. Außerdem möchte ich mich für die allgemeinen Laborarbeiten bedanken.

Alexander Heckmann: So eine lustige und clevere Person gibt es nur einmal. Danke für die so lustige Zeit Sascha (FTD). ☺ Das war unglaublich. Außerdem möchte ich mich für die Unterstützung auch neben der Uni bedanken. ☺ Ich hab deine Anwesenheit immer geschätzt.

Dr. Barbara Geiß: General Towns. ☺ Danke für die geniale Zeit in Göteborg und Toledo. Außerdem danke ich dir für deine Organisation von so vielen Festen und Ereignissen. Die Zeit im AK war super.

Ruben Ramon Müller: Deine Zeit im Arbeitskreis ist bei mir mit so vielen schönen Erinnerungen verbunden: die Diskussionen im Labor und im Caferaum, der Institutsausflug, deine Abschlussfeier und vieles mehr. Deine offene und lustige Art hat mich immer erfreut. ☺ Bis auf den Bodycheck. ☺

Die Ehemaligen (die Generäle a.D.): *Dr. M. Holzapfel, Dr. R. Stahl, Dr. V. Kriegisch, Dr. S. Amthor, D. Rausch.*

DAS CHEMCUP TEAM 2005-2010. Das waren immer besondere Tage, auch wenn der Sieg uns lange Zeit vergönnt blieb. Besonders danke ich der Goldenen Generation 2009-2010 (JACS Caver und Ernies & LAMBERT), die ich als Teammanager und Spieler zum Sieg begleiten durfte. Der ChemCup 2010 war das Größte Ereigniss. Wir haben den Pott. UNGLAUBLICH!!! ☺

P.S.: Ich hoffe das Team 2011 steht in der Tradition der letzten Jahre. Sowohl spielerisch als auch was das Trikot angeht. ☺

Der Pokal: Danke deinem Erfinder und dir. ☺

Ein besonderer Dank gilt auch *Tobias Häuser*, der doch den Dingen immer etwas Humoristisches abgewinnen konnte. Danke für die schöne und ausgiebige Zeit neben der Uni. Irgenwann habe auch ich eine Gibson. ☺

Dr. Fritz Popp: Danke für die geniale Zeit während des Studiums und in den USA. Auch möchte ich dir für deine Korrekturen danken.

Ich möchte mich ganz besonders bei meiner *Familie* und *Eva* für die Unterstützung und Aufbauung danken. Ohne eure Unterstützung wäre sicherlich die Promotion nicht möglich gewesen. Danke, daß ihr an mich geglaubt habt. Vielen DANK!!